Saeed Mehdizadeh

Adaptive beamformers for ultrasound imaging of acoustically hard tissues

Doctoral thesis
for the degree of Philosophiae Doctor (PhD)

Trondheim, August 2012

Norwegian University of Science and Technology
Faculty of Medicine
Department of Circulation and Medical Imaging

NTNU
Innovation and Creativity

Adaptive stråleformere for ultralydavbildning av akustisk hardt vev

Avbildning av skjelettstrukturer gjøres vanligvis ved hjelp av røntgenbaserte teknikker. Ønsket om å minimere bruk av ioniserende stråling, høye kostnader og manglende portabilitet gjør likevel at anvendelsen av disse teknikkene har begrensninger. Ultralyd er et alternativ til de røntgenbaserte teknikkene som ikke har kjente skadelige effekter. Ultralydavbildning av skjelettstrukturer har blitt forsøkt i ulike kliniske prosedyrer, for eksempel som orienteringsverktøy i minimalt invasiv ryggradskirurgi og når spinalbedøvelse skal gis. Generelt er avbildning av skjelettstrukturer med konvensjonell ultralyd mer preget av artefakter enn ved avbildning av bløtvev. Ved avbildning av ryggvirvler bærer bildet ofte preg av akustisk støy og andre artefakter som kan hindre visualisering av viktige strukturer, i tillegg til at det kan være vanskelig å finne beinoverflaten. Den akustiske støyen som sees i bildet kommer delvis på grunn av at ultralydstrålene blokkeres og delvis på grunn av strukturer som ligger utenfor aksen til ultralydstrålen. Blokkeringen kan redusere oppløsningen lateralt, noe som gir en uklar ryggvirveloverflate. Strukturer som ligger utenfor ultralydaksen kan forårsake uønskede ekko i avbildningsområdet på grunn av sidelober i det utsendte ultralydfeltet. Hovedmålet til denne avhandlingen er å forbedre visualiseringen av beinoverflater i ultralydbilder. Dette kan være nyttig i applikasjoner hvor man er interessert i å kartlegge beinstrukturer. Fordi oppløsningen og sidelobenivået som er oppnåelig ved bruk av standard stråleforming er fundamentalt begrenset, har vi undersøkt hvilke muligheter adaptiv stråleforming kan gi med tanke på støyreduksjon og forbedret kantdeteksjon. Denne avhandlingen inkluderer tre artikler. I artikkel A har vi lagt vekt på skyggeeffekter i skjelettavbildning som oppstår på grunn av delvis blokkering av ultralydstrålen. Artikkel B har to hovedmål: Å undersøke robustheten til stråleforming i skjelettavbildning ved hjelp av minimum varians-metoden, og å undersøke om en egenrombasert minimum varians stråleformingsteknikk (ESMV) kan framheve kanter fra akustisk hardt vev. I artikkel C undersøker vi et rammeverk for å detektere beinoverflater i ultralydbilder. I dette rammeverket bruker vi en ESMV stråleformer med rang 1 sammen med en strukturdeteksjonsteknikk basert på fasesymmetri for å gjenkjenne beinoverflater.
Resultatene viser at en robust ESMV stråleformer som bruker et signalunderrom av lav rang kan framheve beinoverflater, til tross for noe forvrengning av speckle-mønsteret. I tillegg har bildene konstruert med den nye teknikken unike fordeler som kan utnyttes videre i postprosesseringsmetoder der målet er å lokalisere bein i ultralydbildet.

Saeed Mehdizadeh
Institutt for sirkulasjon og bildediagnostikk, NTNU
Hovedveileder: Tonni F. Johansen, Biveileder: Sverre Holm

Ovennevnte avhandling er funnet verdig til å forsvares offentlig for graden Philosophiae Doctor(PhD) i medisinsk teknologi. Disputas finner sted i auditoriet, Medisinsk-teknisk forskningssenter, mondag 17, desember 2012, kl. 12:15.

Abstract

The imaging of bone structures is usually done using X-ray based modalities. However, the application of these modalities can be limited due to unwanted ionizing radiation exposure, scanning cost, and lack of portability. Ultrasound addresses these issues, offering a modality without any known harmful effects. Ultrasound imaging of the bone surface has been investigated in different clinical procedures, *e.g.*, guidance for minimal invasive (MI) procedures in spinal surgery, and for administration of spinal anesthesia. In general, bone imaging using conventional ultrasound techniques is prone to higher level of artifacts in comparison with soft tissue imaging. In the case of the spine, images are filled with acoustical noise, and artifacts that can impede visualization of important features, and also make it hard to detect the bone surfaces. The acoustical noise that appears in images of the bone (vertebra) is partly due to the obstruction of ultrasound beams, and to *off-axis* signals. The former can degrade the resolution in the lateral direction, resulting in unclear and stretched boundaries of the vertebrae. The latter is due to the sidelobe levels of ultrasound beams, causing unwanted speckles in the shadow region.

The main objective of this thesis is to enhance the visualization of bone surfaces in ultrasound images. This can be beneficial for applications in which extraction of the bone anatomy from B-mode images is of interest. Because the achievable resolution and sidelobe levels are fundamentally limited in the standard delay-and-sum beamforming technique, we investigate the potential of adaptive beamformers to alleviate some of the acoustical noise observed in the related images, and to improve the bone edges in ultrasound images.

In Paper A, we address artifacts (shadowing effects) resulting from partial obstruction of the imaging aperture in bone imaging scenarios. We investigate the potential of the minimum variance (MV) beamforming method to alleviate these artifacts. We show that the robustness of the MV beamformer degrades when the imaging aperture is highly obstructed by the bone structure due to the weak estimation of the covariance matrix. We suggest that the covariance matrix has to be estimated based only on the data from the un-shadowed elements. Thus, we adaptively determine the shadowed elements and discard their corresponding data from the covariance matrix to improve the MV beamformer performance.

In Paper B, we follow two main goals: to investigate the robustness of the minimum variance based beamformers in bone imaging scenarios, and to study an eigenspace minimum variance beamformer (ESMV) to improve the edges of the acoustically hard

tissues in the ultrasound images. In this paper, we use forward/backward averaging to enhance the covariance matrix estimation in imaging scenarios in which shadowing may occur. The enhanced covariance matrix is used to estimate ESMV weights. We show that the performance of the ESMV beamformer depends on the estimation of the signal subspace rank. The lower ranks of the signal subspace can enhance the edges and reduce noise in ultrasound images; however, the speckle pattern can become distorted. In Paper C, we investigate the potential of a framework for extracting the bone surface from B-mode images. In this framework, we use the ESMV beamformer technique together with a feature detection method as a tool for extracting the bone surfaces. In this paper, we show that an ESMV beamformer with a rank-1 signal subspace can preserve the bone anatomy and enhance the edges reasonably well, despite some distortion of the speckle pattern. Also, this makes the beamformer independent of the signal subspace estimation, which is one of the limitations of the eigenspace beamformers. The beamformed images are post-processed using a feature detection technique, and here we use the phase symmetry (PS). This method utilizes 2D Log-Gabor filters and has been shown to be effective as a ridge detector in bone localization in US images. We examine the proposed framework for imaging the spinal anatomy.

Preface

This thesis is submitted in partial fulfillment of the requirements for the degree of PhD at the Norwegian University of Science and Technology (NTNU). The research was funded by the Research Council of Norway (NFR), and by partners in the FINNUT project (NFR BIA 176899/I40). This work was carried out at the Department of Circulation and Medical Imaging, NTNU. The main supervisor was Associate Professor Tonni F. Johansen of the Department of Circulation and Medical Imaging, and co-supervisor was Professor Sverre Holm of the Department of Circulation and Medical Imaging, NTNU, and the Department of Informatics, University of Oslo.

Acknowledgements

I offer my sincerest gratitude to my main supervisor, Associate Professor Tonni F. Johansen, who has provided me with all kinds of guidance and supports throughout this thesis work. I have greatly benefited from his profound knowledge of both the technical and the practical aspects of ultrasound. In addition, I appreciate his ongoing friendship, care and support on a personal level.

I gratefully acknowledge Professor Sverre Holm, my co-supervisor, for his advice, supervision, and crucial contribution to my PhD. His enthusiasm and the fruitful discussions have helped me to complete this thesis. I also thank his research group at the Department of Informatics, University of Oslo, for their appreciable comments and discussions; particularly Dr. Andreas Austeng, who has been a great help in gaining many valuable insights on the field of array beamforming.

I acknowledge Professor Hans Torp, whose broad technical knowledge has been a great help to my work. Further, I appreciate the helps and efforts of my co-authors Dr. Sebastien Muller, who has been a great help in acquiring images, Dr. Gabriel Kiss, and Dr. Andreas Austeng. I also acknowledge my colleagues Thor Andreas Tangen, Jochen Deibele, and Ingvild Kinn Ekroll for their assistances in the laboratory work.

I thank Gabriel Kiss and Bastien Denarie for their comments and suggestions on this thesis, as well as all my other colleagues at the department for providing a sociable and inspiring work environment.

I thank the partners in the FINNUT project, both for the financial and technical supports, in particular Atle Kleven of Sonowand AS, and Tormodd Selbekk of SINTEF Health Care. I also thank Ole Solheim of St. Olav Hospital for his explanation of many clinical procedures.

I highly appreciate the support and encouragement of my friends in Trondheim, who have been very important to me in this period. My final thanks are reserved for my parents, and my brother for their moral support and their encouragement throughout these years.

Saeed Mehdizadeh
Trondheim, Norway, August 2012

Table of Contents

List of Figures

List of Tables

Chapter 1

Introduction

1.1 Medical ultrasound

Ultrasound has been used as a diagnostic medical tool for more than half a century [1]. The concept of this imaging modality relies on the pulse-echo technique, which in principle is similar to radar and sonar technology. The ultrasound transducer transmits a short pulse along a directed beam, which propagates in biological tissue. When this pulse hits a tissue with different acoustical properties the wave is reflected, refracted, or scattered depending on the size of the object. Part of the energy returns back to the transducer after a time delay of τ corresponding to the travel time. This time delay is used to determine the radial distance r of the tissue from the transducer, $r = \tau/2c$, where c is the sound speed in the tissue. The acoustical properties of a particular tissue are often defined using the acoustic impedance ($Z = \rho c$), where ρ is the density of the medium. The acoustical properties of some biological tissues are presented in TABLE 1.1.

The first development in medical ultrasound imaging was amplitude mode (A-mode) ultrasound, which was a one-dimensional scan. The difficulty of relating 1D signals to the underlying anatomy spurred the development of B-mode (brightness mode). A B-mode image is constructed using several scan-lines to show a two-dimensional cross section of the body. In this display mode, the image points are displayed in gray scale, with the brightness proportional to the amplitude of the reflections. Through technological advances in electronics, circuits design, acoustics, materials, and signal processing, ultrasound has gained widespread use as a diagnostic tool in different clinical procedures, *e.g.*, echocardiography, abdominal examination, and obstetrical sonography [2]. Further, the ultrasound modality due to its portability and real-time characteristic has become a practical guidance tool for surgeons in operating rooms. Although this imaging technique is able to form high quality images of soft tissues, its application in the imaging of bone anatomy remains a challenge due to various acoustical artifacts [3].

In ultrasound imaging, an array of piezoelectric elements is used to transmit the

Table 1.1: Acoustical properties of biological tissues. These values are only indicative of the order of magnitude, due to dramatic biological variability [5, 6].

Tissue	Sound speed c(m/s)	Impedance Z (Rayl)	Attenuation α (dB/cm/MHz)
Cancellous bone	1450-1800	$1.54 \times 10^6 - 2.2 \times 10^6$	10-40
Cortical bone	3000-4000	$4 \times 10^6 - 8 \times 10^6$	1-10
Muscle, skeletal	1580	1.64×10^6	0.74
Tendon[a,b]	1650	1.98×10^6	3.90
Fat	1450	1.36×10^6	0.8
Skin	1600	1.7×10^6	2-4

[a] In the perpendicular direction to the beams.

[b] The microstructure of tendons and ligaments is similar throughout the body and among species [7]. The reported α for ligaments (bovine samples) at 5 MHz frequency is 24.8 dB/cm in the perpendicular direction to fibers and 20.4 dB/cm along the fiber direction [8].

ultrasound pulses into the body, and receive the backscattered echoes from the biological tissue structure. Arrays are used for different applications, but are generally categorized into three groups: flat-linear, phase-linear, and curved-linear arrays. Flat-linear arrays are used for parallel scanning. For each scan-line, a group of the elements is used, and due to the related scan line, they are switched off and on. This type of array typically has an element size of the same order of magnitude as the wavelength (λ); therefore, the steering of the beams is limited due to the generation of grating lobes. Phase-linear arrays are typically used for cardiac applications. In this type of array, the scan-lines have a fixed origin at the center of the transducer surface, but they are steered in different angles to cover a sector. In this kind of array, the elements are smaller than half a wavelength to avoid grating lobe artifacts. A curved-linear array works similarly to a flat-linear array, but its surface is curved and the scan-lines are perpendicular to this surface. This type of array provides a wide scan region, which is useful for abdominal scanning. 1D arrays are able to steer and focus the ultrasound beam in the azimuth plane but they have a fixed focus in the elevation direction. The elevation focusing is done with a lens.

Multi-row arrays have been proposed to achieve uniform elevation resolution over an extended range and to preserve the lateral and axial resolution. The arrays can be divided into four groups based on degrees of control in the elevation plane [4]: 1D, 1.25D, 1.5D, 1.75D, and 2D.

Two-dimensional arrays can be used to make real-time 3D images. However, they require a large number of elements, which increase fabrication, signal processing, and array cooling costs. Thus, 1D arrays can be used instead to construct 3D images. This process can be performed based on two types of techniques: those that use mechanized scanning or freehand image acquisition systems. In the mechanized systems, the transducer can be translated, rotated around its central axis, or moved in a fan-like arc in fixed increments to make a specific number of 2D B-mode images [9]. Freehand systems provide physicians with the possibility to freely move the probe as in a normal

Table 1.2: Elevation properties of multi-row arrays [9].

Array	Elevation Properties
1D	Fixed aperture and focus.
1.25D	Fixed focus but variable aperture
1.5D	Variable apodization, focusing and aperture, but all are symmetric about the centerline of array.
1.75D	Same as 1.5D but no symmetry constraint.
2D	Full steering, focusing, apodization and aperture control.

2D examination. The position of each slice in relation to the others is determined using an optical tracking system.

1.2 Scattering and reflection of sound

Medical ultrasound imaging relies on the scattering of the transmitted pulse by the structure of the biological tissue. The type of scattering process depends on the size and roughness of the scatterer in comparison with the transmitted pulse wavelength. In general, there are three different types of scatterers based on the length scale: Rayleigh, diffractive, and specular scatterers.

- ***Rayleigh scatterer:*** A small scatterer whose dimension is much smaller than the wavelength responds to the sound insonification based on its density or compressibility difference from the surrounding medium. If its density remains the same but its compressibility is different, the scatterer starts to radiate the sound equally in all directions (monopole scattering). If the reverse condition holds, this scatterer moves back and forth in the direction of the insonifying sound (dipole scattering). Fig. 1.2 shows the scattering patterns of monopole

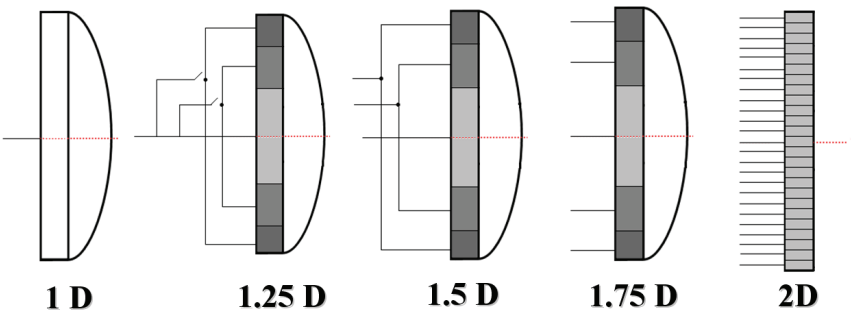

Figure 1.1: An elevation illustration of multi-row arrays.

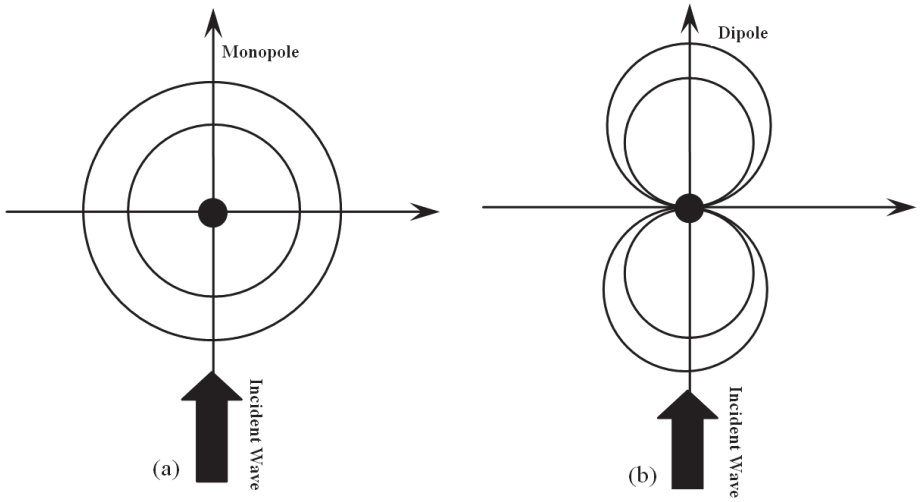

Figure 1.2: Schematic of the scattering pattern of a Rayleigh scatterer. (a) Monopole scatterer, and (b) dipole scatterer.

and dipole scatterers. These sub-wavelength scatterers are known as Rayleigh scatterers and considered to have f^4 intensity dependence [10], where f is the frequency of the insonifying beam. Typically the scattering from the soft tissue is modeled as a diffuse distribution of Rayleigh scatterers. If the distribution of these scatterers is spatially random, their reflections interfere incoherently and build up a granular texture image of the tissue known as the speckle pattern.

- ***Diffractive scatterer:*** If the scatterer size is comparable to the wavelength, the insonified scatterer acts as a secondary source. In such cases the scattering pattern becomes more complex and dependent on the value of ka, where $k = 2\pi/\lambda$, and a is the scatterer size. Fig. 1.3 illustrates angular scattering patterns from a small rigid sphere insonified with a plane wave at an angle of 180°. The illustration indicates that the forward scattering is increased for the higher values of ka, causing destructive interferences with the incident wave and resulting in a shadowing region.

- ***Specular scatterer:*** If the scatterer size is much larger than the wavelength the reflection process can be estimated based on ray theory. That is, the incident ultrasound impinging the surface of such scatterer is partially reflected back at the mirror angle of the incident beam [Fig. 1.4(a), and (b)], and the rest is transmitted. The transmitted beam can be refracted due to the sound speed variation between two different media. This may happen at the tissue interfaces, such as the boundaries of soft tissues and bones. The ratio between incident-reflected pressure, and incident-transmitted pressure is defined by the reflection

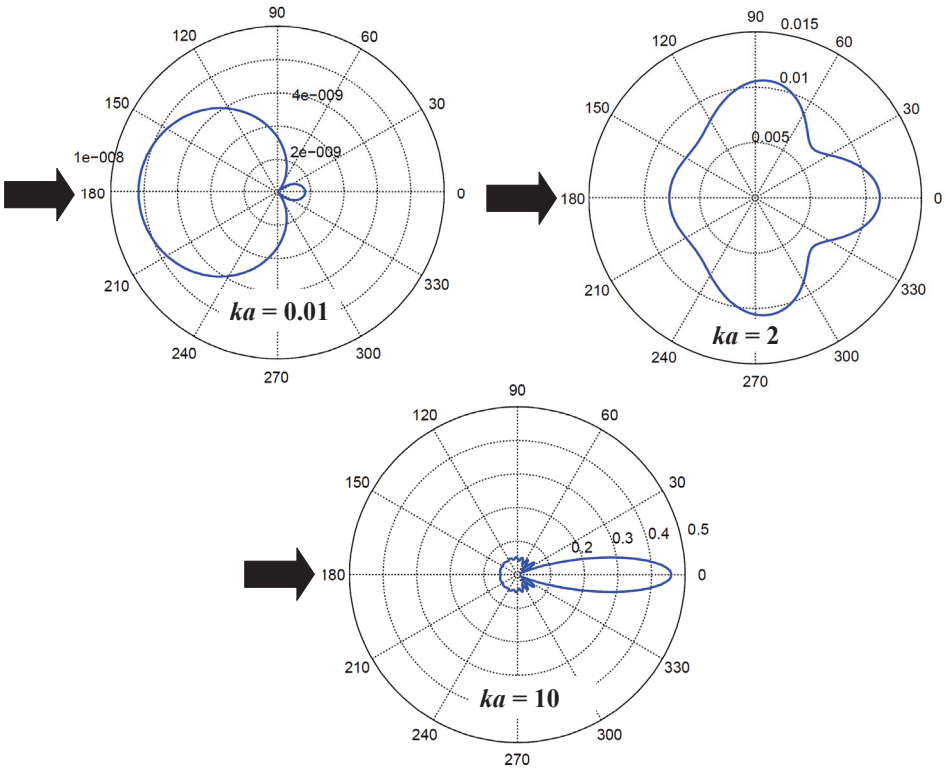

Figure 1.3: Scattering pattern from small rigid sphere insonified by a plane wave at 180° for ka= 0.01, 2, and 10. Reproduced from chapter 5.3.1 in [9].

coefficient (R) and the transmission coefficient (T) as:

$$R = \frac{Z_2 \cos(\theta_i) - Z_1 \cos(\theta_t)}{Z_2 \cos(\theta_i) + Z_1 \cos(\theta_t)}, \quad T = \frac{2Z_2 \cos(\theta_i)}{Z_2 \cos(\theta_i) + Z_1 \cos(\theta_t)}, \tag{1.1}$$

where θ_i and θ_t are the incident and transmit angles, respectively [Fig. 1.4(b)]. When ultrasound hits a cortical bone interface at normal incidence, approximately 25-50% of the incident energy is transferred to the reflected wave and the rest to longitudinal waves. For oblique incidence the refracted longitudinal plane wave in the solid is partially converted into a shear wave due to the wave conversion. It should be noted that the tissue interfaces often have a certain roughness, as shown in Fig. 1.4(c), introducing an additional diffuse scattering component to the reflected wave.

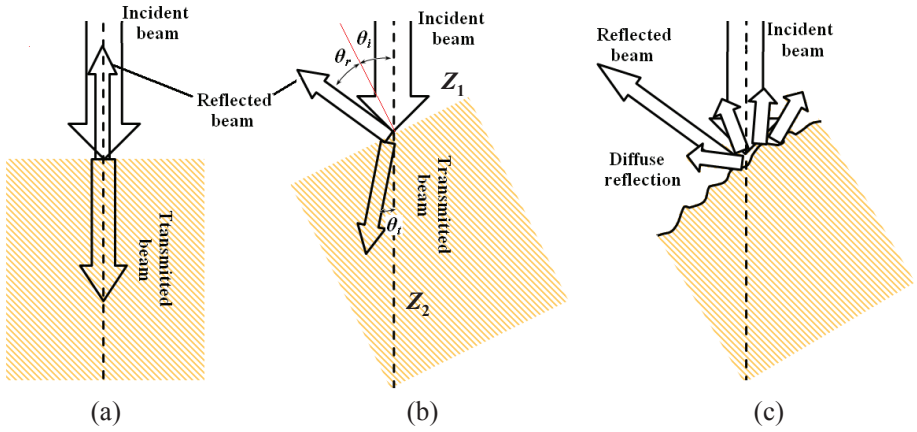

Figure 1.4: Specular reflection of a ultrasound beam impinging on a large scatterer. (a) Specular scattering on a smooth perpendicular surface, (b) specular reflection from a tilted surface, and (c) specular and diffuse scattering from a rough surface.

1.3 Bone imaging

The imaging of bone structures is usually done using X-ray based techniques such as standard projection X-ray or Computed Tomography (CT). However, the application of these modalities can be limited due to unwanted ionizing radiation exposure, scanning cost, and lack of portability. Ultrasound addresses these issues, offering a modality without any known harmful effects [11, 12]. These advantages have spurred researchers to investigate the potential of using ultrasound acquisition as an alternative to X-ray based techniques in some bone imaging scenarios. Ultrasound imaging of bone tissue has been investigated in different clinical procedures, *e.g.*, registration of bone in neurosurgeries and orthopedics [13–15], guidance for diagnosis of skeletal fractures in emergency rooms [16, 17], and pain management interventions [18, 19]. In particular, in some applications, dealing with the spine is of interest, *e.g.* guidance for minimal invasive (MI) procedures in spinal surgery [20, 21], and for administration of spinal anesthesia [19, 22–26].

The trend in surgery is toward minimally invasive procedures. Less invasive procedures are in most cases less traumatic for patients, who experience fewer side effects of the surgery and, thus, recover much faster than with open surgery. However, less invasive procedures introduce challenges for the surgeon, who is not able to directly see the organs that are treated, but only through an operating channel. Typically, the surgeon in many cases uses an endoscope or a microscope for inspection and control of the procedure. In many cases, it is important to be able to get an overview of the tissue surrounding the operating channel, *e.g.* orientation in the organs, compare with preoperative images, detect blood vessels, and inspect the result of the treatment. Thus, image guidance is essential for effective and safe minimally invasive procedures.

Minimally invasive computer assisted spine surgery may require a precise registration of preoperative images which are mainly obtained by CT and Magnetic Resonance Imaging (MRI) corresponding to the intra-operative patient coordinates. Conventional registration techniques are mainly landmark-based, that is, anatomical landmarks or fiducial markers are used [14]. These procedures are time demanding, and they are not able to visualize the anatomical changes during the surgery. By using intra-operative modalities the surgeon can localize the bone through the surface and offer complete anatomical structures for registration purposes [13, 14]. The use of CT, or MRI as intra-operative modalities has major drawbacks in terms of cost, portability, and ionizing radiation. Potentially, ultrasound can be an ideal intra-operative modality for guidance.
The other important procedure in MI spine surgery is the accurate localization of the target vertebra. Conventionally, localizing a vertebral level is performed by manual palpation and direct fluoroscopy. Thus, surgeons identify a specific anatomical landmark such as the sacrum, and, then, start counting under fluoroscopic control up to the targeted vertebral level [27]. This approach exposes the patient to an undesirable level of radiation, and is prone to counting errors due to the similar appearance of vertebrae in projection images [27]. Alternatively, ultrasound can improve patient safety and decrease the risk of wrong level surgery [28].
Additionally, ultrasound imaging is a valuable modality for enhancing the safety of different puncture techniques in regional anesthesia [25, 29]. These procedures are mostly performed landmark based or blind [25]. Ultrasound can facilitate these routines by visualizing the spinal anatomy, assisting to locate the puncture region before performing the injection procedure. Further, ultrasound can be used as a real-time modality for needle trajectory control, or more effective placement of medication [29]. Ultrasound guidance has been shown to be helpful in some superficial applications such as facet joint injections, but is not as useful in epidural injections (see Fig. 1.5), where the spinal structure obstructs the ultrasound beams and makes the images noisy. Fig. 1.6 taken from [29], shows the transversal and sagittal scan of the spine anatomy on the left column, and of the marked spinal anatomy on the right column. Based on the marked anatomy on the right column images, the optimal puncture point and needle direction are selected. However, due to the poor quality of the images, the procedure is heavily dependent on the experience of the anesthesiologist with ultrasound.

1.4 Anatomy of the spine

In this section an overview of the spine anatomy is addressed. The anatomical references used are mostly taken from [32, 33]. In a human, the vertebral column usually consists of 33 vertebrae, 9 of them are fused to form the sacral curve [Fig. 1.7 (a)], and the remaining 24 make up the upper part of the vertebral column. The upper region is also divided into three groups: cervical (C), thoracic (T), and lumbar (L). The number of vertebrae for each group is 7, 12, and 5 respectively.
The individual lumbar vertebrae are designated L1 (the most proximal vertebra),

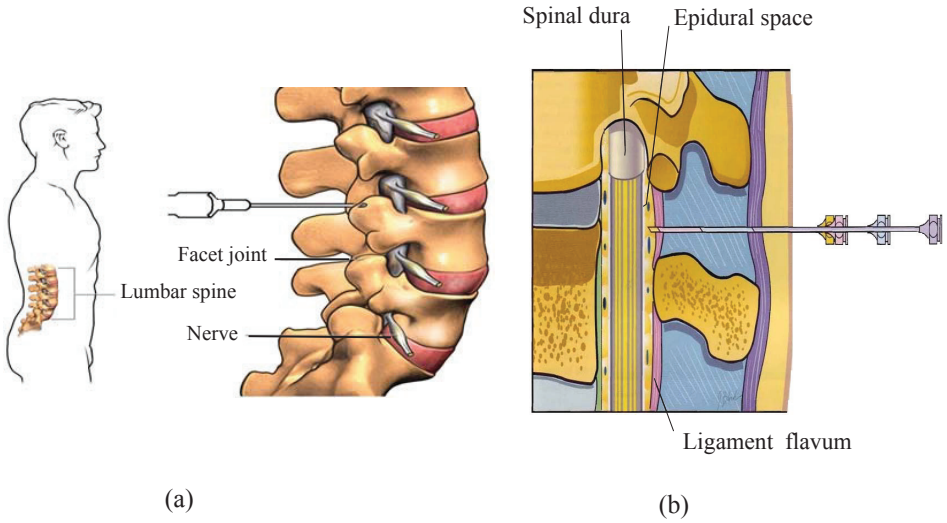

Figure 1.5: An illustration of spinal puncture. (a) Facet joint injection [30], and (b) epidural injection [31].

L2, L3, L4 and L5 (the most distal vertebra). The anterior portion of the vertebra consists of the vertebral body [Fig. 1.7 (b)]. The vertebral body is the main load bearing structure of the vertebra, consisting of an external shell of cortical bone surrounding a core of cancellous bone. The posterior elements of a vertebra are the spinous process, lamina, inferior articulating processes and the left and right transverse processes [Fig. 1.7 (b)]. The lamina basically connects the spinous process to the rest of the posterior elements. The spinous process and transverse processes provide lever arms for muscle attachment to the spine.
Ligaments are static stabilizers and control the joint motion. The ligaments of the lumbar spine can be multi-segmental or inter-segmental. The multi-segmental ligaments attach over multiple vertebrae, whereas the inter-segmental ones connect adjacent vertebrae together. The major ligaments of the lumbar spine are shown in Fig. 1.7 (c).

- ***Anterior longitudinal ligament:*** This multi-segmental ligament connects the anterior and medial surfaces of the vertebral bodies and intervertebral discs along the entire vertebral column. The major role of this ligament is to limit extension.
- ***Posterior longitudinal ligament:*** This multi-segmental ligament is located in the vertebral canal and attaches to the posterior surfaces of the vertebral bodies and intervertebral discs along the entire spinal column. The attachment to the

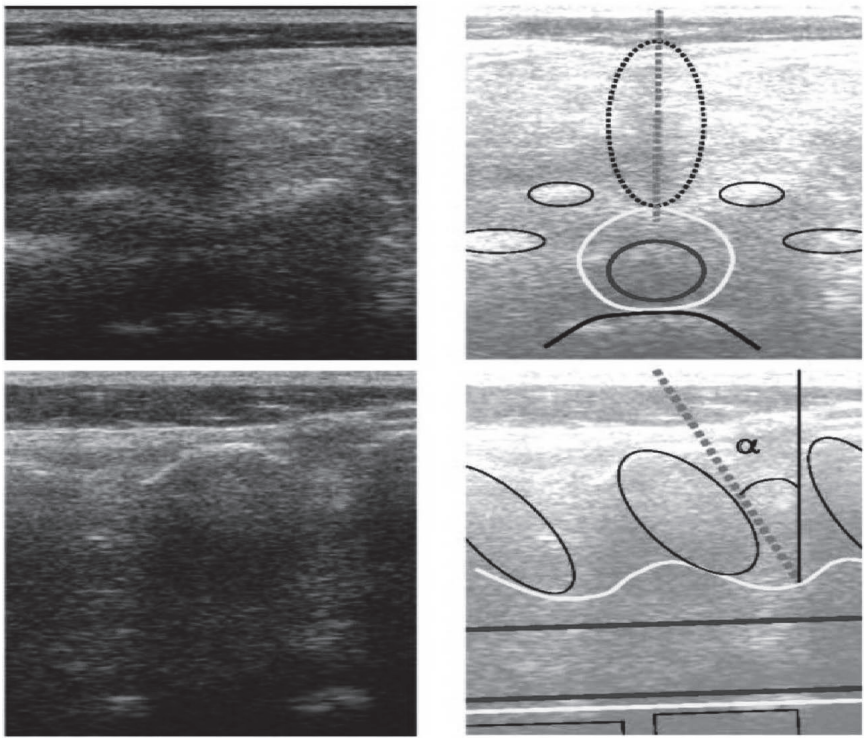

Figure 1.6: Lumbar transversal (top) and sagittal (bottom) scans of the epidural space. The original ultrasound images are presented on the left. The spinal anatomy is marked on the right. The black lines show bony structures, the white lines describe the outer borders of the epidural space, and the gray line shows the inner borders of the epidural space. The angle alpha is the angle between the normal line from the skin to the epidural space.The dotted line shows the expected puncture access [29].

vertebral bodies is limited to the medial portion; however, the attachment of this ligament spans the entire posterior surface of the intervertebral disc. Similar to the anterior longitudinal ligament, the posterior longitudinal ligament serves to restrict the posterior separation of the vertebral bodies.

- ***Ligamentum flavum:*** This is an inter-segmental ligament that connects the laminae of adjacent vertebrae. The ligamentum flavum is a highly elastic ligament. Its major role is to allow limited separation of the laminae of the vertebrae while ensuring no stress on the nearby nerve roots and spinal cord.

- ***Interspinous ligaments:*** These inter-segmental ligaments connect adjacent spinous processes, and they extend from the root to the apex of each process. Their role is to limit the distraction of the spinous processes during flexion.

- ***Supraspinous ligaments:*** These are multi-segmented ligaments that connect the apices of the spinous processes along the entire vertebral column. Similar to interspinous ligaments, they limits movement of the spinous processes during flexion.

1.5 Source of noise in bone imaging

In general, bone imaging using conventional ultrasound techniques is prone to a higher level of artifacts in comparison with soft tissue imaging [23, 34]. In the case of the spine, the images are filled with acoustical noise (Fig. 1.6), and artifacts that can impede visualization of important features, and also make it hard to detect the bone surfaces. The artifacts observed in ultrasound images of bone tissues may be due to high reverberation levels, specular reflections, shadowing effects, and high attenuation coefficients.

- ***Reverberation:*** The high echoic characteristic of the bone surface produces strong multiple scattering of transmit pulses. This effect creates some acoustical noise added as a tail to the main echo from the bone surface, observed as additive noise beneath the bone surface. It is well known that nonlinear imaging techniques such as second harmonic imaging [1], and SURF modality [35] can reduce reverberation artifacts in some cases. SURF utilizes a dual frequency band technique to reduce the reverberation artifact [35]. The SURF pulse complexes consist of a high frequency (HF) imaging pulse added to a low-frequency (LF) manipulation pulse, at a frequency ratio of (1:8-10). In this technique, two pulse complexes having similar HF pulses but opposite polarity LF pulses (180 phase difference) are transmitted in each beam direction. Such polarity difference causes the HF pulses to experience different speeds of sound due to nonlinear elasticity. This generates a time shift between two HF pulses, which is small in shallow depths but accumulates during forward propagation. Such variation in time-shift can be used to reduce reverberation in ultrasound images. For example, in Fig. 1.8(a) the reverberation noise beneath the lamina is observed; this has been reasonably well suppressed in Fig. 1.8(b) corresponding to the SURF imaging modality. The improvement in contrast between two marked areas in the SURF image is about 14 dB in comparison with the B-mode image.

- ***Specular reflection:*** When the scattering surface is smooth and large compared to the wavelength (λ), a specular reflection occurs; *i.e.* if the transmitted beam is not perpendicular to the surface, it will be reflected toward the off-axis direction, resulting in weak echoes. Fig. 1.9 presents schematically the specular reflections from different parts of a vertebra surface. Fig. 1.9(a) shows an orthogonal reflection whereas Fig. 1.9(b) demonstrates an off-axis reflection. Fig. 1.9(c) illustrates which parts of a vertebra can be visualized by the standard ultrasound imaging technique.

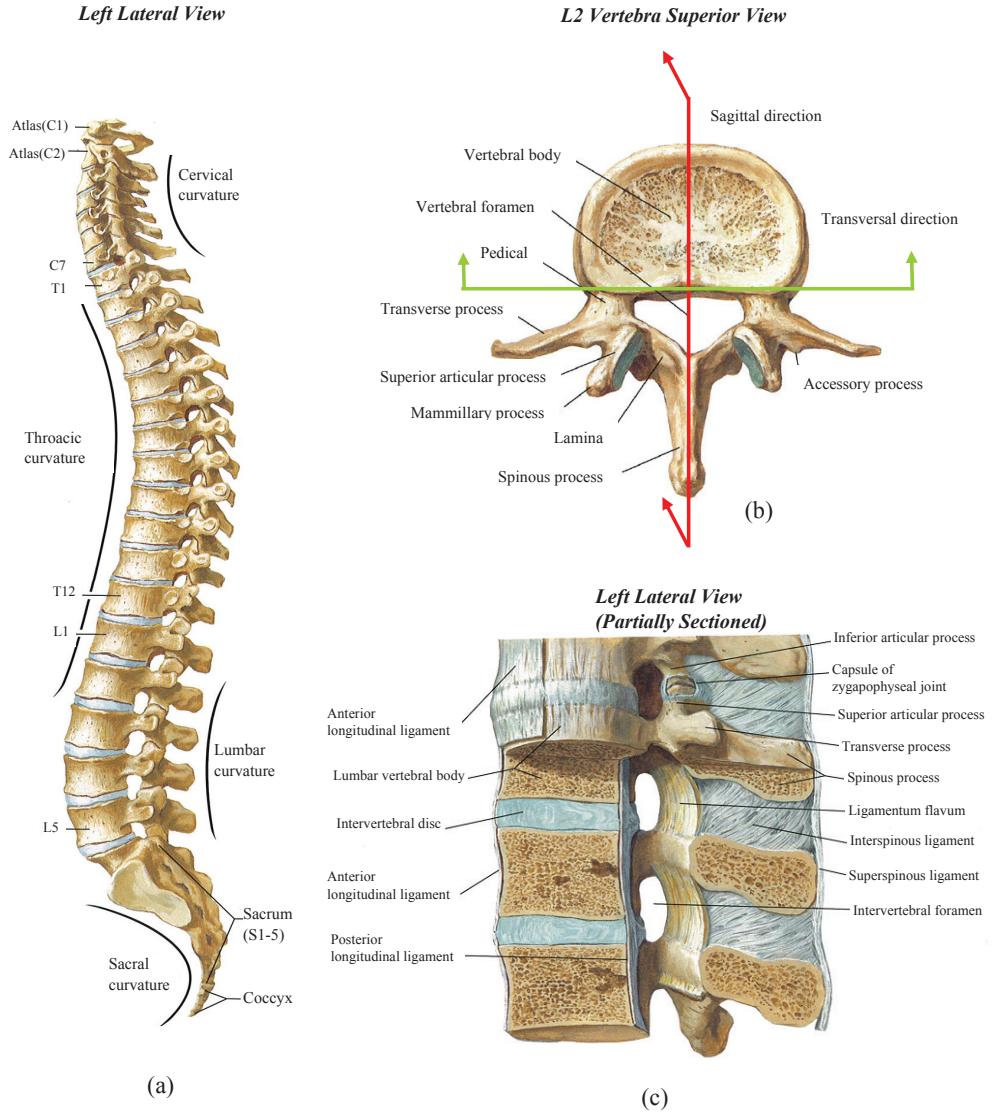

Figure 1.7: Anatomy of the spine. (a) Vertebral column, (b) superior view of a lumbar vertebra, and (c) left lateral view of a lumbar spine [33].

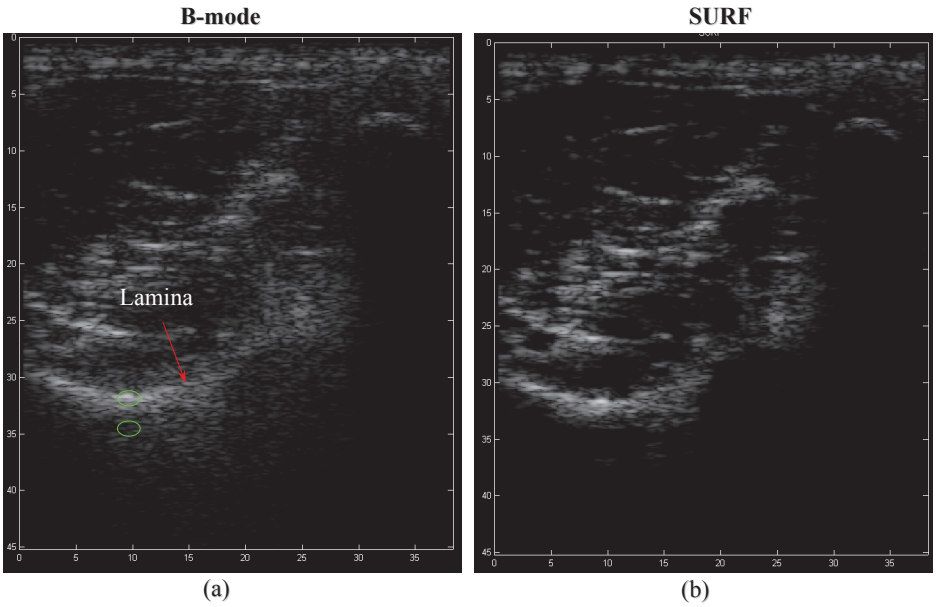

Figure 1.8: Ultrasound imaging of a lumbar vertebra in transversal direction. (a) Standard B-mode Image. (b) SURF image. The focal depth is 32.5mm and the transmit frequency is 10 MHz. Courtesy of Svein-Erik Masoy, NTNU; Sebastien Muller, and Ingerid Reinertsen, SINTEF Health Care.

- ***Shadowing:*** We define this artifact as an effect resulting from partial or total obstruction of ultrasound beams. The shadowing can degrade the resolution of the bone boundaries and the soft tissue located in its neighborhood, resulting in unclear boundaries, noisy shadow inside the bone, and poor resolution image in that region [36]. It should be noted that bony tissues are often identified by their shadow in the ultrasound images. In such case shadowing is not considered as an artifact. More details about shadowing are discussed in Chapter 2 .

- ***Grating lobes:*** The periodicity of the array due to the spacing between elements generates replicas of the mainlobe in the off-axis direction, which leads to an artifact known as grating lobes (Fig. 1.10). The magnitude of grating lobes is a crucial parameter for the ultrasound array design. This artifact can be avoided if the inter-element spacing of the array, or pitch, satisfies the Nyquist criterion in the array sampling context [37]. Thus, when the pitch is equal to $\lambda/2$, the grating lobes are practically eliminated. In some bone imaging scenarios, when the probe is steered toward a lesion close to bone, the grating lobe of the beam can pick up the echoes from the bone surface. This usually results in a haze on the sides of the image, as shown in Fig. 1.11. The figure presents an

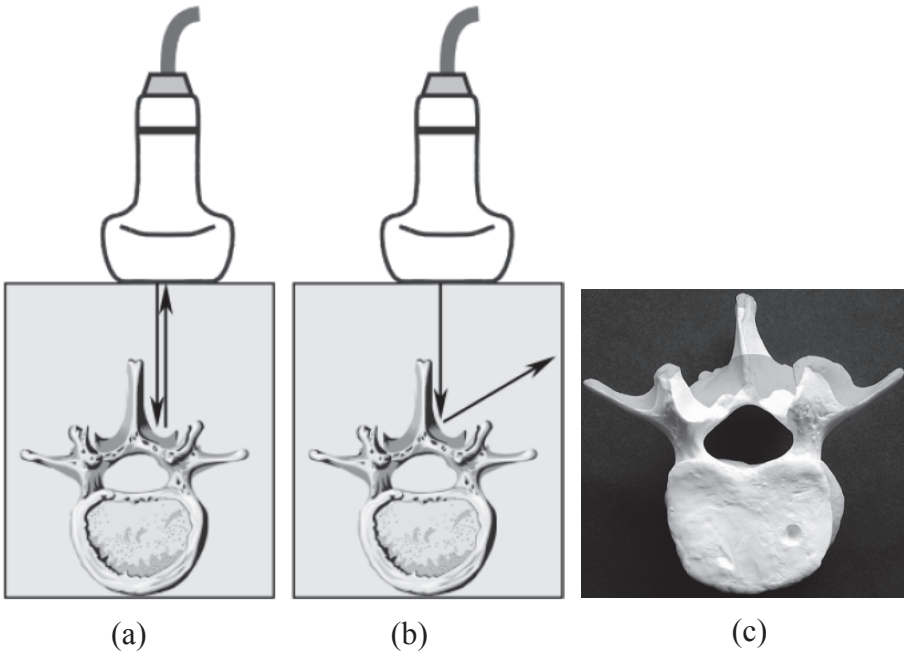

Figure 1.9: Specular reflection of the ultrasound beam when a vertebra is interrogated in the transversal plane. (a) The ultrasound beam perpendicular to the surface, (b) the off-axis specular reflection, and (c) the part of the surface that can be visualized with ultrasound (marked in gray) [14].

image of the spinal anatomy in a disc herniation surgery, obtained using a side-looker probe. An illustration of this procedure is presented in Fig. 1.11(a). In Fig. 1.11(b), the artifacts marked with a red circle may be related to the grating lobes.
In addition, the sidelobes of the ultrasound beam can pick up the off-axis signal with respect to the mainlobe direction, and introduce unwanted speckles in the dark shadow of the bone, or distort the image of a lesion located close to the bony tissue.

- ***Attenuation:*** There are two main mechanisms contributing to ultrasound attenuation: absorption and scattering. Different mechanisms are responsible for absorption phenomena, *e.g.*, thermal conductance effects, chemical effects, viscous effects, and non linearity. The attenuation mechanisms in bone are different from those in fluid-like soft tissues. The bone tissue (cancellous) is a porous medium, in which the attenuation mechanisms are related to: (i) viscous friction effects due to the relative motion of marrow and solid frame, (ii)

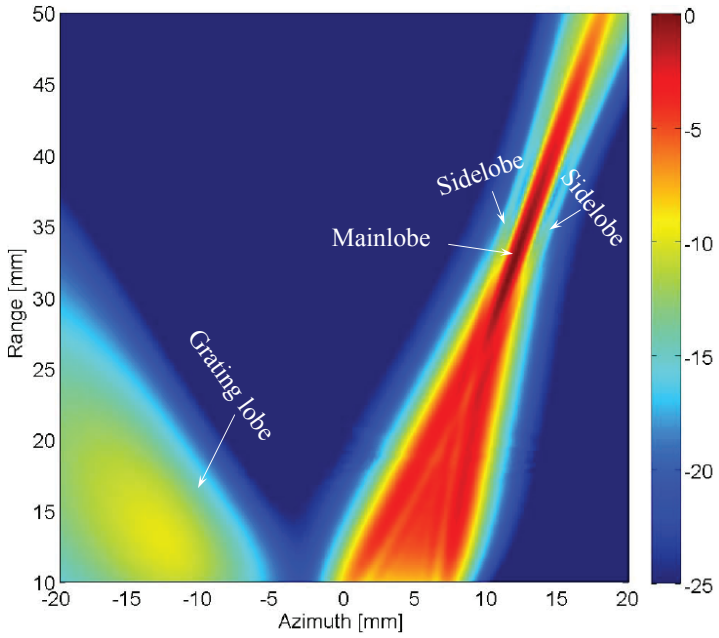

Figure 1.10: Simulation of a 20 ° titled transmit beam for a linear array with 32 active elements. The center frequency is 5 MHz, and the pitch is 300 μm.

scattering of the ultrasonic wave by bone heterogeneity and, (iii) longitudinal to shear mode conversion [6]. The acoustic attenuation in cancellous bone is usually one order of magnitude higher than in cortical bone (TABLE 1.1). Also, the loss mechanisms, such as mode conversion occurring at the bone surface may have a significant contribution to the overall attenuation in bone in the diagnostic frequency range. In mode conversion loss mechanism, transformation of longitudinal waves into shear waves occurs. In most soft tissues, values of the attenuation coefficient (α) are approximately in the range 0.5-1.0 dB/cm/MHz [9]. In bone, the attenuation coefficient is one or two orders of magnitude higher than in soft tissues (TABLE 1.1). Further, the connective tissue such as ligaments and tendons, may have attenuation coefficients of the same order of magnitude as that in the cortical bone. Due to their smoothness, such tissues can also reflect partly the insonifying beams toward the off-axis direction, allowing a small part of the propagating wave to be transmitted to the bone surface.

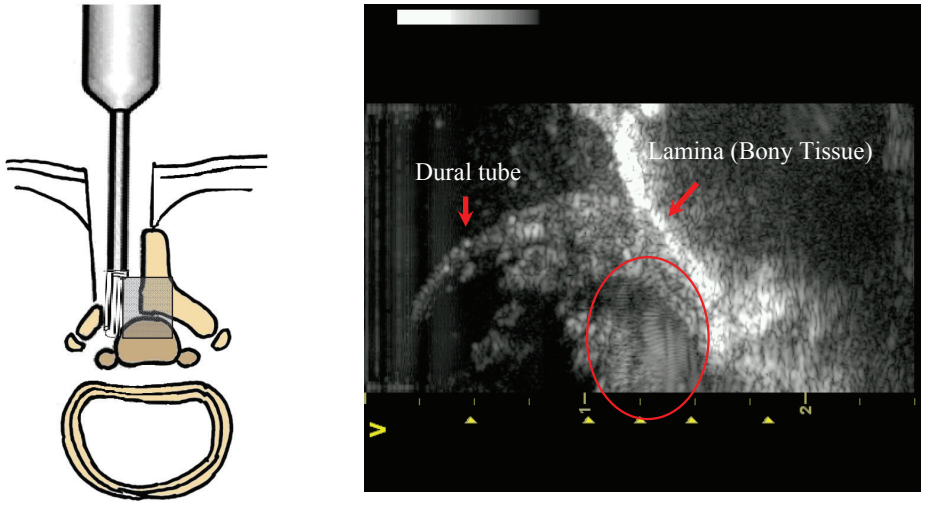

Figure 1.11: Intra-operative ultrasound image from a disc herniation surgery. (a) Schematic illustration, and (b) ultrasound image. Courtesy of Tormod Selbekk, SINTEF Health Care.

1.6 Simulation of bone in ultrasound images

Linear system theory has been used in various scenarios to model the ultrasonic image formation process [38–40]. Although these models are relatively simple, they are able to model reasonably well the physical processes involved in medical ultrasound imaging. These models assume that the structures are much smaller than the wavelength, the scattering process is approximated by Born approximation, and the sound speed is pressure independent. These assumptions allow the imaging system to be characterized by a linear model. Here we use Field II, which is a simulation software developed based on spatial impulse response theory, and is widely used in the ultrasound community [38, 41].

In this work, we deal with the bone structure, particularly the vertebra which is inherently a large scatterer relative to the wavelength and highly attenuating. We present the vertebra surface as a set of triangular surfaces produced from CT volume segmentation techniques using Matlab (MathWorks, Natick, MA) and VTK (Kitware, New York, NY). This discrete version of the surface allows parameterizing the surface based concentration of the scatterers and the surface roughness. For each triangle on the surface, we calculate the number of scatterers as the product of the triangular area and scatterer concentration.

In [39] a scatterer concentration larger than 50 scatterers/mm^2 (at a transmit frequency of 6 MHz) is suggested for the simulation of a vertebra image. These scatterers are required to be positioned randomly in-plane of each triangular element presented by its vertices $v_1, v_2, v_3 \in \Re^3$. For this purpose, we use the Barycentric coordinates of each triangle surface. This means that we select one of the vertices and define all other locations on the plane relative to that point. For example, if v_3 is the origin of the plane, then $(v_1 - v_3)$ and $(v_2 - v_3)$ form the basis vectors. Therefore, we can give coordinate values to all the locations on the plane as:

$$y = v_3 + \zeta_1(v_1 - v_3) + \zeta_2(v_2 - v_3), \tag{1.2}$$

where ζ_1 and ζ_2 are uniformly distributed variables, $\zeta_1, \zeta_2 \in [0, 1]$. To have the points positioned inside the triangle ζ_1 and ζ_2 must satisfy $\zeta_1 + \zeta_2 \leq 1$.
Surface roughness can be also incorporated independently as a perturbation of each scatterer in the direction normal to the surface. The height distribution of a rough surface may be described with a Gaussian function and an exponential autocorrelation function [42]. In [42–44] 2D auto-regressive (2D AR) models were introduced for generating rough surfaces. Trobaugh and Arthur [39] have shown that if the roughness of the bone is in the scale of a wavelength, the coherent scattering from the bone surfaces is decreased. They have also suggested a surface roughness of 0.01 mm in an imaging scenario in which a vertebra is insonified with 6 MHz beams.
As discussed in Chapter 2 ultrasound beams can be partly blocked by the bone structure due to the high bone attenuation and reflection coefficient. This effect can distort the image of a scatterer located in the shadow of the bone, or in parts of the bone structure that are not directly visible in the ultrasound beams. We propose a binary apodization technique to simulate the influence of the shadowing in the corresponding images. In this technique, the visibility of each scatterer or surface triangle is examined for each imaging element of the array using a ray-tracing approach (see Fig. 1.12). This procedure leads to binary apodization functions, which are then used to modify the transmit and receive apodization windows in Field II.
In Fig. 1.13 simulated images of a vertebra in different planes are shown. In these simulations for each triangle the scatterers are located in-plane and all have equal scattering strength. That is, the roughness effects are not considered in these images. However the angle between the triangular surface elements can partly introduce roughness to our simulation model. In Figs. 1.13(a)-(c), the coherent scattering from the perpendicular surfaces to the beams results in echoes with higher intensities. In Fig. 1.13(a), the sidewalls of the vertebra do not appear because they are parallel to the beams. Further on the sides of the spinous process (top), the surface resolution degrades due to shadowing. The same effect is seen in Fig. 1.13(b). In Fig. 1.13(c) the incoherent scattering from the surface is seen on the image top, mainly due to the more oblique surfaces to imaging beams and the sidelobes in the elevation direction. In this figure the coherent scattering from the lamina on the left side of the image is observed.

Connective tissues such as ligaments can produce an ultrasound image that is very sensitive to the insonification angle due to their anisotropic structures. Ligaments

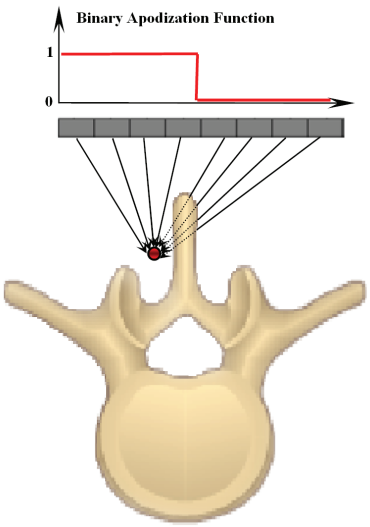

Figure 1.12: Binary apodization function for a scatterer located in the shadow of a vertebra body.

consist of collagen fibers aligned along the long-axis of the fibers. Therefore their backscattering power is angle-dependent. When the direction of the ultrasound beams is perpendicular to the direction of the fibers, the ligaments appear strongly echogenic. Also, their smoothness and high attenuation coefficients can attenuate the ultrasound wavefront before it approaches the bone surface. In case of vertebra imaging, for example, the supraspinous (Fig. 1.7) ligament connecting the top of the spinous processes can attenuate the ultrasound pulses to/from the bone surface. Therefore considering effects of ligaments on simulation models can result in a more realistic image of the vertebra. In a similar approach to [45], a smoothing filter (ellipsoidal Guassian kernel) can be applied to the correlate point scatterers in a specific direction to produce an angle-dependent image of the fibers, allowing the vertebra and the ligament to be simulated independently. The RF data resulting from each simulation can be weighted and summed up together to produce the final image. The weighting step should be used to produce a realistic contrast between the bone surface and the ligament in the simulated image.

1.7 Beamforming

In ultrasound imaging, the array elements can be controlled electronically to produce a focused or steered beam in different depths or directions. This procedure is known as *beamforming*, which is performed by delaying the signals sent to, or received by

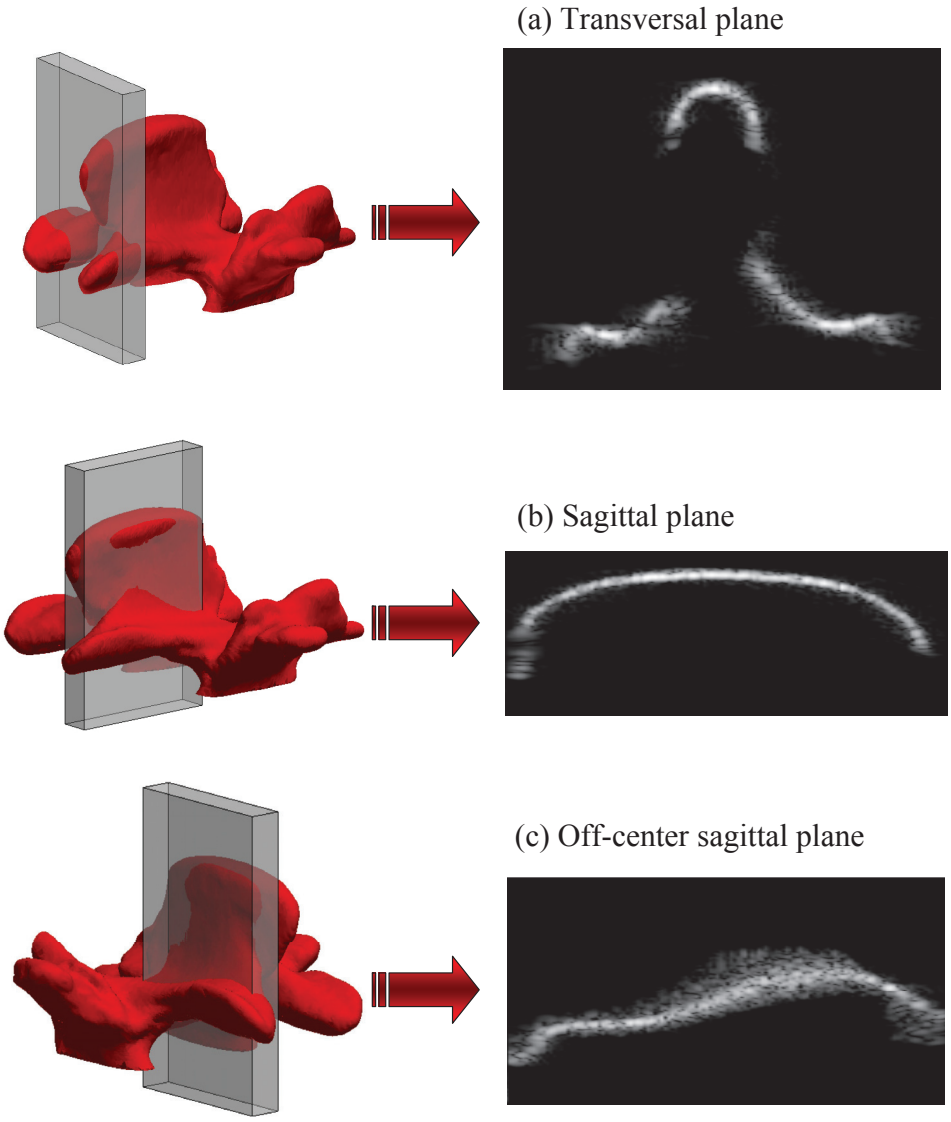

Figure 1.13: Simulated images of a vertebra at different planes. (a) Transversal plane, (b) sagittal plane, and (c) off-center sagittal plane. The transmit frequency is 5 MHz, the scatterer concentration is 200 scatterers/mm^2. The dynamic range in images is 60 dB.

each element. Fig. 1.14(a) schematically illustrates a transmit beamformer. In such a beamformer, a high frequency short pulse is sent to all channels; then, the signal corresponding to each channel is delayed so that the ultrasound waves from each element arrive at the focal point simultaneously. In the receive beamformer the reverse condition holds. In the conventional receive beamforming technique called delay-and-sum (DAS), after a delaying step the signals are summed up in the beamformer [Fig. 1.14(b)]. In the receive beamformer, it is common to use dynamic focusing to produce nearly perfect focusing along the beam. This means that the focus can be dynamically adjusted to follow the transmitted pulse. Also, to optimize the image quality, different weights can be applied to the signals from the array elements to control the mainlobe width and the sidelobe levels. These weights form an apodization function or window, which is mostly used in the receive beamformer due to its simpler implementation.
Most recently, the use of adaptive beamformers have been proposed in medical ultrasound to improve the resolution and contrast in ultrasound images [46–51]. In adaptive beamformers, for each time sample, the delayed received signal from each element is weighted adaptively before the summing operation [Fig. 1.14(c)]. In other words, the apodization function is defined adaptively for each depth in the image. In this work, we deal with a class of beamformers employing a minimum variance (MV) algorithm to determine the optimal weights. An early work on the MV beamforming technique was performed by Capon in seismic imaging [52], and called Capon beamformer. This technique is also known as minimum variance distortion-less response (MVDR) since it tends to keep the signal arriving from the beam direction undistorted. In the following subsections, we address the concept of MV beamformers. Our initial assumption is that narrow-band signals approach from sources located in the far-field of the array. We show that with some considerations we can extend this model for broad-band, near-field applications such as medical ultrasound imaging.

1.7.1 Signal model

Fig. 1.15 shows a uniform linear array of M elements that are spaced equally with a pitch value of d. This array is subjected to a narrow-band plane wave at an angle of θ, resulting in a phase shift between elements denoted as $2\pi dsin\theta/\lambda$. The adaptive array includes a receiver behind each element, and the output signal from these elements into the beamformer can be given as:

$$\mathbf{X} = [xe^{i0}\, xe^{i2\pi d \sin\,\theta/\lambda} \ldots\ xe^{i2\pi(M-1)d\sin\,\theta/\lambda}]^T = x\mathbf{a}, \tag{1.3}$$

where x is the complex baseband signal received at the right-most element, and $\mathbf{a}$ is known as the steering vector. x is modeled as a zero-mean random variable; thus, the signal power can be expressed as $\sigma_s^2 = E\{|x|^2\}$.
In a more complex scenario we assume that p different signals from directions $\theta_i, i = 1...p$ are impinging the array. We assume that these signals are uncorrelated , however, in practice the signals are coherent in medical ultrasound. The steering vectors and powers corresponding to these signals are $\mathbf{a}_i$ and σ_{si}, $i = 1...p$. We consider the signal arising from direction θ_1 as our *desired signal* ($\mathbf{x}_d$), and the signals from the

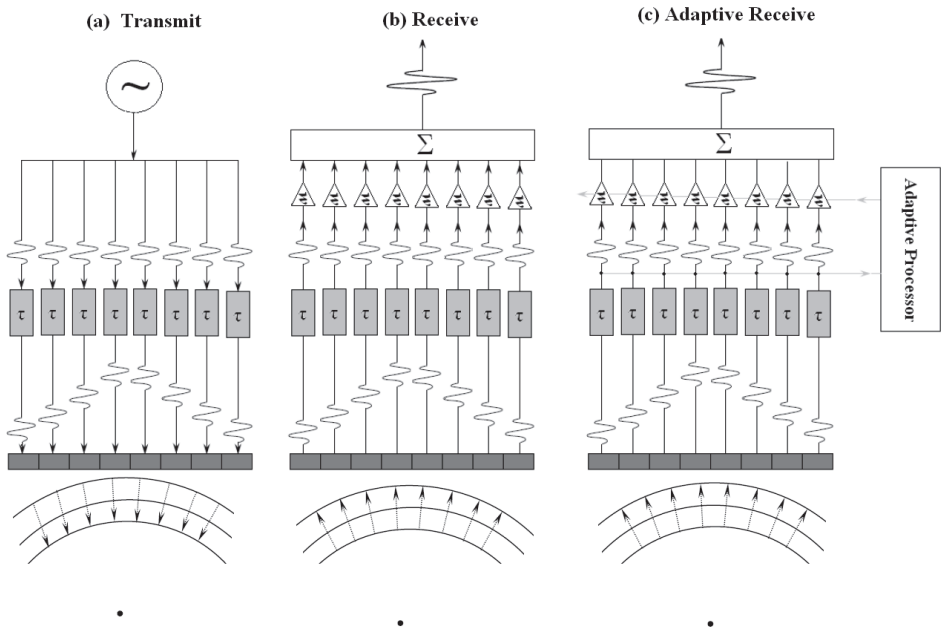

Figure 1.14: (a) Transmit beamformer, (b) conventional receive beamformer, and (c) adaptive receive beamformer.

other directions as *interference signals* ($\mathbf{x}_i$). Also we assume that there is a zero-mean white Gaussian noise with a power of σ_n^2 on each element, resulting in *noise signals* ($\mathbf{x}_n$) on the array elements. Mathematically, the signal output of the elements can be expressed as:

$$\mathbf{X} = x_1\mathbf{a}_1 + \sum_{j=1}^{p} x_j\mathbf{a}_j + \mathbf{x}_n = \mathbf{x}_d + \mathbf{x}_\mathrm{i} + \mathbf{x}_n. \tag{1.4}$$

Here we refer to the second and third terms in (1.4) together as the *undesired signal* ($\mathbf{x}_u$). Because the signals and noise are zero mean, then $E\{X\} = 0$. In such case, the correlation matrix is the same as the covariance matrix. Therefore the true correlation matrix can be expressed as:

$$\mathbf{R} = E\{\mathbf{X}\mathbf{X}^H\} = \sigma_{s1}^2\mathbf{a}_1\mathbf{a}_1^H + \sum_{j=2}^{p} \sigma_{sj}^2\mathbf{a}_j\mathbf{a}_j^H + \sigma_n^2\mathbf{I}_M, \tag{1.5}$$

where $(.)^H$ stands for a Hermitian operator and $\mathbf{I}_M$ is a $M \times M$ unity matrix.

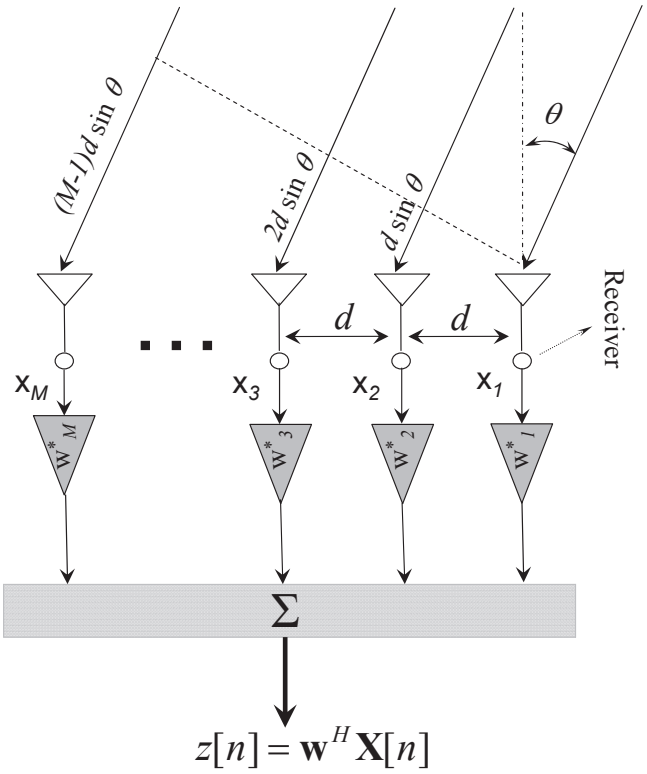

Figure 1.15: A plane wave signal impinging on a uniform linear array.

1.7.2 Minimum variance beamformer

Consider the array shown in Fig. 1.15. The output of this beamformer is given by:

$$z[n] = \mathbf{w}^H \mathbf{X}[n] = \sum_{m=1}^{M} w_m^* x_m[n - \Delta_m^s - \Delta_m^f], \tag{1.6}$$

where $z[n]$ is the beamformer output at a specific time index, M is the number of elements, w_m is weight of m, $x_m[n]$ is the output of element m, and Δ_m^s is a time delay applied to channel m to steer the array toward a specific direction. Further, Δ_m^f is a time delay used to focus on each point in the image. Thus, $\mathbf{X}$[n] is a vector of the aligned (pre-beamformed) signal at the time index n. The beamformer output based on the desired and the undesired signals is expressed as:

$$z[n] = \mathbf{w}^H \mathbf{X}[n] = \mathbf{w}^H \mathbf{x}_d[n] + \mathbf{w}^H \mathbf{x}_u[n]. \tag{1.7}$$

We can also write the output and output power of the beamformer with respect to the desired signal direction as:

$$z_d[n] = \mathbf{w}^H \mathbf{x}_d[n] = x\left(\mathbf{w}^H \mathbf{a_1}\right). \tag{1.8}$$

$$E\left\{z_d[n] {z_d}^H[n]\right\} = E\left\{x_d[n] {x_d}^H[n]\right\}.\left|\mathbf{w}^H \mathbf{a_1}\right|^2 = \sigma_{s1}^2 \left|\mathbf{w}^H \mathbf{a_1}\right|^2. \tag{1.9}$$

Therefore, to have $z_d[n]$ as a *distortion-less* estimator of the desired signal x, we impose a distortion-less constraint as:

$$\mathbf{w}^H \mathbf{a_1} = 1. \tag{1.10}$$

Subsequently the output desired signal power becomes σ_{s1}^2, and the output undesired signal power is:

$$\begin{aligned} E\{|z_u[n]|^2\} &= \mathbf{w}^H E\{x_u[n] x_u^H[n]\}\mathbf{w} \\ &= \mathbf{w}^H \mathbf{R}_u \mathbf{w}. \end{aligned} \tag{1.11}$$

The total power output of the beamformer can be rewritten as:

$$\begin{aligned} P &= \mathbf{w}^H E\{\mathbf{X}[n]\mathbf{X}^H[n]\}\mathbf{w} \\ &= \sigma_{s1}^2 + \mathbf{w}^H \mathbf{R}_u \mathbf{w} = \mathbf{w}^H \mathbf{R} \mathbf{w}, \end{aligned} \tag{1.12}$$

and the output signal to interference-plus-noise (SINR) ratio is:

$$\text{SINR} = \frac{\sigma_{s1}^2}{\mathbf{w}^H \mathbf{R} \mathbf{w} - \sigma_{s1}^2}. \tag{1.13}$$

The quantity shown within parenthesis in (1.8) indicates the response of the beamformer in the direction of the desired signal. If we assume that the beamformer is steering toward a specific direction, *e.g.*, $\Delta_m^s = 0, m = 1...M$, the response of the beamformer with respect to the angle of the plane wave impinging the array is expressed as:

$$\mathbf{W}(\theta) = \mathbf{w}^H \mathbf{a} = \sum_{m=1}^{M} w_m^* e^{j2\pi(m-1)dsin(\theta)/\lambda}. \tag{1.14}$$

$\mathbf{W}(\theta)$ called the *beampattern* and describes how an arriving signal from a given direction θ, is attenuated by the beamformer steered toward a specific direction. It should be noted that the beampattern differs from the steered response (*beam profile*) of the imaging array. To define the steered response (beam profile), we assume a fixed wave field, and scan this field in a systematic way to measure the beamformer response as a function of the steering direction for phase arrays or the beam position for flat-linear arrays. In Fig. 1.16 beam profiles and beampatterns for a pair of point scatterers scanned with a 32 element phase array are shown. In Fig. 1.16(d) , the beamformer is steered toward the point scatter located at 0°.

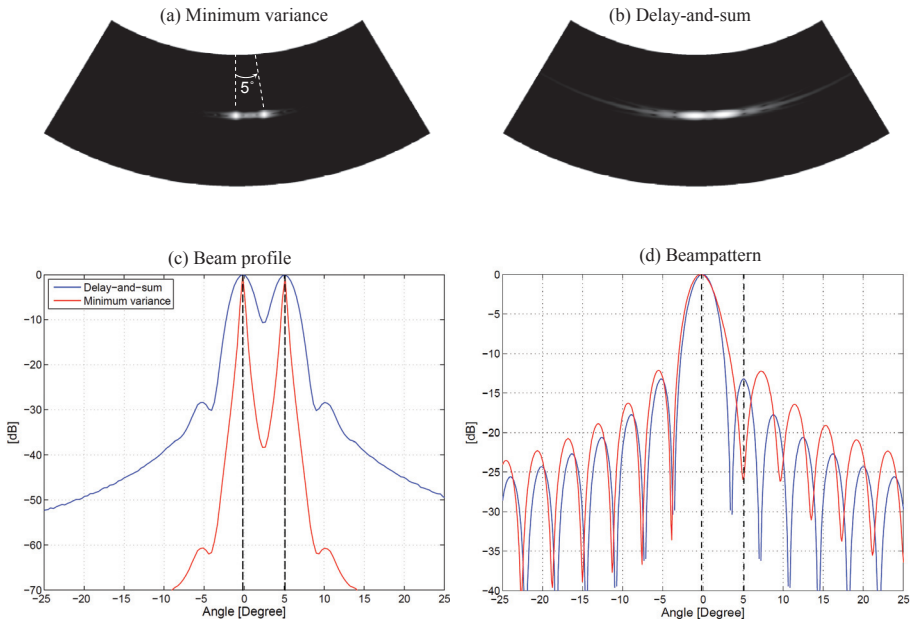

Figure 1.16: Example of minimum variance beamformer (MV) performance. (a) MV image, (b) DSM image, (c) beam profiles, and (d) beampatterns when the beamformer is steered toward the point scatter located at 0°. Two point scatterers are located at a depth of 60 mm and separated by 5°. The transmit frequency is 2.5 MHz, and M= 32. The vertical black dashed lines show the position of the point scatterers.

The maximization of (1.13) is equivalent to minimizing the output interference-plus-noise (undesired) power while maintaining a distortion-less constraint due to the desired signal. In other words the goal is to minimize both off-axis interference and noise by a given optimization criterion. The idea is to find the weights that minimize the variance of $z[n]$ in (1.6), with the constraint that the signal that originates from the steering direction or focal point of the array is passed with unit gain. Hence, the signal in focus is passed undistorted, while the channels are combined such that interference and noise are minimized. Therefore we can mathematically formulate this problem as:

$$\begin{cases} \min\limits_{w} E\left[|z[n]|^2\right] = \min\limits_{w} \mathbf{w}^H \mathbf{R} \mathbf{w} \\ subject\,to\ \mathbf{w}^H \mathbf{a_1} = 1 \end{cases}, \tag{1.15}$$

The optimization problem in (1.15) under the defined constraint can be solved analytically by utilizing the Lagrange multiplier approach [53]. In such case the objective function is:

$$O_F(\mathbf{w}, \gamma) = \mathbf{w}^H \mathbf{R} \mathbf{w} - \gamma(\mathbf{w}^H \mathbf{a_1} - 1), \tag{1.16}$$

where γ is the Lagrange multiplier. Minimizing $O_F(\mathbf{w}, \gamma)$ can be accomplished by setting the gradient of $O_F(\mathbf{w}, \gamma)$ with respect to $\mathbf{w^H}$ equal to zero.

$$\nabla_{\mathbf{W^H}} O_F(\mathbf{w}, \gamma) = \mathbf{R} \mathbf{w} - \gamma \mathbf{a_1} = 0. \tag{1.17}$$

This results in:

$$\mathbf{w} = \gamma \mathbf{R}^{-1} \mathbf{a_1}. \tag{1.18}$$

The value of the Lagrange multiplier is then found by setting the derivative of $O_F(\mathbf{w}, \gamma)$ with respect to γ equal to zero as follow:

$$\frac{\partial O_F(\mathbf{w}, \gamma)}{\partial \gamma} = 1 - \mathbf{w}^H \mathbf{a_1} = 0. \tag{1.19}$$

Substituting (1.18) into (1.19) and solving for γ gives:

$$\gamma = \frac{1}{\mathbf{a_1}^H \mathbf{R}^{-1} \mathbf{a_1}}. \tag{1.20}$$

Finally substituting (1.20) into (1.18) yields:

$$\mathbf{w} = \frac{\mathbf{R}^{-1} \mathbf{a_1}}{\mathbf{a_1}^H \mathbf{R}^{-1} \mathbf{a_1}}. \tag{1.21}$$

Fig. 1.16(a) shows the MV image of two point scatterers insonified with a 32 element, 2.5 MHz transducer. In comparison with Fig. 1.16(b), the DSM image, the resolution is improved and the point scatterers are more resolvable.
As mentioned earlier, the assumption in this section is that narrow-band signals originate from sources in the far-field. In medical ultrasound imaging, this assumption

is violated as the pulses are broad-band, and the sources are located in the near-field of the transducer. Thus, we cannot describe delays simply in phase delays (Δ_m^s) of the steering vector in (1.3). Therefore, we first delay the data, similar to the first step in the DAS beamformer by adding an additional Δ_m^f in (1.6). This process transfers the data from near- to far-field. After applying such delays, the signals arriving from the focal point of the receive beam can be described by a steering vector as $[1...1]^T$. This vector of ones is used as the constraint for (1.15).
The assumption about uncorrelated signals is not valid in ultrasound imaging, due to the presence of an active source. The returned echoes from different scatterers will be correlated because they originate from the same source signal. Hence, signal cancellation may occur. In such case, spatial smoothing (subarray averaging) has been suggested to alleviate this effect [50, 54].
In practice the spatial covariance matrix in (1.21) must be estimated using a limited number of temporal snapshots. This process presents a challenge in medical ultrasound due to the short pulses and rapidly varying signal statistics. In [47, 49] an estimator based on averaging across consecutive transmits and frames has been suggested. In [48] a synthetic aperture approach has been employed to generate a robust covariance matrix. Synnevag *et al.* [50] have used a combination of a temporal averaging and a subarray technique for the covariance matrix estimation. In some of the literatures applying forward/backward averaging is proposed to improve both the covariance matrix estimation, and the robustness of the MV estimation [55–58].
The robustness of the MV beamformer may degrade due to mismatches in the steering vector or gain differences across the array. For example, if the steering vector in (1.21) is not perfectly matched due to imprecise assumption of the propagation velocity, the beamformer tends to suppress the signal of interest, because the only requirement is that a signal coming from the steering direction is passed with zero dB gain. A well known technique for increasing the robustness of adaptive beamformers against these errors is diagonal loading, which involves adding an extra quadratic constraint to the beamformer [59]. In the diagonal loading technique, a term such as $\epsilon = \Delta/L \cdot tr\{\mathbf{R}\}$, is added to the diagonal of the covariance matrix before evaluating (1.21). L is the dimension of $\mathbf{R}$ and $tr\{.\}$ stands for the trace operation. ϵ is proportional to an estimate of the signal power where the factor of proportionality is Δ.

1.7.3 Eigenspace beamformer

Eigenspace beamformers utilize the eigenstructure of the covariance matrix to estimate the beamformer output. In general, we deal with two types of eigenspace beamformers based on the definition in [60]. In the first type, the input signal is projected onto a reduced rank subspace known as the signal subspace, which contains the signal and interferences [61–63]. In the second type, the eigen-decomposition of the covariance matrix is utilized to construct a subspace called the dominant-mode (DM) subspace. The main idea in this algorithm is to reject the significant modes in the DM subspace; therefore, this beamformer is known as the dominant mode rejection (DMR) beamformer [60, 64, 65]. In general, when the statistics of the input signal are

known and there is no signal mismatch, these two classes of beamformers are identical. However in practice errors due to signal mismatch, array mismatch, and estimated sample covariance matrix can make their performance considerably different [60]. In this thesis the first type of the eigenspace beamformer is used, which is explained further below.

Projection eigenspace beamformers:

This class of beamformer has been investigated in the literatures as the eigen-decomposition method [61, 63, 66, 67], the reduced covariance technique [68], or the projection approach [62, 69, 70]. In this thesis, we call this beamforming technique as *eigenspace-based beamforming* (ESMV). In this method, the covariance matrix is eigendecomposed into two groups of large and small eigenvalues. The space that is spanned by the eigenvectors of the first group is called the signal subspace ($\mathbf{E}_s$), whereas the space related to the small group is known as the noise subspace ($\mathbf{E}_N$). In Chapters 3 and 4 we use the first type of eigenspace beamformers as a tool for edge enhancement of the bone in ultrasound images. The eigendecomposed covariance matrix is expressed as:

$$\mathbf{R} = \sum_{l=1}^{D} \lambda_l \mathbf{e}_l \mathbf{e}_l^H + \sum_{l=D+1}^{M} \lambda_l \mathbf{e}_l \mathbf{e}_l^H = \mathbf{E}_s \mathbf{\Lambda}_s \mathbf{E}_s^H + \mathbf{E}_N \mathbf{\Lambda}_N \mathbf{E}_N^H, \tag{1.22}$$

where $\lambda_1 \geq \lambda_2 \geq .... \geq \lambda_D$, are the eigenvalues in descending order, and $\mathbf{e}_l, l = 1, ..., D$ are the corresponding orthonormal eigenvectors. Replacing (1.22) with (1.21) and considering the fact that the steering vector $\mathbf{a_1}$ is orthogonal to $\mathbf{E}_N$, the MV weight vector can be expressed as:

$$\mathbf{w}_{es} = \mu \left[\mathbf{E}_s \mathbf{\Lambda}_s^{-1} \mathbf{E}_s^H\right] \mathbf{a_1}. \tag{1.23}$$

Equation (1.23) can be interpreted as the projection of $\mathbf{w}$ onto the signal subspace ($\mathbf{E}_s$) of $\mathbf{R}$ [62]. In such case a projected steering vector $\mathbf{a_p}$ can be defined as:

$$\mathbf{a}_p = \mathbf{E}_s \mathbf{E}_s^H \mathbf{a_1}, \tag{1.24}$$

because $\mathbf{E}_s^H \mathbf{E}_s = \mathbf{I}$.

Therefore the projected weight vector can be defined as:

$$\mathbf{w}_p = \mu \mathbf{R}^{-1} \mathbf{a}_p = \mu \mathbf{R}^{-1} \mathbf{E}_s \mathbf{E}_s^H \mathbf{a_1}, \tag{1.25}$$

where $\mu = 1/(\mathbf{a_1}^H \mathbf{R}^{-1} \mathbf{a_1})$. In this technique ($\mathbf{E}_s$) has to be estimated so that the significant part of the signal energy is contained in the signal subspace, otherwise the beamformer performance degrades as the noise signal contributes to the signal subspace. The signal subspace may be estimated by the principal component technique (PCI) [71]. In this technique, those eigenvectors of the covariance matrix are considered for the signal subspace that include the eigenvalues of significant values. In Chapter 3 we use the *cross spectral* metric [72] for the signal subspace estimation. In general, in this technique the influence of the steering vector is considered in the

rank ordering of the eigenvectors.
Further, the linear constraint, $\mathbf{a}^H\mathbf{w}_p = 1$, is no longer preserved in (1.25) due to the projection operation, particularly if the rank of the signal subspace is underestimated. In Chapters 3 and 4 we show that this characteristic of the beamformer can be used to locate strong scatterers in ultrasound images. However the unity gain can be preserved if we scale $\mathbf{w}_p$ as:

$$\mathbf{w}_p = \frac{1}{\mathbf{a_1}^H\mathbf{E}_s\mathbf{E}_s^H\mathbf{a_1}}\mathbf{E}_s\mathbf{E}_s^H\mathbf{w}. \tag{1.26}$$

In such case, the performance of the beamformer dramatically depends on the signal subspace estimation.

1.8 Aims of this study

The main objective of this thesis is to enhance the visualization of bone surfaces in ultrasound images. This can be beneficial for applications in which extraction of the bone anatomy from B-mode images is of interest. In such applications feature detection techniques are often used to extract the bone anatomy. The performance of these post-processing methods is heavily dependent on the quality of the images. Therefore, enhancement of the edges and superior distinction of the bone surfaces from the surrounding tissue in B-mode images can facilitate the detection techniques regardless of the quality of the speckle pattern. Particularly, we are interested in the image of the vertebra, which has been shown to be challenging due to its complex anatomy and various types of connective tissue.
Vertebrae are often detected by their shadow on the underlying tissue in ultrasound images. However the shadow regions are often noisy and the boundaries are blurred and unclear. The acoustical noises that appear in the shadow region of the vertebra are partly referred to as *shadowing*, and *off-axis* signals. The former can degrade the resolution in the lateral direction, resulting in unclear and stretched boundaries of the vertebrae. The latter is due to the sidelobe levels of the ultrasound beams, which introduce unwanted speckles in the shadow region. Since the achievable resolution and sidelobe levels are fundamentally limited in the standard delay-and-sum (DAS) beamforming technique, we investigate the potential of adaptive beamformers to alleviate these artifacts. Also, in the case of the imaging a lesion or a biological structure in the neighborhood of the bone, these beamforming techniques reduce the off-axis deteriorating contribution of the bone. Therefore the aims of this thesis are:

- To study the shadowing artifacts in bone imaging scenarios.
- To investigate the potential of minimum variance beamformers so as to enhance the bone surfaces and the lesions in their neighborhood.
- To investigate the robustness of minimum variance based beamformers in bone imaging scenarios.

- To investigate eigenspace minimum variance beamformers for imaging the bone surfaces.
- To design a framework for extracting the spinal anatomy from B-mode ultrasound images.
- To validate the proposed framework using simulation, *in-vitro*, and *in-vivo* data.

1.9 Contribution

The following paragraphs provide a summary of the original contributions of this thesis.

Contribution A:
Minimum Variance Beamforming Applied to Ultrasound Imaging with a Partially Shaded Aperture.
In this paper, we address the shadowing effect resulting from partial obstruction of the imaging aperture in bone imaging scenarios. This effect leads to reduced resolution and in some cases geometrical distortion. To investigate this artifact in more details, we introduce a binary apodization model to simulate the effects of a shaded aperture on the point scatterers located close to a bone structure. In this simulation study, it is assumed that the bone structure is completely attenuating. Further, we investigate the potential of the minimum variance (MV) beamforming method to alleviate this artifact. In general, this adaptive method offers higher lateral resolution, lower sidelobes and improved definition of edges compared to delay and sum beamforming (DAS). Thus, the idea is to use these advantages to improve the imaging of the lesions located next to bone, and also the boundaries of bone. Our study shows that the robustness of the MV beamformer algorithm proposed in [73] degrades when the imaging aperture is highly obstructed by the bone structure. This distortion can be seen as an apparent lateral shift of the point spread function (PSF) and a decrease in sensitivity. We explain this error by the weak estimation of the covariance matrix. Thus, we suggest that the covariance matrix has to be estimated based only on the data from the un-shadowed elements. In practice, we require a criterion to detect the shadowed elements. Therefore, based on the signal power across the aperture, we adaptively determine the shadowed elements and discard their corresponding data from the covariance matrix to improve the MV beamformer performance. This modified MV beamformer can retain the resolution and compensate the apparent lateral shift and signal attenuation of the shadowed point scatterers.

In this paper, the MV beamforming algorithm established by J. F. Synnevåg and Sverre Holm, is used and modified for a new application.
This paper was published in IEEE Transactions on Ultrasonics, Ferroelectrics, and Frequency Control, vol.59, April 2012.

Contribution B:
Eigenspace Based Minimum Variance Beamforming Applied to Ultrasound Imaging of Acoustically Hard Tissues.
In this paper, we follow two main goals: to investigate the robustness of the minimum variance based beamformers in bone imaging scenarios, and to study eigenspace minimum variance (ESMV) beamformers to improve the edges of acoustically hard tissues in the ultrasound images. In the previous paper, we have shown that in bone imaging scenarios the robustness of the standard minimum variance beamformer degrades. This degradation can be avoided if the shadowed elements are detected and discarded in the MV estimation. However, this detection process can be hard for more complex imaging scenarios than that used in Paper A. Alternatively, in this paper, we employ forward/backward (FB) averaging to enhance the covariance matrix estimation in imaging scenarios in which shadowing may occur. Then, the enhanced covariance matrix is used to estimate ESMV weights. We investigate the potential of the ESMV beamforming technique to enhance the edges of acoustically hard tissues. In simulation, *in-vitro*, and *in-vivo* studies, we show that the performance of the ESMV beamformer depends on the estimation of the signal subspace rank. The full rank ESMV exhibits a performance similar to that of the MV beamformer. On the other hand, lower ranks of the signal subspace can enhance edges and reduce noise in ultrasound images but the speckle pattern can be distorted. Nevertheless, if detection of edges is the main purpose, regardless of the speckle pattern, a low rank ESMV beamformer is preferable for edge detection purposes. This also decreases the complexity of the beamformer because only the calculation of a few eigenvalues is required.

This paper was published in IEEE Transactions on Medical Imaging, vol.31, October 2012.

Contribution C:
Joint Beamforming and Feature Detection for Enhanced Visualization of Spinal Bone Surfaces in Ultrasound Images.
In Paper C, we propose a framework for extracting the bone surface from B-mode images. In this framework, we use the ESMV beamformer technique together with a feature detection method as a tool for extracting the bone surfaces. Paper B has shown that the ESMV beamformer can enhance the edges of the bone, but its performance is dependent on the rank of the signal subspace. In this paper, we show that an ESMV beamformer with a rank-1 signal subspace can reasonably well preserve the bone anatomy and enhance the edges, despite causing some distortion of the speckle pattern. Also this makes the beamformer independent of the signal subspace estimation, which is one of the limitations of t eigen-space beamformers. The beamformed images are post-processed using a feature detection technique, and here we use the phase symmetry (PS). This method utilizes 2D Log-Gabor filters and has shown to be effective as a ridge detector for bone localization in US images. First we examine this framework through registration of ultrasound images of a vertebra

(in water tank) against the CT dataset. Then, in *in-vivo* experiments, we employ the proposed framework for imaging the spinal anatomy. We show that the PS images obtained from this beamformer setup have sharper bone boundaries in comparison with the standard DAS ones, and they are reasonably well separated from the surrounding soft tissue.

In this paper for registration, the algorithm established by Gabriel Kiss, NTNU is used. Further, Sebastian Muller has implemented the PS symmetry for post-processing the images.
This paper has been submitted for publication in IEEE Transactions on Medical Imaging.

1.10 General discussion

This work has shown that the minimum variance based beamformers have potential to enhance the visualization of bone edges in ultrasound images. Compared to the standard DAS beamformer, these enhancements include superior definition of the edges, clearer shadow regions inside the bone, and superior definition of the bone anatomy. Also, in the case of the imaging a lesion or a biological structure in the neighborhood of the bone, this beamformer may be employed to reduce the off-axis deterioration contribution of the bone.
Shadowing and *off-axis* reflections are considered as two major sources of the noise in bone imaging. *Reverberation* is another important source of artifacts in such imaging scenarios, however, it is not studied in this work. Because shadowing reduces the effective aperture, the resolution of the boundaries of the vertebra, and the scatterers located in its shadow degrades. An apodization-based model has been proposed to simply simulate effects of the beam obstruction on ultrasound images. Despite simplicity, the suggested model is able to reasonably well describe the shadowing artifacts observed in the experiments.
We have shown that the robustness of the MV is affected by shadowing. This may result in distorted images, mainly due to the asymmetrical signal across the aperture and the weak condition of the covariance matrices in the MV estimator. We conclude that the MV beamformer benefits are maintained as long as the imaging aperture is moderately shaded (*e.g.,* less than 50% of elements). The performance of the MV beamformer can be improved if the shadowed elements are identified and their corresponding data are removed from the beamformer observation vector. Thus, in Paper A, we have adaptively detected the shadowed elements and discarded the corresponding data from the covariance matrix. However, it may not always be straightforward to detect shadowed elements in a robust way.
Therefore, in Paper B, we have proposed the FB averaging technique to alleviate the signal misalignment across the imaging aperture. The combination of the FB and the standard minimum variance is robust but not sufficient for edge enhancement of vertebra or, in general, of the bony tissues. Consequently, in Paper B, we

have introduced a parameter-derived ESMV beamformer. For the eigenspace-based beamformer (ESMV), the covariance matrix is eigendecomposed into two groups of large and small eigenvalues. The space that is spanned by the eigenvectors of the first group, *i.e.,* the most significant ones, is called the signal subspace. Paper B shows that the performance of this beamformer depends on the signal subspace estimation. Lower ranks of the signal subspace can enhance edges and reduce noise in ultrasound images. This behavior of the ESMV can be interesting in light of our goal in this work, which to isolate the bone surface from the surrounding tissue and enhance the bone edges.
Therefore in Paper C, we have investigated a framework for extracting the vertebra surface from the ultrasound images. This framework consisting of an ESMV beamformer with rank-1 and phase symmetry post-processing can preserved the bone structure and improve bone edges. The PS post-processed images demonstrate that this framework can detect reasonably well the spinal structure from US images.
Currently, the computational complexity of the ESMV beamformer limits its application in off-line data analysis. A rank-1 beamformer demands less computational operations; yet far from the real time imaging. There are some applications where the real time image formation is not a crucial, such as 3D segmentation of the spine, or registration of 3D-US datasets to pre-existing CT or MR data. Further, the PS technique depends on several parameters, which should be adapted depending on the specific application. An automatic routine for defining these parameters has been suggested in [74], which is worth investigating for spinal applications.

1.11 Conclusion and further research

This thesis is a part of research on enhancing bone visualization in ultrasound images, and here we have utilized adaptive beamformers. These types of beamformers have received a considerable attention in the recent years, and various implementations of them have been addressed in the literature. Here we have introduced a new application for adaptive beamformers, and investigated the possible implementation of a minimum variance-based beamformer to improve the detection of bone edges before application of post-processing techniques. Our achievements in this thesis are summarized as follows:

- We have proposed a technique for simulating bone surfaces in ultrasound images.
- We have successfully improved the robustness of the MV-based beamformer against signal misalignment by finding adaptively the un-shadowed elements, or by applying the forward/backward averaging technique.
- We have shown that a parameter-derived ESMV beamformer can be beneficial for imaging the bone surface.
- We have investigated a framework for extracting the bone surface from ultrasound images, and validated it on spinal anatomy.

The results on the proposed framework are encouraging, but further research is required to evaluate this framework for related clinical procedures. The achieved results in Paper B and Paper C indicate the low rank ESMV treats images similarly to the adaptive coherence factor (CF) techniques [75, 76]; both techniques weigh the coherent signal and tend to suppress the incoherent signal. In the CF techniques some computationally expensive operations, such as inverting matrices are avoided; thus, such methods may be a good substitute for the ESMV in the proposed framework. In this work a 1D linear array and a single focus transmit beam have mainly been used. This imaging setup may not be optimal for cases in which bone extends from the near-field to the far-field of the probe, *e.g.*, when imaging a vertebra in transversal plane. Thus, using multi-row probes, and multi-focus transmit beams can be beneficial to further improving the images. Because the reverberation artifacts are also important in bone imaging scenarios, the combination of the reverberation suppression techniques and adaptive beamformer methods may be of interest in future research.

1.12 Thesis outline

The thesis is organized as follows: in Chapters 2-4 the technical papers are introduced. Since this thesis includes three papers, some material are repeated in order to be possible to read each paper independently.

1.13 Publication lists

Peer reviewed papers

- S. Mehdizadeh , A. Austeng, T. F. Johansen, and S. Holm, Minimum Variance Beamforming Applied to Ultrasound Imaging With a Partially Shaded Aperture, *IEEE Transactions on Ultrasonics, Ferroelectrics and Frequency Control*, vol. 59, pp. 683 - 693, 2012.

- S. Mehdizadeh , A. Austeng, T. F. Johansen, and S. Holm, "Eigenspace Based Minimum Variance Beamforming applied to Ultrasound Imaging of Acoustically Hard Tissues," *IEEE Transactions on Medical Imaging*, vol.31, no.10, pp.1912-1921, Oct. 2012.

Submitted for publication

- S. Mehdizadeh , S. Muller, Gabriel Kiss, T. F. Johansen, and S. Holm, "Joint Beamforming and Feature Detection for Enhanced Visualization of Spinal Bone Surfaces in Ultrasound Images," *IEEE Transactions on Medical Imaging*,(Under review)

Conference proceedings and abstracts.

- S. Mehdizadeh , S. Muller, T. F. Johansen, and S. Holm, Application of Eigen-Spaced beamformer for Imaging Lamina of vertebral arch, *IEEE Ultrasonics Symposium*, Dresden, Germany , Oct. 2012.

- S. Mehdizadeh , A. Austeng, T. F. Johansen, and S. Holm, "Performance of Adaptive Beamformers for Ultrasound Imaging of a Partially Shaded Object," *IEEE Ultrasonics Symposium*, Orlando, FL, Oct 2011.

Presentations

- S. Mehdizadeh, A. Austeng, T. F. Johansen, S. Holm, Adaptive beamforming in medical ultrasound imaging of acoustically hard tissues, 3rd National PhD Conference in Medical Imaging, Oslo Nov 2011.

References

[1] B. Angelsen, *Ultrasound imaging. Waves, signals and signal processing*, vol. 1. Trondheim: Emantec, 2000.

[2] C. Rumack, S. Wilson, and Charboneau, *Diagnostic ultrasound*. St. Louis: Elsevier, 2005.

[3] A. K. Jain and R. H. Taylor, "Understanding bone responses in b-mode ultrasound images and automatic bone surface extraction using a bayesian probabilistic framework," in *SPIE[0277-786X]* (SPIE, ed.), vol. 5373, p. 131, 2004.

[4] D. Wildes, R. Chiao, C. Daft, K. Rigby, L. Smith, and K. Thomenius, "Elevation performance of 1.25d and 1.5d transducer arrays," *Ultrasonics, Ferroelectrics and Frequency Control, IEEE Transactions on*, vol. 44, pp. 1027 –1037, sept. 1997.

[5] F. A. Duck, *Physical Properties of Tissue : A Comprehensive Reference Book*. London, San Diego: Academic press, 1990.

[6] P. Laugier and G. Haiat, *Bone Quantitative Ultrasound*. Springer Netherlands, 2011.

[7] T. Garcia, W. J. Hornof, and I. F., "On the ultrasonic properties of tendon," *Ultrasound in Medicine & Biology*, vol. 29, no. 12, pp. 1787 – 1797, 2003.

[8] S. A. Goss, R. L. Johnston, and F. Dunn, "Comprehensive compilation of empirical ultrasonic properties of mammalian tissues," *Acoustical Society of America Journal*, vol. 64, pp. 423–457, aug 1978.

[9] R. S. Cobbold, *Foundations of Biomedical Ultrasound*. New York: Oxford university press, 2007.

[10] M. Anderson and G. Trahey, *A seminar on k-space applied to medical ultrasound*. Duke university: Department of Biomedical Engineering, 2006.

[11] S. Barnett, G. T. Haar, M. Ziskin, W. Nyborg, K. Maeda, and J. Bang, "Current status of research on biophysical effects of ultrasound," *Ultrasound in Medicine & Biology*, vol. 20, no. 3, pp. 205 – 218, 1994.

[12] S. B. Barnett, G. R. T. Haar, M. C. Ziskin, H.-D. Rott, F. A. Duck, and K. Maeda, "International recommendations and guidelines for the safe use of diagnostic ultrasound in medicine," *Ultrasound in Medicine & Biology*, vol. 26, no. 3, pp. 355 – 366, 2000.

[13] D. V. Amin, T. Kanade, A. M. Digioia, and B. Jaramaz, "Ultrasound registration of the bone surface for surgical navigation," *Computer Aided Surgery*, vol. 8, no. 1, pp. 1–16, 2003.

[14] B. Brendel, S. Winter, A. Rick, M. Stockheim, and H. Ermert, "Registration of 3d ct and ultrasound datasets of the spine using bone structures," *Computer Aided Surgery*, vol. 7, no. 3, pp. 146 – 155, 2002.

[15] S. Winter, B. Brendel, I. Pechlivanis, K. Schmieder, and C. Igel, "Registration of ct and intraoperative 3-d ultrasound images of the spine using evolutionary and gradient-based methods," *IEEE Transactions on Evolutionary Computation*, vol. 12, no. 3, pp. 284–296, 2008. 1089-778X.

[16] L. Chen, Y. Kim, and C. L. Moore, "Diagnosis and guided reduction of forearm fractures in children using bedside ultrasound," *Pediatric Emergency Care*, vol. 23, no. 8, pp. 528–531, 2007.

[17] C. Stewart Siu-Wa, "Emergency bedside ultrasound for the diagnosis of rib fractures," *The American journal of Emergency Medicine*, vol. 27, no. 5, pp. 617–620, 2009.

[18] "Ultrasound in interventional pain management"," *Techniques in Regional Anesthesia and Pain Management*, vol. 8, no. 4, pp. 171 – 178, 2004.

[19] M. Gofeld, A. Bhatia, S. Abbas, S. Ganapathy, and M. Johnson, "Development and validation of a new technique for ultrasound-guided stellate ganglion block," *Regional Anesthesia and Pain Medicine*, vol. 34, no. 5, pp. 475–479, 2009.

[20] M. M. Bonsanto, R. Metzner, A. Aschoff, V. Tronnier, S. Kunze, and C. R. Wirtz, "3d ultrasound navigation in syrinx surgery - a feasibility study," *Acta Neurochirurgica*, vol. 147, no. 5, pp. 533–541, 2005.

[21] F. Kolstad, O. M. Rygh, T. Selbekk, G. Unsgaard, and O. P. Nygaard, "Three-dimensional ultrasonography navigation in spinal cord tumor surgery," *journal of Neurosurgery: Spine*, vol. 5, no. 3, pp. 264–270, 2006.

[22] C. Arzola, S. Davies, A. Rofaeel, and J. C. Carvalho, "Ultrasound using the transverse approach to the lumbar spine provides reliable landmarks for labor epidurals," *Anesthesia and analgesia*, vol. 104, no. 5, pp. 1188–92, 2007. Comparative Study.

[23] D. Tran, K.-W. Hor, V. A. Lessoway, A. A. Kamani, and R. N. Rohling, "Adaptive ultrasound imaging of the lumbar spine for guidance of epidural anesthesia," *Computerized Medical Imaging and Graphics*, vol. 33, no. 8, pp. 593–601, 2009.

[24] S. N. Narouze, A. Vydyanathan, L. Kapural, D. I. Sessler, and N. Mekhail, "Ultrasound-guided cervical selective nerve root block: A fluoroscopy-controlled feasibility study," *Regional Anesthesia and Pain Medicine*, vol. 34, no. 4, pp. 343–348, 2009.

[25] S. N. Narouze, "Ultrasound-guided interventional procedures in pain management: Evidence-based medicine," *Regional Anesthesia and Pain Medicine*, vol. 35, no. 2, pp. S55–S58, 2010.

[26] J.-K. Shim, J.-C. Moon, K.-B. Yoon, W.-O. Kim, and D.-M. Yoon, "Ultrasound-guided lumbar medial-branch block: A clinical study with fluoroscopy control," *Regional Anesthesia and Pain Medicine*, vol. 31, no. 5, pp. 451–454, 2006. 1098-7339.

[27] Y. Otake, S. Schafer, J. W. Stayman, W. Zbijewski, G. Kleinszig, R. Graumann, A. J. Khanna, and J. Siewerdsen, "Automatic localization of target vertebrae in spine surgery using fast ct-to-fluoroscopy (3d-2d) image registration," 2012.

[28] M. G. Mody, A. Nourbakhsh, D. L. Stahl, M. Gibbs, M. Alfawareh, and K. J. Garges, "The prevalence of wrong level surgery among spine surgeons," *Spine*, vol. 33, no. 2, pp. 194–198, 2008.

[29] T. Grau, "Ultrasonography in the current practice of regional anaesthesia," *Best Practice & Research Clinical Anaesthesiology*, vol. 19, no. 2, pp. 175–200, 2005.

[30] "Facet joint injection." http://www.kypainmed.com/herapies_facetjointinjections.html, 2012.

[31] S. Demir-Deviren, "Epidural steroid injections for spinal pain." http://health-fts.blogspot.no/2012/04/epidural-steroid-injections-for-spinal.html, 2012.

[32] N. Bogduk, *Clinical Anatomy of the Lumbar Spine and Sacrum*. Melbourne: Churchil Livingstone, 3 ed., 1997.

[33] M. Frank H. Netter, *Atlas of Human Anatomy*. Saunders Elsevier, 5 ed., 2011.

[34] J. Mauldin, F.W., K. Owen, M. Tiouririne, and J. Hossack, "The effects of transducer geometry on artifacts common to diagnostic bone imaging with conventional medical ultrasound," *Ultrasonics, Ferroelectrics and Frequency Control, IEEE Transactions on*, vol. 59, pp. 1101 –1114, june 2012.

[35] S. P. Nasholm, R. Hansen, S. e. Masoy, T. Johansen, and B. A. J. Angelsen, "Transmit beams adapted to reverberation noise suppression using dual-frequency surf imaging," *IEEE Transactions on Ultrasonics, Ferroelectrics and Frequency Control*, vol. 56, no. 10, pp. 2124–2133, 2009. 0885-3010.

[36] S. Mehdizadeh, A. Austeng, T. Johansen, and S. Holm, "Minimum variance beamforming applied to ultrasound imaging with a partially shaded aperture," *IEEE Transactions on Ultrasonics, Ferroelectrics and Frequency Control*, vol. 59, no. 4, pp. 683 – 693, 2012.

[37] T. L. Szabo, *Diagnostic ultrasound imaging: inside out*. Boston, USA: Elsevier academic press, 2004.

[38] J. A. Jensen, "Field: A program for simulating ultrasound systems," *Medical & Biological Engineering & Computing*, vol. 34, pp. 351–353, 1996.

[39] J. W. Trobaugh and R. M. Arthur, "A discrete-scatterer model for ultrasonic images of rough surfaces," *IEEE Transactions on Ultrasonics, Ferroelectrics and Frequency Control*, vol. 47, no. 6, pp. 1520–1529, 2000.

[40] T. Hergum, S. Langeland, E. W. Remme, and H. Torp, "Fast ultrasound imaging simulation in k-space," *Ultrasonics, Ferroelectrics and Frequency Control, IEEE Transactions on*, vol. 56, no. 6, pp. 1159–1167, 2009.

[41] J. Jensen and I. Nikolov, "Fast simulation of ultrasound images," in *Ultrasonics Symposium, 2000 IEEE*, vol. 2, pp. 1721 –1724 vol.2, oct 2000.

[42] Y. Hu and K. Tonder, "Simulation of 3-d random rough surface by 2-d digital filter and fourier analysis," *International Journal of Machine Tools and Manufacture*, vol. 32, no. 12, pp. 83 – 90, 1992.

[43] X. Gu and Y. Huang, "The modelling and simulation of a rough surface," *Wear*, vol. 137, no. 2, pp. 275 – 285, 1990.

[44] K. Nemoto, K. Yanagi, M. Aketagawa, I. Yoshida, M. Uchidate, T. Miyaguchi, and H. Maruyama, "Development of a roughness measurement standard with irregular surface topography for improving 3d surface texture measurement," *Measurement Science and Technology*, vol. 20, no. 8, p. 084023, 2009.

[45] J. Crosby, T. Hergum, E. Remme, and H. Torp, "The effect of including myocardial anisotropy in simulated ultrasound images of the heart," *IEEE Transactions on Ultrasonics, Ferroelectrics and Frequency Control*, vol. 56, pp. 326 –333, february 2009.

[46] J. Mann and W. Walker, "A constrained adaptive beamformer for medical ultrasound: initial results," *Proc. Ultrasonics Symposium*, vol. 2, pp. 1807–1810, 2002.

[47] M. Sasso and C. Cohen-Bacrie, "medical ultrasound imaging using the fully adaptive beamformer," *proc. IEEE Acoustics, Speech, and Signal, (ICASSP '05)*, vol. 2, pp. 489–492, 2005.

[48] W. Zhisong, L. Jian, and W. Renbiao, "Time-delay- and time-reversal-based robust capon beamformers for ultrasound imaging," *Medical Imaging, IEEE Transactions on*, vol. 24, pp. 1308 –1322, oct. 2005.

[49] F. Vignon and M. R. Burcher, "Capon beamforming in medical ultrasound imaging with focused beams," *IEEE Transactions on Ultrasonics, Ferroelectrics and Frequency Control*, vol. 55, no. 3, pp. 619–628, 2008.

[50] J. F. Synnevag, A. Austeng, and S. Holm, "Benefits of minimum-variance beamforming in medical ultrasound imaging," *IEEE Transactions on Ultrasonics, Ferroelectrics and Frequency Control*, vol. 56, no. 9, pp. 1868–1879, 2009. 0885-3010.

[51] B. Mohammadzadeh Asl and A. Mahloojifar, "Eigenspace-based minimum variance beamforming applied to medical ultrasound imaging," *IEEE Transactions on Ultrasonics, Ferroelectrics and Frequency Control*, vol. 57, no. 11, pp. 2381–2390, 2010.

[52] J. Capon, "High-resolution frequency-wavenumber spectrum analysis," *Proceedings of the IEEE*, vol. 57, no. 8, pp. 1408–1418, 1969.

[53] M. H.Hayes, *Statistical Digital Signal Processing and Modeling*. New York: John Wiley & Sons, Inc, 1996.

[54] S. Tie-Jun, M. Wax, and T. Kailath, "On spatial smoothing for direction-of-arrival estimation of coherent signals," *IEEE Transactions on Acoustics, Speech and Signal Processing*, vol. 33, no. 4, pp. 806–811, 1985.

[55] I. Holfort, F. Gran, and J. Jensen, "Investigation of sound speed errors in adaptive beamforming," in *Ultrasonics Symposium, 2008. IUS 2008. IEEE*, pp. 1080 –1083, nov. 2008.

[56] B. M. Asl and A. Mahloojifar, "Contrast enhancement and robustness improvement of adaptive ultrasound imaging using forward-backward minimum variance beamforming," *IEEE Transactions on Ultrasonics, Ferroelectrics and Frequency Control*, vol. 58, no. 4, pp. 858–867, 2011.

[57] K. Kim and S. Saunders, "New adaptive beamforming algorithm employing forward/backward averaging and signal enhancement schemes," *Communications Letters, IEEE*, vol. 5, pp. 98 –100, march 2001.

[58] A. Ronhovde, L. Yang, T. Taxt, and S. Holm, "High-resolution beamforming for multibeam echo sounders using raw em3000 data," in *OCEANS '99 MTS/IEEE. Riding the Crest into the 21st Century*, vol. 2, pp. 923 –930, 1999.

[59] J. Li, P. Stoica, and Z. Wang, "On robust capon beamforming and diagonal loading," *Signal Processing, IEEE Transactions on*, vol. 51, pp. 1702 – 1715, july 2003.

[60] H. L. Van Trees, *Optimum Array Processing - Part IV, Detection, Estimation, and Modulation Theory*. New York: John Wiley & Sons, 2002.

[61] L. Chang and C. C. Yeh, "Performance of dmi and eigenspace-based beamformers," *IEEE Transactions on Antennas and Propagation*, vol. 40, no. 11, pp. 1336–1347, 1992.

[62] D. D. Feldman and L. J. Griffiths, "A projection approach for robust adaptive beamforming," *IEEE Transactions on Signal Processing*, vol. 42, no. 4, pp. 867–876, 1994. 1053-587X.

[63] A. M. Haimovich and Y. Bar-Ness, "An eigenanalysis interference canceler," *Signal Processing, IEEE Transactions on*, vol. 39, no. 1, pp. 76–84, 1991.

[64] D. A. Abraham and N. L. Owsley, "Beamforming with dominant mode rejection," in *OCEANS '90. Engineering in the Ocean Environment. Conference Proceedings*, pp. 470–475, 1990.

[65] H. Cox and R. Pitre, "Robust dmr and multi-rate adaptive beamforming," in *Signals, Systems amp; Computers, 1997. Conference Record of the Thirty-First Asilomar Conference on*, vol. 1, pp. 920 –924, nov. 1997.

[66] Y. Jung-Lang and Y. Chien-Chung, "Generalized eigenspace-based beamformers," *IEEE Transactions on Signal Processing*, vol. 43, no. 11, pp. 2453–2461, 1995.

[67] Y. Won Sik and U. Chong Kwan, "Robust adaptive beamforming based on the eigenstructure method," *IEEE Transactions on Signal Processing*, vol. 42, no. 6, pp. 1543–1547, 1994. 1053-587X.

[68] I. Kirsteins and D. Tufts, "On the probability density of signal-to-noise ratio in an improved adaptive detector," in *Acoustics, Speech, and Signal Processing, IEEE International Conference on ICASSP '85.*, vol. 10, pp. 572–575, 1985.

[69] D. D. Feldman, "An analysis of the projection method for robust adaptive beamforming," *IEEE Transactions on Antennas and Propagation*, vol. 44, no. 7, pp. 1023–1030, 1996. 0018-926X.

[70] D. D. Feldman and L. J. Griffiths, "A constraint projection approach for robust adaptive beamforming," in *Acoustics, Speech, and Signal Processing, 1991. ICASSP-91., 1991 International Conference on*, vol. 2, pp. 1381–1384, 1991.

[71] D. Tufts, R. Kumaresan, and I. Kirsteins, "Data adaptive signal estimation by singular value decomposition of a data matrix," *Proceedings of the IEEE*, vol. 70, pp. 684 – 685, june 1982.

[72] J. S. Goldstein and I. S. Reed, "Reduced-rank adaptive filtering," *IEEE Transactions on Signal Processing*, vol. 45, no. 2, pp. 492–496, 1997.

[73] J. F. Synnevag, A. Austeng, and S. Holm, "Adaptive beamforming applied to medical ultrasound imaging," *IEEE Transactions on Ultrasonics, Ferroelectrics and Frequency Control*, vol. 54, no. 8, pp. 1606–1613, 2007. 0885-3010.

[74] I. Hacihaliloglu, R. Abugharbieh, A. J. Hodgson, and R. N. Rohling, "Automatic adaptive parameterization in local phase feature-based bone segmentation in ultrasound," *Ultrasound in Medicine & Biology*, vol. 37, no. 10, pp. 1689–1703, 2011.

[75] C. I. C. Nilsen and S. Holm, "Wiener beamforming and the coherence factor in ultrasound imaging," *IEEE Transactions on Ultrasonics, Ferroelectrics and Frequency Control*, vol. 57, no. 6, pp. 1329–1346, 2010. 0885-3010.

[76] L. Pai-Chi and L. Meng-Lin, "Adaptive imaging using the generalized coherence factor," *IEEE Transactions on Ultrasonics, Ferroelectrics and Frequency Control*, vol. 50, no. 2, pp. 128–141, 2003. 0885-3010.

Chapter 2

Minimum Variance Beamforming Applied to Ultrasound Imaging With a Partially Shaded Aperture

Saeed Mehdizadeh[1], Andreas Austeng[2], Tonni F. Johansen[1], and Sverre Holm[1,2]
[1] Dept. Circulation and Medical Imaging, NTNU, Norway
[2] Dept. Informatics, University of Oslo, Norway

Shadowing of an imaging aperture occurs when ultrasound beams are partially obstructed by an acoustically hard tissue, *e.g.* a bone tissue. This effect leads to reduced resolution and in some cases geometrical distortion. In this paper, we initially introduce a binary apodization model to simulate effects of the shadowing on the point scatterers located close to a bone structure. Further, in a simulation study and an *in-vitro* experiment, minimum variance (MV) beamforming method is employed to image scatterers partly located in the shadow of bone. We show that the MV beamformer can result in a distorted image when the imaging aperture is highly obstructed by the bone structure. This distortion can be seen as an apparent lateral shift of the point spread function and a decrease of the sensitivity. Based on the signal power across the aperture, we adaptively determine the shadowed elements and discard their corresponding data from the covariance matrix to improve the MV beamformer performance. This modified MV beamformer can retain the resolution and compensate the apparent lateral shifting and signal attenuation for the shadowed point scatterers.

2.1 Introduction

Ultrasound has been employed for imaging many organs in diagnosis, guidance during surgery, and therapeutic procedures. In some clinical procedures, imaging the bone surface [1–3] or the tissue in its vicinity [4–7] is of major interest. For example, precise localization of the bone surface in ultrasound images is important for registration of the preoperative to intraoperative images in surgery [1, 2]. However, noisy ultrasound images of the corresponding bone tissue can limit the accuracy of this procedure. In [4] ultrasound has been used for intraoperative assistance for resection control in a transsphenoidal surgery in which the bony cranial base can produce significant artifacts in the corresponding images. Moreover, ultrasonography has been shown to be a helpful tool in guiding syringomyelial and intraspinal surgery, but poor quality of the images limits its applicability [5, 6].
Ultrasound imaging involving bone tissue is often prone to poor image quality due to different artifacts. These may include high reverberation levels, specular reflection, and shadowing effects. The shadowing, which is of interest in this paper, is defined as an effect resulting from partial or total obstruction of the ultrasound beam. The shadowing reduces the image quality due to resolution degradations. This effect is due to the fact that the active part of the aperture is partly obstructed, and the effective aperture is reduced. This might give significant difficulties in the detection of some important anatomic features, *e.g.*, nerves, ligaments, and lesions that are crucial for some clinical procedures [4, 8].
Post processing filters have been employed to improve the appearance of anatomical features in the ultrasound images [9]. However, the low-pass characteristic of these filters can remove the fine details of the structure. Moreover, an adaptive spatial compounding technique was introduced. In this approach the final image is constructed by averaging a number of images taken at different angles, and aligned using a warping technique [10]. Recently, Tran *et al.* [8] employed this technique to improve visibility of the epidural anatomy in the lumbar spine images for the epidural anesthesia application. Nevertheless, the resolution of this method is limited as it is based on delay and sum (DAS) beamforming, which is the standard technique in medical ultrasound imaging. In the DAS technique, received signals from active channels are dynamically delayed and summed up in the beamformer. In this method the achievable resolution and contrast are fundamentally restricted. On the contrary, utilizing an adaptive technique, such as MV beamforming, can enhance the image quality as a result of lower sidelobes and a narrower beamwidth [11]. In the MV approach, for each time sample, the delayed received signal from each element is weighted adaptively. Then these are summed up in the beamformer. This approach was initially developed by Capon for passive narrow-band applications [12]. However, experience has shown that narrow-band methods also may be used for the broad-band medical imaging applications [11].
Several researchers have previously investigated the MV approach in medical ultrasound. They reported appreciable enhancements in the resolution and contrast in comparison with DAS beamforming [13–18]. Mann and Walker [13] used a broad-band constrained adaptive beamforming on experimental data of a single point target

and a cyst phantom. Sasso and Cohen-Bacrie [14] and Synnevag *et al.* [17] applied a spatial smoothing technique [19] to deal with the coherent signal and to have a more robust estimation of the covariance matrix. Wang *et al.* [15] implemented the minimum variance method for a synthetic aperture to take advantage of the dynamic focusing on both transmit and receive. This method generates a robust estimate of the covariance matrix at the expense of a lower signal to noise ratio (SNR). Vignon and Burcher [16] examined MV beamforming to image the heart chambers and abdomen. They demonstrated more clinically significant images with higher resolution and contrast compared to the DAS beamforming. In a simulation study, Mohammadzadeh Asl and Mahloojifar [18] investigated an eigenspace-based MV technique to improve the contrast of MV beamforming. They reported promising results for wire and cyst phantoms.

In these studies, it has been shown that there is a potential for using MV beamforming to improve the resolution and the contrast in the ultrasound images provided that the full imaging aperture receives data. In the case of imaging of a bone and its surrounding region, the aperture may be partly shadowed due to the high attenuation of the bone. To our knowledge, MV beamforming has not been examined for such a case.

In this paper, where technical aspects of the shadowing effects are of interest, we study the MV beamforming method for imaging point scatterers located close to the bone to investigate the influence of the shadowing on the MV beamformer. We propose a binary apodization-based shadowing model to simulate effects of the shaded aperture on the corresponding ultrasound images. This model is applied to Field II [20] to simulate the image of the point scatterers which are affected by the shade of the bone structure. We demonstrate that the MV beamforming can be beneficial to compensate for the shadowing effects provided that the aperture is moderately shaded. However, a significant shadowing can give rise to an apparent point spread function (PSF) shift and signal attenuation in the MV approach in comparison to DAS. In addition, based on the signal power across the imaging aperture, we adaptively determine shadowed elements and discard their corresponding data from the covariance matrix to improve the MV beamformer performance. Further, in an *in-vitro* experiment, the MV beamformer is employed to image a needle partially located in the shadow of a human vertebra specimen.

2.2 Methods

2.2.1 Minimum variance beamforming

We consider a transducer with M elements for which the time sampled signal from element m is $x_m[n]$. The output signal from the beamformer for each sample is expressed as [11, 17]:

$$z\left[n\right]=\mathbf{w}\left[n\right]^{H}\mathbf{X}\left[n\right]=\sum_{m=0}^{M-1}w_{m}^{*}\left[n\right]x_{m}\left[n\right],\tag{2.1}$$

where $w_m\left[n\right]$ is a time varying complex weight, and H stands for Hermitian transpose. It is assumed that $x_m\left[n\right]$ has already been delayed for steering and focusing to the point of interest. In MV beamforming the variance of $z\left[n\right]$ is minimized while the response from the focal point remains undistorted. This optimization problem can be expressed as:

$$\begin{cases}\underset{w[n]}{min}\,E\left[\left|z\left[n\right]\right|^{2}\right]=\underset{w[n]}{min}\,\mathbf{w}[n]^{H}\mathbf{R}[n]\,\mathbf{w}[n]\\ \qquad subject\,to\;\mathbf{w}[n]^{H}\mathbf{a}\;=\;1\end{cases},\tag{2.2}$$

where $E\left[.\right]$ denotes the expectation operator, $\mathbf{R}\left[n\right]=E\left[\mathbf{X}[n],\mathbf{X}[n]^{H}\right]$ is the spatial covariance matrix, $\mathbf{a}$ is the steering vector. Because the data has been delayed, $\mathbf{a}$ is simply a vector of ones. The optimization problem in (2.2) under defined constraint can be solved analytically by utilizing the Lagrange multiplier approach [21]. Accordingly, the optimized weighting coefficients are computed as:

$$\mathbf{w}\left[n\right]=\frac{\mathbf{R}\left[n\right]^{-1}\mathbf{a}}{\mathbf{a}^{H}\mathbf{R}\left[n\right]^{-1}\mathbf{a}}.\tag{2.3}$$

However, in medical ultrasound imaging the signals are nonstationary as the transmit pulses are short. Thus, the covariance matrix should be estimated based on a few time samples and a number of spatial realizations of the data. To generate an ensemble of spatial samples a subarray technique is applied [19]. That is, the array is divided into overlapping subarrays with length of L, and then the corresponding covariance matrices are calculated and averaged across the array to estimate the full covariance matrix as:

$$\hat{\mathbf{R}}[n]=\frac{1}{(2K+1)(M-L+1)}\cdot\sum_{k=-K}^{K}\sum_{l=0}^{M-L}\bar{\mathbf{X}}_{l}[n-k]\,\bar{\mathbf{X}}_{l}[n-k]^{H},\tag{2.4}$$

where

$$\bar{\mathbf{X}}_{l}[n]=\left[\begin{array}{cccc}x_{l}[n] & x_{l+1}[n] & \ldots & x_{l+L-1}[n]\end{array}\right]^{T}.\tag{2.5}$$

In general there is a time averaging over index k which has been found to be necessary in order to get proper speckle statistics in the image [17]. However in this study we mainly deal with point scatterers, and in order to increase execution speed K is set to zero. Substituting $\mathbf{R}$ with $\hat{\mathbf{R}}$ in equation (2.3), the estimated amplitude is obtained by averaging over all subarrays:

$$\hat{z}[n] = \frac{1}{M-L+1} \sum_{l=0}^{M-L} \mathbf{w}[n]^H \bar{\mathbf{X}}_l[n]. \tag{2.6}$$

It should be noticed that the robustness of the MV estimate is a concern due to the invertibility of the covariance matrix. In [11] two techniques are discussed to enhance the robustness of the MV estimate: decreasing of the subarray length, and diagonal loading of the covariance matrix. There is a compromise between the robustness, subarray length, and resolution of the MV estimate. A smaller L results in a more robust estimation at the expense of losing resolution, and in the case of $L = 1$ the method becomes equivalent to that of the DAS approach [11]. To have an invertible covariance matrix estimation without diagonal loading an upper limit of $L \leq M/2$ is required for the length of the subarray [22]. In the diagonal loading technique, a term, $\Delta/L \cdot tr\{\mathbf{R}\}$, is added to the diagonal of the covariance matrix before evaluating (2.3) [11]. This term is proportional to an estimate of the signal power where the factor of proportionality is Δ.

2.2.2 Adaptive detection of shadowed elements

The asymmetrical signal across the aperture due to the shadowed elements violates the statistical invariance assumption. This can introduce errors in the covariance matrix estimation in (2.4), and accordingly degrade the standard MV beamformer performance. In this study, we adaptively detect the shadowed elements and discard their corresponding data from the covariance matrix. Thus, the aperture size reduces from M to M_{ua} which is the number of the unaffected elements. The new subarray length is assigned as $L = M_{ua}/2$. Furthermore, M_{ua} is substituted for M in (2.4) and (2.6) to estimate the covariance matrix and amplitude based on unaffected elements. In the modified MV beamformer, M_{ua} is estimated based on the signal power across the aperture for each depth. The signal power for each element is averaged over $2\bar{K}+1$ time samples and is expressed as:

$$p_m[n] = \frac{1}{2\bar{K}+1} \sum_{\bar{k}=-\bar{K}}^{\bar{K}} \left| x_m\left[n-\bar{k}\right] \right|^2 , \; m = 1 \ldots M \, . \tag{2.7}$$

Furthermore, the power vector across the aperture is expressed as:

$$\bar{\mathbf{P}} = [p_1[n] \; p_2[n] \; \ldots p_M[n]]. \tag{2.8}$$

In general, $\bar{\mathbf{P}}$ is normalized to its maximum value and the elements with power less than a threshold value (P_{lim}) are considered as the shadowed elements. Once the shadowed elements are determined, M_{ua} can be assigned separately for each depth.

2.2.3 Simulating the shadowing effect

In this study, we assume that the bone structure is completely attenuating. Therefore, it shadows the ultrasound beam which is steered to image the tissue in the vicinity

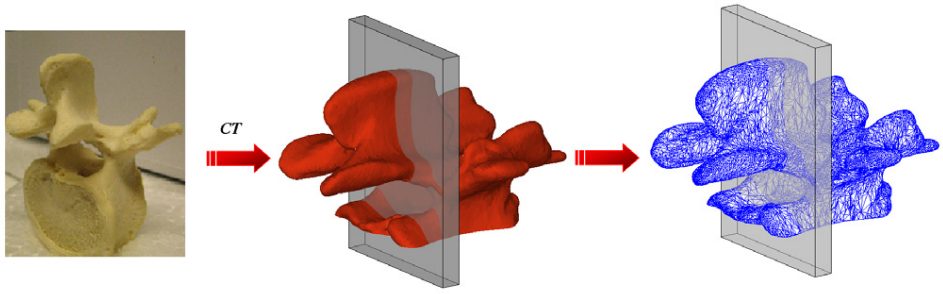

Figure 2.1: Illustration of the vertebra model and the imaging volume.

of the bone structure. Simulation of the bone as a totally occluding body has been discussed by Trobaugh and Arthur [23]. In their approach, after the segmentation of the model, the surfaces which are hidden from the imaging beam are removed. Then, the image of the remaining surfaces is constructed by assuming a spatially invariant PSF for the imaging system. However, the shadowing effect can significantly affect the PSF, as the active part of the imaging aperture varies. In this context, we propose an apodization-based shadowing model for the scatterers located close to the bone. This model is spatially dependent and varies with the position of the point scatterers.
We simulate the shadowing as a binary apodization function, *i.e.* for each point scatterer, the transducer's shaded elements are weighted to zero. This shadowing apodization function is constructed based on a ray tracing method. In this method, the visibility of every single point scatterer as viewed from the center of the transducer's element is tested. Accordingly, first the occluding obstacle is segmented into triangular surfaces in order to have a discrete model of the surface. Then, we cast a ray from each transducer element to the point scatterer of interest. If this ray intersects with any triangular surfaces, the corresponding element is assumed to be shaded. This procedure is repeated for all point scatterers to construct their corresponding apodization functions. These binary functions are used to modify the transmit and receive apodization windows that are employed in Field II [20] to simulate the imaging system.
In this study, the vertebra is considered as the shadowing source. Thus, a 3D geometry of the model has been obtained by CT scanning of a human lumbar vertebra specimen (L3). By utilizing Matlab (the Mathworks, Natick, MA) and VTK (Kitware, New York, NY) the volume has been segmented into triangular surfaces (Fig. 2.1). This model can also be used to simulate the imaging of the bone surface provided that discrete point scatterers are generated on the triangulated surfaces.

2.2.4 Simulation setup

In this study, we simulate a linear array with 128 elements and a center frequency of 5 MHz (f_0). The elevation focus is 19 mm, and the pitch equals 0.308 mm. The

maximum accessible aperture size for this array transducer is 19.35 mm ($M = 64$). In all simulations, a fixed transmit focus, and dynamic receive focusing is used. In addition, f numbers in the transmit and receive beams are set to $\mathrm{FN_{TX}} = 2.5$ and $\mathrm{FN_{RX}} = 1.8$ respectively. Also, the transmit focal depth is 25 mm. The received channel data for each scan line are stored for off-line beamforming. We also add white, Gaussian noise to each receiver channel so that the SNR is approximately 40 dB for the point scatterer located at the focus. In the DAS approach the delayed received channel data are summed up for each scan line, whereas for the MV beamformer the optimal aperture weights are estimated for each time sample before summation. It should be noticed that only the channel data corresponding to the unaffected elements in the active aperture are used for making the DAS image. We use a beam density of 2 beams per element and the point scatterers are adjusted so that they are located exactly on the beams to ensure that the signal peak is not missed in the MV approach. In the MV approach, we have examined different scaling factors between $\Delta = 1\%$ to 10% for diagonal loading of covariance matrices. Considering the adequate robustness and the acceptable performance of the MV beamformer, we use diagonal loading with $\Delta = 0.02$ in all simulations.

In this simulation study, the vertebra is used as a shadowing source and the binary shadowing apodization is separately estimated for each point scatterer as described in Section 2.2.3. We use Field II [20] to image 2 columns of point scatterers located close to the vertebra wall [Fig. 2.2(a)]. The right-hand column is close enough to the wall to be affected by shadowing originating from the vertebra body, whereas the left-hand column is completely unaffected. In the right-hand column, the distance from the point scatterers to the vertebra wall, varies with depth to ensure that different shadowing ratios are achieved. The shadowing ratio is defined as the ratio of the number of unaffected elements to the total number of elements in the active aperture. It should be noticed that the point scatterers' locations may not be so relevant for clinical imaging, but we have chosen this imaging scenario to achieve different shadowing ratios.

In Fig. 2.2(b), the shadowing ratio variation is presented as a function of the depth for the right-hand column of scatterers which are located at depths of 21 mm, 23 mm, 25 mm, and 27 mm. The receive shadowing ratios for these scatterers are 10%, 30%, 52%, and 60% respectively.

Effects originating from other scattering modes, *e.g.* multiple reflection and reverberation are not considered in this study. Furthermore, $\bar{K} = 20$ is considered in (2.7) to estimate the average power of elements approximately over one pulse length. The sampling frequency is $f_s = 100$ MHz and the imaging medium is assumed to be water with sound speed of 1500 m/s.

2.2.5 Experimental setup

In the experimental study, channel data are acquired using a Sonix RP scanner (Ultrasonix medical corporation, Vancouver, Canada), along with a linear array transducer (L14-5/38) with 128 elements, a center frequency of 5 MHz, elevation

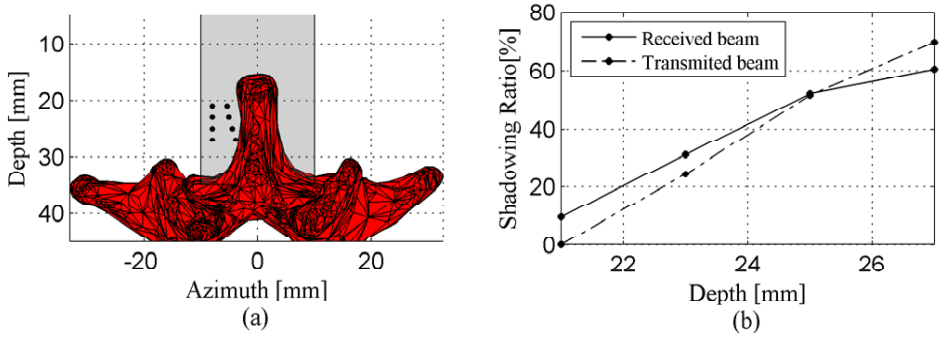

Figure 2.2: (a) Vertebra phantom used for the simulation study, (b) shadowing ratio versus depth for the right-hand column of the point scatterers.

focus of 19 mm, and pitch of 0.308 mm. In all experiments, a fixed transmit focus and dynamic receive focusing is used. In addition, the f number in the transmit is $\mathrm{FN}_{\mathrm{TX}} = 2.8$. Further, the receive aperture walks with the transmit aperture, meaning that the active receive elements are centered on the transmit beam axes. The research module software running on this scanner allows us to operate the scanner in the channel data mode. In this mode, for each focused transmit beam, data on a single channel is recorded. Thus, a succession of transmit beams are applied to acquire data corresponding to all active channels. The maximum aperture size in the receive is 28 elements due to receiver hardware limitations. That is, the maximum aperture size which can be used in the MV beamforming technique is limited to $M = 28$, and the f number in the receive is no longer fixed. Similar to the simulations, the delayed channel data are first stored. Then, two different beamforming methods are implemented to construct images of interest. In the DAS beamformer only the channel data corresponding to the unaffected elements are used for making the DAS image. Similar to the simulations, we use diagonal loading with $\Delta = 0.02$ to ensure a well conditioned covariance matrix unless otherwise specified.

In the experiments, a steel needle's tip is used as a point scatterer. The diameter of the needle is measured at its tip using an optical microscope (Leica MEF4M, Wetzlar, Germany). In this study, we perform two different experiments: verification of the shadowing model and imaging of a needle's tip, located in the shadow of a vertebra body, close to the vertebra's spinal process.

In the first water tank experiment, we investigate the shadowing model introduced in Section 2.2.3, by imaging a 66 μm steel needle's tip fixed close to a wax rectangle block [Fig. 2.3(a)]. The high attenuation of the wax material satisfies reasonably well the totally attenuating assumption of the shadowing obstacle in Section 2.2.3. The regular shape of this wax obstacle allows us to geometrically estimate the shadowing

apodization function around the needle's tip for the corresponding beam, and for the neighboring ones. Thus, by using the direct ray path from the needle's tip to the block edge to the probe surface, we approximate the shadow zone on the probe surface. This can be use to estimate the number of the shaded elements, and the binary apodization function accordingly. In this experiment, we modify the recorded data by multiplication of the estimated binary functions and corresponding channel data. This data can be used to calculate the beam profile around the needle's tip and for comparison with the beam profile calculated from the original data set. In this experiment, the transmit focal depth is set to 23 mm which is the depth where needle's tip is approximately located.
In the second experiment, we image a needle's tip next to bone in a water tank. Thus, a needle is fixed close to a lumbar human vertebra (L3) and immersed in a water tank. The transmit focal depth is set to 23 mm, approximately at the depth at which the 110 μm needle's tip has been located. $\bar{K} = 8$ is considered in (2.7) to estimate the average power of elements approximately over one pulse length. The sampling frequency is $f_s = 40$ MHz and the sound speed is 1500 m/s.

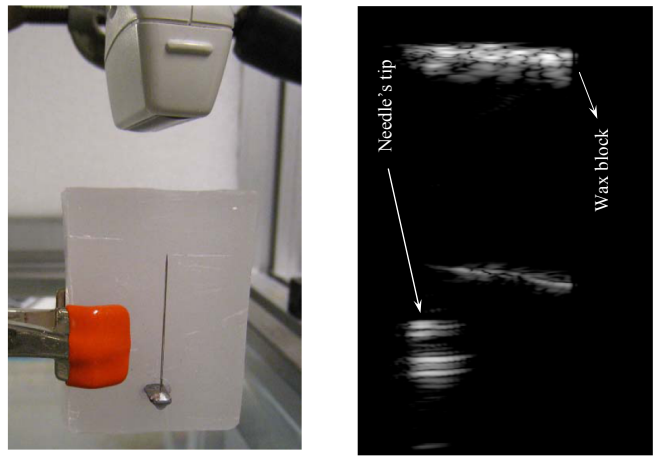

(a) (b)

Figure 2.3: Imaging a needle's tip located close to a wax obstacle using a transducer with 128 elements ($M = 28$), and central frequency of 5 MHz. (a) Illustration of the experiment setup, (b) B-Mode image, for which the dynamic range was set to 40 dB. The transmit focal depth is 23 mm.

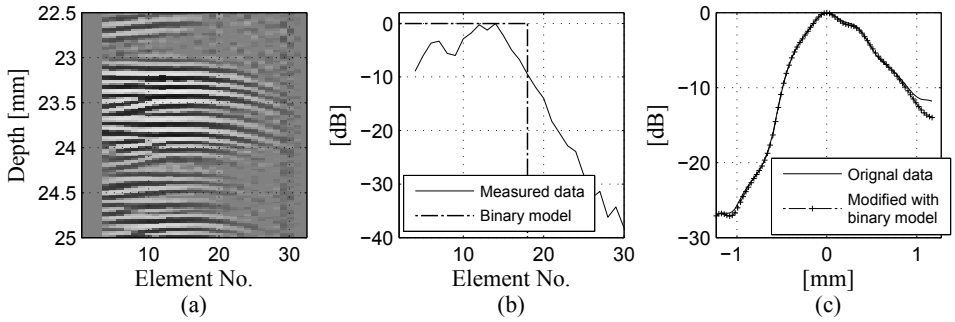

Figure 2.4: Imaging of a needle's tip located next to the wax block using a 128 element ($M = 28$), 5 MHz transducer. (a) Channel data, for which the dynamic range was set to 60 dB, (b) RMS of the signal over depths ranging from 23.2 mm to 23.5 mm, (c) comparison of the two-way beam profiles around the needle's tip corresponding to the original and modified data. The transmit focal depth is 23 mm.

2.3 Results

2.3.1 Experimental verification of the shadowing model

Fig. 2.4(a) shows the channel data corresponding to the beam that is steered toward the tip of the needle. Starting from depth 23.2 mm, the shadow on the right-hand side of the aperture is significant. In Fig. 2.4(b) the root mean square (RMS) of the channel data in Fig. 2.4(a) from depth 23.2 mm to 23.5 mm has been shown, and the estimated shadowing apodization is overlaid. It should be remarked that the geometrically estimated binary apodization function keeps all elements that have an RMS value within 10 dB of the strongest element. A threshold value of $P_{lim} = -10$ dB will therefore be used in later experiments as well. Fig. 2.4(c) shows the two-way beam profiles around the needle's tip for the original data and for the data which has been modified with the binary apodization from Fig. 2.4(b).

2.3.2 Simulation of the point scatterers next to the vertebra

Fig. 2.5(a) shows that increasing the shadowing ratio results in widening of the PSF for the right-hand column of the point scatterers in the DAS image. In Fig. 2.5(b), $L = M/2$ was used for the standard MV beamforming approach. It can be seen that the resolution degrades for the right-hand column of the scatterers as the shadowing ratio is increasing with depth. By comparison with the DAS image, a lateral shifting of the PSF and attenuation of the signal are clearly seen for the two scatterers located at depths of 25 mm and 27 mm, for which the shadowing ratio is approximately 52% and 60% respectively. In Fig. 2.5(c) the modified MV beamformer is used to construct the image of the point scatterers. This image indicates that using unaffected elements (M_{ua}) instead of the full aperture (M) significantly improves the image of the shaded

point scatterers. It can be seen that the resolution is improved and the lateral shifting of the PSF is compensated for at depths of 25 mm and 27 mm.

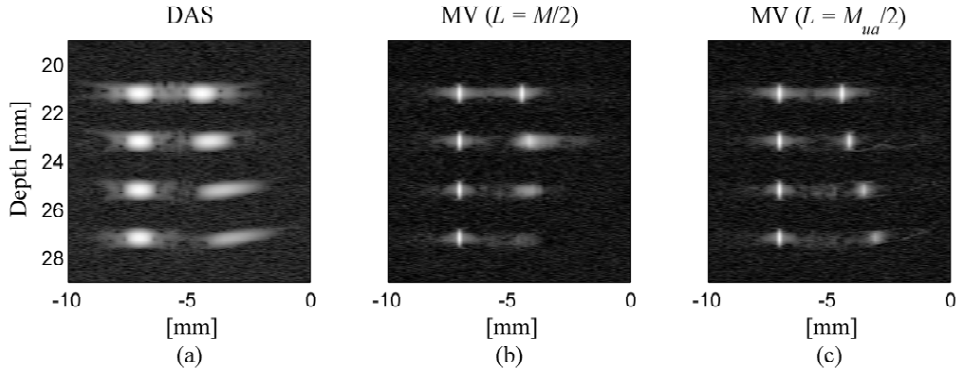

Figure 2.5: Simulated point scatterers close to the vertebra using a 128 element ($M = 64$), 5 MHz transducer. The transmit focal depth is 25 mm and dynamic focusing is used for the received beams. (a) DAS, (b) MV ($L = M/2$, $K = 0$), (c) MV ($L = M_{ua}/2$, $K = 0$, $\bar{K} = 20$). The dynamic range in these images is 60 dB.

Fig. 2.6 demonstrates beam profiles corresponding to the images of the point scatterers in Fig. 2.5. All beam profiles have been individually normalized to their maximum value. Fig. 2.6(a) shows beam profiles at a depth of 21 mm at which the shadowing effect is minor (10%). By comparison with the DAS beamformer, the resolution is significantly higher and the sidelobe levels are lower for the point scatterers in both standard and modified MV beamformers. Fig. 2.6(b) indicates that for the standard MV beamformer with subarray length of $L = M/2$, the resolution degrades and the signal level drops by 4.5 dB as the shadowing ratio increases to almost 30% on the receive aperture. These effects are compensated for in the modified MV beamformer. This beamformer results in a narrower beamwidth than both DAS and standard MV. In Figs. 2.6(c) and (d) by comparison with the DAS approach, we observe that the signal level for shadowed point scatterers are attenuated approximately by 10.5 dB and 17 dB at depths of 25 mm and 27 mm for the standard MV beamformer ($L = M/2$). At a depth of 25 mm, we also observe a 0.45 mm shifting of the peak in the MV beam profile. In comparison, at a depth of 27 mm, the peak shifting increases approximately to 1.49 mm as the shadowing ratio is raised to 60%. By comparison, the modified MV beamformer compensates the shifting artifact for the shaded point scatterers, and approximately retains the signal level as high as that of the DAS beamformer. Also, in Fig. 2.6(d) the modified MV beamformer ($L = M_{ua}/2$) locates more accurately the actual location of the shaded point scatterer than DAS. The true location of the shadowed point scatterers have been marked with a vertical dash-dot line in the figure.

Fig. 2.7 shows effects of the MV subarray length on artifacts originating from the

shaded aperture in the corresponding beam profiles. The results are presented for the DAS and the standard MV beamformer with three different subarray lengths: $L = M/2$, $L = M/3$, and $L = M/6$. All beam profiles have been individually normalized to their maximum value. Figs. 2.7(a) and (b) show the beam profiles at depths where the shadowing ratio is less than 50%. These results indicate that increasing L gives rise to wider beamwidth as it has been discussed in [11]. Fig. 2.7(c) shows that for the shadowed point scatterers, the shifting effect is compensated as L reduces in the MV approach. By comparison with $L = M/2$, the signal level increases approximately by 7 dB and 9 dB for $L = M/3$ and $L = M/6$. Fig. 2.7(d) indicates that at a depth of 27 mm the shifting effect decreases from 1.49 mm for $L = M/2$ to 0.39 mm for $L = M/3$ and it approaches that of DAS when the subarray length equals $L = M/6$. Furthermore, the signal level is elevated almost by 12.5 dB and 15 dB for $L = M/3$ and $L = M/6$ in comparison with $L = M/2$. However, the beamwidth can be wider than that of the DAS beamformer when the shadowing ratio increases over 50%.

In TABLE 2.1 beam profile parameters are listed for the different beamformers. These parameters are related to the right-hand column of the point scatterers in the vertebra phantom, and include beamwidths, variation of the normalized signal levels (dA), and shifting of peak positions (dS). The beamwidths are calculated at -12 dB relative to the peak levels. The dA parameter indicates the difference between the normalized MV level and the corresponding DAS peak level. This measure shows the signal sensitivity variation of the MV beamformers in comparison with the DAS beamformer when the shadowing effect exists. The dS parameter indicates the peak shifting of the shadowed point scatterer with respect to the true position of the point scatterers.

2.3.3 Experimental study: point scatterer next to the bone

Fig. 2.8(a) shows the experimental setup. Fig. 2.8(b) presents the channel data around the tip of the needle without the vertebra specimen, whereas Fig. 2.8(c) shows the channel data at the tip of the needle located next to the vertebra. This display also indicates that elements 19 to 30 have been shadowed and the shadowing ratio is approximately 40%. It should be noticed that elements number 1, 2, 31, 32 are inactive in the receive aperture.

Fig. 2.9 shows images of the needle placed close to the vertebra for the DAS, the standard MV, and the modified MV beamformers. The needle's tip has been located approximately at a depth of 22.7 mm. The reverberation effect inside the needle material introduces weak echoes in the depth direction, which are apparent in the images. In Fig. 2.9(a), at a depth of 22.7 mm the image of the needle's tip widens as the aperture has been partly shaded. In this image, stretching of the signal from the vertebra wall into the shade inside the vertebra is significant. In comparison, in Figs. 2.9(b), and (c) the needle's tip is more resolvable and the boundary of the vertebra's sidewall is better defined. By comparison with the DAS image, the curvature of the vertebra's wall is distorted in Fig. 2.9(b) as a result of the shadowing effect.

Table 2.1: Comparison of beam profile parameters of the MV and DAS beamformers for the right-hand column of the point scatterers in the simulated vertebra phantom.

Depth [mm]	SHR[I] [%]	Beamwidth [mm]				Variation of the normalized signal level $(dA)^{II}$ [dB]				Shifting of the peak position $(dS)^{III}$ [mm]			
		DAS	MV $L = M/2$	MV $L = M/3$	MV $L = M/6$	MV $L = M_{ua}/2$	MV $L = M/2$	MV $L = M/3$	MV $L = M/6$	MV $L = M_{ua}/2$	DAS	MV $L = M/2$	MV $L = M/3$	MV $L = M/6$	MV $L = M_{ua}/2$
21	10	0.89	0.17	0.24	0.63	0.17	0.00	0.00	0.00	0.00	0.00	0.00	0.00	0.00	0.00
23	30	1.06	0.63	1.17	1.10	0.30	4.40	1.52	0.47	0.60	0.00	0.00	0.00	0.00	0.00
25	52	1.86	1.08	2.08	1.83	0.31	10.6	3.88	1.45	0.80	0.10	0.45	0.23	0.10	0.00
27	60	2.21	-	2.59	2.27	0.45	17.1	4.65	1.98	2.50	0.18	1.49	0.39	0.18	0.00

[I]SHR = Shadowing Ratio
[II]dA = DAS signal level - MV signal level
[III]dS = true position of the point scatterer - Signal peak position

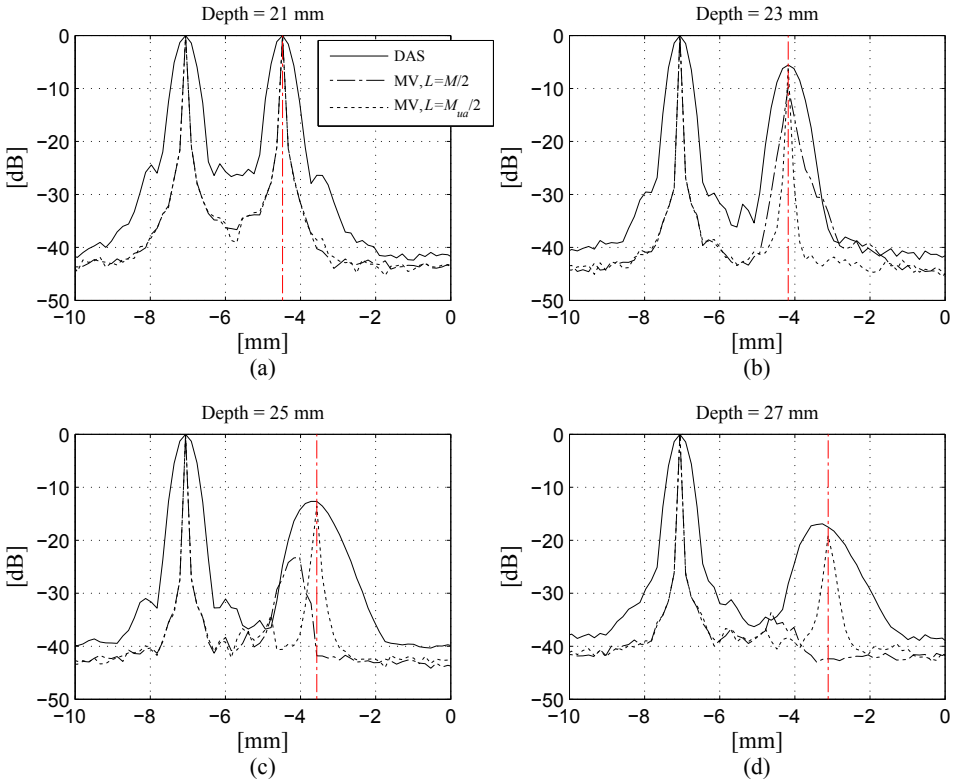

Figure 2.6: Two-way beam profiles of simulated point scatterers for DAS, MV ($L = M/2$, $K = 0$), MV ($L = M_{ua}/2$, $K = 0$, $\bar{K} = 20$) beamformers. (a) Depth = 21 mm, (b) depth = 23 mm, (c) depth = 25 mm, (d) depth = 27 mm. All other parameters are the same as in Fig. 2.5.

This distortion effect has been compensated for in Fig. 2.9(c). This image indicates that using unaffected elements (M_{ua}) instead of the full aperture (M) in Fig. 2.9(c) gives rise in an elevated signal level at the needle's tip in comparison with Fig. 2.9(b). However, this improvement is at expense of a higher sidelobe level around the needle's tip.

Fig. 2.10 shows beam profiles around the needle's tip for different beamformers. In this experiment, P_{lim} is set to -10 dB as in the wax model study of Fig. 2.4. The beam profiles have been normalized to the maximum value of the DAS beam profile. In comparison with the DAS beamformer, for $L = M/2$ a 0.3 mm lateral shift and 12 dB attenuation of the peak is observed, whereas for $L = M/3$, the shifting reduces and the level of the signal rises to -3.5 dB. For the beamformer with subarray length of $L = M_{ua}/2$, the shifting is compensated, and the signal level is elevated to -6.3 dB,

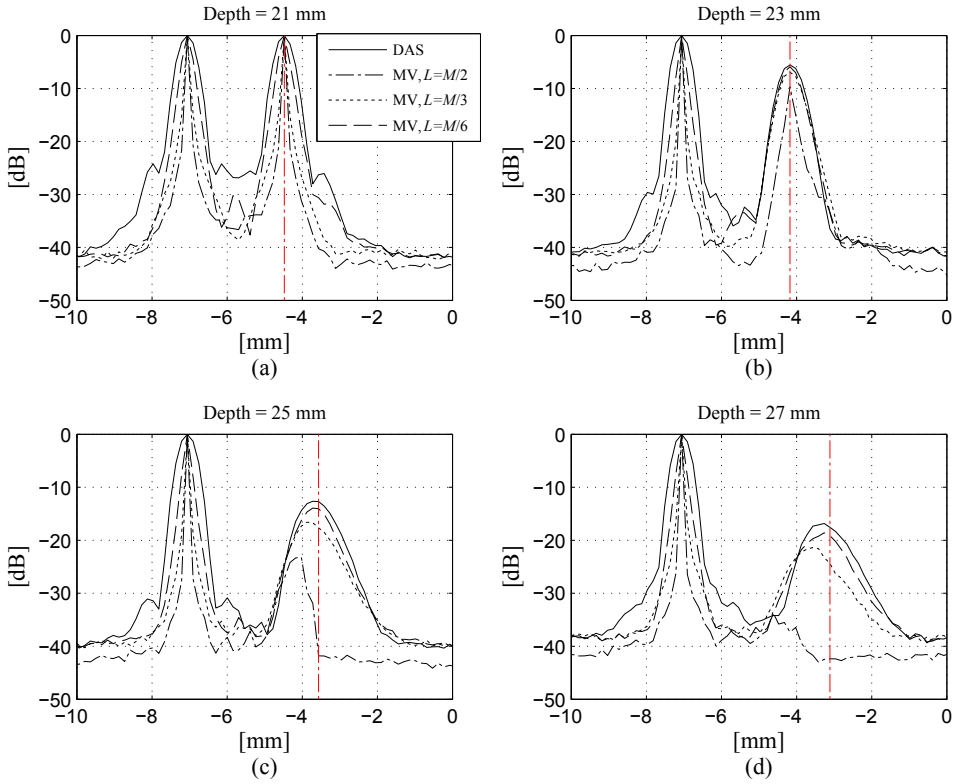

Figure 2.7: Two-way beam profiles of simulated point scatterers in which three different subarray lengths, including $M = L/2$, $M = L/3$, and $M = L/6$ are considered for the standard MV beamforming and compared with the DAS approach. (a) Depth = 21 mm, (b) depth = 23 mm, (c) depth = 25 mm, and (d) depth = 27 mm. All other parameters are the same as in Fig. 2.5.

which is a great improvement compared to the standard MV beamformer with subarray length of $L = M/2$.

2.4 Discussion

In Fig. 2.4 by imaging a needle's tip close to a wax obstacle, we verify the proposed shadowing model introduced in Section 2.2.3. As can be seen in Fig. 2.4, around depth 23.2 mm the pulse echo signals for elements 19-30 have lower levels, and they are retarded in comparison with those of elements 3-18. These effects are related to the diffraction from the edge of the wax obstacle which has not been taken into account in the shadowing model presented in Section 2.2.3. This diffraction effect can also be

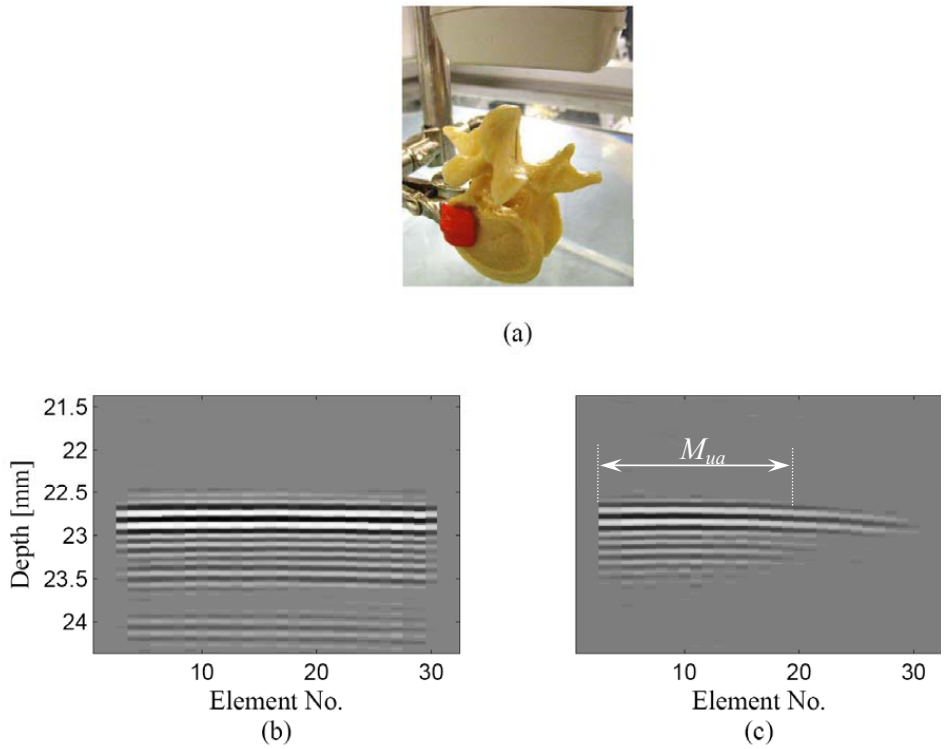

Figure 2.8: Imaging of a needle's tip located at a depth of 22.7 mm using a 128 element ($M = 28$), 5 MHz transducer. (a) Experimental setup, (b) channel data at the tip of the needle when shadowing does not exist, (c) channel data at the tip of the needle located next to the vertebra. The dynamic range is 40 dB.

observed in Fig. 2.8(c) from elements 20-30. The beam profiles in Fig. 2.4(c) indicate that the proposed binary apodization model can reasonably well show the shadowing effect.

The main advantages of MV beamforming are enhanced resolution and contrast in ultrasound images compared to DAS beamforming. From Figs. 2.5, 2.6 and TABLE 2.1 we observe that the benefits are kept as long as the point scatterers are moderately shaded. As the shadowing ratio increases over 50%, the image can be distorted.

The asymmetrical signal across the aperture is the main reason for these artifacts. This can be explained by the minimization which is inherent in the MV method. It relies on the minimum variance distortionless criterion, *i.e.* minimization of the output variance subject to element weights which sum up to unity. This assumes that all elements should be equally sensitive. If one or more elements are less sensitive than the others, the minimum variance criterion will in general put a larger weight on these elements and reduce the weights on the more sensitive ones. The extreme case

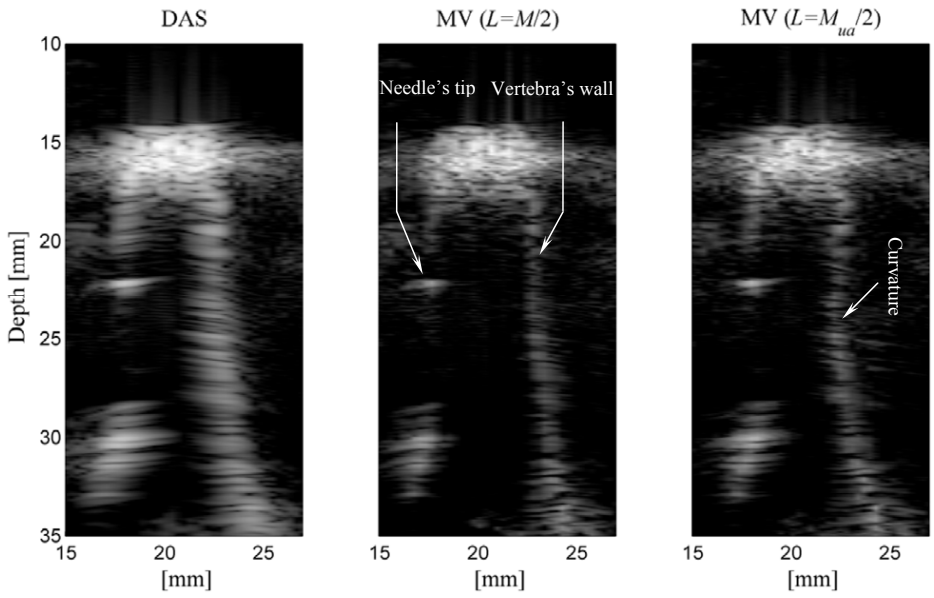

Figure 2.9: Image of a needle's tip next to the vertebra. (a) DAS image, (b) MV image ($L = M/2$, $K = 0$), (c) MV image ($L = M_{ua}/2$, $K = 0$, $\bar{K} = 8$). The needle's tip is located at a depth of 22 mm. The dynamic range is 60 dB and all other parameters are the same as in Fig. 2.8.

occurs when one element is dead. Then, the optimal solution is to set the weight of this element to unity, and the rest to zero. This gives a beamformer output equal to zero. This is a kind of signal cancellation which is different from the signal cancellation which occurs when multiple coherent sources are received by the array.
In the case of element shadowing, the shadowing reduces the energy received on some of the elements, and this type of signal cancellation will to some extent arise. When subarray averaging is used, the effect occurs when the subarray length is larger than the unaffected part of the active aperture. The simulated results in Fig. 2.6(d) show this effect.
Furthermore, spatial smoothing relies on an assumption of statistical invariance across the aperture. When a fraction of the array is shadowed, the subarray length is shorter than the unaffected aperture. Accordingly, part of the covariance matrix in Eq. (2.4) is built from unaffected subarrays, and part of the matrix comes from subarrays have various degrees of shadowed elements. Such an imprecise correlation matrix estimation mixed with a certain degree of uneven element sensitivity will affect the performance of the MV beamformer as observed in Figs. 2.5, 2.6 and Fig. 2.9(b).
The shadowing artifacts are sensitive to the subarray length. For example, selecting a smaller L can compensate both the shifting and the signal sensitivity for the shadowed point scatterers at the expense of the performance degradation in term of the resolution

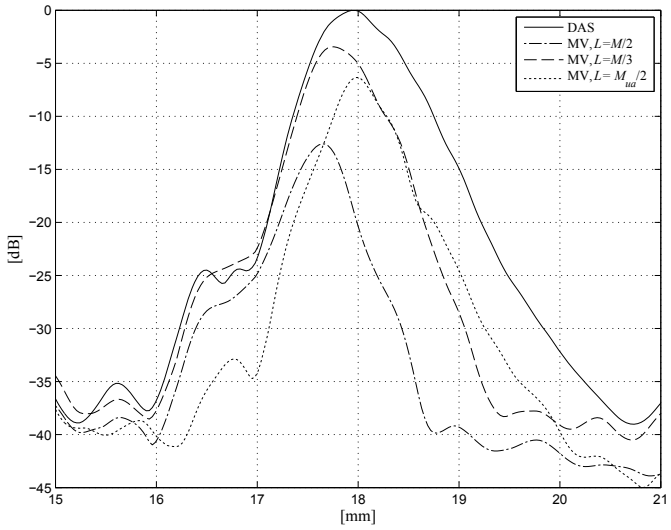

Figure 2.10: Beam profiles for the needle's tip located next to the vertebra, in which three different subarray length, $L = M/2$, $L = M/3$, and $L = M_{ua}/2$ are considered for the MV beamforming method and compared with the DAS approach. The needle's tip is located at a depth of 22 mm. The bottom axis is related to the lateral position in Fig. 2.9. All other parameters are the same as in Fig. 2.8.

(Fig. 2.7).
The performance of the MV beamformer can be improved if the shadowed elements are identified and their corresponding data are removed from the observation vector, $\mathbf{X}$ in (2.1). In Figs. 2.5 and 2.6 the image of the shadowed point scatterers are significantly enhanced as the MV beamforming has been performed just on unaffected elements (M_{ua}). In Fig. 2.6(d), a lateral shift is seen in the DAS beam profile. This error is a result of the tilted PSF due to the shadowed aperture.
From Fig. 2.9 a improvement can be seen in the MV images of the vertebra in comparison to the DAS one. In these images, the boundary of the vertebra's sidewall has been well defined, the shadow inside the vertebra is less noisy, and the tip of the needle is more distinguishable. The modified MV beamformer improves the robustness as it gives rise to an undistorted curvature of the vertebra's wall [Fig. 2.9(c)], the signal level elevation at the needle's tip (Fig. 2.10), and precise localization of the needle's tip (Fig. 2.10). In general, the improvements observed in the MV beamformers are beneficial for many ultrasound applications. For instance, depicting a clearer shadow inside the bone can facilitate spine level detection for inspinal-epidural anaesthesia [24], and better definition of the bone surface can improve the spine registration in image-guide navigation in neurosurgery and orthopaedics [2].

2.5 Conclusion

We have introduced a binary apodization model to simulate effects of the shadowing on the point scatterers located next to an acoustically hard tissue. Employing this model, it has been shown that the performance of the MV beamformer can degrade when the imaging aperture is highly obstructed by an acoustically hard tissue, *i.e.* the shadowing ratio is increased over 50%. This performance degradation can distort the corresponding images due to the apparent PSF lateral shift and sensitivity reduction. The same effects have been observed in an *in-vitro* experiment. It has been demonstrated that these artifacts can be reasonably well compensated for if the MV optimization problem is performed just on unaffected elements. Thus, we have proposed an adaptive technique to detect shadowed elements and discard their corresponding data from the covariance matrix estimation. This technique improves robustness of the MV beamformer against the signal misalignment resulting from the shadowed elements. This modified MV beamformer can retain the resolution and compensate the apparent lateral shift and signal attenuation for the shadowed scatterers.

References

[1] B. Bendel, S. Winter, A. Rick, M. Stockheim, and H. Ermert, "Registration of 3D CT and ultrasound datasets of the spine using bone structures," *Computer Aided Surgery*, vol. 7, no. 3, pp. 146–155, 2002.

[2] S. Winter, B. Brendel, I. Pechlivanis, K. Schmieder, and C. Igel, "Registration of CT and intraoperative 3-D ultrasound images of the spine using evolutionary and gradient-based methods," *IEEE Transactions on Evolutionary Computation*, vol. 12, no. 3, pp. 284–296, 2008.

[3] R. N. R. Denis Tran, "Automatic detection of lumbar anatomy in ultrasound images of human subjects," *IEEE Transactions on Ultrasonics, Ferroelectrics, and Frequency Control*, vol. 57, no. 9, pp. 2248–2256, 2010.

[4] O. Solheim, T. Selbekk, L. Lovstakken, G. A. Tangen, O. V. Solberg, T. F. Johansen, J. Cappelen, and G. Unsgard, "Intrasellar ultrasound in transsphenoidal surgery: A novel technique," *Neurosurgery*, vol. 66, no. 1, pp. 173–186, 2010.

[5] M. M. Bonsanto, R. Metzner, A. Aschoff, V. Tronnier, S. Kunze, and C. R. Wirtz, "3D ultrasound navigation in syrinx surgery ï¿½ a feasibility study," *Acta Neurochirurgica*, vol. 147, no. 5, pp. 533–541, 2005.

[6] F. Kolstad, O. M. Rygh, T. Selbekk, G. Unsgaard, and O. P. Nygaard, "Three-dimensional ultrasonography navigation in spinal cord tumor surgery," *Journal of Neurosurgery: Spine*, vol. 5, no. 3, pp. 264–270, 2006.

[7] A. Takeshi, H. Kazutoshi, A. Minoru, Y. Shunsuke, and I. Yoshinobu, "Detection of residual disc hernia material and confirmation of nerve root decompression at lumbar disc herniation surgery by intraoperative ultrasound," *Ultrasound in medicine & biology*, vol. 35, no. 6, pp. 920–927, 2009.

[8] D. Tran, K.-W. Hor, V. A. Lessoway, A. A. Kamani, and R. N. Rohling, "Adaptive ultrasound imaging of the lumbar spine for guidance of epidural anesthesia," *Computerized Medical Imaging and Graphics*, vol. 33, no. 8, pp. 593–601, 2009.

[9] J. T. M. Verhoeven and J. M. Thijssen, "Improvement of lesion detectability by speckle reduction filtering: A quantitative study," *Ultrasonic Imaging*, vol. 15, no. 3, pp. 181–204, 1993.

[10] A. R. Groves and R. N. Rohling, "Two-dimensional spatial compounding with warping," *Ultrasound in Medicine & Biology*, vol. 30, no. 7, pp. 929–942, 2004.

[11] J. F. Synnevag, A. Austeng, and S. Holm, "Adaptive beamforming applied to medical ultrasound imaging," *IEEE Transactions on Ultrasonics, Ferroelectrics and Frequency Control*, vol. 54, no. 8, pp. 1606–1613, 2007.

[12] J. Capon, "High-resolution frequency-wavenumber spectrum analysis," *Proceedings of the IEEE*, vol. 57, no. 8, pp. 1408–1418, 1969.

[13] J. Mann and W. Walker, "A constrained adaptive beamformer for medical ultrasound: initial results," *Proc. Ultrasonics Symposium*, vol. 2, pp. 1807–1810, 2002.

[14] M. Sasso and C. Cohen-Bacrie, "medical ultrasound imaging using the fully adaptive beamformer," *proc. IEEE Acoustics, Speech, and Signal, (ICASSP '05)*, vol. 2, pp. 489–492, 2005.

[15] Z. Wang, J. Li, and R. Wu, "Time-delay- and time-reversal-based robust capon beamformers for ultrasound imaging," *IEEE Transactions on Medical Imaging*, vol. 24, no. 10, pp. 1308–1322, 2005.

[16] F. Vignon and M. R. Burcher, "Capon beamforming in medical ultrasound imaging with focused beams," *IEEE Transactions on Ultrasonics, Ferroelectrics and Frequency Control*, vol. 55, no. 3, pp. 619–628, 2008.

[17] J. F. Synnevag, A. Austeng, and S. Holm, "Benefits of minimum-variance beamforming in medical ultrasound imaging," *IEEE Transactions on Ultrasonics, Ferroelectrics and Frequency Control*, vol. 56, no. 9, pp. 1868–1879, 2009.

[18] B. Mohammadzadeh Asl and A. Mahloojifar, "Eigenspace-based minimum variance beamforming applied to medical ultrasound imaging," *IEEE Transactions on Ultrasonics, Ferroelectrics and Frequency Control*, vol. 57, no. 11, pp. 2381–2390, 2010.

[19] S. Tie-Jun, M. Wax, and T. Kailath, "On spatial smoothing for direction-of-arrival estimation of coherent signals," *IEEE Transactions on Ultrasonics, Ferroelectrics and Frequency Control*, vol. 33, no. 4, pp. 806–811, 1985.

[20] J. A. Jensen, "Field: A program for simulating ultrasound systems," *Medical and Biological Engineering and Computing*, vol. 34, pp. 351–353, 1996.

[21] M. H.Hayes, *Statistical Digital Signal Processing and Modeling*. New York: John Wiley & Sons, Inc, 1996.

[22] P. Stoica and R. L. Moses, *Introduction to spectral analysis*. New Jersey: Prentice Hall, 1997.

[23] J. W. Trobaugh and R. M. Arthur, "A discrete-scatterer model for ultrasonic images of rough surfaces," *IEEE Transactions on Ultrasonics, Ferroelectrics and Frequency Control*, vol. 47, no. 6, pp. 1520–1529, 2000.

[24] G. Furness, M. P. Reilly, and S. Kuchi, "An evaluation of ultrasound imaging for identification of lumbar intervertebral level," *Anaesthesia*, vol. 57, no. 3, pp. 277–280, 2002.

Chapter 3

Eigenspace Based Minimum Variance Beamforming Applied to Ultrasound Imaging of Acoustically Hard Tissues

Saeed Mehdizadeh[1], Andreas Austeng[2], Tonni F. Johansen[1], and Sverre Holm[1,2]
[1] Dept. Circulation and Medical Imaging, NTNU, Norway
[2] Dept. Informatics, University of Oslo, Norway

Minimum variance (MV) based beamforming techniques have been successfully applied to medical ultrasound imaging. These adaptive methods offer higher lateral resolution, lower sidelobes and better definition of edges compared to delay and sum beamforming (DAS). In standard medical ultrasound, the bone surface is often visualized poorly, and the boundaries region appears unclear. This may happen due to fundamental limitations of the DAS beamformer, and different artifacts due to, *e.g.* specular reflection, and shadowing. The latter can degrade the robustness of the MV beamformers as the statistics across the imaging aperture is violated because of the obstruction of the imaging beams. In this study, we employ forward/backward (FB) averaging to improve the robustness of the MV beamforming techniques. Further, we use an eigenspace minimum variance technique (ESMV) to enhance the edge detection of hard tissues. In simulation, *in-vitro*, and *in-vivo* studies, we show that performance of the ESMV beamformer depends on estimation of the signal subspace rank. The lower ranks of the signal subspace can enhance edges and reduce noise in ultrasound images but the speckle pattern can be distorted.

3.1 Introduction

Ultrasound imaging of bone tissue has been investigated in different clinical procedures, *e.g.* registration of bone in neurosurgeries and orthopedics [1–4], guidance for spinal anesthesia [5, 6], guidance for diagnosis of skeletal fractures in emergency rooms [7, 8]. In a number of these applications automatic detection of bone surface is of interest [3, 4, 9]. Therefore, better localization of the bone surface and enhanced definition of edges can improve efficiency of these procedures. In standard medical ultrasound, bone surface are often visualized poorly, and the boundary region appears blurry [4]. This may happen due to different artifacts, and fundamental limitation of the DAS beamformer.

In the DAS technique received signals from active channels are dynamically delayed and summed up in the beamformer. In this beamforming technique, the achievable resolution, sidelobe level and contrast are limited. Utilizing an adaptive configuration, such as MV-based beamforming techniques, can enhance the image quality as a result of lower sidelobes, a narrower beamwidth, better definition of edges [10]. In the MV approach, for each time sample, the delayed received signal from each element is weighted adaptively before summing up in the beamformer. This approach was initially developed by Capon for passive narrow-band applications [11].

Several researchers have previously investigated the MV approach in medical ultrasound. They reported appreciable enhancements in the resolution and contrast in comparison with DAS beamforming [12–17]. Mann and Walker [12] used a broad-band constrained adaptive beamforming on experimental data of a single point target and a cyst phantom. Sasso and Cohen-Bacrie [13] and Synnevag *et al.* [16] applied a spatial smoothing technique [18] to deal with the coherent signals and to have a more robust estimation of the covariance matrix. Wang *et al.* [14] implemented the MV method for a synthetic aperture to take advantage of the dynamic focusing on both transmit and receive. This method generates a robust estimate of the covariance matrix at the expense of a lower signal to noise ratio (SNR). Vignon and Burcher [15] examined a MV beamforming technique to image the heart chambers and abdomen. They demonstrated more clinically significant images with higher resolution and contrast compared to the DAS beamforming. In a number of studies, forward/backward (FB) averaging has been applied to the covariance matrix estimation in order to improve the robustness of the MV algorithm [19–22]. Further, in a simulation study, Mohammadzadeh Asl and Mahloojfar [17] investigated an eigenspace-based MV (ESMV) technique to improve the contrast of the MV beamforming in medical ultrasound imaging. This technique has been developed based on earlier studies in radar imaging [23–25]. In the ESMV method, the MV weights are modified by projection on the desired signal space of the covariance matrix.

In [26] we have demonstrated that in bone imaging scenarios, shadowing can degrade the MV beamformer robustness due to a poor estimation of the covariance matrix. We have shown that this degradation can be avoided if the shadowed elements are detected and discarded in the MV estimation. That beamformer setup has been able to keep the MV benefits for the shadowed scatterers. However, in addition to the subarray length and the diagonal loading, an extra parameter in the form of a detection threshold is

required in order to detect the shadowed elements. The detection threshold should be determined from the detection probability and false alarm rate [27]. This works well for high signal to noise ratios, but there will be an increased probability for errors for low signal to noise ratios.
Alternatively, in this study, we employ FB averaging to enhance the covariance matrix estimation in imaging scenarios in which shadowing may happen [26]. Then, the enhanced covariance matrix is used to estimate ESMV weights. Subsequently, we investigate the potential of the ESMV beamforming technique to enhance the edges of the acoustically hard tissues, *e.g.* bones. In [22], we have shown the preliminary results from the present work, where performance of MV-based beamformers in imaging of partially shadowed point scatterers are investigated. Herein, the results are elaborated and discussed based on the signal subspace rank. Thus, in simulations, *in-vitro*, and *in-vivo* studies, we show that the lower rank of the signal subspace can give rise to an improved definition of the edges but the speckle pattern around the acoustically hard tissues can be distorted.

3.2 Methods

3.2.1 Minimum variance beamforming

We consider a transducer with M elements for which the time sampled complex data from element m is $x_m[n]$. The output signal from the beamformer for each sample is expressed as [10]:

$$z[n] = \mathbf{w}^H \mathbf{X}[n] = \sum_{m=1}^{M} w_m^* x_m[n], \tag{3.1}$$

where w_m is a time varying complex weight, and $(.)^H$ stands for Hermitian transpose. It is assumed that $x_m[n]$ has already been delayed for steering and focusing to the point of interest, *i.e.* the delay step of the delay-and-sum method has been performed. In MV beamforming the variance of $z[n]$ is minimized while the response from the focal point remains undistorted. This optimization problem can be expressed as:

$$\begin{cases} \min\limits_{\mathbf{w}} E\left[|z[n]|^2\right] = \min\limits_{\mathbf{w}} \mathbf{w}^H \mathbf{R}\, \mathbf{w} \\ subject\ to\ \mathbf{w}^H \mathbf{a} = 1 \end{cases}, \tag{3.2}$$

where $E[.]$ denotes the expectation operator, $\mathbf{R} = E\left[\mathbf{X}[n], \mathbf{X}[n]^H\right]$ is the spatial covariance matrix, $\mathbf{a}$ is the steering vector. Because the data has been delayed, $\mathbf{a}$ is simply a vector of ones. The optimization problem in (3.2) under defined constraint can be solved analytically by utilizing the Lagrange multiplier approach [28]. Accordingly, the optimized weighting coefficients are computed as:

$$\mathbf{w} = \frac{\mathbf{R}^{-1}\mathbf{a}}{\mathbf{a}^H \mathbf{R}^{-1}\, \mathbf{a}}. \tag{3.3}$$

However, in medical ultrasound imaging the signals are nonstationary as the transmit pulses are short. Thus, the covariance matrix should be estimated based on a few time samples and a number of spatial realizations of the data. To generate an ensemble of spatial samples a subarray technique is applied [18]. That is, the array is divided into overlapping subarrays with length of L, and then the corresponding covariance matrices are calculated and averaged across the array to estimate the full covariance matrix. In this method that is also known as the forward averaging technique, the covariance matrix is estimated as:

$$\hat{\mathbf{R}} = \frac{1}{(2K+1)(M-L+1)} \cdot \sum_{k=-K}^{K} \sum_{l=1}^{M-L+1} \bar{\mathbf{X}}_l[n-k]\, \bar{\mathbf{X}}_l[n-k]^H, \tag{3.4}$$

where

$$\bar{\mathbf{X}}_l[n] = \begin{bmatrix} x_l[n] & x_{l+1}[n] & \dots & x_{l+L-1}[n] \end{bmatrix}^T. \tag{3.5}$$

In general there is a time averaging over index k which has been found to be necessary in order to get proper speckle statistics in the image [16]. The subarray technique can be combined with the FB averaging to improve the covariance matrix estimation [29]. The new estimate is expressed as:

$$\hat{\mathbf{R}}_{FB} = \frac{1}{2}(\hat{\mathbf{R}} + \mathbf{J}\hat{\mathbf{R}}^*\mathbf{J}), \tag{3.6}$$

where $\mathbf{J}$ is an exchange matrix, the left/right flipped version of the identity matrix, with the same dimension as $\hat{\mathbf{R}}$. Substituting $\mathbf{R}$ with either $\hat{\mathbf{R}}$ or $\hat{\mathbf{R}}_{FB}$ in (3.3), the estimated amplitude is obtained by averaging over all subarrays:

$$\hat{z}[n] = \frac{1}{M-L+1} \sum_{l=1}^{M-L+1} \mathbf{w}^H \bar{\mathbf{X}}_l[n]. \tag{3.7}$$

It should be noticed that the robustness of the MV estimate is a concern due to the invertibility of the covariance matrix. In order to enhance the robustness of the MV estimate a diagonal loading technique is employed [30]. In this technique, a term, $\Delta/L \cdot tr\{\mathbf{R}\}$, is added to the diagonal of the covariance matrix before evaluating (3.3). This term is proportional to an estimate of the signal power where the factor of proportionality is Δ.

3.2.2 Eigenspace-based beamformer

The eigenspace-based beamformer (ESMV) utilizes the eigen structure of the covariance matrix to estimate MV weights [24, 25, 31]. With assumption of $j \leq L$, the sample covariance matrix $\hat{\mathbf{R}}$ defined by (3.4) is eigendecomposed as:

$$\hat{\mathbf{R}} = \sum_{l=1}^{L} \lambda_l \mathbf{e}_l \mathbf{e}_l^H, \tag{3.8}$$

where $\lambda_1 \geq \lambda_2 \geq .... \geq \lambda_L$, are eigenvalues in descending order, and $\mathbf{e}_l, l = 1, ..., L$ are the corresponding orthonormal eigenvectors. The sample covariance matrix can be expressed as:

$$\hat{\mathbf{R}} = \mathbf{E}\mathbf{\Lambda}\mathbf{E}^H = \mathbf{E}_s\mathbf{\Lambda}_s\mathbf{E}_s^H + \mathbf{E}_N\mathbf{\Lambda}_N\mathbf{E}_N^H, \tag{3.9}$$

where

$$\begin{aligned} \mathbf{E}_s &= [\mathbf{e}_1, ..., \mathbf{e}_j], \qquad \mathbf{E}_N = [\mathbf{e}_{j+1}, ..., \mathbf{e}_L], \\ \mathbf{\Lambda}_s &= diag[\lambda_1, ..., \lambda_j], \quad \mathbf{\Lambda}_N = diag[\lambda_{j+1}, ..., \lambda_L]. \end{aligned} \tag{3.10}$$

We refer to the subspace spanned by the columns of $\mathbf{E}_s$ as signal subspace and to that of $\mathbf{E}_N$ as noise subspace. Employing (3.3) and (3.8), and defining $\mu = 1/(\mathbf{a}^H\hat{\mathbf{R}}^{-1}\,\mathbf{a})$, the MV weight vector can be expressed as:

$$\mathbf{w} = \mu\,[\mathbf{E}_s\mathbf{\Lambda}_s^{-1}\mathbf{E}_s^H + \mathbf{E}_N\mathbf{\Lambda}_N^{-1}\mathbf{E}_N^H]\,\mathbf{a}. \tag{3.11}$$

Ideally, the second term on the right-side, $\mathbf{E}_N\mathbf{\Lambda}_N^{-1}\mathbf{E}_N^T$, should be zero as the direction of the steering vector and noise subspace are orthogonal, *i.e.* $\mathbf{E}_N^H\mathbf{a} = 0$ [31]. Thus, the optimal weight vector in (3.11) is reduced to:

$$\mathbf{w}_p = \mu\,[\mathbf{E}_s\mathbf{\Lambda}_s^{-1}\mathbf{E}_s^H]\,\mathbf{a}. \tag{3.12}$$

Equation (3.12) can be written in an alternative form as [24, 25]:

$$\mathbf{w}_p = \mathbf{E}_s\mathbf{E}_s^H\mathbf{w}. \tag{3.13}$$

Equation (3.13) can be interpreted as the projection of $\mathbf{w}$ on the signal subspace of $\hat{\mathbf{R}}$ [25]. In order to employ the projection method, the signal subspace ($\mathbf{E}_s$) should be identified. In [17] a straightforward eigenvalue thresholding was used to determine the signal subspace rank. Here, we select the rank of the signal subspace employing the cross-spectral metric [32]. This metric indicates the amount of energy projected along the k^{th} basis vector of the space spanned by columns of $\mathbf{R}$ (eigenvectors). Thus, the output signal power of the beamformer can be expressed based on cross-spectral metric as [60]:

$$\sigma_z^2 = (\mathbf{a}^H\mathbf{E}\mathbf{\Lambda}^{-\mathbf{1}}\mathbf{E}^H\mathbf{a})^{-1} = (\sum_{k=1}^{L}\frac{\rho_k^2}{\lambda_k})^{-1},\ \rho = \mathbf{E}^H\mathbf{a}, \tag{3.14}$$

where ρ_k^2/λ_k is the cross-spectral metric for the k^{th} eigenvalue. In a different approach from [32], we select the rank of $\mathbf{E}_s$, the signal subspace, by identifying the j largest eigenvalues for which the sum of their cross-spectral metric is β times smaller than the total output signal power (σ_z^2). The effect of this is that we will always select

the same or a larger number of eigenvalues compared to straightforward eigenvalue thresholding. This has a positive effect on the quality of the speckle.
A large value of the thresholding factor (*e.g.* $\beta \approx 90\%$) results in a full-rank signal subspace. By decreasing β the estimated rank of the signal subspace is reduced. Consequently, a very small value of thresholding factor (*e.g.* $\beta < 0.1\%$) suggests the smallest signal subspace rank, *i.e.* rank-1. In that case, *i.e.*, $\mathbf{E}_s$ is constructed based on the largest eigenvalue (λ_1).

3.2.3 Simulation setup

In this study, we simulate two different phantoms using Field II [33]: a vertebra phantom and a cyst phantom with 4 strong point scatterers. We use the same simulation scenario as in [26] for the vertebra phantom. We assume that the bone structure is completely attenuating. Therefore, it shadows the ultrasound beam which is steered to image the point scatterers in its vicinity. We use a binary apodization-based shadowing model to simulate the effects of the shaded aperture on the corresponding ultrasound images [26]. This model is applied to Field II in order to simulate the image of 2 columns of point scatterers that are located close to the vertebra wall to be affected by the shadow of the vertebra body [Fig. 3.1(a)]. The right-hand column is close enough to the wall to be affected by shadowing originating from the vertebra body, whereas the left-hand column is completely unaffected. In the right-hand column, the distance from the point scatterers to the vertebra wall, varies with depth to ensure that different shadowing ratios are achieved. The shadowing ratio is defined as the ratio of the number of unaffected elements to the total number of elements in the active aperture. In Fig. 3.1(b), the shadowing ratio variation is presented as a function of the depth for the right-hand column of scatterers which are located at depths of 21 mm, 23 mm, 25 mm, and 27 mm. The receive shadowing ratios for these scatterers are 0%, 25%, 50%, and 63% respectively.
The cyst phantom consists of 300000 equal amplitude point scatterers that are uniformly distributed in a region of $10\times8\times35$ mm^3. The number of scatterers per resolution cell exceeds 10, which is recommended to simulate speckle [34]. A 4 mm cyst is centered at a depth of 25 mm by setting the amplitude of scatterers within the cyst region to zero. In this study, the contrast ratio (CR) in the cyst is measured as [35]:

$$CR = \frac{I_{out} - I_{in}}{\sqrt{I_{out}^2 + I_{in}^2}}, \tag{3.15}$$

where I_{in} and I_{out} are the mean intensities in dB that are measured inside and outside of the cyst in predefined regions. The CR value varies in the range of [0,1]. CR= 0 indicates of no contrast between the cyst and the background speckle whereas CR= 1 shows a perfect contrast. Also, two pairs of strong point scatterers are placed at depths of 22 mm and 30 mm. These scatterers are laterally separated by 0.9 mm. We simulated images employing a linear array with 128 elements and a center frequency of 5 MHz (f_0) with 60 percent -6 dB fractional bandwidth. The elevation focus is 19 mm, and the pitch equals 0.308 mm. The maximum accessible aperture size for

this array transducer is 38.70 mm (M=128). The array is excited by 1.5 period of a square wave at center frequency of the array. In all simulations, a beam density of 2 beams per element, a fixed transmit focus, and dynamic receive focusing is used. In addition, f numbers in the transmit and the receive beams are set to FN_{TX}=2.8 and FN_{RX}=2 respectively. The transmit focal depth is set to 25 mm unless otherwise specified. The channel data are acquired for each scan line with sampling frequency of 120 MHz. For all beamformers after applying delays the channel data are down-sampled to 40 MHz. We also add white, Gaussian noise to each receiver channel so that the SNR is approximately 60 dB for the point scatterer located at the focal zone. We computed the analytic signals by applying the Hilbert transform to the delayed channel data. In the DAS approach, the apodization function is rectangular. Thus, the delayed received channel data are equally weighted and summed up for each scan line, whereas for MV-based beamformers the optimal aperture weights are estimated for each time sample before summation. In the adaptive approaches, we have examined different scaling factors between Δ=1% to 10% for diagonal loading of covariance matrices. Considering the adequate robustness and the acceptable performance of the MV-based beamformers, we use diagonal loading with Δ=5% in all simulations.

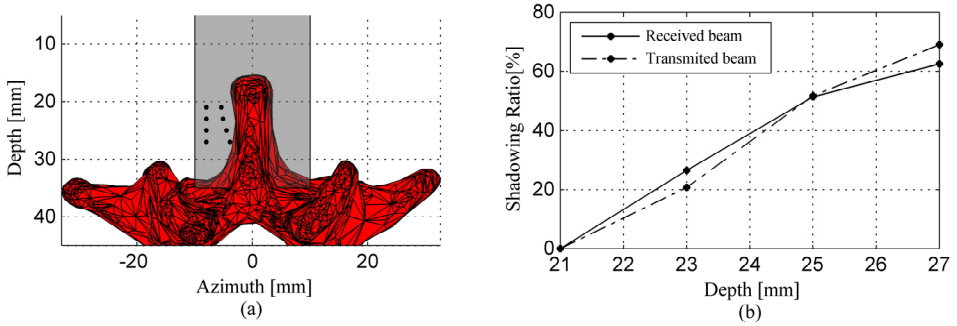

Figure 3.1: (a) Vertebra phantom used for the simulation study, (b) shadowing ratio versus depth for the right-hand column of the point scatterers.

3.2.4 Experimental setup

In the experimental study, channel data are acquired using a SonixMDP scanner (Ultrasonix medical corporation, Vancouver, Canada), along with a linear array transducer (L14-5/38) with 128 elements, centre frequency of 5 MHz, and pitch of 0.308 mm. We use 256 imaging beams, 2 beams per element, which are transmitted with FN_{TX}=2.8, and received with FN_{RX}=2. Further, the receive aperture walks with the transmit aperture, meaning that the active receive elements are centered on the transmit beams axes. The SonixDAQ (Ultrasonix medical corporation, Vancouver,

Canada) is used to capture the channel data. This module allows us to store RF data acquired from 128 elements simultaneously. For the beamforming purpose, the channel data related to each beam is first determined and delayed. Then, different beamforming methods are implemented to construct images of interest. Similar to simulations Δ=5% is used for the MV-based beamformers. Further, after construction of the images a 2D median filter with a window size of 3×3 is applied to the images for smoothing purposes.

3.3 Results

3.3.1 Simulation of the point scatterers next to the vertebra

Fig. 3.2 demonstrates images of the point scatterers shown in Fig. 3.1 for different beamforming techniques. These images are displayed over 60 dB dynamic range. Figs. 3.2(a) and (b) demonstrate the effects of the shadowing on the DAS and MV images of point scatterers as in [26]. Fig. 3.2(a) shows that increasing the shadowing ratio results in widening of the point spread function (PSF) for the right-hand column of the point scatterers in the DAS image. In Fig. 3.2(b), it can be seen that the resolution degrades for the right-hand column of the scatterers as the shadowing ratio is increasing with depth. Compared to DAS, signal attenuation is observed for the shadowed point scatterers, particularly for the point scatterers at depths of 25 mm and 27 mm with shadowing ratio of 50% and 63%. Also, for these two point scatterers, an apparent lateral shift of the PSF is observed. Fig. 3.2(c) indicates that FB averaging can compensate both the signal attenuation and the apparent lateral shift of the PSF for the highly shadowed point scatterers at depths of 25 mm and 27 mm, but the resolution at these points degrades to that of the DAS beamformer. Figs. 3.2(d) and (e) show the ESMV images for different eigenvalue threshold factors (β). In these two images, it can be seen that by decreasing β, the contrast in the images is increased and the sidelobe noises are decreased for the ESMV beamformer compared to MVFB. The highly shadowed point scatterers at depths of 25 mm and 27 mm are better defined for the ESMV images, particularly for β= 1%.

Fig. 3.3 demonstrates effects of the FB averaging on the beam profiles of the simulated point scatterers in Figs. 3.2(a)-(c). All beamprofiles have been individually normalized to their maximum value. Fig. 3.3(a) shows results at a depth of 21 mm, where the shadowing does not exist. In this case, the FB averaging keeps the resolution of the MV beamformer down to -15 dB. In Fig. 3.3(b), for the right-hand point scatterer, beamwidths are about 1.30 mm, 0.75 mm, and 1.10 mm for DAS, MV, and MVFB. The -12 dB beamwidths are measured from the signal peak corresponding to the right-hand point scatterer. Also the signal level drops by -2.5 dB for MV, whereas the MVFB almost keeps the same signal level as DAS. In Figs. 3.3(c) and (d), the lateral shift of the peak and the signal attenuation are significant for the shadowed point scatterers. The lateral shift is measured with respect to the true location of the point scatterer that is marked by vertical dash-dot lines. In Fig. 3.3(c) the shadowing ratio

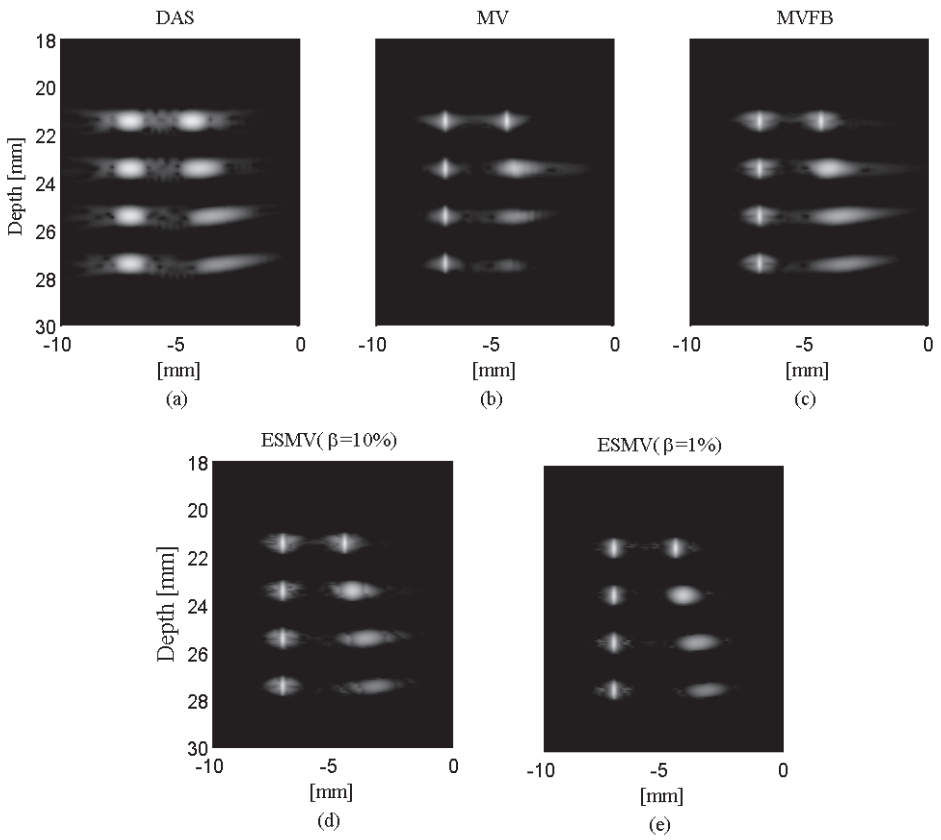

Figure 3.2: Simulated point scatterers next to the vertebra using a 128 element, 5 MHz transducer. The transmit focal depth is 25 mm and dynamic focusing is used for the received beams. (a) DAS, (b) MV, (c) MVFB, (d) ESMV (β =10%), and (e) ESMV (β=1%).The dynamic range is 60 dB. $L = M/2$, $K = 0$ are assumed for (b)-(e).

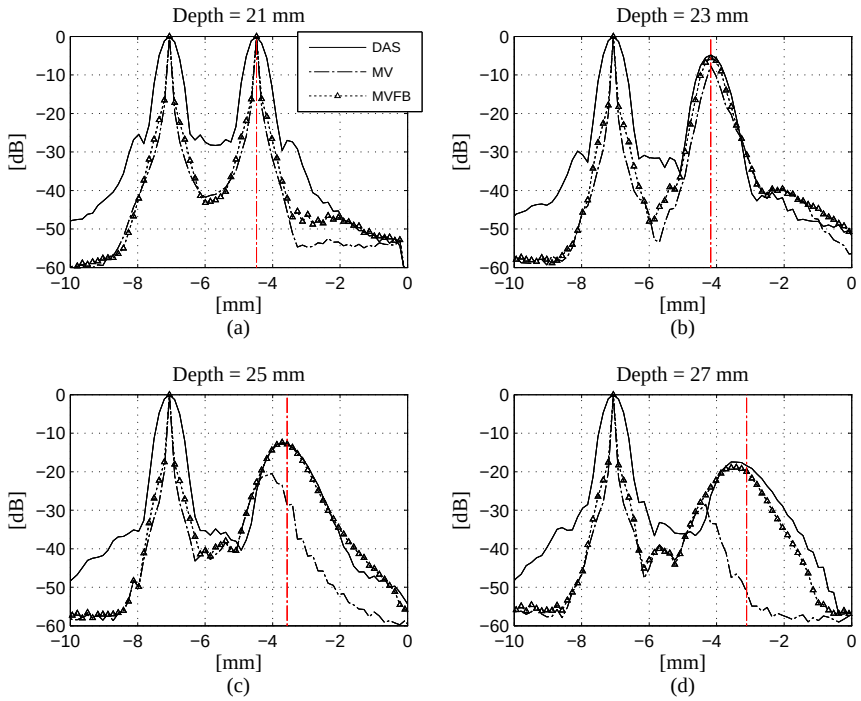

Figure 3.3: Two-way beam profiles of simulated point scatterers in Figs. 3.2(a)-(c). (a) Depth=21 mm, (b) depth=23 mm, (c) depth=25 mm, (d) depth=27 mm. All other parameters are the same as in Fig. 3.2

is about 50% for the shadowed point scatterer. In this figure approximately a 0.40 mm lateral shift of the peak and 8.5 dB signal attenuation are observed for the MV beam profile. The FB averaging gains up the signal level by about 8.5 dB, however the resolution decreases to that of DAS. Fig. 3.3(d) shows that the lateral shift and the signal attenuation increase to 1.22 mm and 11 dB in the MV beamformer as the shadowing ratio is 63%. For MVFB, these errors are reduced to that of the DAS beamformer. Furthermore, it should be noticed that a 0.40 mm lateral shift is also observed for DAS.

Fig. 3.4 presents ESMV beam profiles in comparison with MVFB and DAS ones. Fig. 3.4(a) shows beam profiles at a depth of 21 mm where the shadowing does not exist. The -12 dB beamwidths for the MVFB and ESMV beam profiles are about 1/5 of that of the DAS one. In Fig. 3.4(b) for the right-hand point scatterer, -12 dB beamwidths are about 0.75 mm for both ESMV beam profiles, 1.10 mm for MVFB, and 1.30 mm for DAS. Figs. 3.4(c)and (d) demonstrate that ESMV beamformers can locate the shadowed point scatterer more precisely than MVFB and DAS beamformers. In Fig. 3.4(d) the lateral shift errors are 0.1 mm for the ESMV and 0.4 mm for DAS

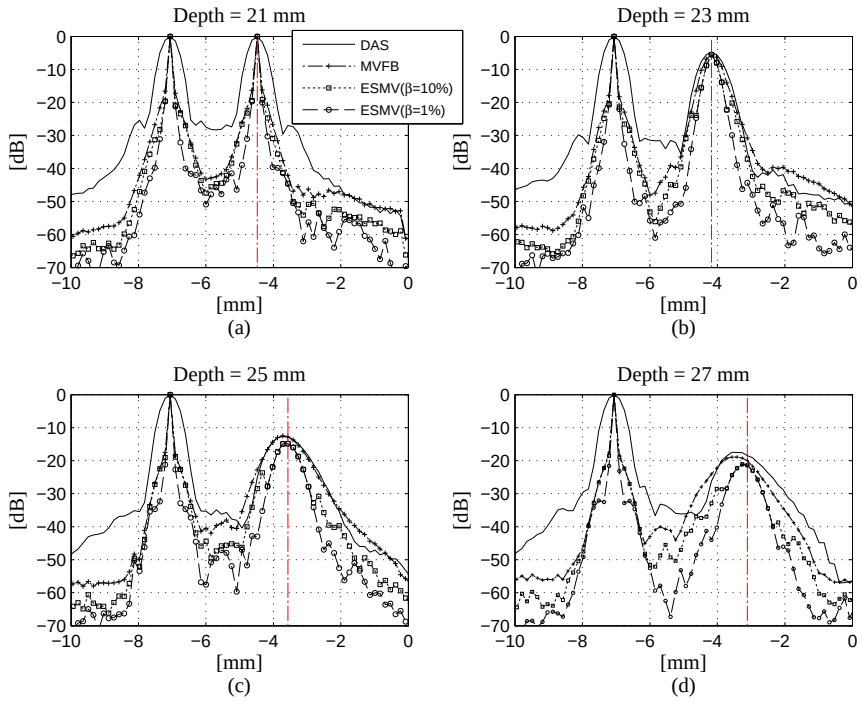

Figure 3.4: Two-way beam profiles of simulated point scatterers in Figs. 3.2(c)-(e) in comparison with Fig. 3.2(a) , the DAS beam profiles. (a) Depth=21 mm, (b) depth=23 mm, (c) depth=25 mm, (d) depth=27 mm. All other parameters are the same as in Fig. 3.2.

and MVFB.

3.3.2 Simulated cyst phantom

Fig. 3.5 shows simulated images of the cyst phantom introduced in Section 3.2.3 for different beamformers over 60 dB dynamic range. The transmit focal depth is set at the center of the cyst, at a depth of 25 mm. Fig. 3.5(a) shows the DAS image of the cyst phantom. Figs. 3.5(b) and (c) correspond to the MV and MVFB beamformers. In these images the contrast ratio in the cyst is measured as 0.5 and 0.52 in comparison with 0.47 in DAS. These values are estimated based on intensity measurements within 2 mm circles that are marked with white solid lines in Fig. 3.5(a). Figs. 3.5(d)-(f) present images using ESMV beamforming with different eigenvalue thresholding values (β). It can be seen that by decreasing β the speckle pattern in the neighboring region of the point scatterers are distorted, and for β=1% it is almost removed. The CR value within the cyst is measured as 0.54, 0.58, and 0.64 for β=30%, 10%, and 1%

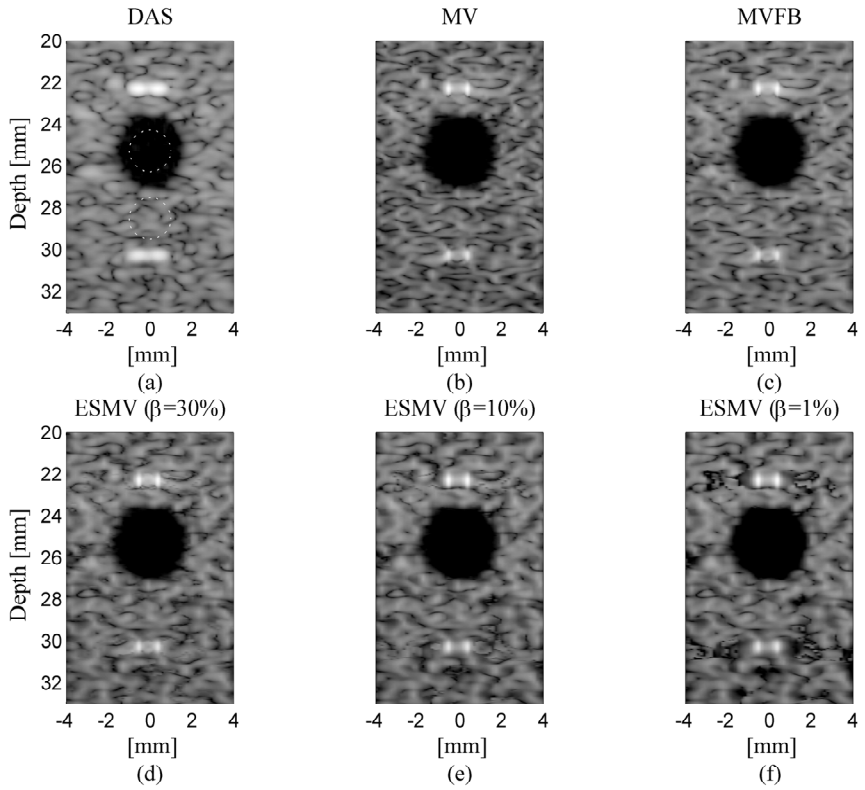

Figure 3.5: Simulated cyst phantoms for different beamformers.(a) DAS, (b) MV, (c) MVFB, (d) ESMV (β=30%), (e) ESMV (β=10%), ESMV (β=1%). $K = 20$, and $L = M/2$ are assumed for adaptive beamformers. All other parameters are the same as in Fig. 3.2.

respectively.

Figs. 3.6(a)-(d) show signal subspace ranks used for image pixels of the simulated cyst phantom introduced in Section 3.2.3, when the ESMV beamformer with different β is employed. The five different values in the images correspond to 1, 2, 3, 4, 5 and higher number of eigenvalues used for those particular pixels. From Fig. 3.6(a), it can be observed that at depths 22 mm and 30 mm at the exact positions of the point scatterers, just the rank-1 signal subspaces are used for the weight estimation in (3.13). However, in the sidelobe regions of the point scatterers, in the range from -2 mm to +2 mm, up to rank-3 signal subspaces are employed. Figs. 3.6(b)-(d) correspond to Figs. 3.5(d)-(f). By decreasing β from 30% in Fig. 3.6(b) to 1% in Fig. 3.6(d), the signal subspace ranks are kept at the location of the point scatterers, but it tends to decrease to rank-1 in sidelobe regions. Figs. 3.6(e)-(h) show the distribution of the

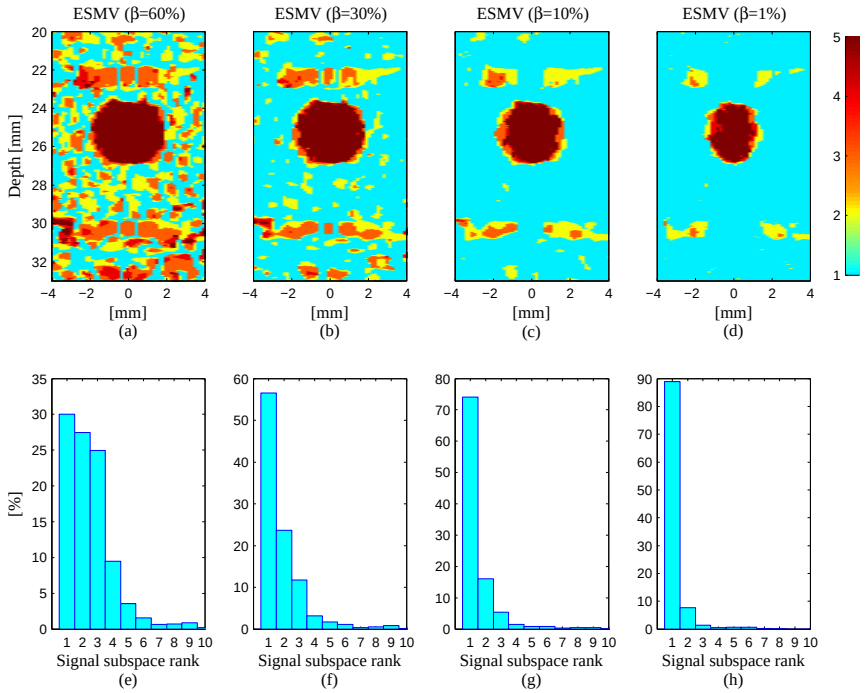

Figure 3.6: Mapping of signal subspace ranks used for simulated cyst phantoms for different thresholding values. (a) β=60%, (b) β=30%, (c) β=10%, and (d) β=1%. In (e)-(h) distribution of the ranks in (a)-(d) are presented.

signal subspace ranks corresponding to Figs. 3.6(a)-(d).

Fig. 3.7 shows beam profiles for the pair of point scatterers located at a depth of 22 mm in the cyst phantom for different beamformers. All beam profiles are normalized to their maximum values. We see that the point scatterers are resolvable by -6 dB for DAS and -14 dB for MV, and -12.5 dB for MVFB. This measure is about -13 dB for β=30%, and -16.5 dB for β=10%, and 1%.

Fig. 3.8 shows a cross section of the cyst presented in Fig. 3.5. We see that in ESMV beamformers by decreasing β from 30% to 1%, the edges around the 4 mm cyst are enhanced as the signal level decreases with a sharper slope between $x_{ld} = \pm 2$ mm and $x_{ld} = \pm 1$ mm. Also, the noise level inside the cyst is decreased from -55 dB for β=30% to -70 dB for β=1%, compared to -40 dB for DAS, and -50 dB for MV and MVFB.

3.3.3 Experimental study: imaging a vertebra in a water bath

Fig. 3.9 shows images of a lumbar human vertebra (L3) in sagittal direction over 80 dB dynamic range. The transmit focal depth is 25 mm. Fig. 3.9(a) presents the DAS image. In this image, the sidelobes are clearly observed around the spinous process(top of the vertebra). The sidelobe noise is measured within a 1.5 mm circle that has been marked with white color on the right-hand side of the DAS image. This metric is about -55 dB for DAS, and -66 dB for MV and MVFB. The sidelobes level decreases

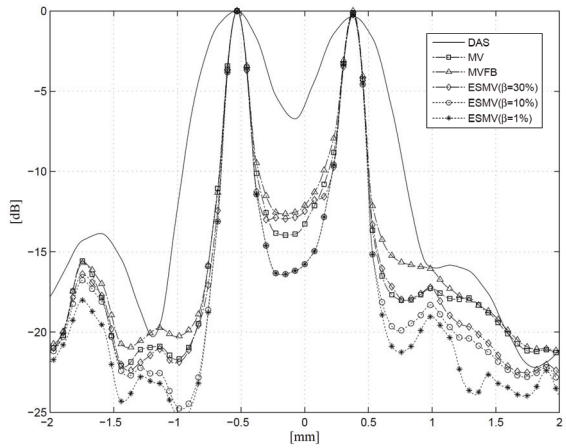

Figure 3.7: Two-way beam profiles around the point scatterers located at the depth of 22 mm in the cyst phantom presented in Fig. 3.5. All other parameters are the same as in Fig. 3.2.

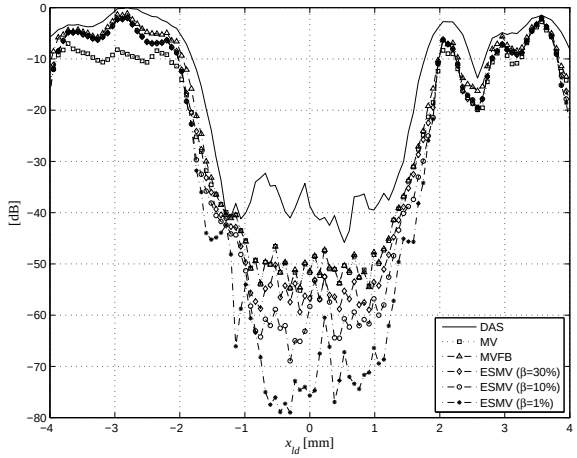

Figure 3.8: Lateral cross section of cysts in Fig. 3.5.

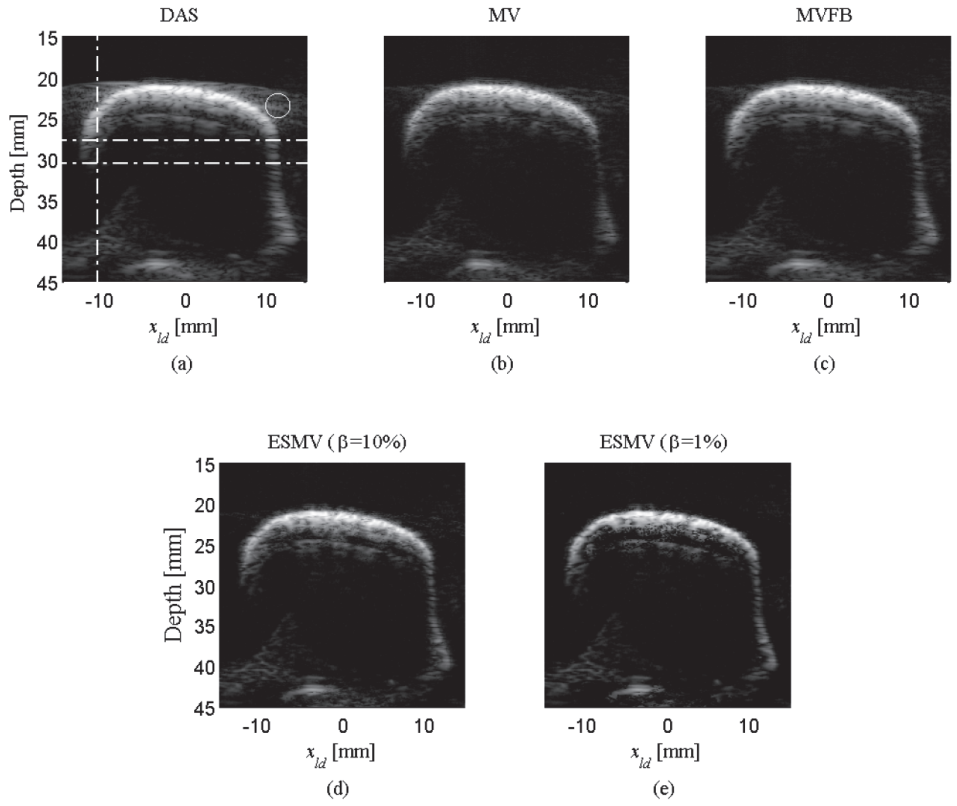

Figure 3.9: Imaging of a vertebra in sagittal direction in a water bath experiment using a 128 element, 5 MHz transducer. (a) DAS, (b) MV, (c) MVFB, (d) ESMV (β=10%), (e) ESMV (β=1%). The focal depth is 25 mm and dynamic range is 80 dB.

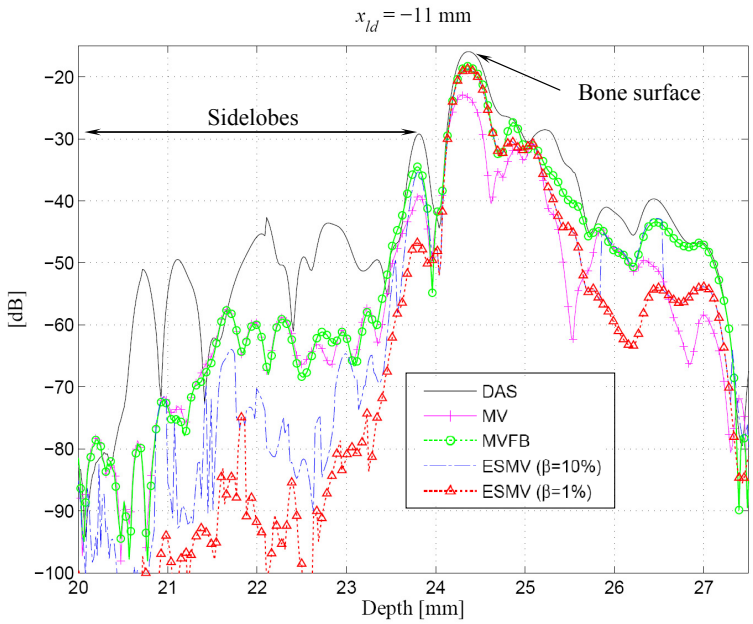

Figure 3.10: Comparison of scan-lines at x_{ld}= -11 mm for DAS, MV, MVFB, ESMV (β=10%), and ESMV (β=1%) beamformers.

to -78 dB, and -93 dB for ESMV beamformers with threshold values of β=10% and β=1%. Compared to the DAS image, the right-hand sidewall of the vertebra has been visualized with higher resolution in MVFB, ESMV (β=10%), and ESMV (β=1%) images. However, it has been distorted in the MV image as the curvature between depths of 30 mm and 35 mm has partly been changed and cancelled.

Fig. 3.10 shows a scan-line at x_{ld}= -11 mm in Fig. 3.9 for DAS, MV, MVFB, ESMV (β=10%), and ESMV (β=1%) beamformers. This line has been marked with vertical dash-dot lines in Fig. 3.9(a). In Fig. 3.10, the sidelobes between a depth of 22 mm and 23 mm are decreased from about -50 dB in the DAS image to -60 dB for MV and MVFB images. They are decreased below -70 dB for ESMV images.

Fig. 3.11 demonstrates two horizontal lines for the vertebra image in Fig. 3.9(a). The lines have been marked at depths of 28 mm and 30.5 mm in Fig. 3.9(a). In Fig. 3.11(a) the -12 dB beamwidth is measured for the left-hand sidewall as 1.36 mm, and 0.98 mm for DAS and MVFB, and 0.75 mm for ESMV with β=10% and 1%. This metric is measured at a depth of 30.5 mm, Fig. 3.11(b), for right-hand wall as 1.55 mm for DAS, 1.24 mm for MVFB, and 0.90 mm for both ESMV beamformers. The -12 dB beamwidth is measured from the signal peaks and marked with horizontal solid line in Figs. 3.11(a) and (b). Also, in Fig. 3.11(b) an apparent shift of 0.48 mm and

a signal cancellation of -9 dB are seen for MV beamformer compared with the DAS one.

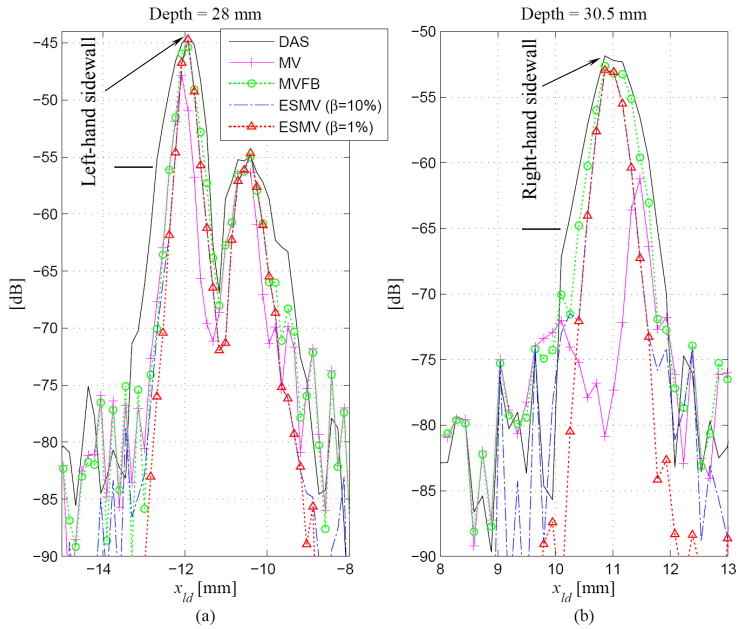

Figure 3.11: Comparison of image lines at depths of 28 mm, and 30.50 mm for DAS, MVFB, ESMV (β=10%), and ESMV (β=1%) beamformers.

Fig. 3.13 shows image of the ankle in a healthy male volunteer for different beamformers. Compared to DAS, in the ESMV images by decreasing β the speckle noise beneath the tendon from x_{ld}= -2.5 mm to 0 mm is reduced. The same effect is observed in the region between talus and tendon. In this imaging scenario, MV and MVFB beamformers do almost the same as the DAS one.

Fig. 3.12 shows two scan-lines of the ankle image in Fig. 3.13 for DAS, ESMV (β=10%), and ESMV (β=1%). These lines have been marked in Fig. 3.13(a) at x_{ld}= -3.5 mm, and 11.4 mm. At x_{ld}= -3.5 mm the signal intensity drops by -55 dB for ESMV (β=1%) beneath the tendon at an approximate depth of 15.5 mm, as opposed to -30 dB for ESMV (β=10%), and -20 dB for DAS. At x_{ld}= -11.4 mm, the signal level between tendon and talus decreases to -75 dB, -50 dB, and -45 dB for ESMV (β=10%), ESMV (β=1%), and DAS.

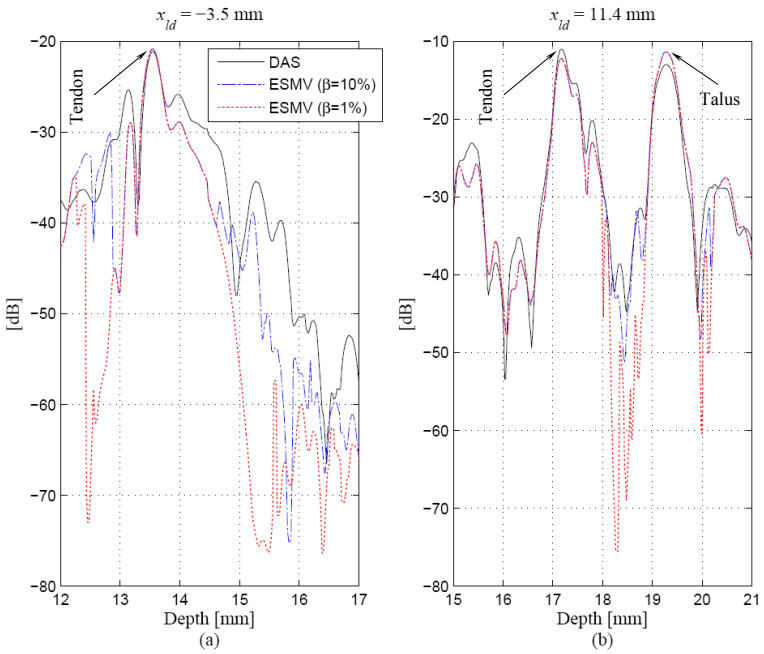

Figure 3.12: Comparison of image scan lines at x_{ld}= -3.5 mm , and 11.4 mm for DAS, ESMV (β=10%), and ESMV (β=1%) beamformers for Fig. 3.13.

3.4 Discussion

The main advantages of MV beamforming are enhanced resolution and contrast, but the performance of the MV beamformer can be very sensitive to a signal misalignment that originates from the shaded aperture. As discussed in [26], this error can occur in bone imaging, and can result in an apparent signal cancellation and a shift of the point spread function (PSF). As shown in Figs. 3.2(b)-(c), and Fig. 3.3, the FB averaging improves the robustness of the MV beamformer against the signal misalignment, but the resolution can degrade to that of the DAS beamformer for the shaded scatterers. By FB averaging, we first flip the imaging aperture and the angle of arrival of the signal (backward aperture), and then average with the original one (forward aperture). As long as the shadowing ratio is less than 50%, this flipping technique assures that all elements receive a signal, which is a requirement for the MV method. The central signals receive the signal twice; yet by averaging, the statistics of the signal across the aperture is correct. For shadowing ratios larger than 50% by FB averaging we make the signal to be symmetrical across the aperture but some elements in the center of the aperture are zeros. Therefore, the shifting effect is compensated for, but a slight signal cancellation may happen. This effect can slightly be seen in Fig. 3.3(d). Thus, the MVFB beamformer can retain the performance of the MV beamformer for un-shadowed scatterers and a robust behavior for the shadowed ones.

The same effect is observed in Fig. 3.9(b) in which the sidewall of the vertebra has been distorted due to the signal cancellation originated most likely from the shaded aperture. However, by applying the FB averaging this signal cancellation error has reasonably been compensated for in Fig. 3.9(c).
In a similar imaging scenario as Fig. 3.2, in [26], we have shown that the covariance matrix can be estimated based on un-shadowed elements. That beamformer setup improves the resolution of shadowed point scatterers (see Fig. 5 in ref.[26]) even more than MVFB beamformer [Fig. 3.2(c)]. However, its performance may degrade if the signal to noise ratio is low, and this is avoided with the MVFB method.
From Figs. 3.2(c)-(d) and Fig. 3.4 it can be observed that the ESMV beamformer for small values of β can locate the shadowed point scatterers more precisely than MVFB. In this study, we have used FB averaging to estimate the covariance matrix for the ESMV beamformer. However, we also examined ESMV technique without FB averaging. In that case, the same shadowing artifacts as the MV beamformer was observed for the ESMV beamformer, except when a very small thresholding factor(β) was used, *e.g.* β=0.1%. This means that that just the most dominant eigenvalue contributes to the signal subspace.
From Figs. 3.5 and 3.7, we see that β=1%, and 10% for the ESMV beamformer can improve resolvability of the point scatterers in comparison with MV and MVFB. In Fig. 3.5(f), there is a distortion which can be seen as losing the speckle in the neighborhood of the strong scatterers, replacing it with black holes. The main reason for this effect is that the ESMV beamformer cannot preserve the linear constraint in equation (3.2) for small β's. In this case, the constraint may vary as $0 < \mathbf{w}^H\mathbf{a} \leq 1$. For the strong scatterer the constraint remains close to 1, but in the sidelobe region of the strong scatterer this value can be close to zero. However, we have found that using the cross-spectral metric for the signal subspace selection (eq. 3.14) was an advantage in some scenarios compared to selection based on straightforward eigenvalue thresholding although it didn't completely eliminate the speckle suppression next to point targets. On the other hand, this constraint variation can partly remove the speckle in the ultrasound images and make the strong scatterers more distinguishable from the surrounding tissue and decrease the sidelobes noise. From Figs. 3.9-3.11, we observe that the sidelobes levels are substantially suppressed around the boundaries of the vertebra for ESMV beamformers, particularly for β=1%. This results in a sharper definition of the vertebra edges. Similar effects are observed in Figs. 3.13(d)-(f), we see that by decreasing β the noise above talus and around the tendon tissue reduces (Fig. 3.12). For β= 1% in Fig. 3.13(f), the edges of the tendon tissue and talus are more resolvable than the other images in Fig. 3.13. This behavior of the ESMV beamformer for small values of β can be beneficial for some clinical applications in which detection of the edges of the hard tissue is the main purpose [4–6, 8, 9]. In these applications, ultrasound speckle and sidelobe noises can decrease accuracy of the detection algorithm. Further, compared to MV or MVFB beamformers, for larger values of β, *e.g.* β=30%, the ESMV beamformer can preserve the constraint close to 1 and improve the image in terms of contrast (Figs. 3.5, 3.8, and 3.9).
It can be observed from Fig. 3.5 particularly that the fineness of the speckle pattern varies from method to method. Ideally, the goal is to have a speckle pattern which

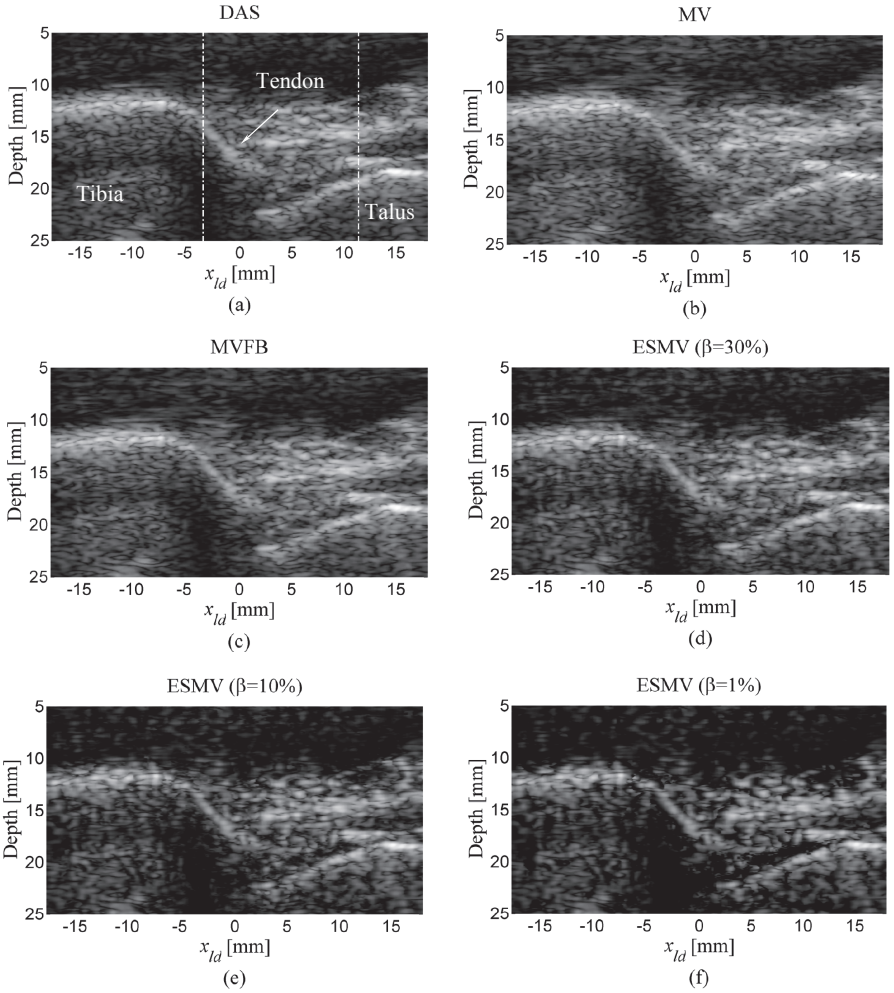

Figure 3.13: Images of the ankle bone for different beamformers using a 128 element, 5 MHz transducer. (a) DAS, (b) MV, (c) MVFB, (d) ESMV (β=30%), (e) ESMV (β=10%), (f) ESMV (β=1%).The focal depth is 20 mm and dynamic range is 60 dB.

as much as possible resembles that of DAS and it has been previously shown that time averaging in the covariance matrix estimation contributes to that [36]. Time averaging of the signal originating from speckle results in a spatial covariance matrix with a predictable statistics [37], and the eigenvector corresponding to the largest eigenvalue of such matrix resembles a vector with uniform elements. From (eq. 3.12), we see that this uniform eigenvector structure gives a response close to DAS. From Figs. 3.6(b)-(d), we observe that the rank-1 covariance matrices are mostly used for the speckle estimation in Figs. 3.5(d)-(f). Thus, this can results in a speckle size similar to DAS image [Fig. 3.5(a)].
The computational complexity of DAS beamformers is $O(M)$ for an aperture size of M elements, increasing up to $O(L^3)$ for MV, MVFB, and ESMV beamformers with a subarray length of L. The major computational demand for MV and MVFB beamformers are originated from the matrix inversion algorithm, which requires $3L^3/2$ flops using Gussian elimination [38]. In ESMV beamformers, the eigendecomposition of $\mathbf{R}$ is the most computional demanding operation, which requires $10L^3$ flops [39]. This can be decreased to $O(L^2)$ using recursive updating eigendecomposition techniques [40]. Currently, the application of these adaptive beamformers is limited to off-line analysis of acquired channel data. However, work in our group on the use of GPU (Graphics Processing Unit) programming has shown a potential for real time implementation of MV-based beamformers.

3.5 Conclusion

We have investigated the possible potential of a ESMV beamformer to enhance localization of acoustically hard scatterers in ultrasound images. In this beamformer we have employed the FB averaging method to improve the robustness of the method against the signal misalignment across the transducer aperture, which can be originated from the shadowing. This averaging technique also improves the performance of the standard MV beamformer. Our results show that the ESMV method can result in enhanced edges if a small enough thresholding factor is considered. However, the speckle pattern can be distorted. If detection of edges is the main purpose, regardless of the speckle pattern, smaller thresholding factor can define edges better.

References

[1] S. Winter, B. Brendel, I. Pechlivanis, K. Schmieder, and C. Igel, "Registration of CT and intraoperative 3-D ultrasound images of the spine using evolutionary and gradient-based methods," *IEEE Transactions on Evolutionary Computation*, vol. 12, no. 3, pp. 284–296, 2008.

[2] D. V. Amin, T. Kanade, A. M. Digioia, and B. Jaramaz, "Ultrasound registration of the bone surface for surgical navigation," *Computer Aided Surgery*, vol. 8, no. 1, pp. 1–16, 2003.

[3] B. Brendel, S. Winter, A. Rick, M. Stockheim, and H. Ermert, "Registration of 3D CT and ultrasound datasets of the spine using bone structures," *Computer Aided Surgery*, vol. 7, no. 3, pp. 146–155, 2002.

[4] I. Hacihaliloglu, R. Abugharbieh, A. J. Hodgson, and R. N. Rohling, "Bone surface localization in ultrasound using image phase-based features," *Ultrasound in Medicine & Biology*, vol. 35, no. 9, pp. 1475–1487, 2009.

[5] D. Tran, K.-W. Hor, V. A. Lessoway, A. A. Kamani, and R. N. Rohling, "Adaptive ultrasound imaging of the lumbar spine for guidance of epidural anesthesia," *Computerized Medical Imaging and Graphics*, vol. 33, no. 8, pp. 593–601, 2009.

[6] C. Arzola, S. Davies, A. Rofaeel, and J. C. Carvalho, "Ultrasound using the transverse approach to the lumbar spine provides reliable landmarks for labor epidurals," *Anesthesia and analgesia*, vol. 104, no. 5, pp. 1188–92, 2007.

[7] C. Stewart Siu-Wa, "Emergency bedside ultrasound for the diagnosis of rib fractures," *The American journal of Emergency Medicine*, vol. 27, no. 5, pp. 617–620, 2009.

[8] L. Chen, Y. Kim, and C. L. Moore, "Diagnosis and guided reduction of forearm fractures in children using bedside ultrasound," *Pediatric Emergency Care*, vol. 23, no. 8, pp. 528–531, 2007.

[9] D. Tran and R. N. Rohling, "Automatic detection of lumbar anatomy in ultrasound images of human subjects," *IEEE Transactions on Ultrasonics, Ferroelectrics, and Frequency Control*, vol. 57, no. 9, pp. 2248–2256, 2010.

[10] J. F. Synnevag, A. Austeng, and S. Holm, "Adaptive beamforming applied to medical ultrasound imaging," *IEEE Transactions on Ultrasonics, Ferroelectrics and Frequency Control*, vol. 54, no. 8, pp. 1606–1613, 2007.

[11] J. Capon, "High-resolution frequency-wavenumber spectrum analysis," *Proceedings of the IEEE*, vol. 57, no. 8, pp. 1408–1418, 1969.

[12] J. Mann and W. Walker, "A constrained adaptive beamformer for medical ultrasound: initial results," *Proc. Ultrasonics Symposium*, vol. 2, pp. 1807–1810, 2002.

[13] M. Sasso and C. Cohen-Bacrie, "medical ultrasound imaging using the fully adaptive beamformer," *proc. IEEE Acoustics, Speech, and Signal, (ICASSP '05)*, vol. 2, pp. 489–492, 2005.

[14] Z. Wang, J. Li, and R. Wu, "Time-delay- and time-reversal-based robust capon beamformers for ultrasound imaging," *IEEE Transactions on Medical Imaging*, vol. 24, no. 10, pp. 1308–1322, 2005.

[15] F. Vignon and M. R. Burcher, "Capon beamforming in medical ultrasound imaging with focused beams," *IEEE Transactions on Ultrasonics, Ferroelectrics and Frequency Control*, vol. 55, no. 3, pp. 619–628, 2008.

[16] J. F. Synnevag, A. Austeng, and S. Holm, "Benefits of minimum-variance beamforming in medical ultrasound imaging," *IEEE Transactions on Ultrasonics, Ferroelectrics and Frequency Control*, vol. 56, no. 9, pp. 1868–1879, 2009.

[17] B. Mohammadzadeh Asl and A. Mahloojifar, "Eigenspace-based minimum variance beamforming applied to medical ultrasound imaging," *IEEE Transactions on Ultrasonics, Ferroelectrics and Frequency Control*, vol. 57, no. 11, pp. 2381–2390, 2010.

[18] S. Tie-Jun, M. Wax, and T. Kailath, "On spatial smoothing for direction-of-arrival estimation of coherent signals," *IEEE Transactions on Ultrasonics, Ferroelectrics and Frequency Control*, vol. 33, no. 4, pp. 806–811, 1985.

[19] B. D. Rao and K. V. S. Hari, "Effect of spatial smoothing on the performance of music and the minimum-norm method," *IEEE Proceedings of Radar and Signal Processing*, vol. 137, no. 6, pp. 449–458, 1990.

[20] B. M. Asl and A. Mahloojifar, "Contrast enhancement and robustness improvement of adaptive ultrasound imaging using forward-backward minimum variance beamforming," *IEEE Transactions on Ultrasonics, Ferroelectrics and Frequency Control*, vol. 58, no. 4, pp. 858–867, 2011.

[21] I. K. Holfort, F. Gran, and J. A. Jensen, "Investigation of sound speed errors in adaptive beamforming," in *IEEE Ultrasonics Symposium*, pp. 1080–1083, 2008.

[22] S. Mehdizadeh, A. Austeng, T. Johansen, and S. Holm, "Performance of adaptive beamformers for ultrasound imaging of a partially shaded object," in *IEEE Ultrasonics Symposium*, (Orlando,FL), 2011.

[23] L. Cheng-Chou and L. Ju-Hong, "Eigenspace-based adaptive array beamforming with robust capabilities," *IEEE Transactions onAntennas and Propagation*, vol. 45, no. 12, pp. 1711–1716, 1997.

[24] Y. Jung-Lang and Y. Chien-Chung, "Generalized eigenspace-based beamformers," *IEEE Transactions on Signal Processing*, vol. 43, no. 11, pp. 2453–2461, 1995.

[25] D. D. Feldman and L. J. Griffiths, "A projection approach for robust adaptive beamforming," *IEEE Transactions on Signal Processing*, vol. 42, no. 4, pp. 867–876, 1994.

[26] S. Mehdizadeh, A. Austeng, T. Johansen, and S. Holm, "Minimum variance beamforming applied to ultrasound imaging with a partially shaded aperture," *IEEE Transactions on Ultrasonics, Ferroelectrics and Frequency Control*, vol. 59, pp. 683–693, 2012.

[27] D. H. Johnson and D. E. Dudgeon, *Array Signal Processing: Concepts and Techniques*. Upper Saddle River, NJ: Prentice Hall, 2002.

[28] M. H.Hayes, *Statistical Digital Signal Processing and Modeling*. New York: John Wiley & Sons, Inc, 1996.

[29] J. S. Thompson, P. M. Grant, and B. Mulgrew, "Performance of spatial smoothing algorithms for correlated sources," *IEEE Transactions on Signal Processing*, vol. 44, no. 4, pp. 1040–1046, 1996.

[30] W. Featherstone, H. Strangeways, M. Zatman, and H. Mewes, "A novel method to improve the performance of capon's minimum variance estimator," in *Antennas and Propagation*, vol. 1, pp. 322 –325 vol.1, apr 1997.

[31] L. Chang and C. C. Yeh, "Performance of dmi and eigenspace-based beamformers," *IEEE Transactions onAntennas and Propagation*, vol. 40, no. 11, pp. 1336–1347, 1992.

[32] J. S. Goldstein and I. S. Reed, "Reduced-rank adaptive filtering," *IEEE Transactions on Signal Processing*, vol. 45, no. 2, pp. 492–496, 1997.

[33] J. A. Jensen, "Field: A program for simulating ultrasound systems," *Medical and Biological Engineering and Computing*, vol. 34, pp. 351–353, 1996.

[34] R. F. Wagner and S. W. Insana, M. F.and Smith, "Fundamental correlation lengths of coherent speckle in medical ultrasonic images," *IEEE Transactions on Ultrasonics, Ferroelectrics and Frequency Control*, vol. 35, no. 10, pp. 34–44, 1988.

[35] S. W. Smith, H. Lopez, and W. J. Bodine Jr, "Frequency independent ultrasound contrast-detail analysis," *Ultrasound in Medicine & Biology*, vol. 11, no. 3, pp. 467–477, 1985.

[36] J.-F. Synnevag, C.-I. Nilsen, and S. Holm, "P2b-13 speckle statistics in adaptive beamforming," in *Ultrasonics Symposium, 2007. IEEE*, pp. 1545 –1548, oct. 2007.

[37] M. Lediju, G. Trahey, B. Byram, and J. Dahl, "Short-lag spatial coherence of backscattered echoes: imaging characteristics," *Ultrasonics, Ferroelectrics and Frequency Control, IEEE Transactions on*, vol. 58, pp. 1377 –1388, july 2011.

[38] J.-F. Synnevag, A. Austeng, and S. Holm, "A low-complexity data-dependent beamformer," *Ultrasonics, Ferroelectrics and Frequency Control, IEEE Transactions on*, vol. 58, pp. 281 –289, february 2011.

[39] R. Lorenz and S. Boyd, "Robust minimum variance beamforming," *Signal Processing, IEEE Transactions on*, vol. 53, pp. 1684 – 1696, may 2005.

[40] K.-B. Yu, "Recursive updating the eigenvalue decomposition of a covariance matrix," *Signal Processing, IEEE Transactions on*, vol. 39, pp. 1136 –1145, may 1991.

Chapter 4

Joint Beamforming and Feature Detection for Enhanced Visualization of Spinal Bone Surfaces in Ultrasound Images

Saeed Mehdizadeh[1], Sebastien Muller[2], Gabriel Kiss[1], Tonni F. Johansen[1], and Sverre Holm[1,3]

[1] Dept. Circulation and Medical Imaging, NTNU, Norway

[2] Dept. Medical Technology, SINTEF, Norway

[3] Dept. Informatics, University of Oslo, Norway

Beamforming and image feature detection are commonly done in two independent steps. We show that it can be beneficial to combine them in an application where ultrasound (US) is used as a guidance tool for spinal interventions. For beamforming, a method with parameter-derived performance is needed, and for that the eigenspace minimum variance beamformer (ESMV) is employed. This beamformer is combined with a post-processing technique, and here the phase symmetry (PS) method is proposed. The signal subspace rank is considered as the adaptable parameter for the beamformer. Thereby, in simulation, *in-vitro* and *in-vivo* studies we show that an ESMV beamformer with a rank-1 signal subspace, can keep the bone structure and improve the edges, despite some distortion of the speckle pattern. The PS images obtained from this beamformer setup have sharper bone boundaries compared with the DAS ones, and they are reasonably well separated from surrounding soft tissue.

4.1 Introduction

Imaging of bone structures is usually done using X-ray or Computer Tomography (CT). However, ionizing radiation, scanner time cost, and lack of portability are the limitations of these modalities. Ultrasound may address these issues in many applications. In particular, spinal ultrasound imaging has been investigated in different clinical procedures [1–6], for instance as a portable and real-time guidance for needle placement in pain management interventions [1–3, 5]. A research group [2] has reported in a non-randomized crossover trial 95% success in lumbar spine injection, using fluoroscopy as a gold standard. In the cervical spine, two of the most recent studies on nerve root injection report 100% placement success, with fluoroscopic gold standard [3, 4].

Another potential application of ultrasound is computed-assisted minimally invasive (MI) spinal surgery [7]. The procedure requires the registration of the patient positioned for surgery, with preoperatively acquired anatomy. The restriction of minimal invasiveness, together with limited radiation exposure, point at ultrasound imaging as a good candidate [7]. Image enhancement, where bone structures stand out more distinctly from surrounding soft tissue, helps to isolate the bone surface out of the B-mode ultrasound. This can facilitate registration to pre-existing CT or MRI for MI surgery. It would also provide meaningful help to distinguish bone structures from surrounding soft tissue for spinal injections.

In other applications such as anatomy rendering with ultrasound, the corresponding images are typically disturbed by speckle, the anisotropic nature of the sound wave propagation, reverberations, shadowing, and attenuation. To automate segmentation of the bone structure, image intensity or gradient-based methods are common [6], but results are sensitive to parameters of image acquisition, *e.g.* frequency and dynamic range. Pattern recognition or statistical shape models [8] provide more robust results but require learning sets, and fail to identify traumatic cases as the pattern searched for is disrupted.

The visual interpretation of images is strongly related to the phase of the underlying signal [9]. Such that the image features (*e.g.* edges, corners, etc.) occur at parts of the image where the Fourier components are maximally in phase with one another [10, 11]. Based on local phase information, a research group [12] has presented a robust method for bone surface detection. They use 2-D Log-Gabor filters to derive the phase symmetry (PS) measure as a ridge detector for bone localization and automatic segmentation of bone surfaces in ultrasound images. However, in standard medical ultrasound the bone surface is often poorly visualized, and the boundary region appears unclear. This can degrade the performance of the post processing techniques.

In the DAS technique received signals from active channels are dynamically delayed and summed up in the beamformer. In this case, the achievable resolution, sidelobes level and contrast are limited. While, utilizing an adaptive method, such as minimum variance (MV) based beamforming techniques, can enhance the image quality as a result of lower sidelobes, a narrower beamwidth, and better definition of edges [13]. In the MV approach, for each time sample, the delayed received signal from each element is weighted adaptively before summing up in the beamformer. This approach was

initially developed by Capon for passive narrow-band applications [14].
Several researchers have previously investigated the MV approach in medical ultrasound. They have reported appreciable enhancements in the resolution and contrast in comparison with DAS beamforming [15–20]. Further, in a simulation study [20] an eigenspace-based MV (ESMV) technique has been employed in order to improve the contrast of the MV beamforming in medical ultrasound imaging. This technique has been developed based on earlier studies in radar imaging [21–23]. Previous work by our group [24] has demonstrated that in bone imaging scenarios, the robustness of the MV beamformer degrades due to a poor estimation of the covariance matrix. The forward/backward (FB) averaging technique has been proposed in order to enhance the covariance matrix estimation against signal misalignment due to the shadowing [25]. More recently, we have investigated the potential of a ESMV beamforming technique to enhance the edges of the acoustically hard tissues [26]. We have also shown that the lower rank of the signal subspace in the ESMV beamformer can give rise to an improved definition of the edges but the speckle pattern around the acoustically hard tissues can be distorted [26]. We are therefore in a situation where the image after beamforming is less appealing from a visual perspective, but is better for feature detection. Therefore we propose that beamforming and feature detection should not be optimized independently. Rather, in applications like this, they should be jointly optimized with the goal of optimizing the feature detection.
As part of this optimization there is a need to determine the rank of signal subspace in the beamformer. Since this estimation is a challenge in ESMV beamformers, in this study we show that the use of a rank one signal subspace can reasonably well keep the vertebra anatomy and enhance the bone edges in spinal imaging. The resulting ESMV images are post-processed using the Phase Symmetry method. In simulation, *in-vitro*, and *in-vivo* studies, we demonstrate that the extracted surfaces are sharper, and the anatomy of the spine is better defined in comparison to their corresponding DAS images.
The rest of this paper is organized as follows: in the next section, we first review the beamformer techniques, and the Phase Symmetry feature detection method that are employed in this study; then, simulation and experimental setups are introduced. We present the results from simulated data of a point scatterer and vertebra phantoms, followed by results from CT-US registration of a vertebra phantom, and *in-vivo* images of the spine. This section is followed by the discussion on the results.

4.2 Methods

4.2.1 Minimum variance beamformer

The minimum variance beamformer employs an element weight vector which minimizes the variance of the beamformer output under the constraint that the signal arriving from a point of interest is unaffected by the beamformer. In this method, the optimized weights are estimated as:

$$\mathbf{w} = \frac{\mathbf{R}^{-1}\mathbf{a}}{\mathbf{a}^H\mathbf{R}^{-1}\mathbf{a}}, \tag{4.1}$$

where $\mathbf{R}$ is the spatial covariance matrix, $\mathbf{a}$ is the steering vector, and $(.)^H$ stands for Hermitian transpose. A common estimator for the data covariance matrix is the sample covariance matrix. Therefore, using a method called subarray technique [27], the sample covariance matrix is estimated as:

$$\hat{\mathbf{R}} = \frac{1}{(2K+1)(M-L+1)} \cdot \sum_{k=-K}^{K} \sum_{l=1}^{M-L+1} \bar{\mathbf{X}}_l[n-k]\, \bar{\mathbf{X}}_l[n-k]^H, \tag{4.2}$$

where

$$\bar{\mathbf{X}}_l[n] = \begin{bmatrix} x_l[n] & x_{l+1}[n] & \dots & x_{l+L-1}[n] \end{bmatrix}^T.$$

The sample covariance matrix has dimension, L, the subarray length, $x_m[n]$ is a time sampled signal from element m of a uniformly spaced linear array with M elements, and $(.)^T$ is transpose operator. In general, there is a time averaging over index k which has been found to be necessary in order to get proper speckle statistics in the image [19]. The subarray technique can be combined with forward-backward averaging to improve the covariance matrix estimation [28]. The new estimate is expressed as:

$$\hat{\mathbf{R}}_{FB} = \frac{1}{2}(\hat{\mathbf{R}} + \mathbf{J}\hat{\mathbf{R}}^*\mathbf{J}), \tag{4.3}$$

where $\mathbf{J}$ is an exchange matrix, the left/right flipped version of the identity matrix, with the same dimension as $\hat{\mathbf{R}}$, and $\hat{\mathbf{R}}^*$ denotes the complex conjugate of $\hat{\mathbf{R}}$. Substituting $\mathbf{R}$ with either $\hat{\mathbf{R}}$ or $\hat{\mathbf{R}}_{FB}$ in (4.1), the beamformer output is obtained as a coherent average over subarrays by:

$$\hat{z}[n] = \frac{1}{M-L+1} \sum_{l=1}^{M-L+1} \mathbf{w}^H \bar{\mathbf{X}}_l[n], \tag{4.4}$$

where, $\mathbf{w}$ is a vector of time varying complex weights of size L. Also, in order to enhance the robustness of the MV estimate a term, $\Delta/L \cdot tr\{\mathbf{R}\}$, is added to the diagonal of the covariance matrix before evaluating (4.1) [29]. There are many details about MV beamforming algorithms applied to medical ultrasound imaging, which have been addressed in previous publications [15–20]. In this paper we use the method that is described in [19].

4.2.2 Eigenspace-Based beamformer

The eigenspace-based beamformer (ESMV) utilizes the eigen structure of the covariance matrix to estimate MV weights [22, 23, 30]. With assumption of $j \leq L$, the sample covariance matrix $\hat{\mathbf{R}}$ defined by (4.2) is eigendecomposed as:

$$\hat{\mathbf{R}} = \mathbf{E}\mathbf{\Lambda}\mathbf{E}^H = \mathbf{E}_s\mathbf{\Lambda}_s\mathbf{E}_s^H + \mathbf{E}_N\mathbf{\Lambda}_N\mathbf{E}_N^H, \tag{4.5}$$

where

$$\begin{aligned} \mathbf{E}_\mathrm{s} &= [\mathbf{e}_1, ..., \mathbf{e}_j], \qquad \mathbf{E}_\mathrm{N} = [\mathbf{e}_{j+1}, ..., \mathbf{e}_L], \\ \mathbf{\Lambda}_\mathrm{s} &= diag[\lambda_1, ..., \lambda_j], \ \mathbf{\Lambda}_\mathrm{N} = diag[\lambda_{j+1}, ..., \lambda_L], \end{aligned} \tag{4.6}$$

and, $\lambda_1 \geq \lambda_2 \geq .... \geq \lambda_L$ are eigenvalues in descending order, and $\mathbf{e}_l$, $l = 1, ..., L$ are the corresponding orthonormal eigenvectors. We refer to the subspace spanned by the columns of $\mathbf{E}_s$ as the signal subspace and to that of $\mathbf{E}_N$ as the noise subspace. Ideally, the direction of the steering vector and the noise subspace are orthogonal, *i.e.* $\mathbf{E}_N^H\mathbf{a} = 0$ [30]. This will result in a weight vector as [22, 26]:

$$\mathbf{w}_p = \mathbf{E}_s\mathbf{E}_s^H\mathbf{w}. \tag{4.7}$$

Equation 4.7 can be interpreted as the projection of $\mathbf{w}$ on the signal subspace of $\hat{\mathbf{R}}$ [23]. We select the rank of the signal subspace employing the cross-spectral metric [31]. The output signal power of the minimum variance beamformer can be expressed based on the cross-spectral metric as given in chapter 6.8.2 of [32].

$$\sigma_z^2 = (\mathbf{a}^H\mathbf{E}\mathbf{\Lambda}^{-1}\mathbf{E}^H\mathbf{a})^{-1} = (\sum_{k=1}^{L}\frac{\rho_k^2}{\lambda_k})^{-1}, \ \rho = \mathbf{E}^H\mathbf{a}, \tag{4.8}$$

where ρ_k^2/λ_k is the cross-spectral metric for the k^{th} eigenvalue. We select the rank of $\mathbf{E}_s$ by identifying the j largest eigenvalues for which the sum of their cross-spectral metric is β times smaller than the total output signal power (σ_z^2) [26].

4.2.3 Feature detection

The images were obtained from different beamforming techniques using Matlab (the Mathworks, Natick, MA, U.S), and resampled to 512×512 isotropic pixels to form the basis for further image processing by phase symmetry filtering. We also implemented the phase symmetry algorithm in Matlab. A log-Gabor filter was defined in polar coordinates as the product of a radial by an angular factor:

$$f(r,\theta) = \exp\left[-\frac{1}{2}\cdot\left(\frac{\log(\frac{r}{r_0})}{\log(\frac{\sigma_r}{r_0})}\right)^2\right]\cdot\exp\left[-\frac{1}{2}\cdot\left(\frac{\alpha(\theta,\theta_0)}{\sigma_\alpha}\right)^2\right], \tag{4.9}$$

where r and θ are the coordinates in the Fourier-transformed image, r_0 the characteristic radius, and σ_r the radial standard deviation (chosen so that σ_r/r_0 is always 0.15), for the radial part. The angular factor $\alpha(\theta,\theta_0)$, shows the angle between the position vector and the direction of the filter, and σ_α is angular standard deviation that is assumed to be $\pi/6$ in this study. The two-dimensional Fast Fourier Transform (F) of the image is multiplied by the filter and their product is inversely transformed

by F^{-1}.
A bank of filters is used with different r_0 and θ_0 in order to enhance features of the image of different sizes and orientations. For each image, we used 15 filters consisting of the combinations of several characteristic radius r_0 exponentially distributed from 2^{-5} to 2^{-9} in pixel space, and 5 characteristic orientations θ_0 ($-\pi + k \cdot \pi/4$, $k = 0..4$), distributed around the main direction of the ultrasound beam (downward). The filters and the corresponding filtered images were marked by the index i.
At each point of the imaging field, the real and imaginary parts of the filtered images are combined to form a metric of the phase symmetry (PS):

$$PS = \frac{\sum_i \lfloor (e_i - |o_i|) - T_n \rfloor}{\sum_i \sqrt{e_i^2 + o_i^2} + \varepsilon}, \tag{4.10}$$

where $\lfloor u \rfloor$ denotes $max(u, 0)$ and e_i and o_i are the even and odd (real and imaginary) part of the image processed by filter i, T_n is a noise threshold set to 15 (dimensionless) and ϵ is included simply to avoid division by zero ($\epsilon = 10^{-10}$). The asymmetrical treatment of even and odd components reflects a polarity choice where only dark-to-light-to-dark features are detected. There are more details about the PS method which have been addressed in previous publications [12, 33, 34].
The threshold, angular and radial standard deviations are chosen empirically to provide images with the least noise yet retaining the most information. They are maintained identical for all images. The central radial frequency combinations are adjusted to best fit different applications. For the patient imaging of the lamina and transverse view, we used 2^{-8} and 2^{-9}, for the spinous process, 2^{-5} to 2^{-9}, and for the water bath images we used, 2^{-5} to 2^{-9}.

4.2.4 Simulation setup

In this study, we simulate two different phantoms using Field II [35]: a single point scatterer phantom, and a vertebra phantom. The vertebra phantom consists of a vertebra body that is embedded in the soft tissue. We use the simulation scenario proposed in [24] for the vertebra phantom. We assume that the bone structure is completely attenuating. Therefore, it shadows point scatterers and surfaces which are not directly visible to the imaging aperture. The 3D geometry of the vertebra body is obtained by CT scanning of a human lumbar vertebra specimen (Fig. 4.1). By utilizing Matlab and VTK (Kitware, New York, NY, U.S) the 3D vertebra dataset has been segmented into triangular surfaces. Then, point scatterers with a concentration of 200 scatterers/mm^2 are generated on the triangulated surfaces. The soft tissue is modeled by 1.5×10^6 equal amplitude point scatterers that are uniformly distributed in a region of $20 \times 6 \times 25$ mm^3. The number of scatterers per resolution cell exceeds 10, which is recommended to simulate speckle [36]. The scatterers that are inside the vertebra body are identified and removed from the phantom. The image of the shadowed surfaces and point scatterers are modified by introducing a binary apodization-based shadowing model [24]. This model is applied to Field II in order to make an image of the vertebra phantom.
We simulate images employing a linear array with 128 elements and a center frequency

of 5 MHz (f_0) with 60 percent -6 dB fractional bandwidth. The array's elevation focus is 19 mm, and its pitch equals 0.308 mm. The maximum accessible aperture size for this array transducer is 38.70 mm ($M = 128$). The array is excited by 1.5 periods of a square wave at the center frequency of the array. In all simulations, a beam density of 1 beam per element, a fixed transmit focus, and dynamic receive focusing is used. In addition, the f number in the transmit is set to $\mathrm{FN}_{TX} = 2.8$ while the receive f number is set to $\mathrm{FN}_{RX} = 2.5$ for the point scatterer phantom, and $\mathrm{FN}_{RX} = 1.5$ for the vertebra phantom. We select a large FN_{RX} for the point scatterer phantom imaging scenario in order to achieve a wide enough beam width to ease further analysis. The transmit focal depth is set to 15 mm unless otherwise specified. The channel data are acquired for each scan line with a sampling frequency of 100 MHz. For all beamformers after applying delays the channel data are down-sampled to 20 MHz. We computed the analytic signals by applying the Hilbert transform to the channel data. Consequently, in the DAS approach the delayed received channel data are summed up for each scan line, without any apodization, whereas for MV-based beamformers the optimal aperture weights are estimated for each time sample before summation. In the adaptive approaches, we use diagonal loading with $\Delta = 5\%$ in all simulations.

4.2.5 Experimental setup

We have 2 different experimental cases: registration of a single vertebra, and imaging the spine in *in-vivo* volunteers. In the first experiment we use a human lumbar vertebra specimen (L3) and align the 3D-CT dataset to 3D-US one. Thus, we secure the vertebra specimen in a rigid holder and glue 4 small plastic balls (fiducials) with a diameter of 2 mm on the vertebra body; two on the spinous process (top) and two on

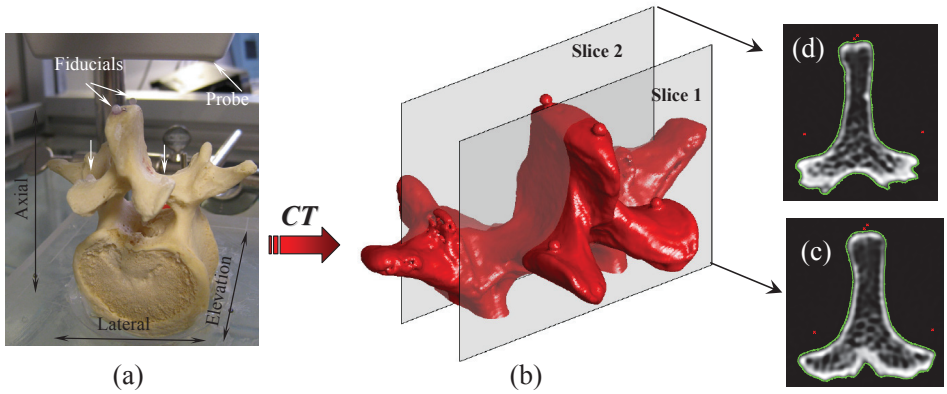

Figure 4.1: (a) Illustration of the vertebra phantom, (b) 3D model constructed from the CT dataset and projection of the selected slices, (c) CT image of slice 1 and its corresponding surface profile and, (d) CT image of slice 2 and its corresponding surface profile.

the laminas. Positions of these fiducials are illustrated in Fig. 4.1(a).
The 3D-US volume is constructed from 2D US slices acquired from imaging the vertebra specimen in a water bath, and by moving the probe using a 2D robot in the elevation direction by a step of 0.5 mm [Fig. 4.1(a)]. The constructed 3D-US volume consists of $512 \times 512 \times 61$ voxels with a resolution of 0.077 mm×0.077 mm×0.5 mm. Subsequently a CT dataset of the vertebra specimen is prepared using a high-resolution CT imager (Siemens, Somantom Definition Flash). This results in a CT volume of $512 \times 512 \times 374$ voxels with a resolution of (0.19 mm×0.19 mm×0.3 mm). For registration, the coordinates of the fiducials' tip are manually selected both in US and CT datasets. A landmark-based rigid registration algorithm is used to transform the CT dataset in order to match the 3D-US volume. The CT slices are resampled to the in-plane US resolution. Since the CT-US registration is performed, the bone iso-surfaces are extracted from the CT volume employing the Marching cubes algorithm in VTK. This is expected to match the ones in US and can be used as the gold standard reference. A thresholding value of -524 Hounsfield unit (HU) is used to extract the surface profile from the CT slices. The extracted surfaces from the CT slices are used as the gold standard reference.
In the *in-vivo* experiments, we use two healthy volunteers. Their lumbar vertebra (L2) are scanned in three different planes: sagittal and transversal plane of the spinous process, and the lamina plane. For scanning the spinous process, we use a 10 mm stand-off (SonarAid, Wolhusen, Lucerne, Switzerland) in order to improve matching between probe and skin. The scans are preformed after obtaining signed consent of the volunteers.
In the experimental studies, channel data are acquired using a SonixMDP scanner (Ultrasonix medical corporation, Vancouver, British Columbia, Canada), along with a linear array transducer (L14-5/38) with 128 elements, centre frequency of 5 MHz, and pitch of 0.308 mm. We use 256 imaging beams which are transmitted with $\mathrm{FN}_{TX} = 2.8$, and received with $\mathrm{FN}_{RX} = 1.5$. Further, the receive aperture walks with the transmit aperture, meaning that the active receive elements are centered on the transmit beam axes. SonixDAQ (Ultrasonix medical corporation, Vancouver, British Columbia, Canada) is used to capture the channel data. This module allows us to store RF data acquired from 128 elements simultaneously. For the beamforming, the channel data related to each beam is first determined and delayed. Then, the ESMV beamforming method is applied to construct images of interest. As for the simulations, $\Delta = 5\%$ is used for the diagonal loading purpose. Further, after construction of the images a 2D median filter with a window size of 3×3 is applied to smooth images.

4.3 Results

4.3.1 Effects of the largest eigenvalue on image of a point scatterer:

Fig. 4.2 demonstrates the effect of using only the largest eigenvalue on the image of a point scatterer. Fig. 4.2(a) shows the DAS image of the simulated point scatterer.

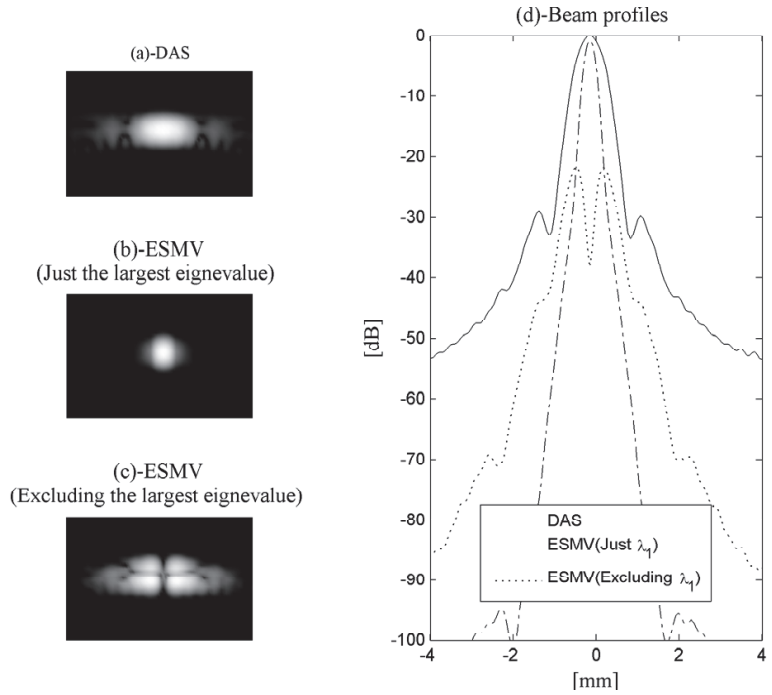

Figure 4.2: Simulated point scatterer using a 128 element, 5 MHz transducer. The point scatterer is located at the transmit focal depth which is 15 mm. Dynamic focusing is used for the received beams. (a) DAS, (b) ESMV (just the largest eigenvalue), (c) ESMV (excluding the largest eigenvalue), (d) two-way beam profiles corresponding to the images in (a)-(c). The dynamic range is 50 dB. $L = M/2$, $K = 0$ are used for (b)-(c). In (a)-(c) image dimensions are 3 mm×5 mm (depth×lateral).

Fig. 4.2(b) presents the ESMV image when only the largest eigenvalue is used for estimation of the signal subspace ($\mathbf{E_s}$). In comparison with Fig. 4.2(a), the point scatterer is defined with higher resolution and the sidelobe level is decreased. In Fig. 4.2(c), it is assumed that all eigenvalues contribute in the signal subspace except the largest one (λ_1). In this scenario, the image of the point scatterer is completely distorted. In Fig. 4.2(d) the beam profiles corresponding to Figs. 4.2(a)-(c) are compared. In this figure it can be seen that using λ_1 in the ESMV beamformer results in a -12 dB beamwidth of 0.35 mm. This value is about 0.8 mm for DAS. Ideally, the sidelobe levels are decreased from -30 dB in DAS to -95 dB for ESMV. Also, it can be seen that when λ_1 is excluded a major part of the mainlobe between 0 and -20 dB is removed [Fig. 4.2(d)].

4.3.2 Simulated vertebra phantom

Fig. 4.3 shows simulated images of the vertebra phantom introduced in the simulation setup section and its corresponding phase symmetry images for different beamformers. In this imaging scenario, the transmit focal depth is also 15 mm. Fig. 4.3(a) shows the DAS image of the vertebra phantom. Figs. 4.3(b)-(d) present ESMV images for different eigenvalue thresholding values (β). In Fig. 4.3(d), $\beta = 0.001\%$ is selected to ensure that just the largest eigenvalue is used. It can be seen that by decreasing β the speckle pattern in the neighboring region of the vertebra body is distorted, and for $\beta = 0.001\%$ it is almost removed, especially between the depths of 20 mm and 35 mm. This effect can be partly seen around the spinous process (top of the vertebra) at a depth of 12 mm. Figs. 4.3(e)-(h) show PS images related to Figs. 4.3(a)-(d). In the DAS-based image of Fig. 4.3(e) the vertebra walls are invisible between depths of 14.2 mm and 30 mm. Figs. 4.3(f)-(h) show that by decreasing β, a larger segment of the right-hand sidewall can be detected with the PS technique. Compared to Fig. 4.3(e), in Figs. 4.3(g) and (h) the wall is more visible below the depth of 20 mm. Also, the mean pixel intensity on the right-hand sidewall is 64, 78, and 126 for DAS, ESMV ($\beta = 1\%$) and ESMV ($\beta = 0.001\%$), measured from a depth of 20 mm to 30 mm.

4.3.3 Registration of a vertebra

Figs. 4.4 and 4.5 show the CT gold standard surface profile overlaid on the ultrasound images for the two different vertebra slices of Fig. 4.1(b). Figs. 4.4(a) and (b) show the DAS and ESMV images of slice 1. The CT profile matches well on outer boundary of the vertebra in both images. In the DAS image [Fig. 4.4(a)] the sidelobe noise is clearly observed around the spinous process between a depth of 15 mm and 20 mm. Also, the sidewall's boundaries are stretched due to the shadowing effect [24], whereas in the ESMV image the sidelobe noise is decreased and the boundaries are enhanced. In Figs. 4.4(c) and (d) a deviation of the surface from the gold standard surface is observed, particularly on spinous process (top of the vertebra). Also in Fig. 4.4(c) the curvature of spinous process profile has been distorted, whereas the anatomy of the vertebra is reasonably well kept in Fig. 4.4(d).

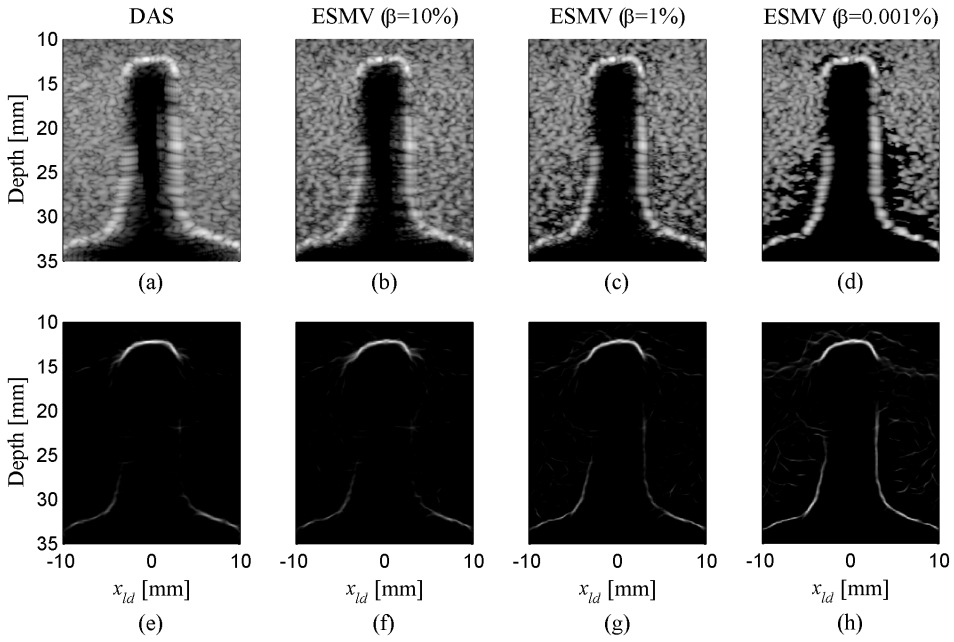

Figure 4.3: Simulated vertebra phantom using a 128 element, 5 MHz transducer. The transmit focal depth is 15 mm and dynamic focusing is used for the received beams. (a) DAS (US), (b) ESMV (US, $\beta = 10\%$), (c) ESMV (US, $\beta = 1\%$), (d) ESMV (US, $\beta = 0.001\%$), (e) DAS (PS), (f) ESMV (PS, $\beta = 10\%$), (g) ESMV (PS, $\beta = 1\%$), and (h) ESMV (PS, $\beta = 0.001\%$). The dynamic range is 60 dB for (a)-(d) and 255 for (e)-(h). $L = M/2$, $K = 4$ are used for (b)-(d).

Figs. 4.5(a) and (b) show the DAS and ESMV images of slice 2, and Figs. 4.5(c) and (d) demonstrate their corresponding PS images. Comparing to the gold standard surface profile, in Fig. 4.5(d) the anatomy of the spinous process is kept whereas it is distorted in Fig. 4.5(c). In Fig. 4.5(d) the PS detects the right-hand sidewall between depths 16.4 mm and 21.8 mm, whereas in Fig. 4.5(c) this part of the vertebra is missed.

In Fig. 4.6, four different scan-lines corresponding to Figs. 4.4(c) and (d) are compared. These lines have been marked in Fig. 4.4(c). In Figs. 4.6(a)-(d) the location of the bone surface obtained from the gold standard reference is marked by vertical dash-dot lines. At $x_{ld} = 13.70$ mm, the DAS and ESMV locate the bone surface with a bias of 0.78 mm and 0.54 mm in comparison with the CT gold standard reference. In this figure, the measured profile width at a pixel intensity of 100 is 0.82 mm and 1.4 mm for DAS, and ESMV respectively. Fig. 4.6(b) shows the scan-line corresponds to $x_{ld} = 21$ mm. The bias is increased to 1.12 mm at spinous process for both DAS and ESMV. Fig. 4.6(c) shows the horizontal scan-line at a depth of 32.10 mm. At this line the

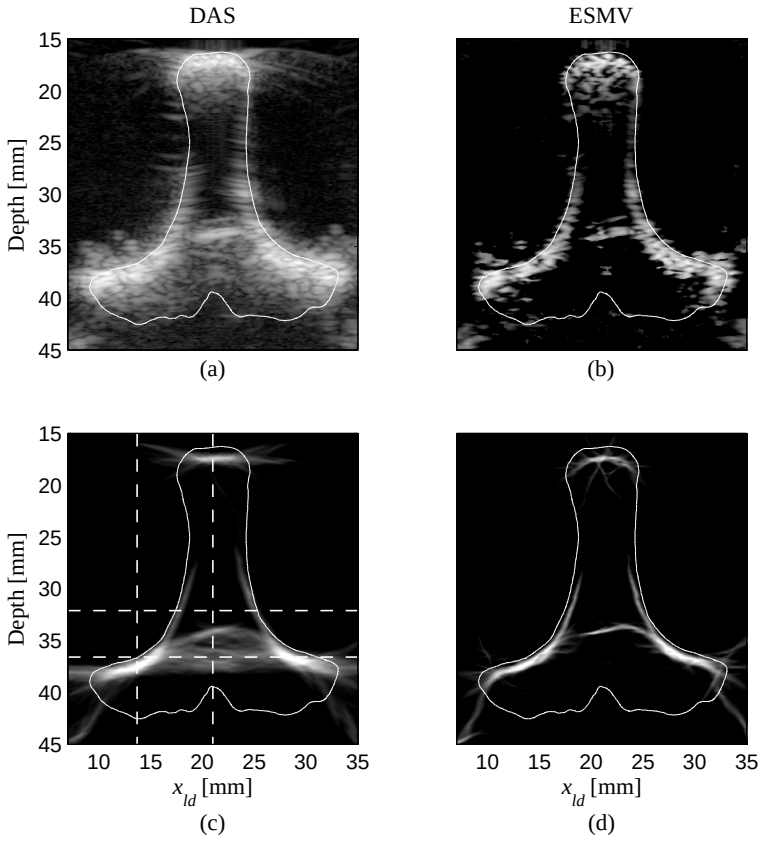

Figure 4.4: Registration of the CT image to ultrasound image slice 1 for DAS and ESMV images and their corresponding PS images. (a) DAS (US), (b) ESMV (US, $\beta = 0.001\%$), (c) DAS (PS), (d) ESMV (PS, $\beta = 0.001\%$). The dynamic range is 70 dB for (a) and (b), and 255 for (c) and (d). $L = M/2, K = 0$ are assumed for (b).

intensity value for both sidewalls increase from 80 for DAS to 125 for ESMV, whereas the bias is increased about 0.12 mm for ESMV compared to DAS. In Fig. 4.6(d) it can be seen that the averaged intensity value for the pixels located between $x_{ld} = 17.3$ mm and $x_{ld} = 26.4$ mm is decreased from about 85 in DAS image to 0 for ESMV one.

In Fig. 4.7, different scan-lines corresponding to Figs. 4.5(c) and (d) are compared. The selected lines are marked with dash white vertical lines in Fig. 4.5(c). In Fig. 4.7(a), at $x_{ld} = 14.32$ mm a bias of 0.8 mm is observed for both DAS and ESMV compared to the gold standard reference. Also the measured profile width at a pixel intensity of 100 is about 1.55 mm and 0.54 mm for DAS and ESMV. Fig. 4.7(b) shows the scan-line corresponding to $x_{ld} = 21$ mm. At this line, the bias increases to 0.78 mm and 0.71

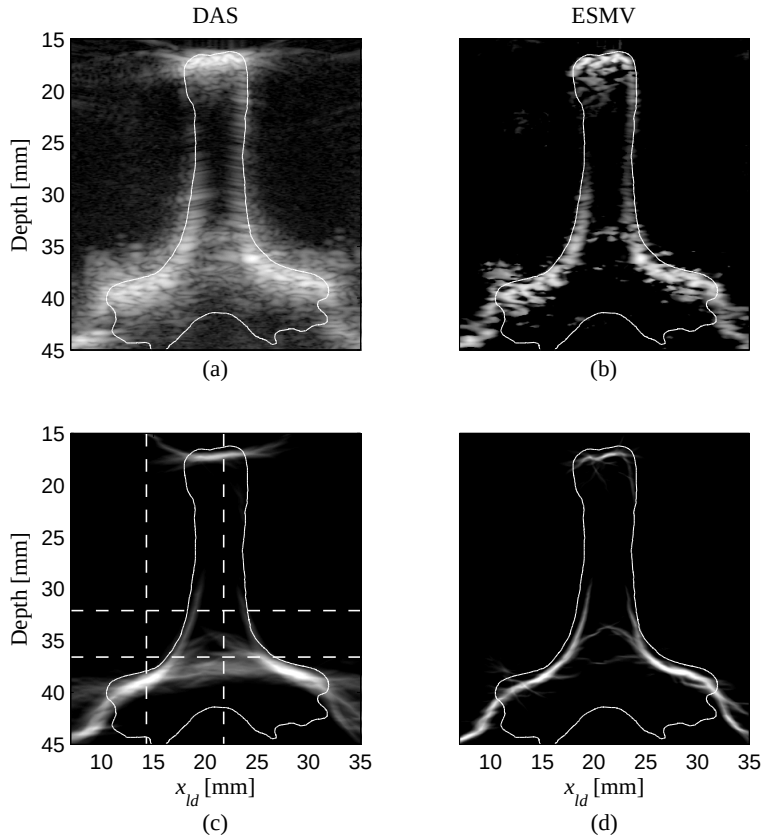

Figure 4.5: Registration of the CT image to ultrasound image slice 2 for DAS and ESMV images and their corresponding PS images. (a) DAS (US), (b) ESMV (US, $\beta = 0.001\%$), (c) DAS (PS), (d) ESMV (PS, $\beta = 0.001\%$). The dynamic range is 70 dB for (a) and (b), and 255 for (c) and (d). $L = M/2, K = 0$ are assumed for (b).

mm for DAS and ESMV. Also, the measured profile width at a pixel intensity of 100 is about 0.3 mm for ESMV and 0.5 mm for DAS. Fig. 4.7(c) shows the horizontal scan-line at a depth of 32.10 mm. At this line the intensity value is decreased by 28 for left-hand wall and 33 for right-hand wall for DAS in comparison to ESMV. In Fig. 4.7(d) at a depth of 36.60 mm the average pixel value between $x_{ld} = 18.5$ mm and $x_{ld} = 24.5$ mm decreases from 50 to 10, indicating lower noise level in the PS image obtained with the ESMV.

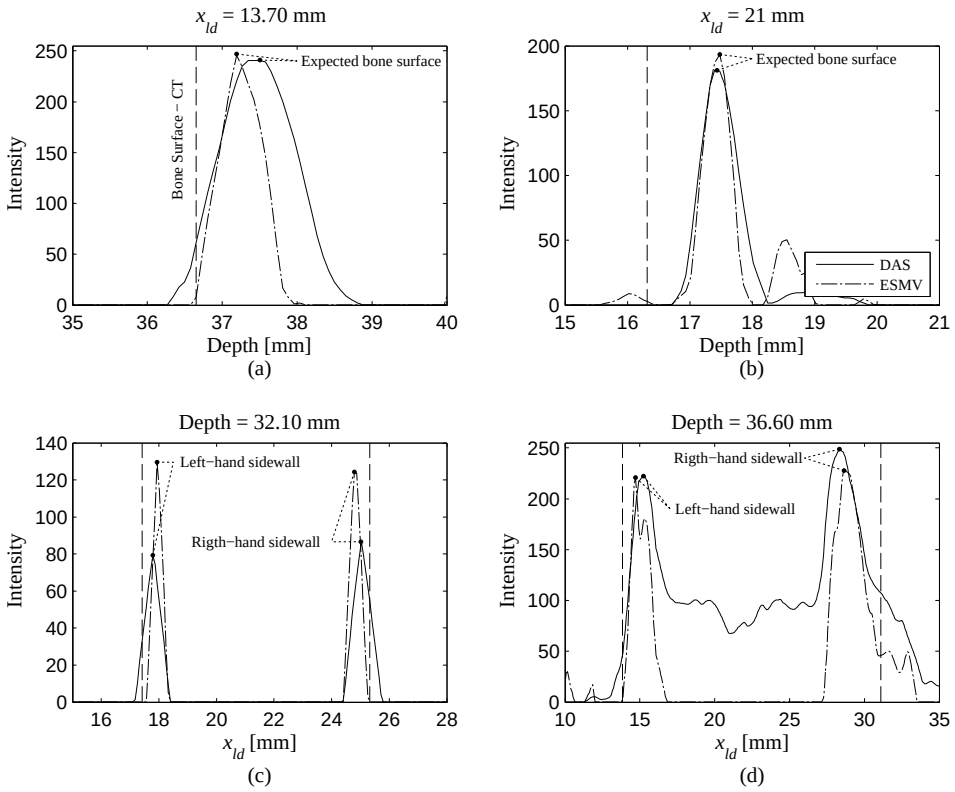

Figure 4.6: Comparison of image lines in Figure 4.4 for PS images obtained from the DAS (solid line) and ESMV (dash-dot line) images. (a) x_{ld} = 13.70 mm, (b) x_{ld} = 21 mm, (c) depth = 32.10 mm, (d) depth = 36.60 mm.

4.3.4 In-vivo images

Figs. 4.8 - 4.12 demonstrate a qualitative comparison between PS images obtained from DAS and ESMV beamformers. Fig. 4.8 shows images of a lamina for volunteer 1. Fig. 4.8(a) corresponds to the DAS image and Fig. 4.8(b) demonstrates the ESMV image for $\beta = 0.001\%$. It can be seen that in the ESMV image, speckle around the bone surface is reduced. Figs. 4.8(c) and (d) show PS images obtained from Figs. 4.8(a) and (b). It is observed that the ESMV beamformer improves the bone surface and results in a thinner definition of the bone boundary. Also on the left-hand side of the DAS image (marked with a white arrow) some unwanted features are observed, which have been removed in Fig. 4.8(d). Similarly, Fig. 4.9 shows the lamina image for the volunteer 2. In Fig. 4.9(d), the ESMV beamformer with $\beta = 0.001\%$ enhances the sharpness of the bone boundary.

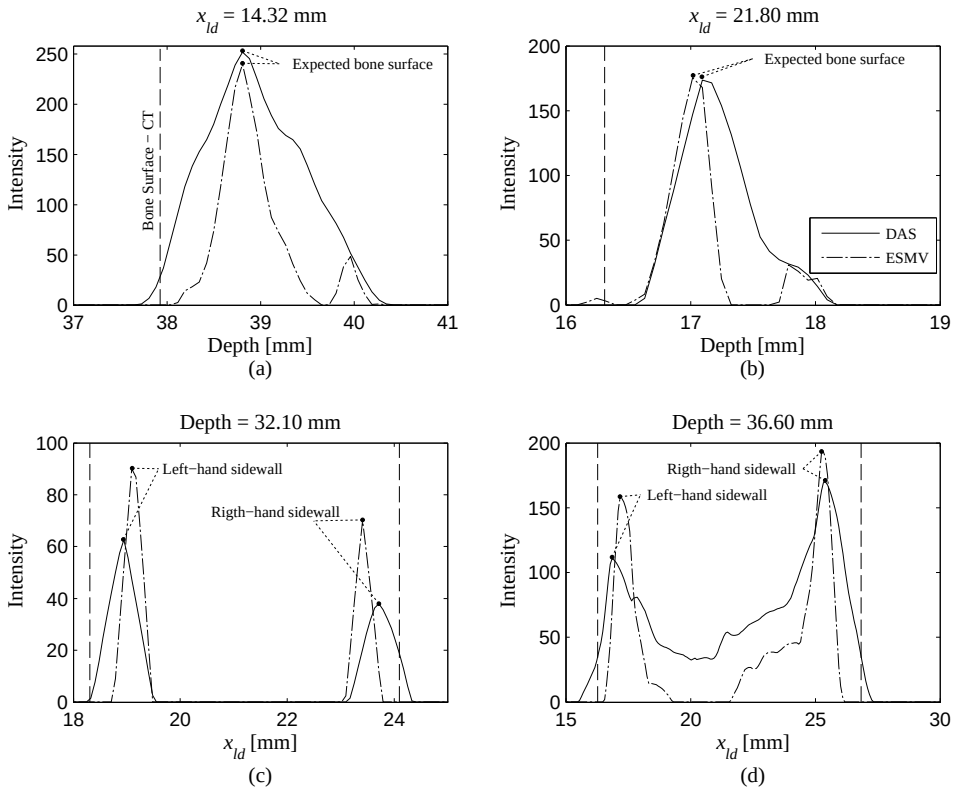

Figure 4.7: Comparison of image lines in Figure 4.5 for PS images obtained from the DAS and ESMV images. (a) $x_{ld} = 14.32$ mm, (b) $x_{ld} = 21.80$ mm, (c) depth = 32.10 mm, (d) depth = 36.60 mm.

Figs. 4.10 and 4.11 show sagittal plane images of spinous process for the two volunteers. Fig. 4.10(a) shows the DAS image for volunteer 1. Fig. 4.10(b) demonstrate the ESMV image with $\beta = 0.001\%$. Comparing with Fig. 4.10(a), in this image the speckle around the bone surface is reduced while the structure of the bone is kept. Fig. 4.10(c) shows the PS image obtained from the DAS image. In this image the bone surface is smeared out and the boundaries are not well delineated, whereas in Fig. 4.10(d) the bone surface is reasonably well isolated from the connective tissue on the top of the surface. In Fig. 4.10(c), the bone boundary, on both side of the spinous process marked with white arrows, is thick and unclear. In comparison, in Fig. 4.10(d) the bone boundary is sharper and a prolongation of the surface is observed. In a similar manner in Fig. 4.11(d) the sharpness of the bone surface is increased for smaller β, and the surface is somewhat better isolated from the connective tissue in comparison with Fig. 4.11(c).

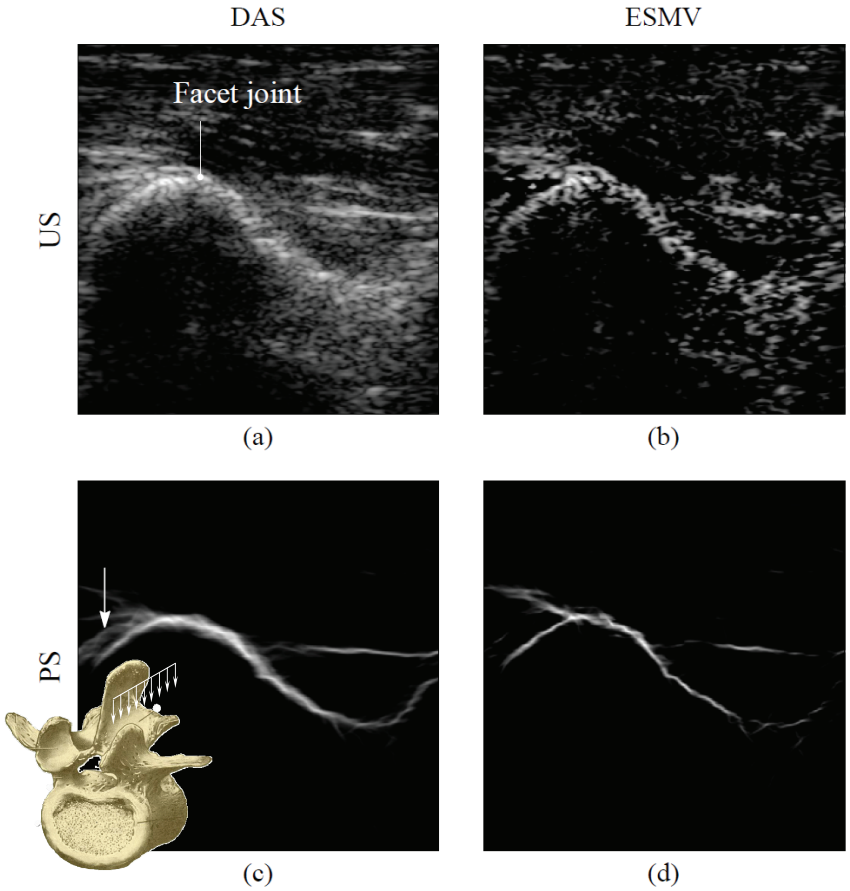

Figure 4.8: Ultrasound and PS post-processed images of lamina for volunteer 1. (a) DAS (US), (b) ESMV (US, $\beta = 0.001\%$), (c) DAS (PS), (d) ESMV (PS, $\beta = 0.001\%$). The dynamic range is 50 dB and $L = M/2, K = 2$ are used for (b).

Fig. 4.12 shows an image of the vertebra in the transversal direction for volunteer 2. In Fig. 4.12(c), the spinous process is not well separated from the connective tissue, whereas in Fig. 4.12(d) the surface is totally isolated from the connective tissue. In Fig. 4.12(d) the lamina (white arrow) is clearly detected by the PS technique, whereas it is missed in Fig. 4.12(c). The two symmetrical features seen on both sides of Fig. 4.12(c) which are marked with two arrows, correspond to the strong scattering from connective tissues, possibly muscle fiber bundles.

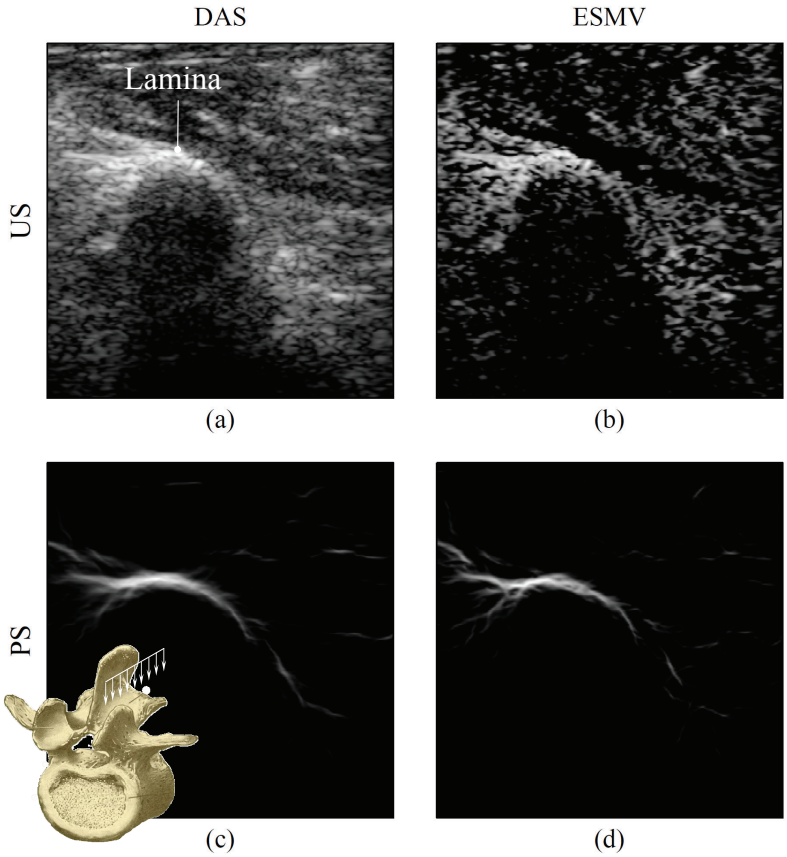

Figure 4.9: Ultrasound and PS post-processed images of lamina for volunteer 2. (a) DAS (US), (b) ESMV (US, $\beta = 0.001\%$), (c) DAS (PS), (d) ESMV (PS, $\beta = 0.001\%$). The dynamic range is 50 dB and $L = M/2, K = 2$ are used for (b).

4.4 Discussion

There is a potential for the ESMV beamformer to enhance the bone edges in the US images, but the performance of this beamformer depends on the signal subspace estimation. From Figs. 4.3(b)-(d), we observe that by a small thresholding value the bone structure is kept while the speckle in its neighborhood is reduced. This effect which has been discussed in [26] can give rise to images with enhanced edges but distorted speckle patterns [Figs. 4.3(a)-(d)]. A very small thresholding value results in a rank-1 signal subspace, *i.e.* just the largest eigenvalue is used for the signal subspace estimation in (4.7). Thus, since detection of edges is the main purpose, regardless of the speckle pattern, a rank-1 signal subspace can enhance the bone edges images obtained from the ESMV beamformer [Figs. 4.8(b) - 4.12(b)]. This can be beneficial

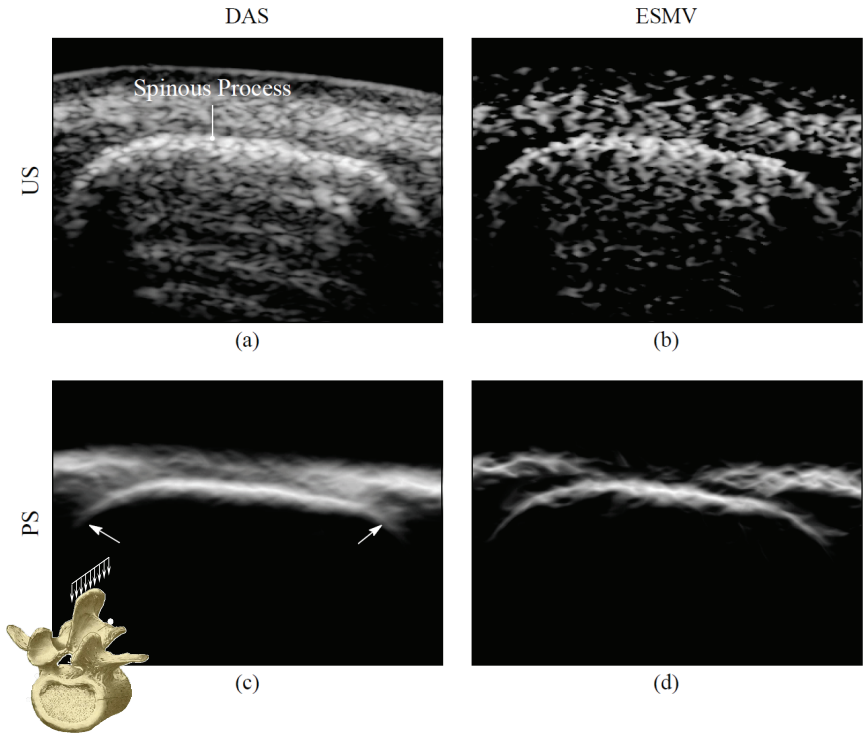

Figure 4.10: Ultrasound and PS post-processed images of spinous process in sagittal direction for volunteer 1 for DAS and ESMV beamformers. (a) DAS (US), (b) ESMV (US, $\beta = 0.001\%$), (c) DAS (PS), (d) ESMV (PS, $\beta = 0.001\%$). The dynamic range is 40 dB and $L = M/2, K = 2$ are used for (b).

for the post-processing techniques, *e.g.* the phase symmetry method, for extracting or locating the bone surfaces. From Fig. 4.3(h) and Figs. 4.8(d) - 4.12(d) we observe that the bone surfaces which are extracted from the ESMV are sharper, the bone boundaries are thinner, and they are reasonably well isolated from the connective tissue. Also, this setup shows more details of the vertebra geometry, as seen in Figs. 4.4(d)-4.5(d). In Fig. 4.5, the PS fails to retain vertical structures on either side of the spinous process, both with and without ESMV beamforming. It is due to the directional nature of the filter, which is set to be selectively downwards aligned with the direction of ultrasound propagation. While it is possible to add more filtering angles, making the resulting filter virtually isotropic, it also enhances structures that are orthogonal to the ultrasound direction. Hence, it is more likely to be a random alignment of speckles, which results in non-bone feature detection.
The registration with CT-contours, shown in Figs. 4.4 and 4.5, suggests that the ultrasound bone response appears within the CT-contours. The PS filtered bone surface is delineated at the maximum of the ultrasound bone response, which places it

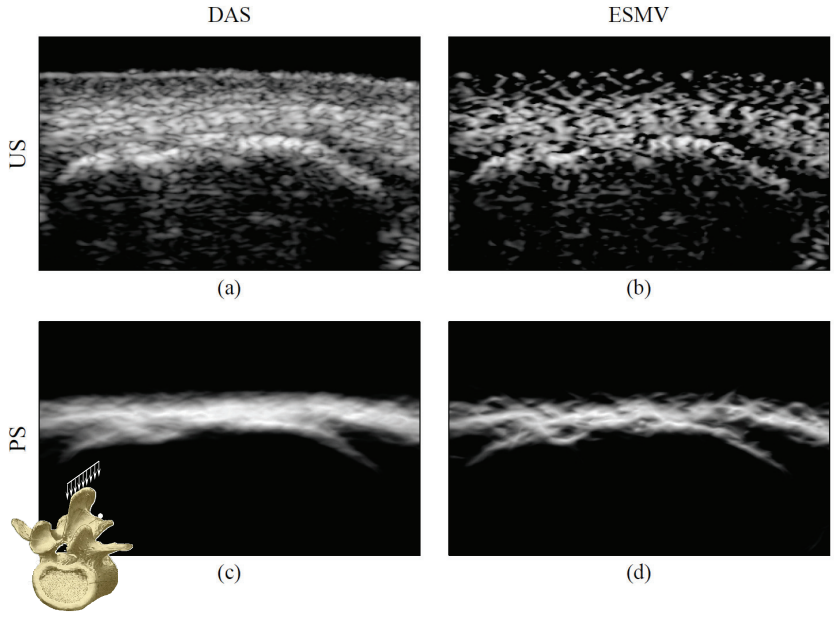

Figure 4.11: Ultrasound and PS post-processed images of spinous process in sagittal direction for volunteer 2 for DAS and ESMV beamformers. (a) DAS (US), (b) ESMV (US, $\beta = 0.001\%$), (c) DAS (PS), (d) ESMV (PS, $\beta = 0.001\%$). The dynamic range is 40 dB and $L = M/2, K = 2$ are used for (b).

even further inside the CT-surface. This behavior of the PS-filter is expected from its mathematical formulation as it identifies the maximum of the response in the signal rather than its rising side. The other reason for observed bias is due to the registration error as pinpointing the balls' tip accurately in the US images was more difficult than in the CT dataset.

The post-processed images in Figs. 4.8 - 4.11, demonstrate that there is a potential for the phase symmetry technique to reasonably well exploit the spinal structure from US images. This can result in an enhanced 3D reconstruction of the spinal anatomy, which facilitates level detection procedure in minimally invasive spinal surgeries [37], and registration of preoperative CT or MR images to intraoperative US in neuronavigation surgeries [38]. Furthermore, the better separation of the bone surface from the connective tissues achieved in Figs. 4.8(d), 4.10(d) and 4.12(d), can ease the model-based automated segmentation of the spine anatomy.

In the transversal imaging scenario, the dataset from volunteer 1 has been discarded due to the unacceptable quality of the images. Also the speckle in the rank-1 ESMV image of volunteer 2 [Fig. 4.12(b)] is highly diffused. However, its corresponding PS image presents the spinous process structure reasonably well. Imaging a vertebra in the transversal plane is more challenging as the spinous process is narrow in this plane, and

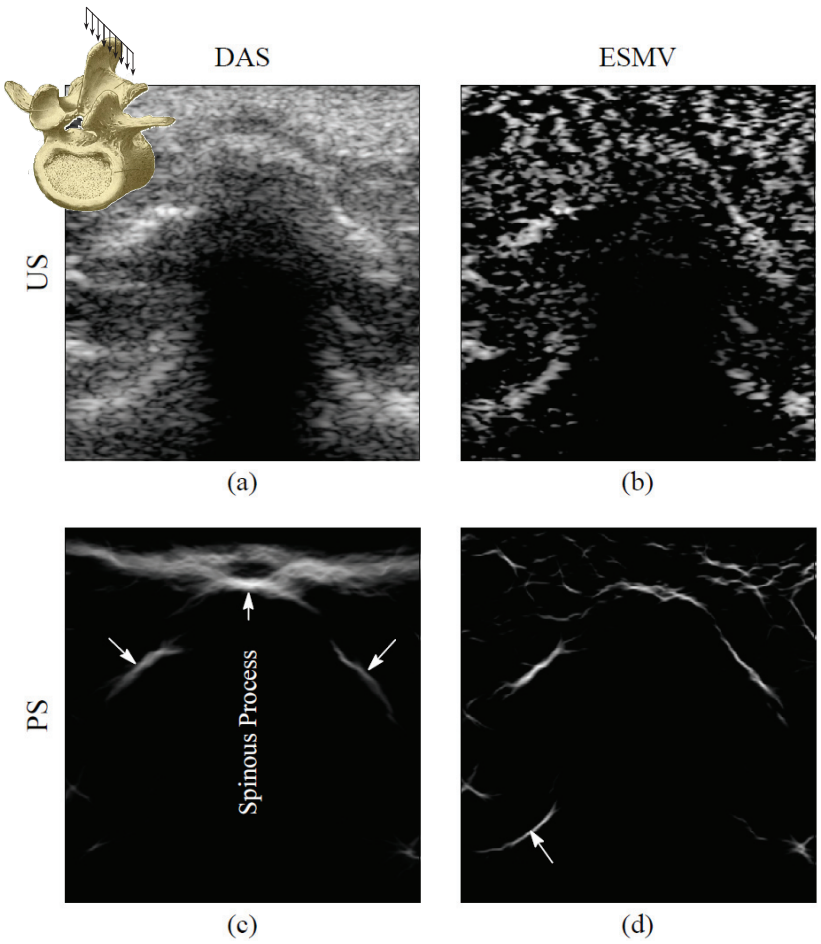

Figure 4.12: Ultrasound and PS post-processed images of the spinous process in transversal direction for volunteer 2. (a) DAS (US), (b) ESMV (US, $\beta = 0.001\%$), (c) DAS (PS), (d) ESMV (PS, $\beta = 0.001\%$). The dynamic range is 50 dB and $L = M/2, K = 2$ are used for (b).

the sidewalls are almost extended along the imaging beams, and the features spread from shallow to deep field.

4.5 Conclusions

We have explored the potential of a rank-1 ESMV beamformer, together with the phase symmetry post-processing method to enhance the spinal anatomy in ultrasound images. The suggested beamformer is independent of the thresholding factor, and its complexity is in the same order as for minimum variance beamformer. This beamforming setup can locate the spinal structure reasonably well, while reducing the speckle from the surrounding tissue. Therefore, the phase symmetry filtering of these images can result in an improved definition of the boundaries and enhanced separation of the spinal anatomy from the neighboring connective tissues in comparison with the DAS technique. This shows that beamforming which is optimized for good visual appearance is not always optimal for feature extraction. This is therefore one of the first examples which demonstrates that it can be beneficial to do joint optimization of the two operations in order to improve feature detection.

References

[1] S. N. Narouze, "Ultrasound-guided interventional procedures in pain management: Evidence-based medicine," *Regional Anesthesia and Pain Medicine*, vol. 35, no. 2, pp. 55–58, 2010.

[2] J.-K. Shim, J.-C. Moon, K.-B. Yoon, W.-O. Kim, and D.-M. Yoon, "Ultrasound-guided lumbar medial-branch block: A clinical study with fluoroscopy control," *Regional Anesthesia and Pain Medicine*, vol. 31, no. 5, pp. 451–454, 2006.

[3] S. N. Narouze, A. Vydyanathan, L. Kapural, D. I. Sessler, and N. Mekhail, "Ultrasound-guided cervical selective nerve root block: A fluoroscopy-controlled feasibility study," *Regional Anesthesia and Pain Medicine*, vol. 34, no. 4, pp. 343–348, 2009.

[4] M. Gofeld, A. Bhatia, S. Abbas, S. Ganapathy, and M. Johnson, "Development and validation of a new technique for ultrasound-guided stellate ganglion block," *Regional Anesthesia and Pain Medicine*, vol. 34, no. 5, pp. 475–479, 2009.

[5] D. C. Barratt, G. P. Penney, C. S. K. Chan, M. Slomczykowski, T. J. Carter, P. J. Edwards, and D. J. Hawkes, "Self-calibrating 3d-ultrasound-based bone registration for minimally invasive orthopedic surgery," *Medical Imaging, IEEE Transactions on*, vol. 25, no. 3, pp. 312–323, 2006.

[6] J. Kowal, C. Amstutz, F. Langlotz, H. Talib, and M. G. Ballester, "Automated bone contour detection in ultrasound b-mode images for minimally invasive registration in computer-assisted surgery-an in vitro evaluation," *The International journal of Medical Robotics and Computer Assisted Surgery*, vol. 3, no. 4, pp. 341–348, 2007.

[7] B. Brendel, S. Winter, A. Rick, M. Stockheim, and H. Ermert, "Registration of 3d ct and ultrasound datasets of the spine using bone structures," *Computer Aided Surgery*, vol. 7, no. 3, pp. 146 – 155, 2002.

[8] A. K. Jain and R. H. Taylor, "Understanding bone responses in b-mode ultrasound images and automatic bone surface extraction using a bayesian probabilistic framework," in *Medical Imaging 2004: Ultrasonic Imaging and Signal Processing*, vol. 5373, (San Diego, CA, USA), pp. 131–142, SPIE, 2004.

[9] A. V. Oppenheim and J. S. Lim, "The importance of phase in signals," *Proceedings of the IEEE*, vol. 69, no. 5, pp. 529–541, 1981.

[10] M. C. Morrone and R. A. Owens, "Feature detection from local energy," *Pattern Recognition Letters*, vol. 6, no. 5, pp. 303–313, 1987.

[11] Z. Xiao and Z. Hou, "Phase based feature detector consistent with human visual system characteristics," *Pattern Recognition Letters*, vol. 25, no. 10, pp. 1115 – 1121, 2004.

[12] I. Hacihaliloglu, R. Abugharbieh, A. J. Hodgson, and R. N. Rohling, "Bone surface localization in ultrasound using image phase-based features," *Ultrasound in Medicine & Biology*, vol. 35, no. 9, pp. 1475–1487, 2009.

[13] J. F. Synnevag, A. Austeng, and S. Holm, "Adaptive beamforming applied to medical ultrasound imaging," *IEEE Transactions on Ultrasonics, Ferroelectrics and Frequency Control*, vol. 54, no. 8, pp. 1606–1613, 2007.

[14] J. Capon, "High-resolution frequency-wavenumber spectrum analysis," *proc. IEEE*, vol. 57, no. 8, pp. 1408–1418, 1969.

[15] J. A. Mann and W. F. Walker, "A constrained adaptive beamformer for medical ultrasound: initial results," *proc. IEEE Ultrasonics Symposium*, vol. 2, pp. 1807–1810, 2002.

[16] M. Sasso and C. Cohen-Bacrie, "medical ultrasound imaging using the fully adaptive beamformer," *proc. IEEE Acoustics, Speech, and Signal, (ICASSP '05)*, vol. 2, pp. 489–492, 2005.

[17] Z. Wang, J. Li, and R. Wu, "Time-delay- and time-reversal-based robust capon beamformers for ultrasound imaging," *IEEE Transactions on Medical Imaging*, vol. 24, no. 10, pp. 1308–1322, 2005.

[18] F. Vignon and M. R. Burcher, "Capon beamforming in medical ultrasound imaging with focused beams," *IEEE Transactions on Ultrasonics, Ferroelectrics and Frequency Control*, vol. 55, no. 3, pp. 619–628, 2008.

[19] J. F. Synnevag, A. Austeng, and S. Holm, "Benefits of minimum-variance beamforming in medical ultrasound imaging," *IEEE Transactions on Ultrasonics, Ferroelectrics and Frequency Control*, vol. 56, no. 9, pp. 1868–1879, 2009.

[20] B. Mohammadzadeh Asl and A. Mahloojifar, "Eigenspace-based minimum variance beamforming applied to medical ultrasound imaging," *IEEE Transactions on Ultrasonics, Ferroelectrics and Frequency Control*, vol. 57, no. 11, pp. 2381–2390, 2010.

[21] L. Cheng-Chou and L. Ju-Hong, "Eigenspace-based adaptive array beamforming with robust capabilities," *IEEE Transactions on Antennas and Propagation*, vol. 45, no. 12, pp. 1711–1716, 1997.

[22] Y. Jung-Lang and Y. Chien-Chung, "Generalized eigenspace-based beamformers," *IEEE Transactions on Signal Processing*, vol. 43, no. 11, pp. 2453–2461, 1995.

[23] D. D. Feldman and L. J. Griffiths, "A projection approach for robust adaptive beamforming," *IEEE Transactions on Signal Processing*, vol. 42, no. 4, pp. 867–876, 1994.

[24] S. Mehdizadeh, A. Austeng, T. Johansen, and S. Holm, "Minimum variance beamforming applied to ultrasound imaging with a partially shaded aperture," *IEEE Transactions on Ultrasonics, Ferroelectrics and Frequency Control*, vol. 59, no. 4, pp. 683–693, 2012.

[25] S. Mehdizadeh, A. Austeng, T. Johansen, and S. Holm, "Performance of adaptive beamformers for ultrasound imaging of a partially shaded object," *IEEE Ultrasonics Symposium*, 2011.

[26] S. Mehdizadeh, A. Austeng, T. Johansen, and S. Holm, "Eigenspace based minimum variance beamforming applied to ultrasound imaging of acoustically hard tissues," *IEEE Transactions on Medical Imaging*, unpublished observations.

[27] S. Tie-Jun, M. Wax, and T. Kailath, "On spatial smoothing for direction-of-arrival estimation of coherent signals," *IEEE Transactions on Acoustics, Speech and Signal Processing*, vol. 33, no. 4, pp. 806–811, 1985.

[28] J. S. Thompson, P. M. Grant, and B. Mulgrew, "Performance of spatial smoothing algorithms for correlated sources," *IEEE Transactions on Signal Processing*, vol. 44, no. 4, pp. 1040–1046, 1996.

[29] W. Featherstone, H. J. Strangeways, M. A. Zatman, and H. Mewes, "A novel method to improve the performance of capon's minimum variance estimator," in *Antennas and Propagation, Tenth International Conference on (Conf. Publ. No. 436)*, vol. 1, pp. 322–325, 1997.

[30] L. Chang and C. C. Yeh, "Performance of dmi and eigenspace-based beamformers," *IEEE Transactions on Antennas and Propagation*, vol. 40, no. 11, pp. 1336–1347, 1992.

[31] J. S. Goldstein and I. S. Reed, "Reduced-rank adaptive filtering," *IEEE Transactions on Signal Processing*, vol. 45, no. 2, pp. 492–496, 1997.

[32] H. L. Van Trees, *Optimum Array Processing - Part IV, Detection, Estimation, and Modulation Theory*. New York: John Wiley & Sons, 2002.

[33] I. Hacihaliloglu, R. Abugharbieh, A. J. Hodgson, and R. N. Rohling, "Automatic adaptive parameterization in local phase feature-based bone segmentation in ultrasound," *Ultrasound in Medicine & Biology*, vol. 37, no. 10, pp. 1689–1703, 2011.

[34] I. Hacihaliloglu, R. Abugharbieh, A. J. Hodgson, R. N. Rohling, and P. Guy, "Automatic bone localization and fracture detection from volumetric ultrasound images using 3-d local phase features," *Ultrasound in Medicine & Biology*, vol. 38, no. 1, pp. 128–144, 2011.

[35] J. A. Jensen, "Field: A program for simulating ultrasound systems," *Medical & Biological Engineering & Computing*, vol. 34, pp. 351–353, 1996.

[36] R. F. Wagner, M. F. Insana, and S. W. Smith, "Fundamental correlation lengths of coherent speckle in medical ultrasonic images," *IEEE Transactions on Ultrasonics, Ferroelectrics and Frequency Control*, vol. 35, no. 1, pp. 34–44, 1988.

[37] Y. Otake, S. Schafer, J. W. Stayman, W. Zbijewski, G. Kleinszig, A. Graumann, A. J. Khanna, and S. J. H., "Automatic localization of target vertebrae in spine surgery using fast ct-to-fluoroscopy (3d-2d) image registration," *SPIE Medical Imaging*, vol. 8316, 2012.

[38] S. Winter, B. Brendel, I. Pechlivanis, K. Schmieder, and C. Igel, "Registration of ct and intraoperative 3-d ultrasound images of the spine using evolutionary and gradient-based methods," *IEEE Transactions on Evolutionary Computation*, vol. 12, no. 3, pp. 284–296, 2008.

Dissertations at the Faculty of Medicine, NTNU

1977

1. Knut Joachim Berg: EFFECT OF ACETYLSALICYLIC ACID ON RENAL FUNCTION
2. Karl Erik Viken and Arne Ødegaard: STUDIES ON HUMAN MONOCYTES CULTURED *IN VITRO*

1978

3. Karel Bjørn Cyvin: CONGENITAL DISLOCATION OF THE HIP JOINT.
4. Alf O. Brubakk: METHODS FOR STUDYING FLOW DYNAMICS IN THE LEFT VENTRICLE AND THE AORTA IN MAN.

1979

5. Geirmund Unsgaard: CYTOSTATIC AND IMMUNOREGULATORY ABILITIES OF HUMAN BLOOD MONOCYTES CULTURED IN VITRO

1980

6. Størker Jørstad: URAEMIC TOXINS
7. Arne Olav Jenssen: SOME RHEOLOGICAL, CHEMICAL AND STRUCTURAL PROPERTIES OF MUCOID SPUTUM FROM PATIENTS WITH CHRONIC OBSTRUCTIVE BRONCHITIS

1981

8. Jens Hammerstrøm: CYTOSTATIC AND CYTOLYTIC ACTIVITY OF HUMAN MONOCYTES AND EFFUSION MACROPHAGES AGAINST TUMOR CELLS *IN VITRO*

1983

9. Tore Syversen: EFFECTS OF METHYLMERCURY ON RAT BRAIN PROTEIN.
10. Torbjørn Iversen: SQUAMOUS CELL CARCINOMA OF THE VULVA.

1984

11. Tor-Erik Widerøe: ASPECTS OF CONTINUOUS AMBULATORY PERITONEAL DIALYSIS.
12. Anton Hole: ALTERATIONS OF MONOCYTE AND LYMPHOCYTE FUNCTIONS IN REALTION TO SURGERY UNDER EPIDURAL OR GENERAL ANAESTHESIA.
13. Terje Terjesen: FRACTURE HEALING AND STRESS-PROTECTION AFTER METAL PLATE FIXATION AND EXTERNAL FIXATION.
14. Carsten Saunte: CLUSTER HEADACHE SYNDROME.
15. Inggard Lereim: TRAFFIC ACCIDENTS AND THEIR CONSEQUENCES.
16. Bjørn Magne Eggen: STUDIES IN CYTOTOXICITY IN HUMAN ADHERENT MONONUCLEAR BLOOD CELLS.
17. Trond Haug: FACTORS REGULATING BEHAVIORAL EFFECTS OG DRUGS.

1985

18. Sven Erik Gisvold: RESUSCITATION AFTER COMPLETE GLOBAL BRAIN ISCHEMIA.
19. Terje Espevik: THE CYTOSKELETON OF HUMAN MONOCYTES.
20. Lars Bevanger: STUDIES OF THE Ibc (c) PROTEIN ANTIGENS OF GROUP B STREPTOCOCCI.
21. Ole-Jan Iversen: RETROVIRUS-LIKE PARTICLES IN THE PATHOGENESIS OF PSORIASIS.
22. Lasse Eriksen: EVALUATION AND TREATMENT OF ALCOHOL DEPENDENT BEHAVIOUR.
23. Per I. Lundmo: ANDROGEN METABOLISM IN THE PROSTATE.

1986

24. Dagfinn Berntzen: ANALYSIS AND MANAGEMENT OF EXPERIMENTAL AND CLINICAL PAIN.
25. Odd Arnold Kildahl-Andersen: PRODUCTION AND CHARACTERIZATION OF MONOCYTE-DERIVED CYTOTOXIN AND ITS ROLE IN MONOCYTE-MEDIATED CYTOTOXICITY.
26. Ola Dale: VOLATILE ANAESTHETICS.

1987

27. Per Martin Kleveland: STUDIES ON GASTRIN.
28. Audun N. Øksendal: THE CALCIUM PARADOX AND THE HEART.
29. Vilhjalmur R. Finsen: HIP FRACTURES

1988

30. Rigmor Austgulen: TUMOR NECROSIS FACTOR: A MONOCYTE-DERIVED REGULATOR OF CELLULAR GROWTH.
31. Tom-Harald Edna: HEAD INJURIES ADMITTED TO HOSPITAL.
32. Joseph D. Borsi: NEW ASPECTS OF THE CLINICAL PHARMACOKINETICS OF METHOTREXATE.
33. Olav F. M. Sellevold: GLUCOCORTICOIDS IN MYOCARDIAL PROTECTION.
34. Terje Skjærpe: NONINVASIVE QUANTITATION OF GLOBAL PARAMETERS ON LEFT VENTRICULAR FUNCTION: THE SYSTOLIC PULMONARY ARTERY PRESSURE AND CARDIAC OUTPUT.
35. Eyvind Rødahl: STUDIES OF IMMUNE COMPLEXES AND RETROVIRUS-LIKE ANTIGENS IN PATIENTS WITH ANKYLOSING SPONDYLITIS.
36. Ketil Thorstensen: STUDIES ON THE MECHANISMS OF CELLULAR UPTAKE OF IRON FROM TRANSFERRIN.
37. Anna Midelfart: STUDIES OF THE MECHANISMS OF ION AND FLUID TRANSPORT IN THE BOVINE CORNEA.
38. Eirik Helseth: GROWTH AND PLASMINOGEN ACTIVATOR ACTIVITY OF HUMAN GLIOMAS AND BRAIN METASTASES - WITH SPECIAL REFERENCE TO TRANSFORMING GROWTH FACTOR BETA AND THE EPIDERMAL GROWTH FACTOR RECEPTOR.
39. Petter C. Borchgrevink: MAGNESIUM AND THE ISCHEMIC HEART.
40. Kjell-Arne Rein: THE EFFECT OF EXTRACORPOREAL CIRCULATION ON SUBCUTANEOUS TRANSCAPILLARY FLUID BALANCE.
41. Arne Kristian Sandvik: RAT GASTRIC HISTAMINE.
42. Carl Bredo Dahl: ANIMAL MODELS IN PSYCHIATRY.

1989

43. Torbjørn A. Fredriksen: CERVICOGENIC HEADACHE.
44. Rolf A. Walstad: CEFTAZIDIME.
45. Rolf Salvesen: THE PUPIL IN CLUSTER HEADACHE.
46. Nils Petter Jørgensen: DRUG EXPOSURE IN EARLY PREGNANCY.
47. Johan C. Ræder: PREMEDICATION AND GENERAL ANAESTHESIA IN OUTPATIENT GYNECOLOGICAL SURGERY.
48. M. R. Shalaby: IMMUNOREGULATORY PROPERTIES OF TNF-α AND THE RELATED CYTOKINES.
49. Anders Waage: THE COMPLEX PATTERN OF CYTOKINES IN SEPTIC SHOCK.
50. Bjarne Christian Eriksen: ELECTROSTIMULATION OF THE PELVIC FLOOR IN FEMALE URINARY INCONTINENCE.
51. Tore B. Halvorsen: PROGNOSTIC FACTORS IN COLORECTAL CANCER.

1990

52. Asbjørn Nordby: CELLULAR TOXICITY OF ROENTGEN CONTRAST MEDIA.
53. Kåre E. Tvedt: X-RAY MICROANALYSIS OF BIOLOGICAL MATERIAL.
54. Tore C. Stiles: COGNITIVE VULNERABILITY FACTORS IN THE DEVELOPMENT AND MAINTENANCE OF DEPRESSION.
55. Eva Hofsli: TUMOR NECROSIS FACTOR AND MULTIDRUG RESISTANCE.
56. Helge S. Haarstad: TROPHIC EFFECTS OF CHOLECYSTOKININ AND SECRETIN ON THE RAT PANCREAS.
57. Lars Engebretsen: TREATMENT OF ACUTE ANTERIOR CRUCIATE LIGAMENT INJURIES.
58. Tarjei Rygnestad: DELIBERATE SELF-POISONING IN TRONDHEIM.
59. Arne Z. Henriksen: STUDIES ON CONSERVED ANTIGENIC DOMAINS ON MAJOR OUTER MEMBRANE PROTEINS FROM ENTEROBACTERIA.
60. Steinar Westin: UNEMPLOYMENT AND HEALTH: Medical and social consequences of a factory closure in a ten-year controlled follow-up study.
61. Ylva Sahlin: INJURY REGISTRATION, a tool for accident preventive work.
62. Helge Bjørnstad Pettersen: BIOSYNTHESIS OF COMPLEMENT BY HUMAN ALVEOLAR MACROPHAGES WITH SPECIAL REFERENCE TO SARCOIDOSIS.
63. Berit Schei: TRAPPED IN PAINFUL LOVE.
64. Lars J. Vatten: PROSPECTIVE STUDIES OF THE RISK OF BREAST CANCER IN A COHORT OF NORWEGIAN WOMAN.

1991

65. Kåre Bergh: APPLICATIONS OF ANTI-C5a SPECIFIC MONOCLONAL ANTIBODIES FOR THE ASSESSMENT OF COMPLEMENT ACTIVATION.
66. Svein Svenningsen: THE CLINICAL SIGNIFICANCE OF INCREASED FEMORAL ANTEVERSION.
67. Olbjørn Klepp: NONSEMINOMATOUS GERM CELL TESTIS CANCER: THERAPEUTIC OUTCOME AND PROGNOSTIC FACTORS.
68. Trond Sand: THE EFFECTS OF CLICK POLARITY ON BRAINSTEM AUDITORY EVOKED POTENTIALS AMPLITUDE, DISPERSION, AND LATENCY VARIABLES.
69. Kjetil B. Åsbakk: STUDIES OF A PROTEIN FROM PSORIATIC SCALE, PSO P27, WITH RESPECT TO ITS POTENTIAL ROLE IN IMMUNE REACTIONS IN PSORIASIS.
70. Arnulf Hestnes: STUDIES ON DOWN´S SYNDROME.
71. Randi Nygaard: LONG-TERM SURVIVAL IN CHILDHOOD LEUKEMIA.
72. Bjørn Hagen: THIO-TEPA.
73. Svein Anda: EVALUATION OF THE HIP JOINT BY COMPUTED TOMOGRAMPHY AND ULTRASONOGRAPHY.

1992

74. Martin Svartberg: AN INVESTIGATION OF PROCESS AND OUTCOME OF SHORT-TERM PSYCHODYNAMIC PSYCHOTHERAPY.
75. Stig Arild Slørdahl: AORTIC REGURGITATION.
76. Harold C Sexton: STUDIES RELATING TO THE TREATMENT OF SYMPTOMATIC NON-PSYCHOTIC PATIENTS.
77. Maurice B. Vincent: VASOACTIVE PEPTIDES IN THE OCULAR/FOREHEAD AREA.
78. Terje Johannessen: CONTROLLED TRIALS IN SINGLE SUBJECTS.
79. Turid Nilsen: PYROPHOSPHATE IN HEPATOCYTE IRON METABOLISM.
80. Olav Haraldseth: NMR SPECTROSCOPY OF CEREBRAL ISCHEMIA AND REPERFUSION IN RAT.
81. Eiliv Brenna: REGULATION OF FUNCTION AND GROWTH OF THE OXYNTIC MUCOSA.

1993

82. Gunnar Bovim: CERVICOGENIC HEADACHE.
83. Jarl Arne Kahn: ASSISTED PROCREATION.
84. Bjørn Naume: IMMUNOREGULATORY EFFECTS OF CYTOKINES ON NK CELLS.
85. Rune Wiseth: AORTIC VALVE REPLACEMENT.
86. Jie Ming Shen: BLOOD FLOW VELOCITY AND RESPIRATORY STUDIES.
87. Piotr Kruszewski: SUNCT SYNDROME WITH SPECIAL REFERENCE TO THE AUTONOMIC NERVOUS SYSTEM.
88. Mette Haase Moen: ENDOMETRIOSIS.
89. Anne Vik: VASCULAR GAS EMBOLISM DURING AIR INFUSION AND AFTER DECOMPRESSION IN PIGS.
90. Lars Jacob Stovner: THE CHIARI TYPE I MALFORMATION.
91. Kjell Å. Salvesen: ROUTINE ULTRASONOGRAPHY IN UTERO AND DEVELOPMENT IN CHILDHOOD.

1994

92. Nina-Beate Liabakk: DEVELOPMENT OF IMMUNOASSAYS FOR TNF AND ITS SOLUBLE RECEPTORS.
93. Sverre Helge Torp: *erb*B ONCOGENES IN HUMAN GLIOMAS AND MENINGIOMAS.
94. Olav M. Linaker: MENTAL RETARDATION AND PSYCHIATRY. Past and present.
95. Per Oscar Feet: INCREASED ANTIDEPRESSANT AND ANTIPANIC EFFECT IN COMBINED TREATMENT WITH DIXYRAZINE AND TRICYCLIC ANTIDEPRESSANTS.
96. Stein Olav Samstad: CROSS SECTIONAL FLOW VELOCITY PROFILES FROM TWO-DIMENSIONAL DOPPLER ULTRASOUND: Studies on early mitral blood flow.
97. Bjørn Backe: STUDIES IN ANTENATAL CARE.
98. Gerd Inger Ringdal: QUALITY OF LIFE IN CANCER PATIENTS.
99. Torvid Kiserud: THE DUCTUS VENOSUS IN THE HUMAN FETUS.
100. Hans E. Fjøsne: HORMONAL REGULATION OF PROSTATIC METABOLISM.
101. Eylert Brodtkorb: CLINICAL ASPECTS OF EPILEPSY IN THE MENTALLY RETARDED.
102. Roar Juul: PEPTIDERGIC MECHANISMS IN HUMAN SUBARACHNOID HEMORRHAGE.
103. Unni Syversen: CHROMOGRANIN A. Phsysiological and Clinical Role.

1995

104. Odd Gunnar Brakstad: THERMOSTABLE NUCLEASE AND THE *nuc* GENE IN THE DIAGNOSIS OF *Staphylococcus aureus* INFECTIONS.
105. Terje Engan: NUCLEAR MAGNETIC RESONANCE (NMR) SPECTROSCOPY OF PLASMA IN MALIGNANT DISEASE.
106. Kirsten Rasmussen: VIOLENCE IN THE MENTALLY DISORDERED.
107. Finn Egil Skjeldestad: INDUCED ABORTION: Timetrends and Determinants.
108. Roar Stenseth: THORACIC EPIDURAL ANALGESIA IN AORTOCORONARY BYPASS SURGERY.
109. Arild Faxvaag: STUDIES OF IMMUNE CELL FUNCTION *in mice infected with* MURINE RETROVIRUS.

1996

110. Svend Aakhus: NONINVASIVE COMPUTERIZED ASSESSMENT OF LEFT VENTRICULAR FUNCTION AND SYSTEMIC ARTERIAL PROPERTIES. Methodology and some clinical applications.
111. Klaus-Dieter Bolz: INTRAVASCULAR ULTRASONOGRAPHY.
112. Petter Aadahl: CARDIOVASCULAR EFFECTS OF THORACIC AORTIC CROSS-CLAMPING.
113. Sigurd Steinshamn: CYTOKINE MEDIATORS DURING GRANULOCYTOPENIC INFECTIONS.
114. Hans Stifoss-Hanssen: SEEKING MEANING OR HAPPINESS?
115. Anne Kvikstad: LIFE CHANGE EVENTS AND MARITAL STATUS IN RELATION TO RISK AND PROGNOSIS OF CANCER.
116. Torbjørn Grøntvedt: TREATMENT OF ACUTE AND CHRONIC ANTERIOR CRUCIATE LIGAMENT INJURIES. A clinical and biomechanical study.
117. Sigrid Hørven Wigers: CLINICAL STUDIES OF FIBROMYALGIA WITH FOCUS ON ETIOLOGY, TREATMENT AND OUTCOME.
118. Jan Schjøtt: MYOCARDIAL PROTECTION: Functional and Metabolic Characteristics of Two Endogenous Protective Principles.
119. Marit Martinussen: STUDIES OF INTESTINAL BLOOD FLOW AND ITS RELATION TO TRANSITIONAL CIRCULATORY ADAPATION IN NEWBORN INFANTS.
120. Tomm B. Müller: MAGNETIC RESONANCE IMAGING IN FOCAL CEREBRAL ISCHEMIA.
121. Rune Haaverstad: OEDEMA FORMATION OF THE LOWER EXTREMITIES.
122. Magne Børset: THE ROLE OF CYTOKINES IN MULTIPLE MYELOMA, WITH SPECIAL REFERENCE TO HEPATOCYTE GROWTH FACTOR.
123. Geir Smedslund: A THEORETICAL AND EMPIRICAL INVESTIGATION OF SMOKING, STRESS AND DISEASE: RESULTS FROM A POPULATION SURVEY.

1997

124. Torstein Vik: GROWTH, MORBIDITY, AND PSYCHOMOTOR DEVELOPMENT IN INFANTS WHO WERE GROWTH RETARDED *IN UTERO*.
125. Siri Forsmo: ASPECTS AND CONSEQUENCES OF OPPORTUNISTIC SCREENING FOR CERVICAL CANCER. Results based on data from three Norwegian counties.
126. Jon S. Skranes: CEREBRAL MRI AND NEURODEVELOPMENTAL OUTCOME IN VERY LOW BIRTH WEIGHT (VLBW) CHILDREN. A follow-up study of a geographically based year cohort of VLBW children at ages one and six years.
127. Knut Bjørnstad: COMPUTERIZED ECHOCARDIOGRAPHY FOR EVALUTION OF CORONARY ARTERY DISEASE.
128. Grethe Elisabeth Borchgrevink: DIAGNOSIS AND TREATMENT OF WHIPLASH/NECK SPRAIN INJURIES CAUSED BY CAR ACCIDENTS.
129. Tor Elsås: NEUROPEPTIDES AND NITRIC OXIDE SYNTHASE IN OCULAR AUTONOMIC AND SENSORY NERVES.
130. Rolf W. Gråwe: EPIDEMIOLOGICAL AND NEUROPSYCHOLOGICAL PERSPECTIVES ON SCHIZOPHRENIA.
131. Tonje Strømholm: CEREBRAL HAEMODYNAMICS DURING THORACIC AORTIC CROSSCLAMPING. An experimental study in pigs

1998

132. Martinus Bråten: STUDIES ON SOME PROBLEMS REALTED TO INTRAMEDULLARY NAILING OF FEMORAL FRACTURES.

133. Ståle Nordgård: PROLIFERATIVE ACTIVITY AND DNA CONTENT AS PROGNOSTIC INDICATORS IN ADENOID CYSTIC CARCINOMA OF THE HEAD AND NECK.
134. Egil Lien: SOLUBLE RECEPTORS FOR **TNF** AND **LPS**: RELEASE PATTERN AND POSSIBLE SIGNIFICANCE IN DISEASE.
135. Marit Bjørgaas: HYPOGLYCAEMIA IN CHILDREN WITH DIABETES MELLITUS
136. Frank Skorpen: GENETIC AND FUNCTIONAL ANALYSES OF DNA REPAIR IN HUMAN CELLS.
137. Juan A. Pareja: SUNCT SYNDROME. ON THE CLINICAL PICTURE. ITS DISTINCTION FROM OTHER, SIMILAR HEADACHES.
138. Anders Angelsen: NEUROENDOCRINE CELLS IN HUMAN PROSTATIC CARCINOMAS AND THE PROSTATIC COMPLEX OF RAT, GUINEA PIG, CAT AND DOG.
139. Fabio Antonaci: CHRONIC PAROXYSMAL HEMICRANIA AND HEMICRANIA CONTINUA: TWO DIFFERENT ENTITIES?
140. Sven M. Carlsen: ENDOCRINE AND METABOLIC EFFECTS OF METFORMIN WITH SPECIAL EMPHASIS ON CARDIOVASCULAR RISK FACTORES.

1999

141. Terje A. Murberg: DEPRESSIVE SYMPTOMS AND COPING AMONG PATIENTS WITH CONGESTIVE HEART FAILURE.
142. Harm-Gerd Karl Blaas: THE EMBRYONIC EXAMINATION. Ultrasound studies on the development of the human embryo.
143. Noèmi Becser Andersen:THE CEPHALIC SENSORY NERVES IN UNILATERAL HEADACHES. Anatomical background and neurophysiological evaluation.
144. Eli-Janne Fiskerstrand: LASER TREATMENT OF PORT WINE STAINS. A study of the efficacy and limitations of the pulsed dye laser. Clinical and morfological analyses aimed at improving the therapeutic outcome.
145. Bård Kulseng: A STUDY OF ALGINATE CAPSULE PROPERTIES AND CYTOKINES IN RELATION TO INSULIN DEPENDENT DIABETES MELLITUS.
146. Terje Haug: STRUCTURE AND REGULATION OF THE HUMAN UNG GENE ENCODING URACIL-DNA GLYCOSYLASE.
147. Heidi Brurok: MANGANESE AND THE HEART. A Magic Metal with Diagnostic and Therapeutic Possibilites.
148. Agnes Kathrine Lie: DIAGNOSIS AND PREVALENCE OF HUMAN PAPILLOMAVIRUS INFECTION IN CERVICAL INTRAEPITELIAL NEOPLASIA. Relationship to Cell Cycle Regulatory Proteins and HLA DQBI Genes.
149. Ronald Mårvik: PHARMACOLOGICAL, PHYSIOLOGICAL AND PATHOPHYSIOLOGICAL STUDIES ON ISOLATED STOMACS.
150. Ketil Jarl Holen: THE ROLE OF ULTRASONOGRAPHY IN THE DIAGNOSIS AND TREATMENT OF HIP DYSPLASIA IN NEWBORNS.
151. Irene Hetlevik: THE ROLE OF CLINICAL GUIDELINES IN CARDIOVASCULAR RISK INTERVENTION IN GENERAL PRACTICE.
152. Katarina Tunòn: ULTRASOUND AND PREDICTION OF GESTATIONAL AGE.
153. Johannes Soma: INTERACTION BETWEEN THE LEFT VENTRICLE AND THE SYSTEMIC ARTERIES.
154. Arild Aamodt: DEVELOPMENT AND PRE-CLINICAL EVALUATION OF A CUSTOM-MADE FEMORAL STEM.
155. Agnar Tegnander: DIAGNOSIS AND FOLLOW-UP OF CHILDREN WITH SUSPECTED OR KNOWN HIP DYSPLASIA.
156. Bent Indredavik: STROKE UNIT TREATMENT: SHORT AND LONG-TERM EFFECTS
157. Jolanta Vanagaite Vingen: PHOTOPHOBIA AND PHONOPHOBIA IN PRIMARY HEADACHES

2000

158. Ola Dalsegg Sæther: PATHOPHYSIOLOGY DURING PROXIMAL AORTIC CROSS-CLAMPING CLINICAL AND EXPERIMENTAL STUDIES
159. xxxxxxxxx (blind number)
160. Christina Vogt Isaksen: PRENATAL ULTRASOUND AND POSTMORTEM FINDINGS – A TEN YEAR CORRELATIVE STUDY OF FETUSES AND INFANTS WITH DEVELOPMENTAL ANOMALIES.
161. Holger Seidel: HIGH-DOSE METHOTREXATE THERAPY IN CHILDREN WITH ACUTE LYMPHOCYTIC LEUKEMIA: DOSE, CONCENTRATION, AND EFFECT CONSIDERATIONS.

162. Stein Hallan: IMPLEMENTATION OF MODERN MEDICAL DECISION ANALYSIS INTO CLINICAL DIAGNOSIS AND TREATMENT.
163. Malcolm Sue-Chu: INVASIVE AND NON-INVASIVE STUDIES IN CROSS-COUNTRY SKIERS WITH ASTHMA-LIKE SYMPTOMS.
164. Ole-Lars Brekke: EFFECTS OF ANTIOXIDANTS AND FATTY ACIDS ON TUMOR NECROSIS FACTOR-INDUCED CYTOTOXICITY.
165. Jan Lundbom: AORTOCORONARY BYPASS SURGERY: CLINICAL ASPECTS, COST CONSIDERATIONS AND WORKING ABILITY.
166. John-Anker Zwart: LUMBAR NERVE ROOT COMPRESSION, BIOCHEMICAL AND NEUROPHYSIOLOGICAL ASPECTS.
167. Geir Falck: HYPEROSMOLALITY AND THE HEART.
168. Eirik Skogvoll: CARDIAC ARREST Incidence, Intervention and Outcome.
169. Dalius Bansevicius: SHOULDER-NECK REGION IN CERTAIN HEADACHES AND CHRONIC PAIN SYNDROMES.
170. Bettina Kinge: REFRACTIVE ERRORS AND BIOMETRIC CHANGES AMONG UNIVERSITY STUDENTS IN NORWAY.
171. Gunnar Qvigstad: CONSEQUENCES OF HYPERGASTRINEMIA IN MAN
172. Hanne Ellekjær: EPIDEMIOLOGICAL STUDIES OF STROKE IN A NORWEGIAN POPULATION. INCIDENCE, RISK FACTORS AND PROGNOSIS
173. Hilde Grimstad: VIOLENCE AGAINST WOMEN AND PREGNANCY OUTCOME.
174. Astrid Hjelde: SURFACE TENSION AND COMPLEMENT ACTIVATION: Factors influencing bubble formation and bubble effects after decompression.
175. Kjell A. Kvistad: MR IN BREAST CANCER – A CLINICAL STUDY.
176. Ivar Rossvoll: ELECTIVE ORTHOPAEDIC SURGERY IN A DEFINED POPULATION. Studies on demand, waiting time for treatment and incapacity for work.
177. Carina Seidel: PROGNOSTIC VALUE AND BIOLOGICAL EFFECTS OF HEPATOCYTE GROWTH FACTOR AND SYNDECAN-1 IN MULTIPLE MYELOMA.

2001

178. Alexander Wahba: THE INFLUENCE OF CARDIOPULMONARY BYPASS ON PLATELET FUNCTION AND BLOOD COAGULATION – DETERMINANTS AND CLINICAL CONSEQUENSES
179. Marcus Schmitt-Egenolf: THE RELEVANCE OF THE MAJOR hISTOCOMPATIBILITY COMPLEX FOR THE GENETICS OF PSORIASIS
180. Odrun Arna Gederaas: BIOLOGICAL MECHANISMS INVOLVED IN 5-AMINOLEVULINIC ACID BASED PHOTODYNAMIC THERAPY
181. Pål Richard Romundstad: CANCER INCIDENCE AMONG NORWEGIAN ALUMINIUM WORKERS
182. Henrik Hjorth-Hansen: NOVEL CYTOKINES IN GROWTH CONTROL AND BONE DISEASE OF MULTIPLE MYELOMA
183. Gunnar Morken: SEASONAL VARIATION OF HUMAN MOOD AND BEHAVIOUR
184. Bjørn Olav Haugen: MEASUREMENT OF CARDIAC OUTPUT AND STUDIES OF VELOCITY PROFILES IN AORTIC AND MITRAL FLOW USING TWO- AND THREE-DIMENSIONAL COLOUR FLOW IMAGING
185. Geir Bråthen: THE CLASSIFICATION AND CLINICAL DIAGNOSIS OF ALCOHOL-RELATED SEIZURES
186. Knut Ivar Aasarød: RENAL INVOLVEMENT IN INFLAMMATORY RHEUMATIC DISEASE. A Study of Renal Disease in Wegener's Granulomatosis and in Primary Sjögren's Syndrome
187. Trude Helen Flo: RESEPTORS INVOLVED IN CELL ACTIVATION BY DEFINED URONIC ACID POLYMERS AND BACTERIAL COMPONENTS
188. Bodil Kavli: HUMAN URACIL-DNA GLYCOSYLASES FROM THE UNG GENE: STRUCTRUAL BASIS FOR SUBSTRATE SPECIFICITY AND REPAIR
189. Liv Thommesen: MOLECULAR MECHANISMS INVOLVED IN TNF- AND GASTRIN-MEDIATED GENE REGULATION
190. Turid Lingaas Holmen: SMOKING AND HEALTH IN ADOLESCENCE; THE NORD-TRØNDELAG HEALTH STUDY, 1995-97
191. Øyvind Hjertner: MULTIPLE MYELOMA: INTERACTIONS BETWEEN MALIGNANT PLASMA CELLS AND THE BONE MICROENVIRONMENT

192. Asbjørn Støylen: STRAIN RATE IMAGING OF THE LEFT VENTRICLE BY ULTRASOUND. FEASIBILITY, CLINICAL VALIDATION AND PHYSIOLOGICAL ASPECTS
193. Kristian Midthjell: DIABETES IN ADULTS IN NORD-TRØNDELAG. PUBLIC HEALTH ASPECTS OF DIABETES MELLITUS IN A LARGE, NON-SELECTED NORWEGIAN POPULATION.
194. Guanglin Cui: FUNCTIONAL ASPECTS OF THE ECL CELL IN RODENTS
195. Ulrik Wisløff: CARDIAC EFFECTS OF AEROBIC ENDURANCE TRAINING: HYPERTROPHY, CONTRACTILITY AND CALCUIM HANDLING IN NORMAL AND FAILING HEART
196. Øyvind Halaas: MECHANISMS OF IMMUNOMODULATION AND CELL-MEDIATED CYTOTOXICITY INDUCED BY BACTERIAL PRODUCTS
197. Tore Amundsen: PERFUSION MR IMAGING IN THE DIAGNOSIS OF PULMONARY EMBOLISM
198. Nanna Kurtze: THE SIGNIFICANCE OF ANXIETY AND DEPRESSION IN FATIQUE AND PATTERNS OF PAIN AMONG INDIVIDUALS DIAGNOSED WITH FIBROMYALGIA: RELATIONS WITH QUALITY OF LIFE, FUNCTIONAL DISABILITY, LIFESTYLE, EMPLOYMENT STATUS, CO-MORBIDITY AND GENDER
199. Tom Ivar Lund Nilsen: PROSPECTIVE STUDIES OF CANCER RISK IN NORD-TRØNDELAG: THE HUNT STUDY. Associations with anthropometric, socioeconomic, and lifestyle risk factors
200. Asta Kristine Håberg: A NEW APPROACH TO THE STUDY OF MIDDLE CEREBRAL ARTERY OCCLUSION IN THE RAT USING MAGNETIC RESONANCE TECHNIQUES

2002

201. Knut Jørgen Arntzen: PREGNANCY AND CYTOKINES
202. Henrik Døllner: INFLAMMATORY MEDIATORS IN PERINATAL INFECTIONS
203. Asta Bye: LOW FAT, LOW LACTOSE DIET USED AS PROPHYLACTIC TREATMENT OF ACUTE INTESTINAL REACTIONS DURING PELVIC RADIOTHERAPY. A PROSPECTIVE RANDOMISED STUDY.
204. Sylvester Moyo: STUDIES ON STREPTOCOCCUS AGALACTIAE (GROUP B STREPTOCOCCUS) SURFACE-ANCHORED MARKERS WITH EMPHASIS ON STRAINS AND HUMAN SERA FROM ZIMBABWE.
205. Knut Hagen: HEAD-HUNT: THE EPIDEMIOLOGY OF HEADACHE IN NORD-TRØNDELAG
206. Li Lixin: ON THE REGULATION AND ROLE OF UNCOUPLING PROTEIN-2 IN INSULIN PRODUCING ß-CELLS
207. Anne Hildur Henriksen: SYMPTOMS OF ALLERGY AND ASTHMA VERSUS MARKERS OF LOWER AIRWAY INFLAMMATION AMONG ADOLESCENTS
208. Egil Andreas Fors: NON-MALIGNANT PAIN IN RELATION TO PSYCHOLOGICAL AND ENVIRONTENTAL FACTORS. EXPERIENTAL AND CLINICAL STUDES OF PAIN WITH FOCUS ON FIBROMYALGIA
209. Pål Klepstad: MORPHINE FOR CANCER PAIN
210. Ingunn Bakke: MECHANISMS AND CONSEQUENCES OF PEROXISOME PROLIFERATOR-INDUCED HYPERFUNCTION OF THE RAT GASTRIN PRODUCING CELL
211. Ingrid Susann Gribbestad: MAGNETIC RESONANCE IMAGING AND SPECTROSCOPY OF BREAST CANCER
212. Rønnaug Astri Ødegård: PREECLAMPSIA – MATERNAL RISK FACTORS AND FETAL GROWTH
213. Johan Haux: STUDIES ON CYTOTOXICITY INDUCED BY HUMAN NATURAL KILLER CELLS AND DIGITOXIN
214. Turid Suzanne Berg-Nielsen: PARENTING PRACTICES AND MENTALLY DISORDERED ADOLESCENTS
215. Astrid Rydning: BLOOD FLOW AS A PROTECTIVE FACTOR FOR THE STOMACH MUCOSA. AN EXPERIMENTAL STUDY ON THE ROLE OF MAST CELLS AND SENSORY AFFERENT NEURONS

2003

216. Jan Pål Loennechen: HEART FAILURE AFTER MYOCARDIAL INFARCTION. Regional Differences, Myocyte Function, Gene Expression, and Response to Cariporide, Losartan, and Exercise Training.

217. Elisabeth Qvigstad: EFFECTS OF FATTY ACIDS AND OVER-STIMULATION ON INSULIN SECRETION IN MAN
218. Arne Åsberg: EPIDEMIOLOGICAL STUDIES IN HEREDITARY HEMOCHROMATOSIS: PREVALENCE, MORBIDITY AND BENEFIT OF SCREENING.
219. Johan Fredrik Skomsvoll: REPRODUCTIVE OUTCOME IN WOMEN WITH RHEUMATIC DISEASE. A population registry based study of the effects of inflammatory rheumatic disease and connective tissue disease on reproductive outcome in Norwegian women in 1967-1995.
220. Siv Mørkved: URINARY INCONTINENCE DURING PREGNANCY AND AFTER DELIVERY: EFFECT OF PELVIC FLOOR MUSCLE TRAINING IN PREVENTION AND TREATMENT
221. Marit S. Jordhøy: THE IMPACT OF COMPREHENSIVE PALLIATIVE CARE
222. Tom Christian Martinsen: HYPERGASTRINEMIA AND HYPOACIDITY IN RODENTS – CAUSES AND CONSEQUENCES
223. Solveig Tingulstad: CENTRALIZATION OF PRIMARY SURGERY FOR OVARAIN CANCER. FEASIBILITY AND IMPACT ON SURVIVAL
224. Haytham Eloqayli: METABOLIC CHANGES IN THE BRAIN CAUSED BY EPILEPTIC SEIZURES
225. Torunn Bruland: STUDIES OF EARLY RETROVIRUS-HOST INTERACTIONS – VIRAL DETERMINANTS FOR PATHOGENESIS AND THE INFLUENCE OF SEX ON THE SUSCEPTIBILITY TO FRIEND MURINE LEUKAEMIA VIRUS INFECTION
226. Torstein Hole: DOPPLER ECHOCARDIOGRAPHIC EVALUATION OF LEFT VENTRICULAR FUNCTION IN PATIENTS WITH ACUTE MYOCARDIAL INFARCTION
227. Vibeke Nossum: THE EFFECT OF VASCULAR BUBBLES ON ENDOTHELIAL FUNCTION
228. Sigurd Fasting: ROUTINE BASED RECORDING OF ADVERSE EVENTS DURING ANAESTHESIA – APPLICATION IN QUALITY IMPROVEMENT AND SAFETY
229. Solfrid Romundstad: EPIDEMIOLOGICAL STUDIES OF MICROALBUMINURIA. THE NORD-TRØNDELAG HEALTH STUDY 1995-97 (HUNT 2)
230. Geir Torheim: PROCESSING OF DYNAMIC DATA SETS IN MAGNETIC RESONANCE IMAGING
231. Catrine Ahlén: SKIN INFECTIONS IN OCCUPATIONAL SATURATION DIVERS IN THE NORTH SEA AND THE IMPACT OF THE ENVIRONMENT
232. Arnulf Langhammer: RESPIRATORY SYMPTOMS, LUNG FUNCTION AND BONE MINERAL DENSITY IN A COMPREHENSIVE POPULATION SURVEY. THE NORD-TRØNDELAG HEALTH STUDY 1995-97. THE BRONCHIAL OBSTRUCTION IN NORD-TRØNDELAG STUDY
233. Einar Kjelsås: EATING DISORDERS AND PHYSICAL ACTIVITY IN NON-CLINICAL SAMPLES
234. Arne Wibe: RECTAL CANCER TREATMENT IN NORWAY – STANDARDISATION OF SURGERY AND QUALITY ASSURANCE

2004

235. Eivind Witsø: BONE GRAFT AS AN ANTIBIOTIC CARRIER
236. Anne Mari Sund: DEVELOPMENT OF DEPRESSIVE SYMPTOMS IN EARLY ADOLESCENCE
237. Hallvard Lærum: EVALUATION OF ELECTRONIC MEDICAL RECORDS – A CLINICAL TASK PERSPECTIVE
238. Gustav Mikkelsen: ACCESSIBILITY OF INFORMATION IN ELECTRONIC PATIENT RECORDS; AN EVALUATION OF THE ROLE OF DATA QUALITY
239. Steinar Krokstad: SOCIOECONOMIC INEQUALITIES IN HEALTH AND DISABILITY. SOCIAL EPIDEMIOLOGY IN THE NORD-TRØNDELAG HEALTH STUDY (HUNT), NORWAY
240. Arne Kristian Myhre: NORMAL VARIATION IN ANOGENITAL ANATOMY AND MICROBIOLOGY IN NON-ABUSED PRESCHOOL CHILDREN
241. Ingunn Dybedal: NEGATIVE REGULATORS OF HEMATOPOIETEC STEM AND PROGENITOR CELLS
242. Beate Sitter: TISSUE CHARACTERIZATION BY HIGH RESOLUTION MAGIC ANGLE SPINNING MR SPECTROSCOPY
243. Per Arne Aas: MACROMOLECULAR MAINTENANCE IN HUMAN CELLS – REPAIR OF URACIL IN DNA AND METHYLATIONS IN DNA AND RNA

244. Anna Bofin: FINE NEEDLE ASPIRATION CYTOLOGY IN THE PRIMARY INVESTIGATION OF BREAST TUMOURS AND IN THE DETERMINATION OF TREATMENT STRATEGIES
245. Jim Aage Nøttestad: DEINSTITUTIONALIZATION AND MENTAL HEALTH CHANGES AMONG PEOPLE WITH MENTAL RETARDATION
246. Reidar Fossmark: GASTRIC CANCER IN JAPANESE COTTON RATS
247. Wibeke Nordhøy: MANGANESE AND THE HEART, INTRACELLULAR MR RELAXATION AND WATER EXCHANGE ACROSS THE CARDIAC CELL MEMBRANE

2005

248. Sturla Molden: QUANTITATIVE ANALYSES OF SINGLE UNITS RECORDED FROM THE HIPPOCAMPUS AND ENTORHINAL CORTEX OF BEHAVING RATS
249. Wenche Brenne Drøyvold: EPIDEMIOLOGICAL STUDIES ON WEIGHT CHANGE AND HEALTH IN A LARGE POPULATION. THE NORD-TRØNDELAG HEALTH STUDY (HUNT)
250. Ragnhild Støen: ENDOTHELIUM-DEPENDENT VASODILATION IN THE FEMORAL ARTERY OF DEVELOPING PIGLETS
251. Aslak Steinsbekk: HOMEOPATHY IN THE PREVENTION OF UPPER RESPIRATORY TRACT INFECTIONS IN CHILDREN
252. Hill-Aina Steffenach: MEMORY IN HIPPOCAMPAL AND CORTICO-HIPPOCAMPAL CIRCUITS
253. Eystein Stordal: ASPECTS OF THE EPIDEMIOLOGY OF DEPRESSIONS BASED ON SELF-RATING IN A LARGE GENERAL HEALTH STUDY (THE HUNT-2 STUDY)
254. Viggo Pettersen: FROM MUSCLES TO SINGING: THE ACTIVITY OF ACCESSORY BREATHING MUSCLES AND THORAX MOVEMENT IN CLASSICAL SINGING
255. Marianne Fyhn: SPATIAL MAPS IN THE HIPPOCAMPUS AND ENTORHINAL CORTEX
256. Robert Valderhaug: OBSESSIVE-COMPULSIVE DISORDER AMONG CHILDREN AND ADOLESCENTS: CHARACTERISTICS AND PSYCHOLOGICAL MANAGEMENT OF PATIENTS IN OUTPATIENT PSYCHIATRIC CLINICS
257. Erik Skaaheim Haug: INFRARENAL ABDOMINAL AORTIC ANEURYSMS – COMORBIDITY AND RESULTS FOLLOWING OPEN SURGERY
258. Daniel Kondziella: GLIAL-NEURONAL INTERACTIONS IN EXPERIMENTAL BRAIN DISORDERS
259. Vegard Heimly Brun: ROUTES TO SPATIAL MEMORY IN HIPPOCAMPAL PLACE CELLS
260. Kenneth McMillan: PHYSIOLOGICAL ASSESSMENT AND TRAINING OF ENDURANCE AND STRENGTH IN PROFESSIONAL YOUTH SOCCER PLAYERS
261. Marit Sæbø Indredavik: MENTAL HEALTH AND CEREBRAL MAGNETIC RESONANCE IMAGING IN ADOLESCENTS WITH LOW BIRTH WEIGHT
262. Ole Johan Kemi: ON THE CELLULAR BASIS OF AEROBIC FITNESS, INTENSITY-DEPENDENCE AND TIME-COURSE OF CARDIOMYOCYTE AND ENDOTHELIAL ADAPTATIONS TO EXERCISE TRAINING
263. Eszter Vanky: POLYCYSTIC OVARY SYNDROME – METFORMIN TREATMENT IN PREGNANCY
264. Hild Fjærtoft: EXTENDED STROKE UNIT SERVICE AND EARLY SUPPORTED DISCHARGE. SHORT AND LONG-TERM EFFECTS
265. Grete Dyb: POSTTRAUMATIC STRESS REACTIONS IN CHILDREN AND ADOLESCENTS
266. Vidar Fykse: SOMATOSTATIN AND THE STOMACH
267. Kirsti Berg: OXIDATIVE STRESS AND THE ISCHEMIC HEART: A STUDY IN PATIENTS UNDERGOING CORONARY REVASCULARIZATION
268. Björn Inge Gustafsson: THE SEROTONIN PRODUCING ENTEROCHROMAFFIN CELL, AND EFFECTS OF HYPERSEROTONINEMIA ON HEART AND BONE

2006

269. Torstein Baade Rø: EFFECTS OF BONE MORPHOGENETIC PROTEINS, HEPATOCYTE GROWTH FACTOR AND INTERLEUKIN-21 IN MULTIPLE MYELOMA
270. May-Britt Tessem: METABOLIC EFFECTS OF ULTRAVIOLET RADIATION ON THE ANTERIOR PART OF THE EYE
271. Anne-Sofie Helvik: COPING AND EVERYDAY LIFE IN A POPULATION OF ADULTS WITH HEARING IMPAIRMENT

272. Therese Standal: MULTIPLE MYELOMA: THE INTERPLAY BETWEEN MALIGNANT PLASMA CELLS AND THE BONE MARROW MICROENVIRONMENT
273. Ingvild Saltvedt: TREATMENT OF ACUTELY SICK, FRAIL ELDERLY PATIENTS IN A GERIATRIC EVALUATION AND MANAGEMENT UNIT – RESULTS FROM A PROSPECTIVE RANDOMISED TRIAL
274. Birger Henning Endreseth: STRATEGIES IN RECTAL CANCER TREATMENT – FOCUS ON EARLY RECTAL CANCER AND THE INFLUENCE OF AGE ON PROGNOSIS
275. Anne Mari Aukan Rokstad: ALGINATE CAPSULES AS BIOREACTORS FOR CELL THERAPY
276. Mansour Akbari: HUMAN BASE EXCISION REPAIR FOR PRESERVATION OF GENOMIC STABILITY
277. Stein Sundstrøm: IMPROVING TREATMENT IN PATIENTS WITH LUNG CANCER – RESULTS FROM TWO MULITCENTRE RANDOMISED STUDIES
278. Hilde Pleym: BLEEDING AFTER CORONARY ARTERY BYPASS SURGERY - STUDIES ON HEMOSTATIC MECHANISMS, PROPHYLACTIC DRUG TREATMENT AND EFFECTS OF AUTOTRANSFUSION
279. Line Merethe Oldervoll: PHYSICAL ACTIVITY AND EXERCISE INTERVENTIONS IN CANCER PATIENTS
280. Boye Welde: THE SIGNIFICANCE OF ENDURANCE TRAINING, RESISTANCE TRAINING AND MOTIVATIONAL STYLES IN ATHLETIC PERFORMANCE AMONG ELITE JUNIOR CROSS-COUNTRY SKIERS
281. Per Olav Vandvik: IRRITABLE BOWEL SYNDROME IN NORWAY, STUDIES OF PREVALENCE, DIAGNOSIS AND CHARACTERISTICS IN GENERAL PRACTICE AND IN THE POPULATION
282. Idar Kirkeby-Garstad: CLINICAL PHYSIOLOGY OF EARLY MOBILIZATION AFTER CARDIAC SURGERY
283. Linn Getz: SUSTAINABLE AND RESPONSIBLE PREVENTIVE MEDICINE. CONCEPTUALISING ETHICAL DILEMMAS ARISING FROM CLINICAL IMPLEMENTATION OF ADVANCING MEDICAL TECHNOLOGY
284. Eva Tegnander: DETECTION OF CONGENITAL HEART DEFECTS IN A NON-SELECTED POPULATION OF 42,381 FETUSES
285. Kristin Gabestad Nørsett: GENE EXPRESSION STUDIES IN GASTROINTESTINAL PATHOPHYSIOLOGY AND NEOPLASIA
286. Per Magnus Haram: GENETIC VS. AQUIRED FITNESS: METABOLIC, VASCULAR AND CARDIOMYOCYTE ADAPTATIONS
287. Agneta Johansson: GENERAL RISK FACTORS FOR GAMBLING PROBLEMS AND THE PREVALENCE OF PATHOLOGICAL GAMBLING IN NORWAY
288. Svein Artur Jensen: THE PREVALENCE OF SYMPTOMATIC ARTERIAL DISEASE OF THE LOWER LIMB
289. Charlotte Björk Ingul: QUANITIFICATION OF REGIONAL MYOCARDIAL FUNCTION BY STRAIN RATE AND STRAIN FOR EVALUATION OF CORONARY ARTERY DISEASE. AUTOMATED VERSUS MANUAL ANALYSIS DURING ACUTE MYOCARDIAL INFARCTION AND DOBUTAMINE STRESS ECHOCARDIOGRAPHY
290. Jakob Nakling: RESULTS AND CONSEQUENCES OF ROUTINE ULTRASOUND SCREENING IN PREGNANCY – A GEOGRAPHIC BASED POPULATION STUDY
291. Anne Engum: DEPRESSION AND ANXIETY – THEIR RELATIONS TO THYROID DYSFUNCTION AND DIABETES IN A LARGE EPIDEMIOLOGICAL STUDY
292. Ottar Bjerkeset: ANXIETY AND DEPRESSION IN THE GENERAL POPULATION: RISK FACTORS, INTERVENTION AND OUTCOME – THE NORD-TRØNDELAG HEALTH STUDY (HUNT)
293. Jon Olav Drogset: RESULTS AFTER SURGICAL TREATMENT OF ANTERIOR CRUCIATE LIGAMENT INJURIES – A CLINICAL STUDY
294. Lars Fosse: MECHANICAL BEHAVIOUR OF COMPACTED MORSELLISED BONE – AN EXPERIMENTAL IN VITRO STUDY
295. Gunilla Klensmeden Fosse: MENTAL HEALTH OF PSYCHIATRIC OUTPATIENTS BULLIED IN CHILDHOOD
296. Paul Jarle Mork: MUSCLE ACTIVITY IN WORK AND LEISURE AND ITS ASSOCIATION TO MUSCULOSKELETAL PAIN

297. Björn Stenström: LESSONS FROM RODENTS: I: MECHANISMS OF OBESITY SURGERY – ROLE OF STOMACH. II: CARCINOGENIC EFFECTS OF *HELICOBACTER PYLORI* AND SNUS IN THE STOMACH

2007

298. Haakon R. Skogseth: INVASIVE PROPERTIES OF CANCER – A TREATMENT TARGET ? IN VITRO STUDIES IN HUMAN PROSTATE CANCER CELL LINES
299. Janniche Hammer: GLUTAMATE METABOLISM AND CYCLING IN MESIAL TEMPORAL LOBE EPILEPSY
300. May Britt Drugli: YOUNG CHILDREN TREATED BECAUSE OF ODD/CD: CONDUCT PROBLEMS AND SOCIAL COMPETENCIES IN DAY-CARE AND SCHOOL SETTINGS
301. Arne Skjold: MAGNETIC RESONANCE KINETICS OF MANGANESE DIPYRIDOXYL DIPHOSPHATE (MnDPDP) IN HUMAN MYOCARDIUM. STUDIES IN HEALTHY VOLUNTEERS AND IN PATIENTS WITH RECENT MYOCARDIAL INFARCTION
302. Siri Malm: LEFT VENTRICULAR SYSTOLIC FUNCTION AND MYOCARDIAL PERFUSION ASSESSED BY CONTRAST ECHOCARDIOGRAPHY
303. Valentina Maria do Rosario Cabral Iversen: MENTAL HEALTH AND PSYCHOLOGICAL ADAPTATION OF CLINICAL AND NON-CLINICAL MIGRANT GROUPS
304. Lasse Løvstakken: SIGNAL PROCESSING IN DIAGNOSTIC ULTRASOUND: ALGORITHMS FOR REAL-TIME ESTIMATION AND VISUALIZATION OF BLOOD FLOW VELOCITY
305. Elisabeth Olstad: GLUTAMATE AND GABA: MAJOR PLAYERS IN NEURONAL METABOLISM
306. Lilian Leistad: THE ROLE OF CYTOKINES AND PHOSPHOLIPASE A_2S IN ARTICULAR CARTILAGE CHONDROCYTES IN RHEUMATOID ARTHRITIS AND OSTEOARTHRITIS
307. Arne Vaaler: EFFECTS OF PSYCHIATRIC INTENSIVE CARE UNIT IN AN ACUTE PSYCIATHRIC WARD
308. Mathias Toft: GENETIC STUDIES OF LRRK2 AND PINK1 IN PARKINSON'S DISEASE
309. Ingrid Løvold Mostad: IMPACT OF DIETARY FAT QUANTITY AND QUALITY IN TYPE 2 DIABETES WITH EMPHASIS ON MARINE N-3 FATTY ACIDS
310. Torill Eidhammer Sjøbakk: MR DETERMINED BRAIN METABOLIC PATTERN IN PATIENTS WITH BRAIN METASTASES AND ADOLESCENTS WITH LOW BIRTH WEIGHT
311. Vidar Beisvåg: PHYSIOLOGICAL GENOMICS OF HEART FAILURE: FROM TECHNOLOGY TO PHYSIOLOGY
312. Olav Magnus Søndenå Fredheim: HEALTH RELATED QUALITY OF LIFE ASSESSMENT AND ASPECTS OF THE CLINICAL PHARMACOLOGY OF METHADONE IN PATIENTS WITH CHRONIC NON-MALIGNANT PAIN
313. Anne Brantberg: FETAL AND PERINATAL IMPLICATIONS OF ANOMALIES IN THE GASTROINTESTINAL TRACT AND THE ABDOMINAL WALL
314. Erik Solligård: GUT LUMINAL MICRODIALYSIS
315. Elin Tollefsen: RESPIRATORY SYMPTOMS IN A COMPREHENSIVE POPULATION BASED STUDY AMONG ADOLESCENTS 13-19 YEARS. YOUNG-HUNT 1995-97 AND 2000-01; THE NORD-TRØNDELAG HEALTH STUDIES (HUNT)
316. Anne-Tove Brenne: GROWTH REGULATION OF MYELOMA CELLS
317. Heidi Knobel: FATIGUE IN CANCER TREATMENT – ASSESSMENT, COURSE AND ETIOLOGY
318. Torbjørn Dahl: CAROTID ARTERY STENOSIS. DIAGNOSTIC AND THERAPEUTIC ASPECTS
319. Inge-Andre Rasmussen jr.: FUNCTIONAL AND DIFFUSION TENSOR MAGNETIC RESONANCE IMAGING IN NEUROSURGICAL PATIENTS
320. Grete Helen Bratberg: PUBERTAL TIMING – ANTECEDENT TO RISK OR RESILIENCE ? EPIDEMIOLOGICAL STUDIES ON GROWTH, MATURATION AND HEALTH RISK BEHAVIOURS; THE YOUNG HUNT STUDY, NORD-TRØNDELAG, NORWAY
321. Sveinung Sørhaug: THE PULMONARY NEUROENDOCRINE SYSTEM. PHYSIOLOGICAL, PATHOLOGICAL AND TUMOURIGENIC ASPECTS
322. Olav Sande Eftedal: ULTRASONIC DETECTION OF DECOMPRESSION INDUCED VASCULAR MICROBUBBLES
323. Rune Bang Leistad: PAIN, AUTONOMIC ACTIVATION AND MUSCULAR ACTIVITY RELATED TO EXPERIMENTALLY-INDUCED COGNITIVE STRESS IN HEADACHE PATIENTS

324. Svein Brekke: TECHNIQUES FOR ENHANCEMENT OF TEMPORAL RESOLUTION IN THREE-DIMENSIONAL ECHOCARDIOGRAPHY
325. Kristian Bernhard Nilsen: AUTONOMIC ACTIVATION AND MUSCLE ACTIVITY IN RELATION TO MUSCULOSKELETAL PAIN
326. Anne Irene Hagen: HEREDITARY BREAST CANCER IN NORWAY. DETECTION AND PROGNOSIS OF BREAST CANCER IN FAMILIES WITH *BRCA1*GENE MUTATION
327. Ingebjørg S. Juel : INTESTINAL INJURY AND RECOVERY AFTER ISCHEMIA. AN EXPERIMENTAL STUDY ON RESTITUTION OF THE SURFACE EPITHELIUM, INTESTINAL PERMEABILITY, AND RELEASE OF BIOMARKERS FROM THE MUCOSA
328. Runa Heimstad: POST-TERM PREGNANCY
329. Jan Egil Afset: ROLE OF ENTEROPATHOGENIC *ESCHERICHIA COLI* IN CHILDHOOD DIARRHOEA IN NORWAY
330. Bent Håvard Hellum: *IN VITRO* INTERACTIONS BETWEEN MEDICINAL DRUGS AND HERBS ON CYTOCHROME P-450 METABOLISM AND P-GLYCOPROTEIN TRANSPORT
331. Morten André Høydal: CARDIAC DYSFUNCTION AND MAXIMAL OXYGEN UPTAKE MYOCARDIAL ADAPTATION TO ENDURANCE TRAINING

2008

332. Andreas Møllerløkken: REDUCTION OF VASCULAR BUBBLES: METHODS TO PREVENT THE ADVERSE EFFECTS OF DECOMPRESSION
333. Anne Hege Aamodt: COMORBIDITY OF HEADACHE AND MIGRAINE IN THE NORD-TRØNDELAG HEALTH STUDY 1995-97
334. Brage Høyem Amundsen: MYOCARDIAL FUNCTION QUANTIFIED BY SPECKLE TRACKING AND TISSUE DOPPLER ECHOCARDIOGRAPHY – VALIDATION AND APPLICATION IN EXERCISE TESTING AND TRAINING
335. Inger Anne Næss: INCIDENCE, MORTALITY AND RISK FACTORS OF FIRST VENOUS THROMBOSIS IN A GENERAL POPULATION. RESULTS FROM THE SECOND NORD-TRØNDELAG HEALTH STUDY (HUNT2)
336. Vegard Bugten: EFFECTS OF POSTOPERATIVE MEASURES AFTER FUNCTIONAL ENDOSCOPIC SINUS SURGERY
337. Morten Bruvold: MANGANESE AND WATER IN CARDIAC MAGNETIC RESONANCE IMAGING
338. Miroslav Fris: THE EFFECT OF SINGLE AND REPEATED ULTRAVIOLET RADIATION ON THE ANTERIOR SEGMENT OF THE RABBIT EYE
339. Svein Arne Aase: METHODS FOR IMPROVING QUALITY AND EFFICIENCY IN QUANTITATIVE ECHOCARDIOGRAPHY – ASPECTS OF USING HIGH FRAME RATE
340. Roger Almvik: ASSESSING THE RISK OF VIOLENCE: DEVELOPMENT AND VALIDATION OF THE BRØSET VIOLENCE CHECKLIST
341. Ottar Sundheim: STRUCTURE-FUNCTION ANALYSIS OF HUMAN ENZYMES INITIATING NUCLEOBASE REPAIR IN DNA AND RNA
342. Anne Mari Undheim: SHORT AND LONG-TERM OUTCOME OF EMOTIONAL AND BEHAVIOURAL PROBLEMS IN YOUNG ADOLESCENTS WITH AND WITHOUT READING DIFFICULTIES
343. Helge Garåsen: THE TRONDHEIM MODEL. IMPROVING THE PROFESSIONAL COMMUNICATION BETWEEN THE VARIOUS LEVELS OF HEALTH CARE SERVICES AND IMPLEMENTATION OF INTERMEDIATE CARE AT A COMMUNITY HOSPITAL COULD PROVIDE BETTER CARE FOR OLDER PATIENTS. SHORT AND LONG TERM EFFECTS
344. Olav A. Foss: "THE ROTATION RATIOS METHOD". A METHOD TO DESCRIBE ALTERED SPATIAL ORIENTATION IN SEQUENTIAL RADIOGRAPHS FROM ONE PELVIS
345. Bjørn Olav Åsvold: THYROID FUNCTION AND CARDIOVASCULAR HEALTH
346. Torun Margareta Melø: NEURONAL GLIAL INTERACTIONS IN EPILEPSY
347. Irina Poliakova Eide: FETAL GROWTH RESTRICTION AND PRE-ECLAMPSIA: SOME CHARACTERISTICS OF FETO-MATERNAL INTERACTIONS IN DECIDUA BASALIS
348. Torunn Askim: RECOVERY AFTER STROKE. ASSESSMENT AND TREATMENT; WITH FOCUS ON MOTOR FUNCTION
349. Ann Elisabeth Åsberg: NEUTROPHIL ACTIVATION IN A ROLLER PUMP MODEL OF CARDIOPULMONARY BYPASS. INFLUENCE ON BIOMATERIAL, PLATELETS AND COMPLEMENT

350. Lars Hagen: REGULATION OF DNA BASE EXCISION REPAIR BY PROTEIN INTERACTIONS AND POST TRANSLATIONAL MODIFICATIONS
351. Sigrun Beate Kjøtrød: POLYCYSTIC OVARY SYNDROME – METFORMIN TREATMENT IN ASSISTED REPRODUCTION
352. Steven Keita Nishiyama: PERSPECTIVES ON LIMB-VASCULAR HETEROGENEITY: IMPLICATIONS FOR HUMAN AGING, SEX, AND EXERCISE
353. Sven Peter Näsholm: ULTRASOUND BEAMS FOR ENHANCED IMAGE QUALITY
354. Jon Ståle Ritland: PRIMARY OPEN-ANGLE GLAUCOMA & EXFOLIATIVE GLAUCOMA. SURVIVAL, COMORBIDITY AND GENETICS
355. Sigrid Botne Sando: ALZHEIMER'S DISEASE IN CENTRAL NORWAY. GENETIC AND EDUCATIONAL ASPECTS
356. Parvinder Kaur: CELLULAR AND MOLECULAR MECHANISMS BEHIND METHYLMERCURY-INDUCED NEUROTOXICITY
357. Ismail Cüneyt Güzey: DOPAMINE AND SEROTONIN RECEPTOR AND TRANSPORTER GENE POLYMORPHISMS AND EXTRAPYRAMIDAL SYMPTOMS. STUDIES IN PARKINSON'S DISEASE AND IN PATIENTS TREATED WITH ANTIPSYCHOTIC OR ANTIDEPRESSANT DRUGS
358. Brit Dybdahl: EXTRA-CELLULAR INDUCIBLE HEAT-SHOCK PROTEIN 70 (Hsp70) – A ROLE IN THE INFLAMMATORY RESPONSE ?
359. Kristoffer Haugarvoll: IDENTIFYING GENETIC CAUSES OF PARKINSON'S DISEASE IN NORWAY
360. Nadra Nilsen: TOLL-LIKE RECEPTOR 2 –EXPRESSION, REGULATION AND SIGNALING
361. Johan Håkon Bjørngaard: PATIENT SATISFACTION WITH OUTPATIENT MENTAL HEALTH SERVICES – THE INFLUENCE OF ORGANIZATIONAL FACTORS.
362. Kjetil Høydal : EFFECTS OF HIGH INTENSITY AEROBIC TRAINING IN HEALTHY SUBJECTS AND CORONARY ARTERY DISEASE PATIENTS; THE IMPORTANCE OF INTENSITY,, DURATION AND FREQUENCY OF TRAINING.
363. Trine Karlsen: TRAINING IS MEDICINE: ENDURANCE AND STRENGTH TRAINING IN CORONARY ARTERY DISEASE AND HEALTH.
364. Marte Thuen: MANGANASE-ENHANCED AND DIFFUSION TENSOR MR IMAGING OF THE NORMAL, INJURED AND REGENERATING RAT VISUAL PATHWAY
365. Cathrine Broberg Vågbø: DIRECT REPAIR OF ALKYLATION DAMAGE IN DNA AND RNA BY 2-OXOGLUTARATE- AND IRON-DEPENDENT DIOXYGENASES
366. Arnt Erik Tjønna: AEROBIC EXERCISE AND CARDIOVASCULAR RISK FACTORS IN OVERWEIGHT AND OBESE ADOLESCENTS AND ADULTS
367. Marianne W. Furnes: FEEDING BEHAVIOR AND BODY WEIGHT DEVELOPMENT: LESSONS FROM RATS
368. Lene N. Johannessen: FUNGAL PRODUCTS AND INFLAMMATORY RESPONSES IN HUMAN MONOCYTES AND EPITHELIAL CELLS
369. Anja Bye: GENE EXPRESSION PROFILING OF *INHERITED* AND *ACQUIRED* MAXIMAL OXYGEN UPTAKE – RELATIONS TO THE METABOLIC SYNDROME.
370. Oluf Dimitri Røe: MALIGNANT MESOTHELIOMA: VIRUS, BIOMARKERS AND GENES. A TRANSLATIONAL APPROACH
371. Ane Cecilie Dale: DIABETES MELLITUS AND FATAL ISCHEMIC HEART DISEASE. ANALYSES FROM THE HUNT1 AND 2 STUDIES
372. Jacob Christian Hølen: PAIN ASSESSMENT IN PALLIATIVE CARE: VALIDATION OF METHODS FOR SELF-REPORT AND BEHAVIOURAL ASSESSMENT
373. Erming Tian: THE GENETIC IMPACTS IN THE ONCOGENESIS OF MULTIPLE MYELOMA
374. Ole Bosnes: KLINISK UTPRØVING AV NORSKE VERSJONER AV NOEN SENTRALE TESTER PÅ KOGNITIV FUNKSJON
375. Ola M. Rygh: 3D ULTRASOUND BASED NEURONAVIGATION IN NEUROSURGERY. A CLINICAL EVALUATION
376. Astrid Kamilla Stunes: ADIPOKINES, PEROXISOME PROFILERATOR ACTIVATED RECEPTOR (PPAR) AGONISTS AND SEROTONIN. COMMON REGULATORS OF BONE AND FAT METABOLISM
377. Silje Engdal: HERBAL REMEDIES USED BY NORWEGIAN CANCER PATIENTS AND THEIR ROLE IN HERB-DRUG INTERACTIONS
378. Kristin Offerdal: IMPROVED ULTRASOUND IMAGING OF THE FETUS AND ITS CONSEQUENCES FOR SEVERE AND LESS SEVERE ANOMALIES

379. Øivind Rognmo: HIGH-INTENSITY AEROBIC EXERCISE AND CARDIOVASCULAR HEALTH
380. Jo-Åsmund Lund: RADIOTHERAPY IN ANAL CARCINOMA AND PROSTATE CANCER

2009

381. Tore Grüner Bjåstad: HIGH FRAME RATE ULTRASOUND IMAGING USING PARALLEL BEAMFORMING
382. Erik Søndenaa: INTELLECTUAL DISABILITIES IN THE CRIMINAL JUSTICE SYSTEM
383. Berit Rostad: SOCIAL INEQUALITIES IN WOMEN'S HEALTH, HUNT 1984-86 AND 1995-97, THE NORD-TRØNDELAG HEALTH STUDY (HUNT)
384. Jonas Crosby: ULTRASOUND-BASED QUANTIFICATION OF MYOCARDIAL DEFORMATION AND ROTATION
385. Erling Tronvik: MIGRAINE, BLOOD PRESSURE AND THE RENIN-ANGIOTENSIN SYSTEM
386. Tom Christensen: BRINGING THE GP TO THE FOREFRONT OF EPR DEVELOPMENT
387. Håkon Bergseng: ASPECTS OF GROUP B STREPTOCOCCUS (GBS) DISEASE IN THE NEWBORN. EPIDEMIOLOGY, CHARACTERISATION OF INVASIVE STRAINS AND EVALUATION OF INTRAPARTUM SCREENING
388. Ronny Myhre: GENETIC STUDIES OF CANDIDATE TENE3S IN PARKINSON'S DISEASE
389. Torbjørn Moe Eggebø: ULTRASOUND AND LABOUR
390. Eivind Wang: TRAINING IS MEDICINE FOR PATIENTS WITH PERIPHERAL ARTERIAL DISEASE
391. Thea Kristin Våtsveen: GENETIC ABERRATIONS IN MYELOMA CELLS
392. Thomas Jozefiak: QUALITY OF LIFE AND MENTAL HEALTH IN CHILDREN AND ADOLESCENTS: CHILD AND PARENT PERSPECTIVES
393. Jens Erik Slagsvold: N-3 POLYUNSATURATED FATTY ACIDS IN HEALTH AND DISEASE – CLINICAL AND MOLECULAR ASPECTS
394. Kristine Misund: A STUDY OF THE TRANSCRIPTIONAL REPRESSOR ICER. REGULATORY NETWORKS IN GASTRIN-INDUCED GENE EXPRESSION
395. Franco M. Impellizzeri: HIGH-INTENSITY TRAINING IN FOOTBALL PLAYERS. EFFECTS ON PHYSICAL AND TECHNICAL PERFORMANCE
396. Kari Hanne Gjeilo: HEALTH-RELATED QUALITY OF LIFE AND CHRONIC PAIN IN PATIENTS UNDERGOING CARDIAC SURGERY
397. Øyvind Hauso: NEUROENDOCRINE ASPECTS OF PHYSIOLOGY AND DISEASE
398. Ingvild Bjellmo Johnsen: INTRACELLULAR SIGNALING MECHANISMS IN THE INNATE IMMUNE RESPONSE TO VIRAL INFECTIONS
399. Linda Tømmerdal Roten: GENETIC PREDISPOSITION FOR DEVELOPMENT OF PREEMCLAMPSIA – CANDIDATE GENE STUDIES IN THE HUNT (NORD-TRØNDELAG HEALTH STUDY) POPULATION
400. Trude Teoline Nausthaug Rakvåg: PHARMACOGENETICS OF MORPHINE IN CANCER PAIN
401. Hanne Lehn: MEMORY FUNCTIONS OF THE HUMAN MEDIAL TEMPORAL LOBE STUDIED WITH fMRI
402. Randi Utne Holt: ADHESION AND MIGRATION OF MYELOMA CELLS – IN VITRO STUDIES –
403. Trygve Solstad: NEURAL REPRESENTATIONS OF EUCLIDEAN SPACE
404. Unn-Merete Fagerli: MULTIPLE MYELOMA CELLS AND CYTOKINES FROM THE BONE MARROW ENVIRONMENT; ASPECTS OF GROWTH REGULATION AND MIGRATION
405. Sigrid Bjørnelv: EATING– AND WEIGHT PROBLEMS IN ADOLESCENTS, THE YOUNG HUNT-STUDY
406. Mari Hoff: CORTICAL HAND BONE LOSS IN RHEUMATOID ARTHRITIS. EVALUATING DIGITAL X-RAY RADIOGRAMMETRY AS OUTCOME MEASURE OF DISEASE ACTIVITY, RESPONSE VARIABLE TO TREATMENT AND PREDICTOR OF BONE DAMAGE
407. Siri Bjørgen: AEROBIC HIGH INTENSITY INTERVAL TRAINING IS AN EFFECTIVE TREATMENT FOR PATIENTS WITH CHRONIC OBSTRUCTIVE PULMONARY DISEASE
408. Susanne Lindqvist: VISION AND BRAIN IN ADOLESCENTS WITH LOW BIRTH WEIGHT
409. Torbjørn Hergum: 3D ULTRASOUND FOR QUANTITATIVE ECHOCARDIOGRAPHY

410. Jørgen Urnes: PATIENT EDUCATION IN GASTRO-OESOPHAGEAL REFLUX DISEASE. VALIDATION OF A DIGESTIVE SYMPTOMS AND IMPACT QUESTIONNAIRE AND A RANDOMISED CONTROLLED TRIAL OF PATIENT EDUCATION
411. Elvar Eyjolfsson: 13C NMRS OF ANIMAL MODELS OF SCHIZOPHRENIA
412. Marius Steiro Fimland: CHRONIC AND ACUTE NEURAL ADAPTATIONS TO STRENGTH TRAINING
413. Øyvind Støren: RUNNING AND CYCLING ECONOMY IN ATHLETES; DETERMINING FACTORS, TRAINING INTERVENTIONS AND TESTING
414. Håkon Hov: HEPATOCYTE GROWTH FACTOR AND ITS RECEPTOR C-MET. AUTOCRINE GROWTH AND SIGNALING IN MULTIPLE MYELOMA CELLS
415. Maria Radtke: ROLE OF AUTOIMMUNITY AND OVERSTIMULATION FOR BETA-CELL DEFICIENCY. EPIDEMIOLOGICAL AND THERAPEUTIC PERSPECTIVES
416. Liv Bente Romundstad: ASSISTED FERTILIZATION IN NORWAY: SAFETY OF THE REPRODUCTIVE TECHNOLOGY
417. Erik Magnus Berntsen: PREOPERATIV PLANNING AND FUNCTIONAL NEURONAVIGATION – WITH FUNCTIONAL MRI AND DIFFUSION TENSOR TRACTOGRAPHY IN PATIENTS WITH BRAIN LESIONS
418. Tonje Strømmen Steigedal: MOLECULAR MECHANISMS OF THE PROLIFERATIVE RESPONSE TO THE HORMONE GASTRIN
419. Vidar Rao: EXTRACORPOREAL PHOTOCHEMOTHERAPY IN PATIENTS WITH CUTANEOUS T CELL LYMPHOMA OR GRAFT-vs-HOST DISEASE
420. Torkild Visnes: DNA EXCISION REPAIR OF URACIL AND 5-FLUOROURACIL IN HUMAN CANCER CELL LINES

2010

421. John Munkhaugen: BLOOD PRESSURE, BODY WEIGHT, AND KIDNEY FUNCTION IN THE NEAR-NORMAL RANGE: NORMALITY, RISK FACTOR OR MORBIDITY ?
422. Ingrid Castberg: PHARMACOKINETICS, DRUG INTERACTIONS AND ADHERENCE TO TREATMENT WITH ANTIPSYCHOTICS: STUDIES IN A NATURALISTIC SETTING
423. Jian Xu: BLOOD-OXYGEN-LEVEL-DEPENDENT-FUNCTIONAL MAGNETIC RESONANCE IMAGING AND DIFFUSION TENSOR IMAGING IN TRAUMATIC BRAIN INJURY RESEARCH
424. Sigmund Simonsen: ACCEPTABLE RISK AND THE REQUIREMENT OF PROPORTIONALITY IN EUROPEAN BIOMEDICAL RESEARCH LAW. WHAT DOES THE REQUIREMENT THAT BIOMEDICAL RESEARCH SHALL NOT INVOLVE RISKS AND BURDENS DISPROPORTIONATE TO ITS POTENTIAL BENEFITS MEAN?
425. Astrid Woodhouse: MOTOR CONTROL IN WHIPLASH AND CHRONIC NON-TRAUMATIC NECK PAIN
426. Line Rørstad Jensen: EVALUATION OF TREATMENT EFFECTS IN CANCER BY MR IMAGING AND SPECTROSCOPY
427. Trine Moholdt: AEROBIC EXERCISE IN CORONARY HEART DISEASE
428. Øystein Olsen: ANALYSIS OF MANGANESE ENHANCED MRI OF THE NORMAL AND INJURED RAT CENTRAL NERVOUS SYSTEM
429. Bjørn H. Grønberg: PEMETREXED IN THE TREATMENT OF ADVANCED LUNG CANCER
430. Vigdis Schnell Husby: REHABILITATION OF PATIENTS UNDERGOING TOTAL HIP ARTHROPLASTY WITH FOCUS ON MUSCLE STRENGTH, WALKING AND AEROBIC ENDURANCE PERFORMANCE
431. Torbjørn Øien: CHALLENGES IN PRIMARY PREVENTION OF ALLERGY. THE PREVENTION OF ALLERGY AMONG CHILDREN IN TRONDHEIM (PACT) STUDY.
432. Kari Anne Indredavik Evensen: BORN TOO SOON OR TOO SMALL: MOTOR PROBLEMS IN ADOLESCENCE
433. Lars Adde: PREDICTION OF CEREBRAL PALSY IN YOUNG INFANTS. COMPUTER BASED ASSESSMENT OF GENERAL MOVEMENTS
434. Magnus Fasting: PRE- AND POSTNATAL RISK FACTORS FOR CHILDHOOD ADIPOSITY
435. Vivi Talstad Monsen: MECHANISMS OF ALKYLATION DAMAGE REPAIR BY HUMAN AlkB HOMOLOGUES
436. Toril Skandsen: MODERATE AND SEVERE TRAUMATIC BRAIN INJURY. MAGNETIC RESONANCE IMAGING FINDINGS, COGNITION AND RISK FACTORS FOR DISABILITY

437. Ingeborg Smidesang: ALLERGY RELATED DISORDERS AMONG 2-YEAR OLDS AND ADOLESCENTS IN MID-NORWAY – PREVALENCE, SEVERITY AND IMPACT. THE PACT STUDY 2005, THE YOUNG HUNT STUDY 1995-97
438. Vidar Halsteinli: MEASURING EFFICIENCY IN MENTAL HEALTH SERVICE DELIVERY: A STUDY OF OUTPATIENT UNITS IN NORWAY
439. Karen Lehrmann Ægidius: THE PREVALENCE OF HEADACHE AND MIGRAINE IN RELATION TO SEX HORMONE STATUS IN WOMEN. THE HUNT 2 STUDY
440. Madelene Ericsson: EXERCISE TRAINING IN GENETIC MODELS OF HEART FAILURE
441. Marianne Klokk: THE ASSOCIATION BETWEEN SELF-REPORTED ECZEMA AND COMMON MENTAL DISORDERS IN THE GENERAL POPULATION. THE HORDALAND HEALTH STUDY (HUSK)
442. Tomas Ottemo Stølen: IMPAIRED CALCIUM HANDLING IN ANIMAL AND HUMAN CARDIOMYOCYTES REDUCE CONTRACTILITY AND INCREASE ARRHYTHMIA POTENTIAL – EFFECTS OF AEROBIC EXERCISE TRAINING
443. Bjarne Hansen: ENHANCING TREATMENT OUTCOME IN COGNITIVE BEHAVIOURAL THERAPY FOR OBSESSIVE COMPULSIVE DISORDER: THE IMPORTANCE OF COGNITIVE FACTORS
444. Mona Løvlien: WHEN EVERY MINUTE COUNTS. FROM SYMPTOMS TO ADMISSION FOR ACUTE MYOCARDIAL INFARCTION WITH SPECIAL EMPHASIS ON GENDER DIFFERECES
445. Karin Margaretha Gilljam: DNA REPAIR PROTEIN COMPLEXES, FUNCTIONALITY AND SIGNIFICANCE FOR REPAIR EFFICIENCY AND CELL SURVIVAL
446. Anne Byriel Walls: NEURONAL GLIAL INTERACTIONS IN CEREBRAL ENERGY – AND AMINO ACID HOMEOSTASIS – IMPLICATIONS OF GLUTAMATE AND GABA
447. Cathrine Fallang Knetter: MECHANISMS OF TOLL-LIKE RECEPTOR 9 ACTIVATION
448. Marit Følsvik Svindseth: A STUDY OF HUMILIATION, NARCISSISM AND TREATMENT OUTCOME IN PATIENTS ADMITTED TO PSYCHIATRIC EMERGENCY UNITS
449. Karin Elvenes Bakkelund: GASTRIC NEUROENDOCRINE CELLS – ROLE IN GASTRIC NEOPLASIA IN MAN AND RODENTS
450. Kirsten Brun Kjelstrup: DORSOVENTRAL DIFFERENCES IN THE SPATIAL REPRESENTATION AREAS OF THE RAT BRAIN
451. Roar Johansen: MR EVALUATION OF BREAST CANCER PATIENTS WITH POOR PROGNOSIS
452. Rigmor Myran: POST TRAUMATIC NECK PAIN. EPIDEMIOLOGICAL, NEURORADIOLOGICAL AND CLINICAL ASPECTS
453. Krisztina Kunszt Johansen: GENEALOGICAL, CLINICAL AND BIOCHEMICAL STUDIES IN *LRRK2* – ASSOCIATED PARKINSON'S DISEASE
454. Pål Gjerden: THE USE OF ANTICHOLINERGIC ANTIPARKINSON AGENTS IN NORWAY. EPIDEMIOLOGY, TOXICOLOGY AND CLINICAL IMPLICATIONS
455. Else Marie Huuse: ASSESSMENT OF TUMOR MICROENVIRONMENT AND TREATMENT EFFECTS IN HUMAN BREAST CANCER XENOGRAFTS USING MR IMAGING AND SPECTROSCOPY
456. Khalid S. Ibrahim: INTRAOPERATIVE ULTRASOUND ASSESSMENT IN CORONARY ARTERY BYPASS SURGERY – WITH SPECIAL REFERENCE TO CORONARY ANASTOMOSES AND THE ASCENDING AORTA
457. Bjørn Øglænd: ANTHROPOMETRY, BLOOD PRESSURE AND REPRODUCTIVE DEVELOPMENT IN ADOLESCENCE OF OFFSPRING OF MOTHERS WHO HAD PREECLAMPSIA IN PREGNANCY
458. John Olav Roaldset: RISK ASSESSMENT OF VIOLENT, SUICIDAL AND SELF-INJURIOUS BEHAVIOUR IN ACUTE PSYCHIATRY – A BIO-PSYCHO-SOCIAL APPROACH
459. Håvard Dalen: ECHOCARDIOGRAPHIC INDICES OF CARDIAC FUNCTION – NORMAL VALUES AND ASSOCIATIONS WITH CARDIAC RISK FACTORS IN A POPULATION FREE FROM CARDIOVASCULAR DISEASE, HYPERTENSION AND DIABETES: THE HUNT 3 STUDY
460. Beate André: CHANGE CAN BE CHALLENGING. INTRODUCTION TO CHANGES AND IMPLEMENTATION OF COMPUTERIZED TECHNOLOGY IN HEALTH CARE
461. Latha Nrugham: ASSOCIATES AND PREDICTORS OF ATTEMPTED SUICIDE AMONG DEPRESSED ADOLESCENTS – A 6-YEAR PROSPECTIVE STUDY

462. Håvard Bersås Nordgaard: TRANSIT-TIME FLOWMETRY AND WALL SHEAR STRESS ANALYSIS OF CORONARY ARTERY BYPASS GRAFTS – A CLINICAL AND EXPERIMENTAL STUDY

Cotutelle with University of Ghent: Abigail Emily Swillens: A MULTIPHYSICS MODEL FOR IMPROVING THE ULTRASONIC ASSESSMENT OF LARGE ARTERIES

2011

463. Marte Helene Bjørk: DO BRAIN RHYTHMS CHANGE BEFORE THE MIGRAINE ATTACK? A LONGITUDINAL CONTROLLED EEG STUDY
464. Carl-Jørgen Arum: A STUDY OF UROTHELIAL CARCINOMA: GENE EXPRESSION PROFILING, TUMORIGENESIS AND THERAPIES IN ORTHOTOPIC ANIMAL MODELS
465. Ingunn Harstad: TUBERCULOSIS INFECTION AND DISEASE AMONG ASYLUM SEEKERS IN NORWAY. SCREENING AND FOLLOW-UP IN PUBLIC HEALTH CARE
466. Leif Åge Strand: EPIDEMIOLOGICAL STUDIES AMONG ROYAL NORWEGIAN NAVY SERVICEMEN. COHORT ESTABLISHMENT, CANCER INCIDENCE AND CAUSE-SPECIFIC MORTALITY
467. Katrine Høyer Holgersen: SURVIVORS IN THEIR THIRD DECADE AFTER THE NORTH SEA OIL RIG DISASTER OF 1980. LONG-TERM PERSPECTIVES ON MENTAL HEALTH
468. MarianneWallenius: PREGNANCY RELATED ASPECTS OF CHRONIC INFLAMMATORY ARTHRITIDES: DISEASE ONSET POSTPARTUM, PREGNANCY OUTCOMES AND FERTILITY. DATA FROM A NORWEGIAN PATIENT REGISTRY LINKED TO THE MEDICAL BIRTH REGISTRY OF NORWAY
469. Ole Vegard Solberg: 3D ULTRASOUND AND NAVIGATION – APPLICATIONS IN LAPAROSCOPIC SURGERY
470. Inga Ekeberg Schjerve: EXERCISE-INDUCED IMPROVEMENT OF MAXIMAL OXYGEN UPTAKE AND ENDOTHELIAL FUNCTION IN OBESE AND OVERWEIGHT INDIVIDUALS ARE DEPENDENT ON EXERCISE-INTENSITY
471. Eva Veslemøy Tyldum: CARDIOVASCULAR FUNCTION IN PREECLAMPSIA – WITH REFERENCE TO ENDOTHELIAL FUNCTION, LEFT VENTRICULAR FUNCTION AND PRE-PREGNANCY PHYSICAL ACTIVITY
472. Benjamin Garzón Jiménez de Cisneros: CLINICAL APPLICATIONS OF MULTIMODAL MAGNETIC RESONANCE IMAGING
473. Halvard Knut Nilsen: ASSESSING CODEINE TREATMENT TO PATIENTS WITH CHRONIC NON-MALIGNANT PAIN: NEUROPSYCHOLOGICAL FUNCTIONING, DRIVING ABILITY AND WEANING
474. Eiliv Brenner: GLUTAMATE RELATED METABOLISM IN ANIMAL MODELS OF SCHIZOPHRENIA
475. Egil Jonsbu: CHEST PAIN AND PALPITATIONS IN A CARDIAC SETTING; PSYCHOLOGICAL FACTORS, OUTCOME AND TREATMENT
476. Mona Høysæter Fenstad: GENETIC SUSCEPTIBILITY TO PREECLAMPSIA : STUDIES ON THE NORD-TRØNDELAG HEALTH STUDY (HUNT) COHORT, AN AUSTRALIAN/NEW ZEALAND FAMILY COHORT AND DECIDUA BASALIS TISSUE
477. Svein Erik Gaustad: CARDIOVASCULAR CHANGES IN DIVING: FROM HUMAN RESPONSE TO CELL FUNCTION
478. Karin Torvik: PAIN AND QUALITY OF LIFE IN PATIENTS LIVING IN NURSING HOMES
479. Arne Solberg: OUTCOME ASSESSMENTS IN NON-METASTATIC PROSTATE CANCER
480. Henrik Sahlin Pettersen: CYTOTOXICITY AND REPAIR OF URACIL AND 5-FLUOROURACIL IN DNA
481. Pui-Lam Wong: PHYSICAL AND PHYSIOLOGICAL CAPACITY OF SOCCER PLAYERS: EFFECTS OF STRENGTH AND CONDITIONING
482. Ole Solheim: ULTRASOUND GUIDED SURGERY IN PATIENTS WITH INTRACRANIAL TUMOURS
483. Sten Roar Snare: QUANTITATIVE CARDIAC ANALYSIS ALGORITHMS FOR POCKET-SIZED ULTRASOUND DEVICES
484. Marit Skyrud Bratlie: LARGE-SCALE ANALYSIS OF ORTHOLOGS AND PARALOGS IN VIRUSES AND PROKARYOTES
485. Anne Elisabeth F. Isern: BREAST RECONSTRUCTION AFTER MASTECTOMY – RISK OF RECURRENCE AFTER DELAYED LARGE FLAP RECONSTRUCTION – AESTHETIC OUTCOME, PATIENT SATISFACTION, QUALITY OF LIFE AND SURGICAL RESULTS;

HISTOPATHOLOGICAL FINDINGS AND FOLLOW-UP AFTER PROPHYLACTIC MASTECTOMY IN HEREDITARY BREAST CANCER

486. Guro L. Andersen: CEREBRAL PALSY IN NORWAY – SUBTYPES, SEVERITY AND RISK FACTORS
487. Frode Kolstad: CERVICAL DISC DISEASE – BIOMECHANICAL ASPECTS
488. Bente Nordtug: CARING BURDEN OF COHABITANTS LIVING WITH PARTNERS SUFFERING FROM CHRONIC OBSTRUCTIVE PULMONARY DISEASE OR DEMENTIA
489. Mariann Gjervik Heldahl: EVALUATION OF NEOADJUVANT CHEMOTHERAPY IN LOCALLY ADVANCED BREAST CANCER BASED ON MR METHODOLOGY
490. Lise Tevik Løvseth: THE SUBJECTIVE BURDEN OF CONFIDENTIALITY
491. Marie Hjelmseth Aune: INFLAMMATORY RESPONSES AGAINST GRAM NEGATIVE BACTERIA INDUCED BY TLR4 AND NLRP12
492. Tina Strømdal Wik: EXPERIMENTAL EVALUATION OF NEW CONCEPTS IN HIP ARTHROPLASTY
493. Solveig Sigurdardottir: CLINICAL ASPECTS OF CEREBRAL PALSY IN ICELAND. A POPULATION-BASED STUDY OF PRESCHOOL CHILDREN
494. Arne Reimers: CLINICAL PHARMACOKINETICS OF LAMOTRIGINE
495. Monica Wegling: KULTURMENNESKETS BYRDE OG SYKDOMMENS VELSIGNELSE. KAN MEDISINSK UTREDNING OG INTERVENSJON HA EN SELVSTENDIG FUNKSJON UAVHENGIG AV DET KURATIVE?
496. Silje Alvestad: ASTROCYTE-NEURON INTERACTIONS IN EXPERIMENTAL MESIAL TEMPORAL LOBE EPILEPSY – A STUDY OF UNDERLYING MECHANISMS AND POSSIBLE BIOMARKERS OF EPILEPTOGENESIS
497. Javaid Nauman: RESTING HEART RATE: A MATTER OF LIFE OR DEATH – PROSPECTIVE STUDIES OF RESTING HEART RATE AND CARDIOVASCULAR RISK (THE HUNT STUDY, NORWAY)
498. Thuy Nguyen: THE ROLE OF C-SRC TYROSINE KINASE IN ANTIVIRAL IMMUNE RESPONSES
499. Trine Naalsund Andreassen: PHARMACOKINETIC, PHARMACODYNAMIC AND PHARMACOGENETIC ASPECTS OF OXYCODONE TREATMENT IN CANCER PAIN
500. Eivor Alette Laugsand: SYMPTOMS IN PATIENTS RECEIVING OPIOIDS FOR CANCER PAIN – CLINICAL AND PHARMACOGENETIC ASPECTS
501. Dorthe Stensvold: PHYSICAL ACTIVITY, CARDIOVASCULAR HEALTH AND LONGEVITY IN PATIENTS WITH METABOLIC SYNDROME
502. Stian Thoresen Aspenes: PEAK OXYGEN UPTAKE AMONG HEALTHY ADULTS – CROSS-SECTIONAL DESCRIPTIONS AND PROSPECTIVE ANALYSES OF PEAK OXYGEN UPTAKE, PHYSICAL ACTIVITY AND CARDIOVASCULAR RISK FACTORS IN HEALTHY ADULTS (20-90 YEARS)
503. Reidar Alexander Vigen: PATHOBIOLOGY OF GASTRIC CARCINOIDS AND ADENOCARCINOMAS IN RODENT MODELS AND PATIENTS. STUDIES OF GASTROCYSTOPLASTY, GENDER-RELATED FACTORS, AND AUTOPHAGY
504. Halvard Høilund-Kaupang: MODELS AND METHODS FOR INVESTIGATION OF REVERBERATIONS IN NONLINEAR ULTRASOUND IMAGING
505. Audhild Løhre: WELLBEING AMONG SCHOOL CHILDREN IN GRADES 1-10: PROMOTING AND ADVERSE FACTORS
506. Torgrim Tandstad: VOX POPULI. POPULATION-BASED OUTCOME STUDIES IN TESTICULAR CANCER
507. Anna Brenne Grønskag: THE EPIDEMIOLOGY OF HIP FRACTURES AMONG ELDERLY WOMEN IN NORD-TRØNDELAG. HUNT 1995-97, THE NORD-TRØNDELAG HEALTH STUDY
508. Kari Ravndal Risnes: BIRTH SIZE AND ADULT MORTALITY: A SYSTEMATIC REVIEW AND A LONG-TERM FOLLOW-UP OF NEARLY 40 000 INDIVIDUALS BORN AT ST. OLAV UNIVERSITY HOSPITAL IN TRONDHEIM 1920-1960
509. Hans Jakob Bøe: LONG-TERM POSTTRAUMATIC STRESS AFTER DISASTER – A CONTROLLED STUDY OF SURVIVORS' HEALTH 27 YEARS AFTER THE CAPSIZED NORTH SEA OIL RIG
510. Cathrin Barbara Canto, Cotutelle with University of Amsterdam: LAYER SPECIFIC INTEGRATIVE PROPERTIES OF ENTORHINAL PRINCIPAL NEURONS
511. Ioanna Sandvig: THE ROLE OF OLFACTORY ENSHEATHING CELLS, MRI, AND BIOMATERIALS IN TRANSPLANT-MEDIATED CNS REPAIR

512. Karin Fahl Wader: HEPATOCYTE GROWTH FACTOR, C-MET AND SYNDECAN-1 IN MULTIPLE MYELOMA
513. Gerd Tranø: FAMILIAL COLORECTAL CANCER
514. Bjarte Bergstrøm: INNATE ANTIVIRAL IMMUNITY – MECHANISMS OF THE RIG-I-MEDIATED RESPONSE
515. Marie Søfteland Sandvei: INCIDENCE, MORTALITY, AND RISK FACTORS FOR ANEURYSMAL SUBARACHNOID HEMORRHAGE. PROSPECTIVE ANALYZES OF THE HUNT AND TROMSØ STUDIES
516. Mary-Elizabeth Bradley Eilertsen: CHILDREN AND ADOLESCENTS SURVIVING CANCER: PSYCHOSOCIAL HEALTH, QUALITY OF LIFE AND SOCIAL SUPPORT
517. Takaya Saito: COMPUTATIONAL ANALYSIS OF REGULATORY MECHANISM AND INTERACTIONS OF MICRORNAS

Godkjent for disputas, publisert post mortem: Eivind Jullumstrø: COLORECTAL CANCER AT LEVANGER HOSPITAL 1980-2004

518. Christian Gutvik: A PHYSIOLOGICAL APPROACH TO A NEW DECOMPRESSION ALGORITHM USING NONLINEAR MODEL PREDICTIVE CONTROL
519. Ola Storrø: MODIFICATION OF ADJUVANT RISK FACTOR BEHAVIOURS FOR ALLERGIC DISEASE AND ASSOCIATION BETWEEN EARLY GUT MICROBIOTA AND ATOPIC SENSITIZATION AND ECZEMA. EARLY LIFE EVENTS DEFINING THE FUTURE HEALTH OF OUR CHILDREN
520. Guro Fanneløb Giskeødegård: IDENTIFICATION AND CHARACTERIZATION OF PROGNOSTIC FACTORS IN BREAST CANCER USING MR METABOLOMICS
521. Gro Christine Christensen Løhaugen: BORN PRETERM WITH VERY LOW BIRTH WEIGHT – NEVER ENDING COGNITIVE CONSEQUENCES?
522. Sigrid Nakrem: MEASURING QUALITY OF CARE IN NURSING HOMES – WHAT MATTERS?
523. Brita Pukstad: CHARACTERIZATION OF INNATE INFLAMMATORY RESPONSES IN ACUTE AND CHRONIC WOUNDS

2012

524. Hans H. Wasmuth: ILEAL POUCHES
525. Inger Økland: BIASES IN SECOND-TRIMESTER ULTRASOUND DATING RELATED TO PREDICTION MODELS AND FETAL MEASUREMENTS
526. Bjørn Mørkedal: BLOOD PRESSURE, OBESITY, SERUM IRON AND LIPIDS AS RISK FACTORS OF ISCHAEMIC HEART DISEASE
527. Siver Andreas Moestue: MOLECULAR AND FUNCTIONAL CHARACTERIZATION OF BREAST CANCER THROUGH A COMBINATION OF MR IMAGING, TRANSCRIPTOMICS AND METABOLOMICS
528. Guro Aune: CLINICAL, PATHOLOGICAL, AND MOLECULAR CLASSIFICATION OF OVARIAN CARCINOMA
529. Ingrid Alsos Lian: MECHANISMS INVOLVED IN THE PATHOGENESIS OF PRE-ECLAMPSIA AND FETAL GROWTH RESTRICTION. TRANSCRIPTIONAL ANALYSES OF PLACENTAL AND DECIDUAL TISSUE
530. Karin Solvang-Garten: X-RAY REPAIR CROSS-COMPLEMENTING PROTEIN 1 – THE ROLE AS A SCAFFOLD PROTEIN IN BASE EXCISION REPAIR AND SINGLE STRAND BREAK REPAIR
531. Toril Holien: BONE MORPHOGENETIC PROTEINS AND MYC IN MULTIPLE MYELOMA
532. Rooyen Mavenyengwa: *STREPTOCOCCUS AGALACTIAE* IN PREGNANT WOMEN IN ZIMBABWE: EPIDEMIOLOGY AND SEROTYPE MARKER CHARACTERISTICS
533. Tormod Rimehaug: EMOTIONAL DISTRESS AND PARENTING AMONG COMMUNITY AND CLINIC PARENTS
534. Maria Dung Cao: MR METABOLIC CHARACTERIZATION OF LOCALLY ADVANCED BREAST CANCER – TREATMENT EFFECTS AND PROGNOSIS
535. Mirta Mittelstedt Leal de Sousa: PROTEOMICS ANALYSIS OF PROTEINS INVOLVED IN DNA BASE REPAIR AND CANCER THERAPY
536. Halfdan Petursson: THE VALIDITY AND RELEVANCE OF INTERNATIONAL CARDIOVASCULAR DISEASE PREVENTION GUIDELINES FOR GENERAL PRACTICE
537. Marit By Rise: LIFTING THE VEIL FROM USER PARTICIPATION IN CLINICAL WORK – WHAT IS IT AND DOES IT WORK?

538. Lene Thoresen: NUTRITION CARE IN CANCER PATIENTS. NUTRITION ASSESSMENT: DIAGNOSTIC CRITERIA AND THE ASSOCIATION TO SURVIVAL AND HEALTH-RELATED QUALITY OF LIFE IN PATIENTS WITH ADVANCED COLORECTAL CARCINOMA
539. Berit Doseth: PROCESSING OF GENOMIC URACIL IN MAN AND MOUSE
540. Gro Falkenér Bertheussen: PHYSICAL ACTIVITY AND HEALTH IN A GENERAL POPULATION AND IN CANCER SURVIVORS – METHODOLOGICAL, OBSERVATIONAL AND CLINICAL ASPECTS
541. Anne Kari Knudsen: CANCER PAIN CLASSIFICATION
542. Sjur Urdson Gjerald: A FAST ULTRASOUND SIMULATOR
543. Harald Edvard Mølmen Hansen: CARDIOVASCULAR EFFECTS OF HIGH INTENSITY AEROBIC INTERVAL TRAINING IN HYPERTENSITIVE PATIENTS, HEALTHY AGED AND YOUNG PERSONS
544. Sasha Gulati: SURGICAL RESECTION OF HIGH-GRADE GLIOMAS
545. John Chr. Fløvig: FREQUENCY AND EFFECT OF SUBSTANCES AND PSYCHOACTIVE MEDICATIONS THE WEEK BEFORE ADMISSION TO AN ACUTE PSYCHIATRIC DEPARTMENT
546. Kristin Moksnes Husby: OPTIMIZING OPIOID TREATMENT FOR CANCER PAIN – CLINICAL AND PHARMACOLOGICAL ASPECTS
547. Audun Hanssen-Bauer: X-RAY REPAIR CROSS-COMPLEMENTING PROTEIN 1 ASSOCIATED MULTIPROTEIN COMPLEXES IN BASE EXCISION REPAIR
548. Marit Saunes: ECZEMA IN CHILDREN AND ADOLESCENTS – EPIDEMIOLOGY, COURSE AND IMPACT. THE PREVENTION OF ALLERGY AMONG CHILDREN IN TRONDHEIM (PACT) STUDY, YOUNG-HUNT 1995-97
549. Guri Kaurstad: CARDIOMYOCYTE FUNCTION AND CALCIUM HANDLING IN ANIMAL MODELS OF INBORN AND ACQUIRED MAXIMAL OXYGEN UPTAKE
550. Kristian Svendsen: METHODOLOGICAL CHALLENGES IN PHARMACOEPIDEMIOLOGICAL STUDIES OF OPIOID CONSUMPTION
551. Signe Nilssen Stafne: EXERCISE DURING PREGNANCY
552. Marius Widerøe: MAGNETIC RESONANCE IMAGING OF HYPOXIC-ISCHEMIC BRAIN INJURY DEVELOPMENT IN THE NEWBORN RAT – MANGANESE AND DIFFUSION CONTRASTS
553. Andreas Radtke: MOLECULAR METHODS FOR TYPING *STREPTOCOCCUS AGALACTIAE* WITH SPECIAL EMPHASIS ON THE DEVELOPMENT AND VALIDATION OF A MULTI-LOCUS VARIABLE NUMBER OF TANDEM REPEATS ASSAY (MLVA)
554. Thor Wilhelm Bjelland: PHARMACOLOGICAL ASPECTS OF THERAPEUTIC HYPOTHERMIA
555. Caroline Hild Hakvåg Pettersen: THE EFFECT OF OMEGA-3 POLYUNSATURATED FATTY ACIDS ON HUMAN CANCER CELLS – MOLECULAR MECHANISMS INVOLVED
556. Inga Thorsen Vengen: INFLAMMATION AND ATHEROSCLEROSIS – RISK ASSOCIATIONS IN THE HUNT SURVEYS
557. Elisabeth Balstad Magnussen: PREECLAMPSIA, PRETERM BIRTH AND MATERNAL CARDIOVASCULAR RISK FACTORS
558. Monica Unsgaard-Tøndel: MOTOR CONTROL EXERCISES FOR PATIENTS WITH LOW BACK PAIN
559. Lars Erik Sande Laugsand: INSOMNIA AND RISK FOR CARDIOVASCULAR DISEASE
560. Kjersti Grønning: PATIENT EDUCATION AND CHRONIC INFLAMMATORY POLYARTHRITIS – COPING AND EFFECT
561. Hanne Gro Wenzel: PRE AND POST-INJURY HEALTH IN PERSONS WITH WHIPLASH: THE HUNT STUDY. EXPLORATION OF THE FUNCTIONAL SOMATIC MODEL FOR CHRONIC WHIPLASH
562. Øystein Grimstad: TOLL-LIKE RECEPTOR-MEDIATED INFLAMMATORY RESPONSES IN KERATINOCYTES
563. Håkon Olav Leira: DEVELOPMENT OF AN IMAGE GUIDANCE RESEARCH SYSTEM FOR BRONCHOSCOPY
564. Michael A. Lang: DIVING IN EXTREME ENVIRONMENTS: THE SCIENTIFIC DIVING EXPERIENCE

565. Helena Bertilsson: PROSTATE CANCER-TRANSLATIONAL RESEARCH. OPTIMIZING TISSUE SAMPLING SUITABLE FOR HISTOPATHOLOGIC, TRANSCRIPTOMIC AND METABOLIC PROFILING
566. Kirsten M. Selnæs: MR IMAGING AND SPECTROSCOPY IN PROSTATE AND COLON CANCER DIAGNOSTICS
567. Gunvor Steine Fosnes: CONSTIPATION AND DIARRHOEA. EFFECTIVENESS AND ADVERSE EFFECTS OF DRUGS
568. Areej Elkamil: SPASTIC CEREBRAL PALSY: RISK FACTORS, BOTULINUM TOXIN USE AND PREVENTION OF HIP DISLOCATION
569. Ruth Derdikman Eiron: SYMPTOMS OF ANXIETY AND DEPRESSION AND PSYCHOSOCIAL FUNCTION IN MALES AND FEMALES FROM ADOLESCENCE TO ADULTHOOD: LONGITUDINAL FINDINGS FROM THE NORD-TRØNDELAG HEALTH STUDY
570. Constantin Sergiu Jianu: PROTON PUMP INHIBITORS AND GASTRIC NEOPLASIA IN MAN
571. Øystein Finset Sørdal: THE ROLE OF GASTRIN AND THE ECL CELL IN GASTRIC CARCINOGENESIS
572. Lisbeth Østgaard Rygg: GROUP EDUCATION FOR PATIENTS WITH TYPE 2 DIABETES – NEEDS, EXPERIENCES AND EFFECTS
573. Viola Lobert: IDENTIFICATION OF NOVEL REGULATORS OF EPITHELIAL POLARITY AND CELL MIGRATION
574. Maria Tunset Grinde: CHARACTERIZATION OF BREAST CANCER USING MR METABOLOMICS AND GENE EXPRESSION ANALYSIS
575. Grete Kjelvik: HUMAN ODOR IDENTIFICATION STUDIES IN HEALTHY INDIVIDUALS, MILD COGNITIVE IMPAIRMENT AND ALZHEIMER'S DISEASE
576. Tor Eivind Bernstein: RECTAL CANCER SURGERY. PROGNOSTIC FACTORS RELATED TO TREATMENT
577. Kari Sand: INFORMED CONSENT DOCUMENTS FOR CANCER RESEARCH: TEXTUAL AND CONTEXTUAL FACTORS OF RELEVANCE FOR UNDERSTANDING
578. Laurent Francois Thomas: EFFECTS OF SINGLE-NUCLEOTIDE POLYMORPHISMS ON microRNA-BASED GENE REGULATION AND THEIR ASSOCIATION WITH DISEASE
579. Øystein Sandanger: THE INNATE IMMUNE SYSTEM: A PARADOXICAL MEDIATOR OF HOST DEFENSE, TISSUE REPAIR AND COLLATERAL DAMAGE
580. Line Knutsen Lund: MENTAL HEALTH IN LOW BIRTH WEIGHT INDIVIDUALS APPROACHING ADULTHOOD
581. Nils Kristian Skjærvold: AUTOMATED BLOOD GLUCOSE CONTROL – DEVELOPMENT AND TESTING OF AN ARTIFICIAL ENDOCRINE PANCREAS USING AV NOVEL INTRAVASCULAR GLUCOSE MONITOR AND A NEW APPROACH TO INSULIN PHARMACOLOGY
582. Håvard Kallestad: SLEEP DISTURBANCE: CLINICAL SIGNIFICANCE IN MENTAL HEALTH CARE AND COGNITIVE FACTORS
583. Anders Wallenius: URACIL-DNA GLYCOSYLASE, ACTIVATION-INDUCED DEAMINASE AND REGULATION OF ADAPTIVE IMMUNE RESPONSES
584. Gry Børmark Hoftun: CHRONIC NON-SPECIFIC PAIN IN ADOLESCENCE PREVALENCE, DISABILITY, AND ASSOCIATED FACTORS – YOUNG-HUNT AND HUNT 3, 2006-2008
585. Elisabeth Hansen: THE SIGNIFICANCE OF RESISTANCE TRAINING AND PSYCHOBIOLOGY IN PRIMARY PREVENTION OF TYPE 2 DIABETES AMONG PEOPLE WITH IMPAIRED GLUCOSE TOLERANCE
586. Ragnhild Omli: URINARY INCONTINENCE AND URINARY TRACT INFECTIONS IN THE ELDERLY: RISK FACTORS AND CONSEQUENCES
587. Christina Sæten Fjeldbo: GASTRIN-MEDIATED REGULATION OF GENE EXPRESSION; A SYSTEMS BIOLOGY APPROACH
588. Yunita Widyastuti: RISK FACTORS FOR COMMON COMPLICATIONS FOLLOWING ADULT HEART SURGERY
589. Anders Thorstensen: 2D AND 3D ECHOCARDIOGRAPHY DURING INOTROPIC ALTERATIONS AND AFTER RECENT MYOCARDIAL INFARCTION
590. Torstein Schrøder-Aasen: EFFECTS OF PURPLE CONEFLOWER (ECHINACEA PURPUREA) ON CYP3A4 METABOLISM AND P-GLYCOPROTEIN MEDIATED TRANSPORT *IN VITRO*

591. Saeed Mehdizadeh: ADAPTIVE BEAMFORMERS FOR ULTRASOUND IMAGING OF ACOUSTICALLY HARD TISSUES